Small-Crack Effects in High-Strength Aluminum Alloys

A NASA/CAE Cooperative Program

J. C. Newman, Jr., X. R. Wu, S. L. Venneri, and C. G. Li

Small-Crack Effects in High-Strength Aluminum Alloys

A NASA/CAE Cooperative Program

J. C. Newman, Jr.
Langley Research Center • Hampton, Virginia

X. R. Wu
Institute of Aeronautical Materials • Beijing, People's Republic of China

S. L. Venneri
National Aeronautics and Space Administration • Washington, D.C.

C. G. Li
Institute of Aeronautical Materials • Beijing, People's Republic of China

May 1994

The use of trademarks or names of manufacturers in this report is for accurate reporting and does not constitute an official endorsement, either expressed or implied, of such products or manufacturers by the National Aeronautics and Space Administration.

Contents

Preface

In May 1985, the National Aeronautics and Space Administration (NASA) and the Chinese Aeronautical Establishment (CAE) held a symposium on structural analysis methods in Beijing, China. During technical discussions and subsequent visits of NASA scientists to several CAE research institutes, areas of mutual interest for technical cooperation were identified. A joint working group meeting was held in late 1985 in Washington, D.C. Annex III to the Protocol on Cooperation in Aeronautical Science and Technology between NASA of the United States of America and the CAE of the People's Republic of China was signed in February 1987. During 1986 and early 1987, a joint technology plan on fatigue and fracture mechanics was established.

This report describes the findings of the Fatigue and Fracture Mechanics Cooperative Program. The cooperative program was initiated, organized, directed, and completed by many members of each research organization. Participants included

Function	NASA	CAE
Technical Representative	S. L. Venneri	C. G. Li
Coordinator	J. C. Newman, Jr.	X. R. Wu
Contributor	M. H. Swain	W. Zhao
Contributor	E. P. Phillips	C. F. Ding
Contributor	P. W. Tan	H. Y. Li
Contributor	I. S. Raju	
Contributor	K. N. Shivakumar	
International Affairs	L. Parker	X. Y. Zhu

The cooperative program demonstrated that international cooperation among research organizations can be fruitful. The program has also advanced the state of the art in fatigue and fracture mechanics and has provided aerospace industries with useful data from experiments and with efficient analysis methods for improving life prediction. These results should ultimately improve the reliability and safety of aircraft structures.

PRECEDING PAGE BLANK NOT FILMED

Nomenclature

a	one-half surface- or total corner-crack depth, m
a_i	initial one-half material defect (or crack) depth, m
a_x	crack depth in slice model, m
B	specimen thickness, m
b	material defect (or void) height, m
c	surface-, corner-, or through-crack length, m
c_i	initial material defect (or crack) length, m
c_n	initial crack starter notch length, m
c_y	crack length in slice model, m
c'	crack length plus hole radius, m
da/dN	crack-growth rate in a-direction, m per cycle
dc/dN	crack-growth rate in c-direction, m per cycle
d_S	inclusion particle size in short direction, m
d_T	inclusion particle size in transverse direction, m
E	Young's modulus, MPa
E_s	elastic modulus for spring slices, MPa
F'_c	boundary correction stress intensity factor for corner crack with clad correction
F_j	boundary correction stress intensity factor (j = c, s, or t)
G_c	clad correction on stress intensity factor
g_i	fitting functions for boundary-correction factor
h	one-half specimen height, m
K	stress intensity factor, MPa-m$^{1/2}$
K_{ce}	stress intensity factor for partially loaded edge crack, MPa-m$^{1/2}$
K_e	stress intensity factor for edge crack, MPa-m$^{1/2}$
K'_o	crack opening stress intensity factor, MPa-m$^{1/2}$
K_T	stress concentration factor
k_i	spring stiffness in slice model (i = a or c), N/m
L	total depth of surface ($2a$) or corner crack (a) along notch, m
ℓ	clad-layer thickness, m
N	cycles
N_f	cycles to failure
$P(x, y)$	weight-function spring forces, N
Q	shape factor for surface or corner crack
R	stress ratio $\left(\dfrac{S_{\min}}{S_{\max}} \right)$
R_i	restraining areas in slice model (i = a or c), m^2

r	semicircular notch radius, m
S	applied gross stress, MPa
S_{max}	maximum applied gross stress, MPa
S_{mf}	mean flight stress in Mini-TWIST spectrum, MPa
S_{min}	minimum applied gross stress, MPa
S'_o	crack-opening stress, MPa
S, T, L	short, transverse, and longitudinal directions, figure 5
T_1, T_2, T_3	transition points in ΔK-rate relation
t	one-half or full specimen thickness, m
t_i	distance from sheet centerline to crack initiation site, m
u, v	displacement in x- and y-directions, respectively, m
W_i	weight function in slice model ($i = a$ or c), m$^{-1/2}$
w	one-half specimen width or full specimen width, m
w_n	width of crack-tip element, m
x, y, z	Cartesian coordinates
α	constraint factor
β_R	crack-closure factor ratio
ΔK	stress intensity factor range, MPa-m$^{1/2}$
ΔK_{eff}	effective stress intensity factor range, MPa-m$^{1/2}$
$(\Delta K_{eff})_{th}$	effective threshold stress intensity factor range, MPa-m$^{1/2}$
ΔK_{th}	large-crack threshold stress intensity factor range, MPa-m$^{1/2}$
ΔN	interval between plastic replicas, cycles
ΔS	applied stress range ($S_{max} - S_{min}$), MPa
ρ	length of tensile plastic zone, m
σ	uniform stress, MPa
σ_o	flow stress (average between σ_{ys} and σ_u), MPa
σ_u	ultimate tensile strength, MPa
σ_{ys}	yield stress (0.2-percent offset), MPa
σ_{yy}	normal stress in y-direction, MPa
φ	parametric angle of ellipse, rad
ω	length of cyclic plastic zone, m

Subscripts:

c	corner crack at notch
s	surface crack at notch
t	through crack at notch

Abbreviations:

ASTM	American Society for Testing and Materials
BFM	boundary force method
BIAM	Beijing Institute of Aeronautical Materials
CAE	Chinese Aeronautical Establishment
CCT	center-crack tension
DOF	degree of freedom
EDI	equivalent domain integral
EDM	electrical discharge machining
FEM	finite-element method
LaRC	Langley Research Center
LEFM	linear-elastic fracture mechanics
NASA	National Aeronautics and Space Administration
PRC	People's Republic of China
SEM	scanning electron microscope
SENT	single-edge-notch tension
S-N	material stress-cyclic life relation
2D	two dimensional
3D	three dimensional
US	United States
VCCT	virtual crack closure technique
WFM	weight-function method

Summary

From 1987 to 1992 the National Aeronautics and Space Administration and the Chinese Aeronautical Establishment participated in a Fatigue and Fracture Mechanics Cooperative Program, the first cooperative exchange between the scientific organizations of the two countries. The program objectives were to study crack initiation and the growth of small cracks in two high-strength aluminum alloys, to compare test and analysis results from each laboratory, and to evaluate an existing analytical model to predict the growth of such cracks. Experimental and analytical studies were conducted on various aspects of fatigue crack growth of small and large cracks.

In the experimental program, three types of tests were conducted: fatigue tests on single-edge-notch tension (SENT) specimens, small-crack tests on the SENT specimens, and large-crack tests on center-crack tension (CCT) specimens. The initiation and growth of small fatigue cracks (10 μm to 2 mm long) from the edge of a semicircular notch in 7075-T6 and LC9cs aluminum alloy sheets were monitored for various load histories by means of a plastic replica method. In both alloys, small cracks were initiated as naturally occurring from material defects or cladding.

In the 7075-T6 bare alloy, cracks initiated from inclusion particles or voids on the notch surface and generally grew as surface cracks. Cracks in the LC9cs clad alloy, however, initiated at slip bands in the cladding layer and grew as corner cracks. Tests were conducted for both constant-amplitude (stress ratios of $R = -1$, 0, and 0.5) and spectrum (Mini-TWIST) loading conditions at two or three stress levels each. The replica method was found to affect fatigue life and apparently small-crack-growth rates of the 7075-T6 alloy, but the method did not appear to affect fatigue lives for the LC9cs clad alloy. Data on large-crack growth (cracks greater than 2 mm long) were obtained for a wide range in rates (10^{-8} to 10^{-1} mm per cycle) for all constant-amplitude loading conditions. Data on large-crack growth for the Mini-TWIST loading sequence were also obtained on the same materials.

The experimental results from the participants in the cooperative program showed good agreement on small- and large-crack-growth rates and on fatigue lives. The small cracks exhibited the classical "small-crack" effect because they grew faster than large cracks for the same stress intensity factor range. They also grew at stress intensity factor ranges that were lower than the thresholds obtained from large-crack tests for constant-amplitude loading. During small-crack tests at the higher stress levels, multiple cracks initiated along the bore of the notch. At the lower stress levels, particularly those near the fatigue limit, the tests produced only a few cracks along the bore. The small-crack data showed a larger amount of scatter than observed in large-crack data due to crack-grain boundary interactions and crack interactions with neighboring cracks. Noninteraction criteria were used to eliminate data where cracks interacted. This approach greatly reduced the scatter in the stress intensity factor against crack-growth rate data. Results from the study showed that fatigue life, even near the fatigue limit, was mostly crack propagation from a material defect or from the cladding layer.

In the analysis program, three-dimensional finite-element and weight-function methods were used to determine stress intensity factors for a surface crack and a corner crack at the notch in the SENT specimen. In general, the two analysis methods gave very similar results for a wide range of crack shapes and sizes. Stress intensity factor equations were developed for a wide range of crack configuration parameters. These equations were used in the small-crack data correlations and in life predictions. An indirect boundary element method and an experimental technique were used to obtain stress intensity factors and equations for a through crack in the SENT specimens tested in remote, fixed-grip (displacement) conditions.

A crack-growth model that incorporated crack-closure effects was used to analyze the growth of small cracks along the bore of the notch. Small cracks were assumed to initiate either at inclusion-particle defects (surface crack) or in the cladding layer (corner crack). In the 7075-T6 alloy, the initial defect size was consistent with observations of initiation sites at inclusion-particle clusters or voids. In the LC9cs clad alloy, an initial defect slightly larger than the clad-layer thickness was used. For both materials, the effective stress intensity factor against crack-growth rate relations was different in the crack-depth (through the sheet thickness) and crack-length (sheet width) directions. At high crack-growth rates and, especially for the Mini-TWIST loading sequence, a variable-constraint method was used to correlate and predict crack growth. Reasonable agreement was found between measured and predicted small- and large-crack-growth rates, surface- and corner-crack shapes, and fatigue lives for most loading conditions. For loading at a high stress ratio ($R = 0.5$), the model predicted slightly faster rates than those measured experimentally. This particular loading condition involved a local notch root that yielded while in tension, a condition approximated in the model. The

closure model did confirm the experimental findings that the small-crack effect was more pronounced in those tests involving compressive loads, such as constant-amplitude loading at a negative stress ratio ($R = -1$).

The cooperative program demonstrated that international cooperation among research organizations can be fruitful. The program also has advanced the state of the art in fatigue and fracture mechanics and has provided aerospace industries with useful data from experiments and with efficient analysis methods for improving life prediction. These results should ultimately improve the reliability and safety of aircraft structures.

1. Introduction

Linear-elastic fracture mechanics methods are widely accepted for damage tolerance analyses. The trend has also been toward the use of the same methodology for fatigue durability analyses. To obtain acceptably large lives without a significant weight penalty, durability analyses must assume very small initial cracks. Numerous investigators (refs. 1–20) have observed that the growth characteristics of small fatigue cracks in plates and at notches differ from those of large cracks in the same material. These studies have concentrated on the growth of small cracks 10 μm to 1 mm long. On the basis of linear-elastic fracture mechanics (LEFM), small cracks grew much faster than predicted from large-crack data. This behavior is illustrated in figure 1, where the crack-growth rate is plotted against the linear-elastic stress intensity factor range ΔK. The solid (sigmoidal) curve shows typical results for a given material and environment for constant-amplitude loading. The solid curve is usually obtained from tests with large cracks. At low growth rates, the threshold stress intensity factor range ΔK_{th} is usually obtained from load-reduction (ΔK-decreasing) tests. Typical experimental results for small cracks in plates and at notches are shown by the dashed curves. These results show that small cracks grow at ΔK levels below the large-crack threshold and that they also can grow faster than large cracks at the same ΔK level above threshold. Small-crack effects have been shown to be more prevalent in tests with compressive loads and negative stress ratios. (See refs. 19 and 20.)

During the last decade, research on the small- or short-crack effect has concentrated on three possible explanations for the behavior of such cracks: plasticity effects, metallurgical effects, and crack closure. All of these features contribute to a breakdown of
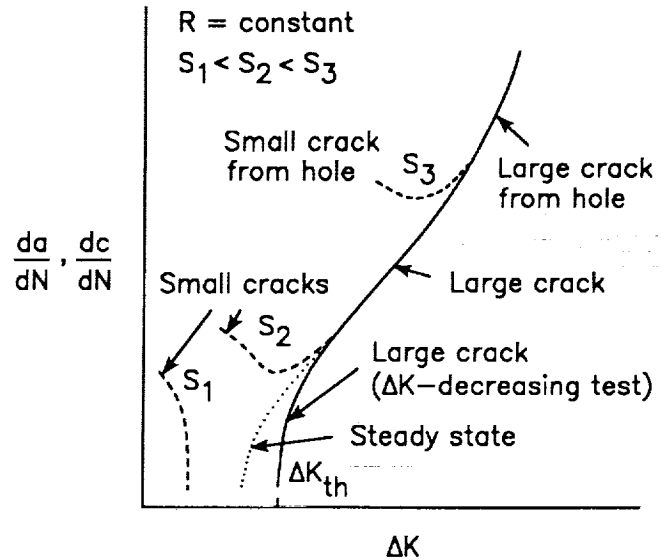
Figure 1. Typical fatigue crack-growth rate data for small and large cracks under constant-amplitude loading.

LEFM and to the use of the ΔK concept to correlate fatigue crack-growth rates.

Some of the earliest small-crack experiments (refs. 1–4) were conducted at high stress levels that were expected to invalidate LEFM procedures. Nonlinear or elastic-plastic fracture mechanics concepts, such as the J integral and an empirical length parameter (refs. 3 and 4), were developed to explain the observed small-crack effects. Recent research on the cyclic Dugdale model and the use of ΔJ (cyclic J integral) as a crack-driving parameter suggest that plasticity effects are small for many of the early and more recent small-crack experiments. (See ref. 21.) However, the effect of plasticity on small-crack growth and on the appropriate crack-driving parameter is still being debated.

Small cracks generally initiate in metallic materials at inclusion particles or voids, in regions of intense slip, or at weak interfaces and grains. In these cases, metallurgical similitude (refs. 10, 16, and 17) breaks down—that is, the growth rate is no longer an average over many grains. Thus, the local growth behavior is controlled by metallurgical features. (See refs. 6 and 12.) If the material is markedly anisotropic (differences in modulus and yield stress in different crystallographic directions), the local grain orientation will strongly affect the rate of growth. Crack-front irregularities and small particles or inclusions do affect the local stresses and, therefore, crack growth. For large cracks (with large fronts), all these metallurgical effects are averaged over many grains, except in very coarse-grained materials. Researchers

in linear elastic and nonlinear fracture mechanics are only beginning to explore how metallurgical features affect stress intensity factors, strain-energy densities, J integrals, and other crack-driving parameters.

Very early in small-crack research, fatigue crack closure (ref. 22) was recognized as a possible explanation for rapid small-crack growth. (See refs. 5–11 and 23.) Fatigue crack closure is caused by residual plastic deformations left in the wake of an advancing crack. Only that portion of the load cycle for which the crack is fully open is used to compute an effective stress intensity factor range ΔK_{eff} from LEFM solutions. A small crack that initiates at an inclusion particle, a void, or a weak grain does not have the prior plastic history to develop closure. Thus, a small crack may not be closed for as much of the loading cycle as a larger crack. If a small crack is fully open, the stress intensity factor range is fully effective and the growth rate will be greater than that for steady-state crack growth. (A steady-state crack is one in which the residual plastic deformations and crack closure along the crack surfaces are fully developed.) In contrast, the development of the large-crack threshold, as illustrated in figure 1, has been associated with a rise in crack closure as the load is reduced. (See ref. 24.) Thus, steady-state crack-growth behavior may be between the small-crack and near-threshold large-crack behavior, as illustrated by the dotted curve. The results from this study suggest this possibility.

As the crack size approaches zero, a crack size must exist below which the assumptions of continuum mechanics and the ΔK concept are violated because of microstructural features. However, the transition from valid to invalid conditions does not occur abruptly. For many engineering applications, a ΔK-based analysis that extends into the "gray area" of validity may still prove useful. Certainly for structural designers, a single analysis methodology that applies to all crack sizes is desirable, as demonstrated in a total-life analysis in reference 25. If for no other reason than that ΔK analyses are already being used for large-crack problems, the application of a ΔK analysis to small-crack problems should be thoroughly explored. The approach in this report is to apply both continuum mechanics and ΔK_{eff} concepts to small- and large-crack growth.

2. Cooperative Program Overview

In May 1985, the United States (US) National Aeronautics and Space Administration (NASA) and the People's Republic of China (PRC) Chinese Aeronautical Establishment (CAE) held a symposium on structural analysis methods in Beijing, China. During technical discussions between NASA and CAE scientists, several research areas of mutual interest were identified for technical cooperation. Small-crack growth and the breakdown of linear-elastic fracture mechanics concepts particularly were identified as important problems to the aircraft industries of both nations. The CAE had recently developed a simple weight-function method (WFM) for analyzing cracks in two-dimensional (2D) crack configurations. Also, a new three-dimensional (3D) WFM had emerged for analyzing surface and corner cracks at stress concentrations. These new approaches offered an excellent basis for comparison with existing methods and solutions that NASA had developed using the finite-element method (FEM). In addition, NASA had recently improved a life-prediction method based on the crack-closure concept. These new developments offered an opportunity to develop a research plan between the two organizations.

A joint technology plan on fatigue and fracture mechanics was established during late 1986 and early 1987. Scientists in the cooperative program were to study small-crack growth, to develop a link between classical stress-cyclic life (S-N) fatigue behavior and modern damage-tolerance methodologies, to bridge durability and damage tolerance analyses, to improve life-prediction capabilities by developing more accurate stress intensity factor solutions for small cracks, and to evaluate an existing analytical model to predict the growth of such cracks. Exchange of materials and analysis methods began in early 1987. Three joint meetings were held between NASA and CAE for data exchanges and in-depth discussions. Meetings were held at the Beijing Institute of Aeronautical Materials (BIAM) in Beijing, China, in 1987 and 1992 and at the Langley Research Center (LaRC) in Hampton, Virginia, in 1989.

The cooperative program brought together fatigue and fracture mechanics researchers to study the small-crack effects in high-strength aluminum alloys of interest to each country. The program objectives were to identify and characterize through experiments and analyses the initiation and growth of small cracks (10 μm to 2 mm long) in common US and PRC aluminum alloys, to improve fracture mechanics analyses of surface- and corner-crack configurations, and to develop improved life-prediction methods to correlate and predict the growth of small and large cracks for constant-amplitude and aircraft spectrum loading.

To achieve the objectives of the cooperative program, experiments and analyses were conducted in each laboratory on two high-strength aluminum

alloys, 7075-T6 bare and LC9cs clad sheet. Three types of tests were conducted: fatigue tests on single-edge-notch tension (SENT) specimens, small-crack tests on the SENT specimens, and large-crack tests on CCT specimens. The initiation and growth of small fatigue cracks (10 μm to 2 mm long) at the semicircular notch were monitored based on the plastic-replica method. Tests were conducted at several constant-amplitude ($R = -1$, 0, and 0.5) and spectrum (Mini-TWIST) loading conditions at two or three stress levels each. Large-crack-growth rates (cracks greater than 2 mm long) were obtained for a wide range in rates (10^{-8} to 10^{-1} mm per cycle) for all constant-amplitude loading conditions. Rates of large-crack growth from the Mini-TWIST loading sequence were also obtained for the same alloys.

The small-crack specimen was selected to produce naturally occurring cracks at material defects or discontinuities and to propagate cracks through a stress field similar to that in aircraft structures. A SENT specimen was used. (See fig. 2.) The notch was semicircular, had a radius r of 3.2 mm, and a width w of 50 mm. The stress concentration factor was 3.15, based on gross section stress. (See ref. 26.) Figure 3 shows the normal stress distribution near the notch root for the SENT specimen (solid curve). For comparison, the normal stress distribution for a circular hole in an infinite plate is shown as the dashed curve. The normal stress distribution for the SENT specimen is similar to that for an open hole in an infinite plate, but the stresses are slightly higher because of the finite width. Thus, the SENT specimen simulates a hole in an aircraft structure. Use of a side notch rather than a hole allows the notch root to be observed with a microscope and plastic replicas to be taken with ease during tests. A typical test stand with the SENT specimen and the guide plates that were used for compressive loading tests is shown in figure 4.

The three-dimensional FEM and the WFM were used to determine stress intensity factors for surface and corner cracks at the notch in the SENT specimen. The results from these two methods were then compared for a range of crack-configuration parameters. A brief description of the FEM and the WFM is presented in appendixes A and B, respectively. Two-dimensional weight-function analyses were used to develop weight functions for use in the 3D WFM. These analyses are discussed in appendix C. An indirect boundary element method, referred to as the boundary force method (BFM), was also used to obtain stress intensity factors for a through crack in the SENT specimen for either uniform remote stress or displacement boundary conditions. Numerical re-
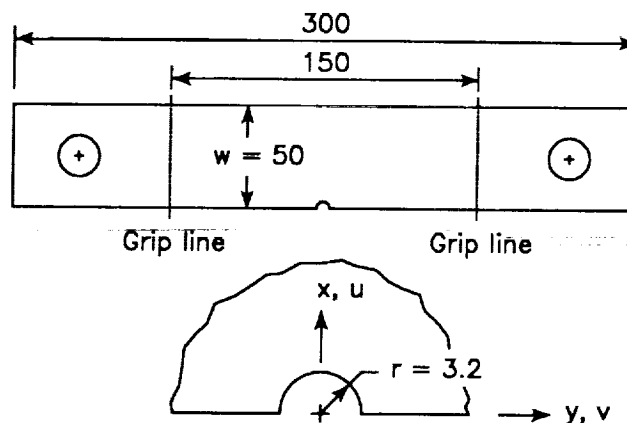
Figure 2. Single-edge-notch tension (SENT) fatigue specimen. All dimensions are in millimeters.
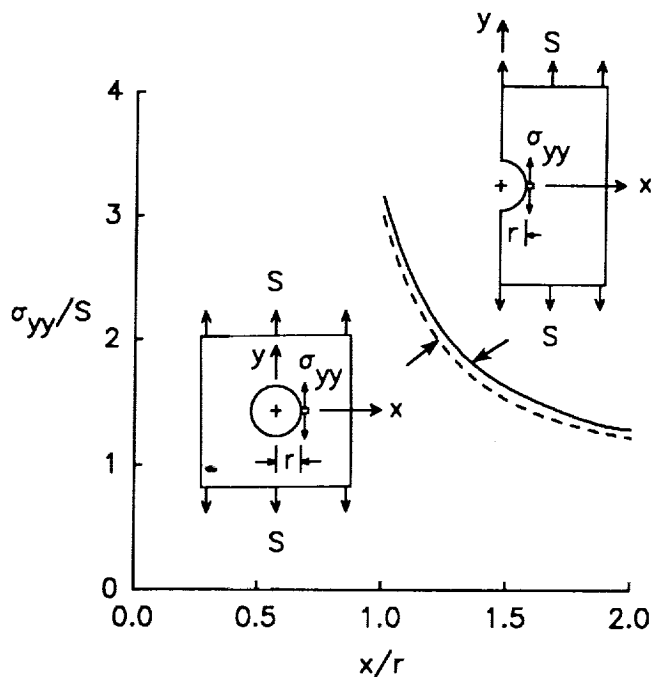
Figure 3. Normal stress distributions for SENT specimen and open circular hole in infinite plate for remote stress.

sults from the BFM and stress intensity factors determined from an experimental technique are also given in appendix C. Stress intensity factor equations based on the results from these analyses were developed for a range of crack-configuration parameters; they are presented in appendix D. These equations were used in the small-crack data correlations and in the life predictions.

A crack-growth model that incorporates crack-closure effects was used to analyze the growth of small cracks along the bore of the notch and of large cracks away from the notch. Small cracks were
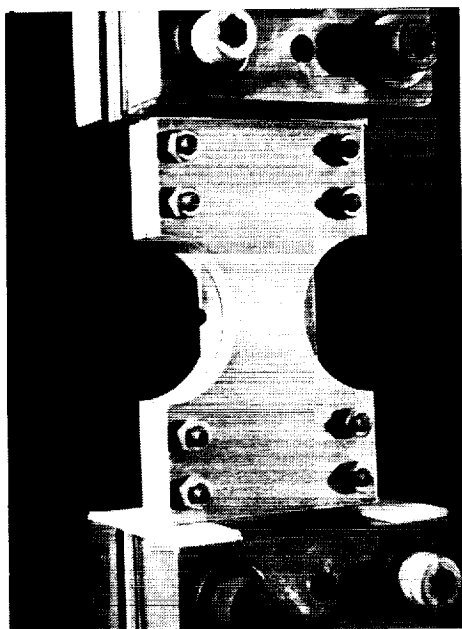
L-88-3166
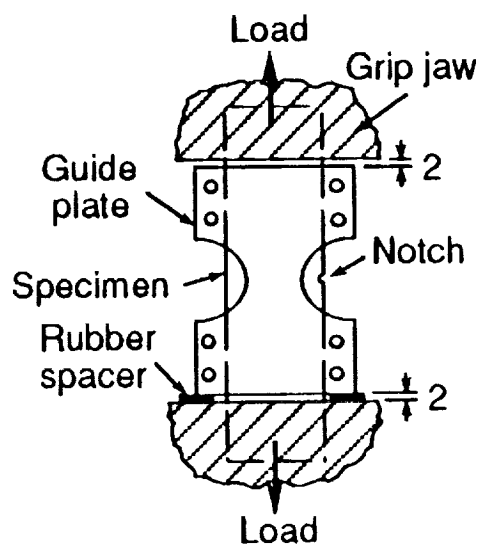
Figure 4. Typical test stand with SENT specimen and guide plates for compressive load tests. All dimensions are in millimeters.

assumed to initiate at either inclusion-particle defects (surface cracks) or in the cladding layer (corner cracks). Comparisons were made between experimental and predicted surface- and corner-crack shape changes, small-crack-growth rates, large-crack growth, and total fatigue life for constant-amplitude and spectrum loading.

3. Test Program

Three types of fatigue tests were conducted for both constant-amplitude and spectrum loading. Standard fatigue tests on SENT specimens were conducted to determine the S-N curves for the two alloys, especially near the endurance limit. Fatigue tests were also conducted on LC9cs alloy without the cladding layer. The primary experiments in the cooperative program were on small cracks and were conducted on the SENT specimens at stress levels selected from the S-N fatigue test results. Large-crack tests on CCT specimens were also conducted to obtain fatigue crack-growth rate data for a wide range of rates; in these tests the same loading histories were used as in the small-crack tests. All tests were conducted at room temperature and in laboratory air.

This section describes the materials, fatigue and small-crack test specimens, loading conditions, test procedures, and data analysis procedures used to obtain small-crack-growth rates. The procedures used to obtain large-crack-growth rates from CCT specimens are also presented.

Table I. Nominal Chemical Composition (wt%) of Materials

| Element | Aluminum alloy— | |
	7075-T6	LC9cs
Aluminum	Balance	Balance
Chromium	0.2	0.2
Copper	1.6	1.6
Iron	.2	.5
Manganese	.2	.15
Magnesium	2.6	2.5
Silicon	.1	.5
Titanium	.1	
Zinc	5.7	5.6

3.1. Materials

Two high-strength aluminum alloy sheets commonly used for aircraft structures were selected for the test program: 7075-T6 aluminum alloy (2.3 mm thick) and LC9cs clad aluminum alloy (2 mm thick). The 7075-T6 alloy was selected because the growth of small cracks was expected to be significantly affected by grain boundary interactions and to severely test continuum mechanics concepts. (See ref. 12.) The LC9cs sheet, similar in chemical composition and tensile properties to 7075-T6 alloy, was selected because clad aluminum alloy is used extensively in the aircraft industry. Tables I and II give the nominal chemical compositions and average tensile properties, respectively. Tensile properties for the 7075-T6

5

Table II. Average Tensile Properties of Materials

Material[a]	Thickness B, mm	Ultimate tensile strength, MPa	Yield stress (0.2-percent offset), MPa	Modulus of elasticity, MPa	Elongation (51-mm gage length), percent
7075-T6	2.3	575	520	70 000	12
LC9cs	[b]2	538	481	66 400	12.5
Bare LC9cs	[c]1.8	575	514	69 200	12.3

[a]Longitudinal (or rolling) direction.
[b]Cladding thickness 80 to 100 μm on each side (as received).
[c]Cladding layer removed, core material.

alloy were obtained from standard American Society for Testing and Materials (ASTM) tensile specimens. Tensile properties are also given for the LC9cs alloy with the cladding layers removed.

The most significant difference between the two materials is the surface condition. The LC9cs alloy had a cladding layer 80 to 100 μm thick on each surface of the sheet; however, that thickness was reduced to about 50 to 70 μm after the SENT specimens were chemically polished. The 7075-T6 alloy was a bare material, although 7075-T6 clad sheet is also used in the aircraft industry. The thin cladding layer, containing mainly Al-Zn, is used to enhance corrosion resistance. The tensile strength of the cladding material is only about 10 percent of that of the bare material. Consequently, the nominal tensile strength of the LC9cs sheet is reduced by the cladding. (See table II.) Yield stress and ultimate tensile strength of the bare LC9cs alloy were about 7 percent higher than those of the LC9cs clad alloy. Bare LC9cs alloy properties agreed well with those of the bare 7075-T6 aluminum alloy.

Microstructures typical of each material are shown in figure 5. Clusters of inclusion particles, similar in both the 7075-T6 and bare LC9cs alloys, appear as black regions. The cladding layer was cleaner than the bare material, but it still contained many small inclusion particles. The inclusion-particle size distributions are shown in figure 6. The large dimensions of the inclusion-particle clusters d_T were aligned perpendicular to the notch surface in the SENT specimen, as illustrated in the insert. The distributions were similar for both alloys. The average grain sizes in the short S-, transverse T-, and longitudinal L-directions are shown in figure 7. The grain sizes in the 7075-T6 alloy in the T- and L-directions were about twice as large as those in the LC9cs alloy.

3.2. Specimens

Two types of specimens were used in the test program. Fatigue (S-N) and small-crack tests were conducted on the SENT specimens. (See fig. 2.) The large-crack tests were conducted on CCT specimens. (See appendix E, fig. E1.)

The small-crack SENT specimens were selected to produce naturally occurring cracks at material defects or discontinuities and to propagate cracks through a stress field similar to that encountered in aircraft structures. The semicircular edge notch permitted easy access to the notch surface; thus, crack monitoring by the replication technique was convenient.

The specimen blanks for the SENT and CCT specimens were cut from aluminum alloy sheets (610 by 1830 by 2.3 mm for 7075-T6 alloy and 1000 by 2000 by 2 mm for LC9cs alloy). The long dimension of the specimens was parallel to the rolling direction of the sheet. Each specimen blank was labeled with a specimen number. All blanks were milled to final overall dimensions. Some blanks were reserved for alignment specimens so they did not contain a notch. In the SENT blanks, the semicircular notch was milled with a process designed to minimize residual stresses at the notch root. Details on the machining process are given in appendix E. All of the 7075-T6 alloy specimens were machined at LaRC and the LC9cs alloy specimens were machined at BIAM.

The SENT specimens were chemically polished to debur the edge of the notch, to remove machining marks from the notch surface, and to eliminate any residual stresses from the fabrication process. Details on the polishing process are also given in appendix E. The polishing process removed about 30 μm of material from all surfaces. In a few specimens, the notch root residual stresses were measured by X-ray diffraction. These measurements indicated that the residual stress was negligible (1–2 MPa). Figure 8 shows some typical notch surface finishes on an aluminum alloy after 1 and 5 minutes of polishing. The 5-minute polishing procedure removed more material from the surfaces than did the 1-minute process. In addition, the edges of the specimens polished for 5 minutes were deburred and mildly rounded during

6
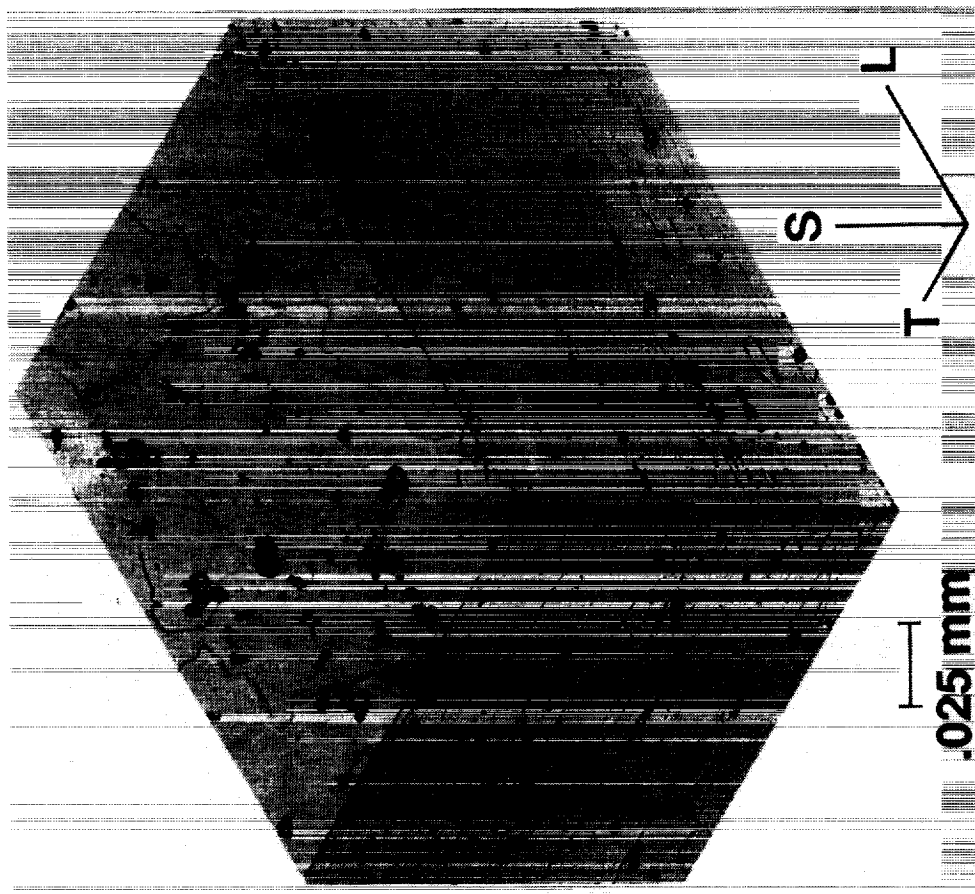
(b) LC9cs alloy.

L-89-8548

(a) 7075-T6 alloy.
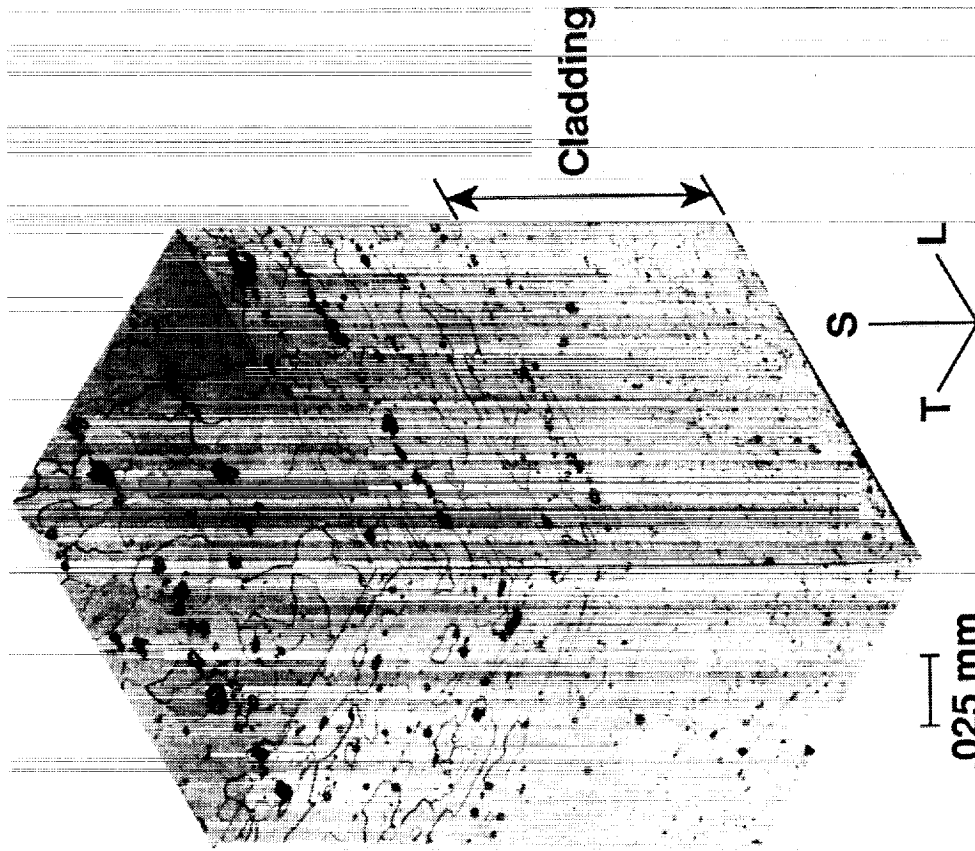
L-89-8549

Figure 5. Microstructure of two aluminum alloy materials in short (S), transverse (T), and longitudinal (L) directions.
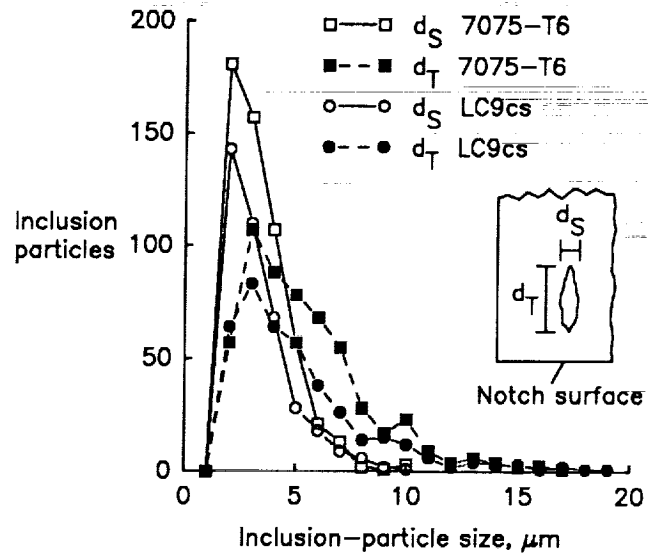
Figure 6. Inclusion-particle size distributions for aluminum alloys in short and transverse directions.
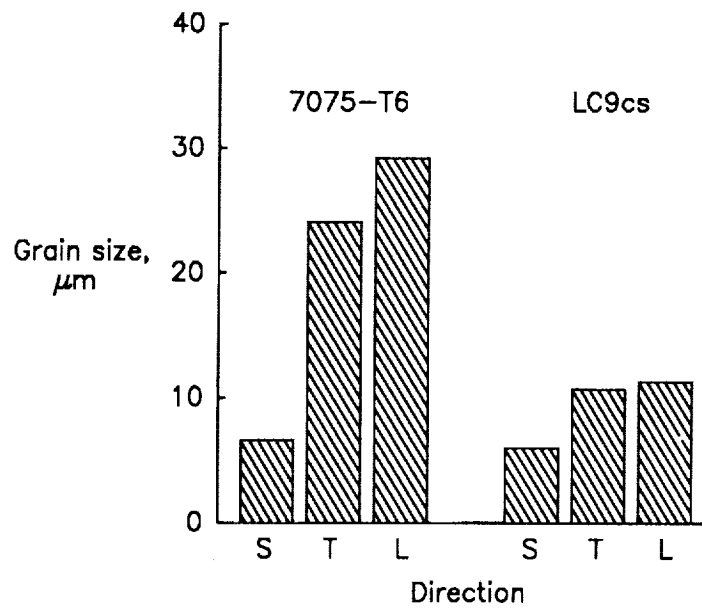
Figure 7. Grain sizes for aluminum alloy materials.
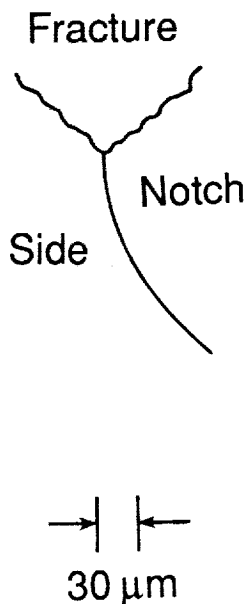
(a) One minute.
(b) Five minutes.

Figure 8. Effect of chemical polishing time on notch surface finish.

the polishing process, thus preventing premature crack initiation at the edge of the notch. Therefore, the 5-minute polishing procedure was selected for the current study. In some cases, the notch surface of the LC9cs alloy was lightly etched beforehand to reveal the microstructure.

All large-crack tests were conducted on 75-mm-wide CCT specimens made from the two alloys in the as-received condition. The LC9cs alloy specimens had about 90-μm-thick cladding on each surface.

Specimens were tested in either hydraulic or flat-plate friction grips. Bolt holes were machined in the specimens to facilitate the application of uniform gripping pressure. However, the specimens were not gripped directly; either brass or plastic spacers were used between the specimens and the grip jaws so that the specimens would not crack in the gripping area. Details on the grip design used in both laboratories are given in appendix F.

3.3. Loading Conditions

A range of loading conditions was applied in the test program. Fatigue, small-crack, and large-crack

tests were conducted for three constant-amplitude loading conditions and for a standardized aircraft wing spectrum. (See Mini-TWIST ref. 27.) A summary of the cooperative program test matrix for the two aluminum alloys is given in table III.

Each laboratory was required to align the test machines and gripping fixtures to produce a nearly uniform tensile stress field on an unnotched sheet specimens that had been instrumented with strain gages. Blank specimens (identical to the small-crack specimens without a notch) were machined for alignment verification. The alignment procedures are presented in appendix F.

Antibuckling guide plates that had been lined with tetrafluoroethylene fluorocarbon polymer sheets were used on all tests where compressive loads were applied. They were loosely bolted together on both sides of the specimens. Guide plates were not used when the minimum applied load was zero or positive. If a test was interrupted, the steady-state minimum load was maintained at a level greater than or equal to the required minimum load in the test. The following sections briefly describe the various load histories.

Table III. Cooperative Program Test
Matrix for Aluminum Alloys

Loading		Number tested		
		7075-T6	LC9cs	
			Clad	Bare
Fatigue SENT tests; cladding = 50–70 μm after polishing				
Constant amplitude	$R = -1$	12 [a](4)	16 [a](3)	0
	$R = 0$	17 [a](4)	14 [a](2)	18
	$R = 0.5$	17 [a](3)	19 [a](2)	17
Spectrum [b]		14 [a](7)	13 [a](8)	0
Small-crack SENT tests; cladding = 50–70 μm after polishing				
Constant amplitude	$R = -1$	10	10	0
	$R = 0$	9	8	3
	$R = 0.5$	10	9	1
Spectrum [b]		8	9	0
Large-crack CCT tests; cladding = 80–100 μm as received				
Constant amplitude	$R = -1$	7	6	0
	$R = 0$	6	6	1
	$R = 0.5$	5	6	1
Spectrum [b]		9	8	0

[a] Replica-effects tests.
[b] Mini-TWIST loading sequence (ref. 27).

Table IV. Local Notch Root Elastic Stresses for
Small-Crack Test Conditions

Loading	S_{max}, MPa	$\dfrac{K_T S_{max}}{\sigma_{ys}}$	$\dfrac{K_T S_{min}}{\sigma_{ys}}$
7075-T6 alloy			
$R = -1$	80	0.48	-0.48
	95	.58	$-.58$
$R = 0$	120	.73	0
	140	.85	0
$R = 0.5$	195	1.18	.59
	220	1.33	.67
Mini-TWIST	190	1.15	$-.26$
	208	1.26	$-.29$
LC9cs alloy; multiply by 1.07 for notch root stresses in core			
$R = -1$	70	0.46	-0.46
	90	.59	$-.59$
$R = 0$	100	.65	0
	115	.75	0
$R = 0.5$	165	1.08	.54
	185	1.21	.60
Mini-TWIST	125	.82	$-.19$
	140	.91	$-.21$
	170	1.11	$-.26$

3.3.1. Constant-Amplitude Loading

Three stress ratios, -1, 0, and 0.5, were used in the test program. The negative stress ratio was selected because, as mentioned, the small-crack effect is more pronounced for compressive loading conditions. In contrast, the small-crack effect is less evident at high R. At each R, two maximum stress levels were selected; also the lower stress level was slightly higher than the fatigue limit. The cyclic frequencies ranged from 5 to 20 Hz for the fatigue and small-crack tests. Frequencies for the large-crack tests ranged from 5 to 30 Hz for the constant-amplitude tests and from 30 to 50 Hz for the threshold tests.

Table IV shows the local notch root elastic stresses at maximum and minimum applied stress for the SENT small-crack test conditions. For all stress conditions with $R = -1$ and 0, the local stresses were elastic for both materials. However, at $R = 0.5$, the notch root yielded under tension for both alloys.

3.3.2. Mini-TWIST Spectrum Loading

The Mini-TWIST loading sequence (ref. 27) was used for all spectrum loading tests. Mini-TWIST is a European standard gust load sequence for flight simulation tests on transport aircraft wing structures. Load spectra pertaining to wing root stresses were obtained from several transport aircraft types. The standardized flight loading sequence was taken as the average of the different load spectra. Mini-TWIST represents a load sequence for a block of 4000 flights that are composed of 10 distinct flight types. Stress levels in each flight have been normalized by $1g$ mean stress in flight S_{mf} during cruise conditions. The highest peak stress $S_{max} = 2.6 S_{mf}$ occurs only once in the total sequence. The lowest trough (or minimum stress) is $S_{min} = -0.6 S_{mf}$. Figure 9 shows a flight of the Mini-TWIST spectrum that is the third most severe (2936) of 4000 flights. Thus, S_{max} and S_{min} are the highest and lowest values of stress in the total sequence. The cumulative distribution of peaks and troughs for both the Mini-TWIST and TWIST flight load sequences in 40 000 flights is shown in figure 10.

The aim of the Mini-TWIST sequence was to develop a standardized flight sequence that would
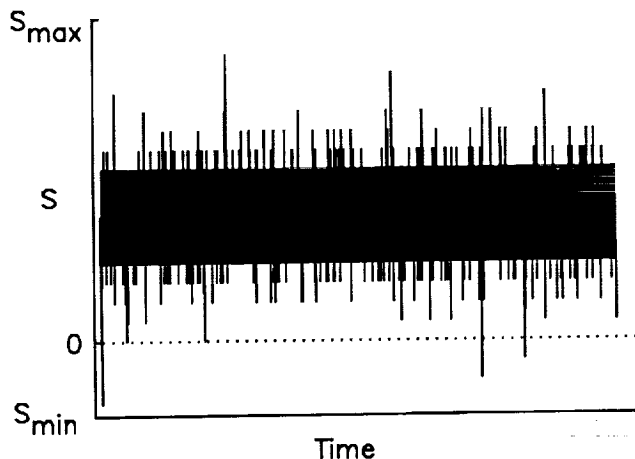
Figure 9. Third most severe flight (2936) in Mini-TWIST and TWIST flight load sequences.
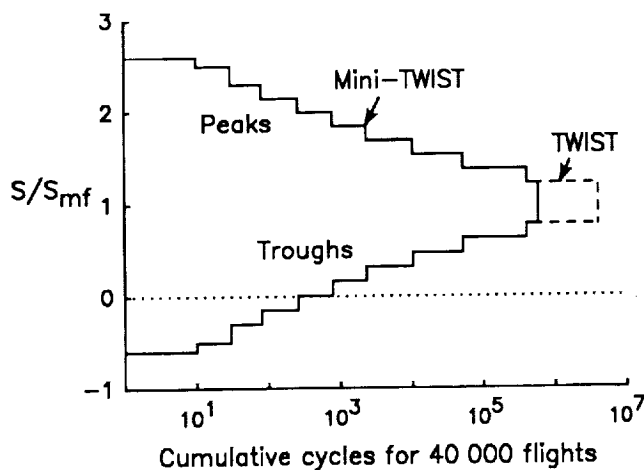

Figure 10. Cumulative peaks and troughs in Mini-TWIST and TWIST flight load sequences for 40 000 flights.

reduce the time and cost involved in tests of the TWIST sequence. (See ref. 27.) The difference between these two spectra is the number of cycles applied at the two lower stress levels. In the Mini-TWIST sequence, the cumulative number of flight load cycles per block of 4000 flights is 58 442 cycles, whereas the TWIST sequence has 398 665 cycles. Also, 4000 additional cycles were included for the ground-air-ground loading ($S_{min} = -0.5S_{mf}$). These cycles were placed at the end of each flight. Reference 27 gives a complete Mini-TWIST sequence in flight types and a FORTRAN program to generate the sequence. This computer program was used to generate the sequence.

To ensure that the load sequences and magnitudes were identical for the two laboratories, the same FORTRAN load generator code was used at

LaRC and BIAM and the loading sequence was carefully verified. Loading accuracy was well within 1 percent for each local maximum load and 2 to 3 percent for each local minimum load. In the SENT specimens, the highest stress level in some of the Mini-TWIST program loading sequences caused the notch root to yield under tension. (See table IV.)

3.4. Fatigue Test Conditions and Procedures

Because the participants may have been unfamiliar with the other's material, eight SENT specimens were exchanged for use in the exploratory fatigue tests. These tests verified proposed test procedures and contributed to understanding the fatigue behavior of each material.

Standard S-N tests on the SENT specimens at various maximum stress levels for both constant-amplitude and spectrum loading were used to aid in the selection of the applied stress levels and plastic-replica intervals for the tests involving small-crack growth. The fatigue life data were also used to assess a method for total fatigue life prediction based solely on crack propagation from material microstructural defects or from the cladding layer.

For constant-amplitude loading, tests were conducted at $R = -1$, 0, and 0.5. The Mini-TWIST program loading sequence was used for the spectrum tests. Guide plates, as shown in figure 4, were used for all tests with compressive loads. The SENT specimens were cycled to complete failure (or stopped without failure after 2 million cycles for tests to establish the fatigue or endurance limit for constant-amplitude loading). The maximum number allowed for the spectrum tests was 5 million cycles. (Specimens removed after these cycles were not retested.) The test matrix for the fatigue tests is shown in table III. This table shows the number of specimens tested at each condition for each material. In parentheses is the number of tests conducted to study the effects of the plastic-replica method on fatigue life. The LC9cs alloy was also tested without the cladding to study the effects of the cladding layer on fatigue life.

### 3.5. Small-Crack Test Conditions and Procedures

The test matrix for the small-crack program is summarized in table IV. The two objectives for the small-crack tests were to obtain data on surface- or corner-crack length against cycles and to obtain surface- or corner-crack depths. To achieve these objectives, two types of tests were required. Some

11

specimens were tested for crack length against cycles until one continuous crack extended across the notch root and the specimen was pulled to failure. The method of recording small-crack growth is given in appendix G. Other specimens were tested until the total crack length along the bore of the notch was much less than the sheet thickness. The specimen was then monotonically pulled to failure. The fracture surfaces were examined to reveal the surface- or corner-crack shapes.

3.5.1. Small-Crack Measurement Method

Newman and Edwards (ref. 19) investigated several methods for measuring the growth of naturally initiated cracks 10 μm to 2 μm long for a test program on small-crack growth in an aluminum alloy. These methods were electrical potential (ref. 28), ultrasonic surface waves (ref. 29), marker bands (ref. 30), and plastic replicas (ref. 31). Of these, only in the plastic-replica method was able to monitor the growth and location of single and multiple cracks as small as 10 μm along the bore of a notch. Because the plastic-replica method was accurate to the small-crack lengths required in the program, that method was also selected for this study. The method is simple to apply, but it is labor intensive; that is, many replicas must be taken for adequate descriptions of crack length against cycles. The plastic-replica procedures are presented in appendix H.

Figure 11 shows the area of the specimen notch root over which cracks were to be monitored. The crack depth L_1 was measured along the bore of the notch. The value of L_1 and its location were recorded on a data chart as a function of cycles. A sample data chart, shown in appendix G, includes the specimen number, cycles, and a grid upon which the information obtained from a replica was recorded. Each record of crack length, location, and cycles was taken at specified cyclic intervals. Cyclic intervals were chosen so that at least 25 to 30 replicas were taken during each test. The intervals were determined by dividing the fatigue life at each test stress level by 25 or 30. Replicas were also taken while the specimens were tensile loaded ($S = 0.6$ to $0.8S_{max}$). (The procedures for taking replicas for constant-amplitude and spectrum loading are presented in the next section.) Figure 12 shows scanning-electron-microscope (SEM) photographs of notch surface replicas for the two alloys. Crack depth measurements L were the horizontal projections. For surface cracks, $L = 2a$ and for corner cracks, $L = a$. The test was terminated when a crack had grown across the specimen thickness B. Then, the specimen was statically pulled to failure. Some tests, however, were statically
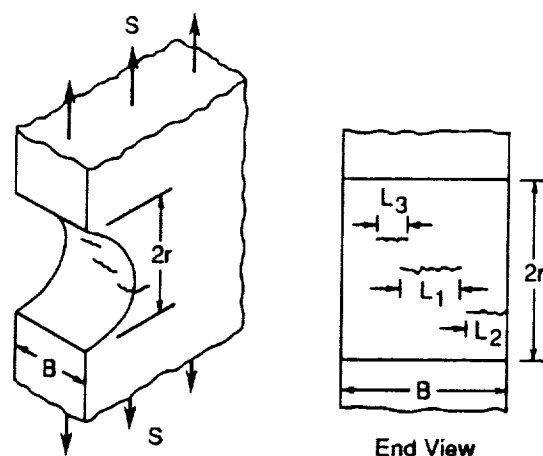
(a) Cracks in notch root.   (b) Crack length measurements.

Figure 11. Notch configuration and crack-length measurements.

pulled to failure early in life to determine the shape of the crack or cracks. (See sec. 3.5.3.)

At the lower stress levels selected in table IV, a single crack was expected to initiate naturally and dominate for most of the fatigue life. However, at the higher stress levels, several cracks may develop along the bore of the notch, as shown in figure 11. If several cracks developed in the test, these cracks were also recorded on the data chart as L_i ($i = 1$ to n). An example of the recorded multiple crack data is shown in figure G1 of appendix G. Starting with the lowest number of cycles (early in life) where cracks could be measured, researchers numbered them and recorded the lengths ± 0.001 mm on the data chart. At the next cyclic interval, crack lengths were recorded and any new cracks were included. If two cracks had joined, the lower crack number was used as the identifier. These data charts provided approximate locations for determining crack initiation sites, for calculating stress intensity factors, and for applying the crack noninteraction criteria. (See sec. 6.5.)

The following were collected for each test: data charts, a small-crack data table (see appendix G), a photograph of the surface or corner cracks for the full thickness of the specimen, and a photograph of a replica near the end of each test for the full thickness. The data for crack length against cycles were then used to obtain stress intensity factor ranges against crack-growth rates. The method of calculating stress intensity factors and crack-growth rates is presented in section 3.6.

Crack length, L (2a)

Initiation site
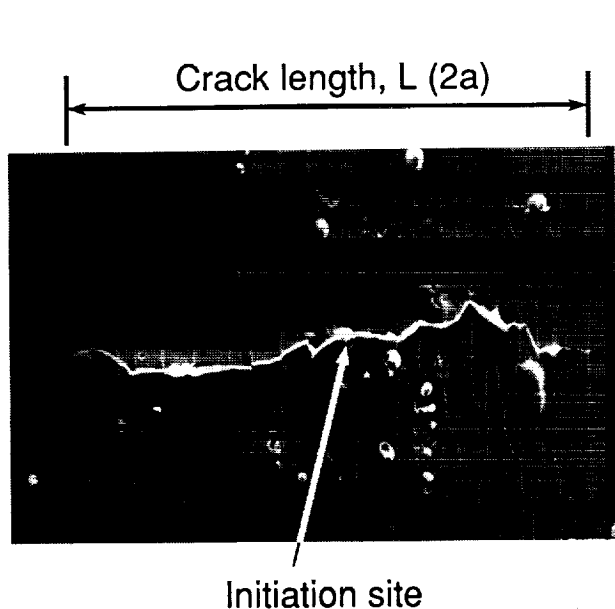
L-93-48

(a) Surface crack in 7075-T6 alloy.

Crack length, L (a)

60-μm

Cladding   Core
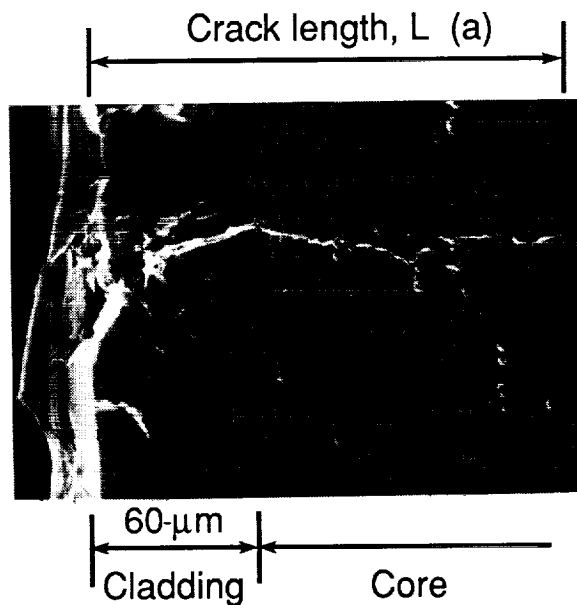
L-93-49

(b) Corner crack in LC9cs alloy.

Figure 12. SEM photographs of replicas of notch surfaces.

3.5.2. Constant-Amplitude and Spectrum Loading

Replicas were taken while the specimens were tensile loaded so that any cracks would be open and would allow the replica material to infiltrate. The procedures for each type of loading were as follows.

3.5.2.1. Constant-amplitude loading.
The test was stopped at mean (or minimum) load. The applied load was then manually increased to 80 percent of the maximum test load. This load was held while a replica was taken along the bore of the notch. (See procedures in appendix H.) After the replica was removed from the notch, the load was reduced to the mean and the test was restarted.

3.5.2.2. Spectrum loading.
To take replicas for the Mini-TWIST loading sequence, the test machine was programmed (or manually set) to stop and hold at a specified peak level after the desired number of cycles. The replica was taken along the bore of the notch. A peak load of level VIII was specified in the Mini-TWIST loading sequence. (See fig. 2 of ref. 27.) This level corresponds to about 60 percent of the maximum applied stress. After the replica was removed from the notch, the test machine was restarted and it continued from the specified peak level.

3.5.3. Crack Shape Determination

The replica method provides information only on surface- or corner-crack lengths along the notch root. The surface- and corner-crack depths had to be determined either by an experiment or by analytical calibration. For each test condition, several specimens were to be tested until the total crack length along the bore of the notch was at different percentages of the sheet thickness. The specimen was then pulled to failure to reveal the crack locations, shape, and size.

3.6. Small-Crack Data Analysis Procedures

In the following sections, stress intensity factor equations are presented for a surface or corner crack emanating from a semicircular edge notch. These equations are used later to compare crack-growth rates measured for small cracks with those measured for large cracks as a function of the stress intensity factor range. The method of calculating the crack-growth rates for small cracks is also presented.

3.6.1. Calculation of Stress Intensity Factors

The calculation of stress intensity factors assumes either a semielliptical surface crack at the center of the edge notch, as shown in figure 13(a), or a

13
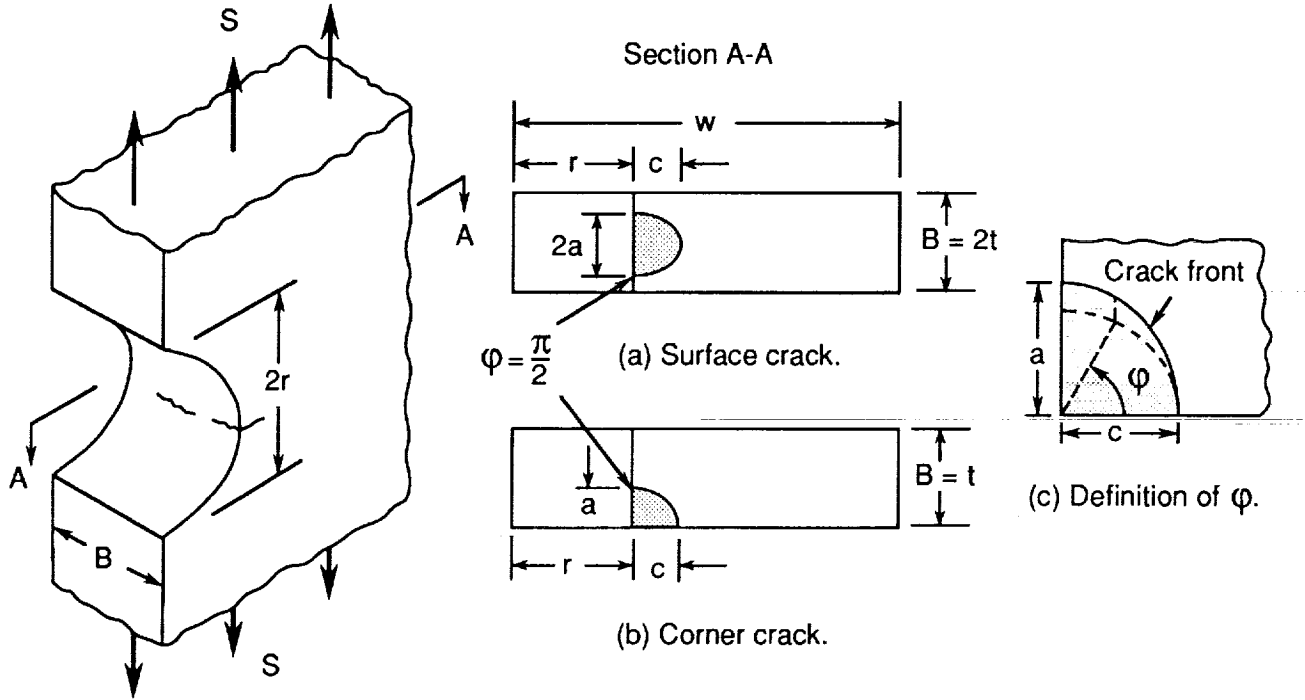
Figure 13. Definition of dimensions for specimens, surface- and corner-crack configurations, and parametric angle φ.

quarter-elliptical corner crack at an edge, as shown in figure 13(b). The crack depth L (a or $2a$) is always measured in the B direction and the length of crack c is measured in the w direction. For a surface crack at a notch, thickness is denoted $2t$ for convenience in expressing stress intensity factors as a function of a/t; that is, a/t varies from 0 to 1. This nomenclature was selected so that both surface and corner cracks will become a through crack of length c when a/t approaches unity. For surface cracks at other places along the bore of the notch, the equations presented herein are adequate if the crack is small compared with thickness. However, if several cracks are close to one another, then the calculation of stress intensity factors is in error. No provisions have been made to account for multiple crack interactions in the calculation of stress intensity factors. Instead, data were simply rejected if an interaction was likely. (See sec. 6.5, "Small-Crack-Growth Noninteraction Criteria.")

To calculate the stress intensity factor at the point where the crack intersects the notch surface ($\varphi = \pi/2$), a and c must be known. For a surface crack, $2a$ (L) was measured as the projection of the crack on a horizontal plane, as shown in figure 12(a). The crack aspect ratio a/c and c were calculated from

$$\frac{a}{c} = 1 + 0.1 \left(\frac{a}{t}\right) \quad \left(\text{for } \frac{a}{t} \geq 0.02\right) \qquad (1a)$$

and

$$\frac{a}{c} = 40 \left(\frac{a}{t}\right) + 0.2 \quad \left(\text{for } \frac{a}{t} < 0.02\right) \qquad (1b)$$

For a corner crack, a (L) is again the projection of the crack on a horizontal plane, as shown in figure 12(b), and the ratio a/c was calculated from

$$\frac{a}{c} = 1.1 + 0.1 \left(\frac{a}{t}\right) \qquad (2)$$

for $a > \ell$, the cladding-layer thickness. Equations (1a) and (2) were determined by visual straight-line fits to the experimental data; these comparisons are shown in section 6.3. Equation (1b) was selected to match predicted results from the crack-growth analyses based on a typical material (inclusion-particle cluster) defect size and shape. The measured crack shapes are compared later with those predicted from the stress intensity factor equations and the crack-growth rate properties.

The stress intensity factor range equation for a surface crack at the center of the edge notch (fig. 13(a)) for uniform remote stress is

$$\Delta K = \Delta S \left(\frac{\pi a}{Q}\right)^{1/2} F_s \qquad (3a)$$

Equations for the shape factor Q and the boundary-correction factor F_s are given in appendix D.

14

For a corner crack,

$$\Delta K = \Delta S \left(\frac{\pi a}{Q}\right)^{1/2} F_c \tag{3b}$$

Equations for F_c also are given in appendix D. Equations (3a) and (3b) apply to a range of crack configuration parameters (a/c, a/t), but they are restricted to the SENT specimens with $r/w = 1/16$ and $1 < r/t < 3.5$. For corner cracks in the LC9cs alloy, a correction for the cladding was developed in section 4.5.3 to modify the calculation of the stress intensity factor range.

The stress range ΔS is full range ($S_{max} - S_{min}$) for constant-amplitude and spectrum loading. For example, $\Delta S = 2S_{max}$ for $R = -1$ loading. For spectrum loading, the highest peak stress is S_{max} and the lowest trough is S_{min}.

3.6.2. Calculation of Crack-Growth Rates

The calculation of crack-growth rate for constant-amplitude and spectrum loading for small cracks was a simple point-to-point calculation. That is,

$$\frac{da}{dN} = \frac{\Delta a}{\Delta N} = \frac{a_{i+1} - a_i}{N_{i+1} - N_i} \tag{4}$$

where a_i is the crack length at N_i cycles. The cyclic interval ΔN is the interval between replicas. The cyclic interval was chosen so that at least 25 to 30 replicas were taken during a test. The corresponding ΔK is calculated at an average crack depth as

$$a = \frac{a_i + a_{i+1}}{2} \tag{5}$$

and c is calculated from equations (1) or (2).

3.7. Large-Crack Test Conditions and Procedures

Fatigue crack-growth rate tests were conducted for large cracks ($c > 2$ mm) at the three constant-amplitude stress ratios and for the Mini-TWIST loading sequence. Data were generated for the two materials for a range of rates, especially in the near-threshold crack-growth regime. Tests were performed on 75-mm-wide CCT specimens made of the 7075-T6 and LC9cs alloys. (See appendix E.) The method of recording large-crack data is presented in appendix G. These data were used to define the regime in which small-crack data from the SENT specimens correlated with large-crack data. The results from this study are presented and discussed in section 5.

3.7.1. Constant-Amplitude Loading

Constant-amplitude tests were conducted at $R = -1$, 0, and 0.5. At each R, both constant-amplitude loading and threshold tests were conducted. In the threshold tests, crack-growth rates were obtained for a load-shedding (decreasing ΔK) procedure. The LaRC researchers used a load-shedding procedure that was consistent with the guidelines of the ASTM Standard Test for Measurement of Fatigue Crack-Growth Rates (E647-87) in which the loading was reduced by 6 percent every 1 mm of crack growth, whereas the CAE researchers employed a procedure in which the load was decreased by 10 percent every 1 mm of crack growth for rates greater than 2×10^{-6} mm per cycle and 6 percent for rates lower than 2×10^{-6} mm per cycle. After they reached threshold conditions, some specimens were then tested for load-increasing conditions to obtain more crack-growth data.

3.7.2. Mini-TWIST Spectrum Loading Program

Spectrum tests were controlled by a computer program that allowed the mean flight stress to be changed at any stage by the operator, to stop the test at zero load, or to stop the test at the required stress level so that replicas could be taken on the SENT specimens. This program also allowed load-decreasing or load-increasing tests to be conducted without interrupting the flight history, except when S_{mf} was changed.

3.7.3. Large-Crack Data Reduction

Crack-growth rates were calculated from crack length against cycles using the secant (point-to-point) method. The stress intensity factor range was computed from the well-known equation for a central crack in a strip in tension (ref. 32),

$$\Delta K = \Delta S \sqrt{\pi c \sec\left(\frac{\pi c}{2w}\right)} \tag{6}$$

where ΔS is the full cyclic range, c is the average of the crack length measured on the right and left sides of the specimen, and w is half-width of the specimen. Visual best-fit lines (piecewise linear segments) were drawn through the ΔK rate data. These baseline relations were developed to compare with small-crack data generated for the same test conditions.

4. Analysis Program

To understand small-crack growth and to improve life-prediction methods, accurate stress intensity

factor solutions must be obtained for small surface and corner cracks in plates or at stress concentrations. Because of their practical importance, analyses of 3D crack configurations have been a central issue in fracture mechanics for the past two decades. Although several solution methods have been used for these analyses, most solutions were obtained from the 3D FEM in conjunction with various techniques to extract stress intensity factors. (See refs. 33–37 for examples.)

For the SENT specimens, an engineering estimate (ref. 30) was the only stress intensity factor solution in the literature for a surface crack at a notch. The approximate solution was developed from an analysis of a similar crack configuration, a surface crack at a circular hole, and the assumed proportionality between through-the-thickness and part-through cracks. (See ref. 30.) This approximate solution has been widely used in the past decade to characterize small cracks. (See refs. 19 and 20.) However, the accuracy of the solution was unknown. In addition, stress intensity factor solutions or equations were unavailable for corner cracks at the notch. Because the stress intensity factor is important in correlations of small-crack growth and in life predictions, a joint effort was undertaken in the analysis program to develop new and more accurate stress intensity factor solutions for surface and corner cracks at the notch root of the SENT specimens. The approach was to apply two radically different analysis methods—finite elements and weight functions.

The three-dimensional FEM and a 3D WFM were used to determine stress intensity factors for surface and corner cracks at the notch in the SENT specimens. These crack configurations are shown in figure 13. The surface crack was at the center of the semicircular notch (fig. 13(a)) and the corner crack was at the edge of the notch (fig. 13(b)). Analyses of off-center surface cracks or multiple interacting cracks were not considered.

Two-dimensional weight-function analyses were used to help develop the stress intensity factor equations used in the 3D WFM. In addition, the 2D BFM was used to obtain the stress distribution in an uncracked SENT specimen and the stress intensity factors for a through crack in the SENT specimens. These solutions were used to develop weight functions. An experimental technique was also used to obtain stress intensity factors for through cracks in the SENT specimens to help determine the appropriate remote boundary conditions. Stress intensity factor equations, which were fitted to the calculated stress intensity factors, were developed for a range of crack configuration parameters.

The following sections briefly describe the methods used in the program and compare the stress intensity factors determined from various methods. The general form is presented for the stress intensity factor equations that were used to correlate and predict small- and large-crack-growth rates. Comparisons are made among the results from the FEM, WFM, and equations. A cladding correction on stress intensity factors for corner cracks in the LC9cs material is derived and discussed.

4.1. Finite-Element Analyses

Two finite-element programs and three methods to extract stress intensity factors were used to determine stress intensity factors for surface and corner cracks that emanate from a semicircular notch. The finite-element program and method (singularity element and nodal-force method) developed by Raju and Newman (refs. 33 and 34) were used for semicircular cracks and cracks with low a/c ratios. For $a/c = 2$, the finite-element program (nonsingular elements) developed by Shivakumar and Newman (ref. 35) and the equivalent-domain integral (EDI) method (ref. 36) were used because this approach required less effort to generate large a/c models than the former one. The virtual crack closure technique (VCCT) (ref. 37) was also used to verify the stress intensity factors for particular cases.

The stress intensity factors were obtained for a range of semielliptical surface cracks at the center of the semicircular edge notch and of quarter-elliptical corner cracks at the edge of the notch in a specimen of finite thickness. The SENT specimen was subjected to remote tensile loads. Solutions for off-center surface cracks were not considered necessary because the stress distribution along the bore of the notch showed only a small variation, as shown in figure 14 for a circular hole in a plate of finite thickness. (See ref. 38.) The results in figure 14 show the normal stresses σ_{yy} along the bore of a circular hole ($x/r = 1$) in a plate subjected to remote uniform stress for two values of r/t, the ratio of hole radius to plate thickness. The results for $r/t = 3$ are indicative of the normal stresses in the SENT specimens used in the test program. Thus, the stress intensity factor solution for a small surface crack anywhere in the midregion ($z/t < 0.6$) would not be adversely affected by the finite thickness. The ratio of crack depth along the notch root to crack length away from the notch root a/c considered in the analyses ranged from 0.4 to 2 and the ratio of crack depth to plate thickness a/t ranged from 0.2 to 0.8. Also, the ratio was $r/t = 3$ for surface cracks and $r/t = 1.5$ for corner cracks. These are the nominal values used in
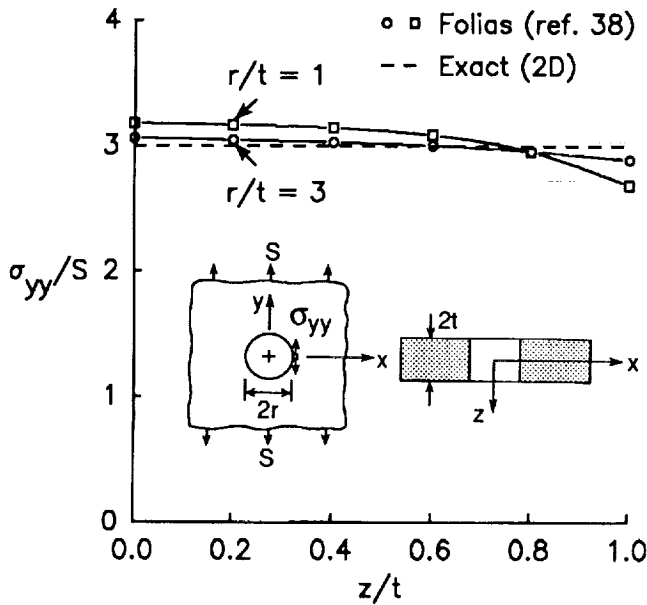
Figure 14. Stress concentration along bore of circular hole in finite-thickness plate for remote tensile loading.

the test program. Appendix A gives more details of the finite-element analyses. Tables of stress intensity factors for various crack configurations are also presented.

4.2. Weight-Function Analyses

The 3D WFM developed in references 39 and 40 was based on the slice-synthesis procedure (refs. 41–43) and the general expressions for 2D weight functions. (See refs. 44–46.) Reference 47 reviews the 2D and 3D WFM's and their solutions. Basically, the 3D WFM transforms the restraining effect of the uncracked part of a 3D cracked body into a kind of elastic boundary condition on 2D slices. Thus, some 3D nature is built into these slices. The weight functions for these slices are constructed through two limiting cases, one for zero constraint and the other for fixed constraint, by using the general weight functions for 2D crack configurations. For an infinite, semi-infinite, or quarter-infinite body wherein the restraining areas tend to infinity, the 2D weight functions with fixed boundary conditions are directly applied. However, for a finite body, a reference solution is needed to determine an unknown parameter in the weight functions for the slices. For the present problems with $r/w = 1/16$, the 2D weight functions with fixed boundary conditions are applicable, as discussed in appendixes B and C.

The 3D WFM has previously been applied to embedded elliptical cracks (refs. 39 and 40), semi-elliptical surface cracks (refs. 40 and 48), and quarter-

elliptical corner cracks (ref. 40), in plates of finite thickness subjected to mode I loading. Results from the WFM agreed well with other accepted solutions for these crack configurations.

Herein, the method was applied to surface and corner cracks at the semicircular notch in the SENT specimens (refs. 49 and 50). The 3D WFM formulated here, however, assumed that the normal stress distribution around the notch root was uniform through the thickness. This assumption was justified for the SENT specimen configurations in the current study because through-the-thickness variations in normal stress are small, as shown in figure 14. Basically, the current 3D WFM uses the normal stress distribution shown by the dashed line. The normal stress distribution, together with the corresponding stress intensity factors for through cracks (calculated from the BFM), was used to derive the 2D weight function (ref. 45) for a through crack emanating from an edge notch. The 2D weight function was then used in the 3D WFM to derive stress intensity factors for surface and corner cracks at the notch. The 3D WFM allows for the determination of stress intensity factors at any location along a crack periphery for the crack configurations shown in figure 13. The a/c ranged from 0.2 to 2 and a/t ranged from 0.05 to 0.5. Note that the WFM was applied to a different range of a/c and a/t values than the FEM. The WFM was applied to smaller cracks (lower a/t), but the FEM was applied to larger cracks (larger a/t). For surface cracks, $r/t = 2.78$ and 3.2 and $r/t = 1.39$ and 1.6 for corner cracks. These are the particular r/t values used in the test program for the two materials. Appendix B gives the details of the 3D WFM. Tables of stress intensity factors for various crack configurations also are presented.

4.3. Boundary Force Method

The BFM was formulated for 2D stress analysis of complex configurations, with and without cracks, subjected to internal loading and traction or displacement boundary conditions. (See refs. 26 and 51.) The BFM uses the elasticity solution for concentrated forces and a moment in an infinite plate as the fundamental solution. For plates without a crack, Muskhelishvili's solution (ref. 52) for a pair of concentrated forces P_x, P_y and moment M in an infinite plate is used as the fundamental solution. For a plate with a crack, Erdogan's solution (ref. 53) for P_x and P_y and for M in an infinite plate with a crack is used as the fundamental solution. With Erdogan's solution, the crack faces need not be modeled as part of the boundary because the stress-free conditions on the crack faces are exactly satisfied.
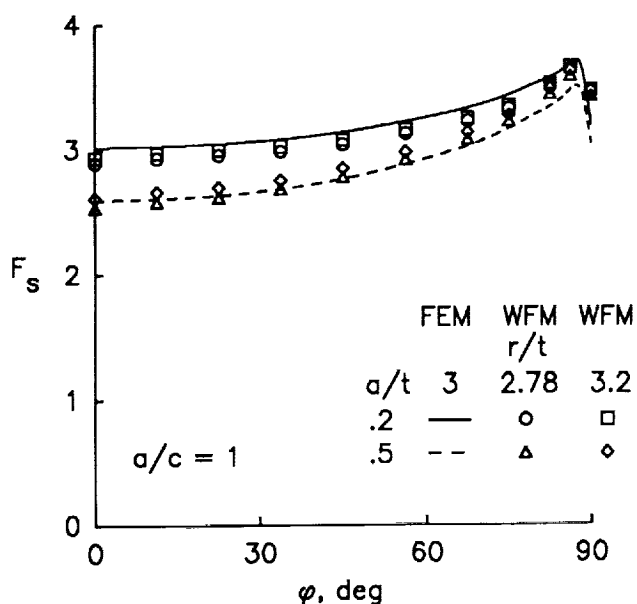
17

Figure 15. Boundary-correction factors from FEM and WFM for semicircular surface crack at notch.

Figure 16. Boundary-correction factors from FEM and WFM for quarter-circular corner crack at notch.

The BFM was used to analyze the uncracked SENT specimens to obtain the stress concentration factor and the normal stress distribution along the net section. In addition, the BFM was used to analyze a through crack emanating from the SENT specimens subjected to either remote uniform stress or displacement. The James and Anderson technique (ref. 54), to extract experimental stress intensity factors, was used to verify the remote boundary conditions on the SENT specimens. Appendix C gives some details of the BFM analysis and of the 2D solutions used in the cooperative program.

4.4. Comparison of Methods

Typical comparisons of the stress intensity boundary-correction factors from the FEM and WFM are shown in figures 15 and 16 for a semicircular surface crack and quarter-circular corner crack at a notch, respectively. The FEM analyses were conducted on a large mainframe computer with about 15 000 degrees of freedom (DOF), whereas the WFM analyses were performed on a personal computer. The boundary-correction factor is plotted against the parametric angle φ. The WFM results are shown as symbols for the two particular values of r/t used in the test program. The curves show the results from the FEM for a nominal value of r/t. Results for $a/t = 0.5$ agree well (within 3 percent) with the FEM analyses, except where the crack intersects the free boundaries ($\varphi = 90°$ for surface cracks; $\varphi = 0°$ and $90°$ for corner cracks). The results for the smaller crack ($a/t = 0.2$) show

that the FEM results are slightly higher (2 percent) for surface cracks and slightly lower (3 percent) for corner cracks than are the WFM results. This small variation may have been caused by the slightly higher normal stresses shown in figure 14 for $z/t < 0.2$ for surface cracks and the slightly lower normal stresses for $z/t > 0.8$ for corner cracks. This nominal stress variation was accounted for in the FEM. The WFM did not account for through-the-thickness variations in the normal stresses. For the configurations used in the cooperative test program, however, neglecting the small through-the-thickness variations was justified.

The stress intensity boundary-correction factors from the FEM and those for the WFM for an elliptical crack ($a/c = 2$) are shown in figure 17. Again, the boundary-correction factor is plotted against φ for several values of r/t. The WFM results (solid symbols) are average results between $r/t = 1.39$ and 1.6. For all crack configurations considered in the analysis program, these results show the largest difference (about 10 percent) between the FEM and WFM. To resolve these differences, two finite-element programs, three methods of extracting stress intensity factors, and several finite-element models were used. These results are shown in figure 18. The open circles show the results from the FEM and the model (model A with 13 wedges of elements along the crack front and the EDI method) used in the cooperative program for $a/c = 2$. Model B contained singularity elements around the crack front (about
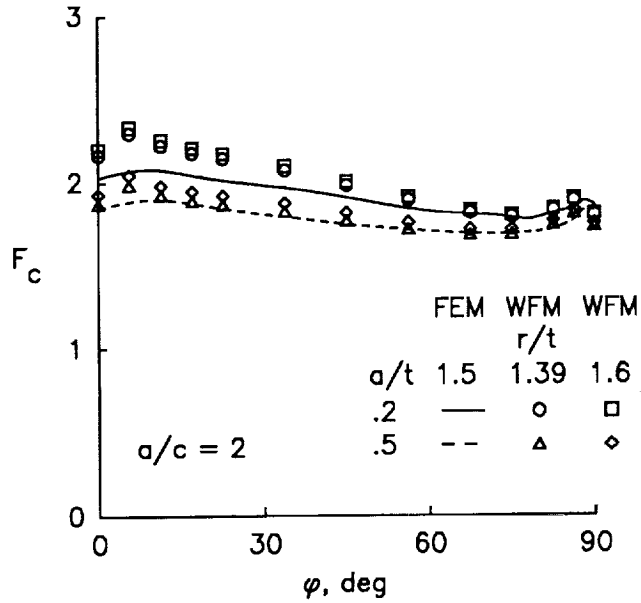
18

Figure 17. Boundary-correction factors from FEM and WFM for quarter-elliptical corner crack at notch.
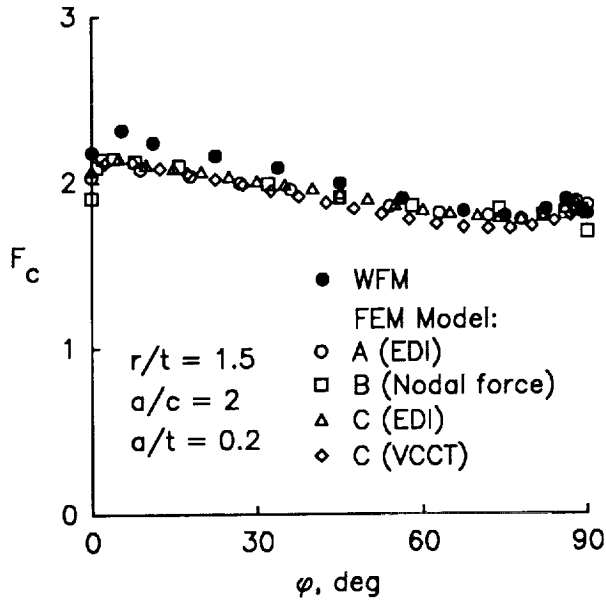

Figure 18. Boundary-correction factors from various finite-element models and methods and weight-function results for quarter-elliptical corner crack at notch.

15 000 DOF) and the nodal-force method was used to calculate stress intensity factors. Model C contained nonsingular elements around the crack front but had 20 wedges of elements along the crack front with about 18 000 DOF. Two methods, EDI and the VCCT, were used to extract stress intensity factors. All FEM's show similar results in the region of concern ($\varphi < 30°$).

The higher WFM results for the corner-crack configuration may, to some extent, be attributed to neglecting the normal stress variation in the thickness direction near the plate surface. The results from a 3D stress analysis of a hole in a plate of finite thickness (fig. 14) show that the z variation of the normal stress is largest at the hole and plate surface. The actual normal stresses are lower than the 2D stress distribution used in the 2D weight-function analyses. Thus, the 2D stress distribution will overestimate the stress intensity factors for corner cracks in the SENT specimens when the ratio of crack length to notch radius c/r is small. If the actual 3D stress distribution had been used as the applied crack-face loading in the WFM, lower stress intensity factors would have been obtained. However, no further effort was taken here to clarify this point because the precise 3D stress distribution in the notch-root region was not known and the refined 3D finite-element analyses provided confidence in the FEM solution.

4.5. Stress Intensity Factor Equations

The FEM and WFM stress intensity factor solutions for surface and corner cracks at a notch (appendixes A and B) and the BFM solutions for a through crack at a notch (appendix C) were used to develop equations. The stress intensity factor equations and their functional forms are given here for a semi-elliptical surface crack at the center of a semicircular edge notch, a quarter-elliptical corner crack at the edge of the notch, and a through crack at the notch subjected to remote uniform stress or displacement (where the ratio of one-half the specimen height h divided by width w was 1.5). Thus,

$$K = S \left(\frac{\pi a}{Q}\right)^{1/2} F_j \left(\frac{a}{c}, \frac{a}{t}, \frac{c}{r}, \frac{c}{w}, \frac{r}{t}, \frac{r}{w}, \varphi\right) \quad (7)$$

where F_j is the boundary-correction factor. (See ref. 34.) The equations were developed for a range of crack configurations with $r/w = 1/16$ (the r/w value for the SENT configuration). Note that here t is defined as one-half the full sheet thickness for surface cracks ($j = s$) and t is full sheet thickness for corner cracks ($j = c$). Here Q is given by

$$Q = 1 + 1.464 \left(\frac{a}{c}\right)^{1.65} \quad \text{(for } a/c \leq 1) \quad (8a)$$

$$Q = 1 + 1.464 \left(\frac{c}{a}\right)^{1.65} \quad \text{(for } a/c > 1) \quad (8b)$$
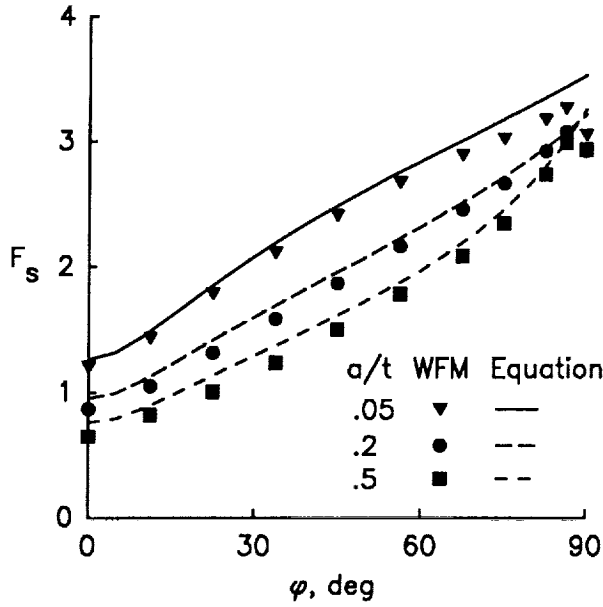
(a) $a/c = 0.2$.
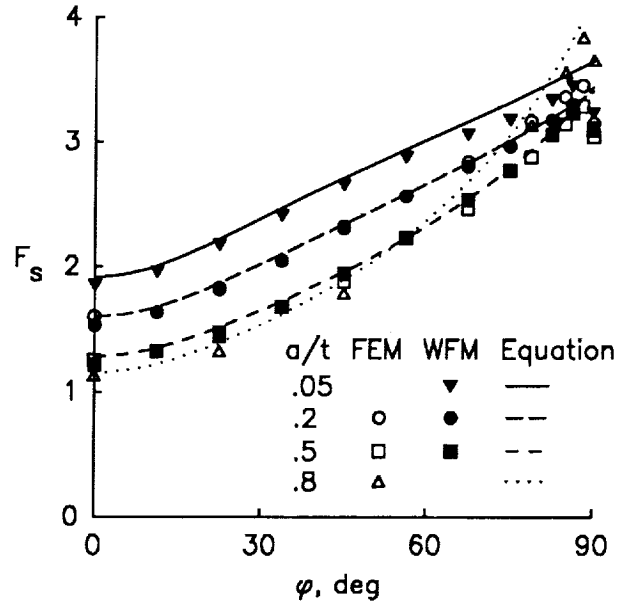
(b) $a/c = 0.4$.
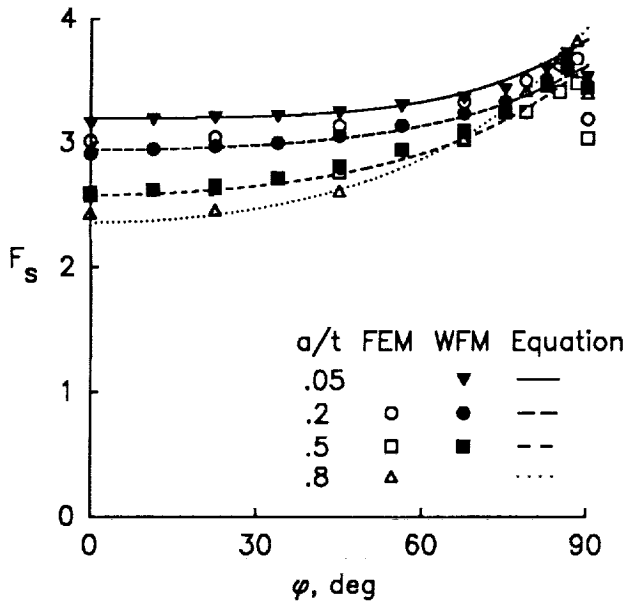
(c) $a/c = 1$.

(d) $a/c = 2$.

Figure 19. Boundary-correction factors from FEM, WFM, and equations for surface crack at notch. $r/t = 3$.

4.5.1. Surface and Corner Cracks at Notch

4.5.1.1. Surface crack at a semicircular notch.
The boundary-correction factor equation for a semi-elliptical surface crack at the center of a semicircular edge notch (fig. 13(a)) subjected to remote uniform stress or displacement is

$$F_s = \left[M_1 + M_2 \left(\frac{a}{t} \right)^2 + M_3 \left(\frac{a}{t} \right)^4 \right] g_1 g_2 g_3 g_4 g_5 f_\varphi f_w \quad (9)$$

for $0.2 < a/c < 2$, $a/t < 1$, $1 < r/t < 3.5$, $(r + c)/w < 0.5$, $r/w = 1/16$, and $-\pi/2 < \varphi < \pi/2$. The equations for all other terms in equation (9) are given in appendix D.

Figures 19(a)–19(d) show comparisons among the FEM, WFM, and stress intensity factor equations for a surface crack at the notch root in the SENT specimens. Each figure is for a constant value of a/c and r/t. The WFM results (solid symbols) are the averages of the results for the two values of r/t used in

the test program. The open symbols in figures 19(b)–19(d) show the FEM results. The equations are shown by the curves for various values of a/t. The equations are well within ± 4 percent of the WFM and FEM results, except where the crack intersects the notch boundary ($\varphi = 90°$). In applications, the stress intensity factors near the free surface have been shown to control fatigue crack growth. (See ref. 55.) (Note that the percentage of error is defined in reference to the largest stress intensity factor for any particular configuration.)

4.5.1.2. Corner crack at a semicircular notch.

The boundary-correction factor equation for a quarter-elliptical corner crack at the edge of a semicircular edge notch (fig. 13(b)) subjected to uniform remote stress or displacement is

$$F_c = \left[M_1 + M_2 \left(\frac{a}{t} \right)^2 + M_3 \left(\frac{a}{t} \right)^4 \right] g_1 g_2 g_3 g_4 g_5 f_\varphi f_w \quad (10)$$

for $0.2 < a/c < 2$, $a/t < 1$, $1 < r/t < 2$, $(r + c)/w < 0.5$, $r/w = 1/16$, and $0 < \varphi < \pi/2$. Again, the equations for other terms in equation (10) are given in appendix D.

Figures 20(a)–20(d) show comparisons among the FEM, WFM, and stress intensity factor equations for a corner crack at the notch root in the SENT specimens. Here, too, each figure is for a constant value of a/c and r/t. The WFM results (solid symbols) are the averages of results for the two values of r/t (1.39 and 1.6). Open symbols show the FEM results for $r/t = 1.5$. Again, the corner-crack equations are shown by the curves for various values of a/t. The equations are generally within ± 5 percent of the FEM and WFM results except for the differences noted between the methods for shallow cracks with $a/c = 2$ (fig. 20(d)) and deep cracks with $a/c = 0.4$ (fig. 20(b)). In these two cases, the equations were made to fit the FEM results.

4.5.2. Through Crack at Notch

The stress intensity factor for a through crack emanating from a semicircular notch subjected to remote uniform stress or displacement is expressed as

$$K = S(\pi c)^{1/2} F_t \left(\frac{c}{w}, \frac{c}{r}, \frac{r}{w} \right) \quad (11)$$

where F_t is the boundary-correction factor that accounts for the effect of the notch and external boundaries for $r/w = 1/16$. Equations are given in appendix C for F_t for uniform remote stress or displacement.

Figure 21 shows a comparison between the BFM results and stress intensity factor equations for a through crack at the notch in a SENT specimen subjected to either remote uniform stress or displacement ($h/w = 1.5$). Figure 21(a) shows the results for small through cracks and figure 21(b) the results for large cracks. These results indicate that the boundary-correction factors are strongly influenced by the remote boundary condition for large-crack lengths. Through-crack equations, fitted to these results, are shown by the curves. The equations are within ± 2 percent of the BFM results. Stress intensity factors from experiments were also determined from the fatigue crack-growth-rate test in appendix C, and agreed well with the numerical results for uniform displacement boundary conditions. Thus, the equations for uniform displacement with $h/w = 1.5$ were used in the life-prediction code FASTRAN II (ref. 56) to predict small- and large-crack growth in the SENT specimens.

4.5.3. Effect of Cladding

In the LC9cs alloy, cracks initiated in the cladding layer and grew as corner cracks into the core material. To account for this growth, the stress intensity factor solution for corner cracks was modified to approximately model cracks in a multiple-layer medium. The yield stress of the cladding was estimated to be about 50 MPa. In the SENT specimens, the cladding layer (ℓ) always yielded and developed multiple cracks from slip-band formation along the edges of the notch. Thus, as a first approximation, ℓ was assumed to carry no load. To estimate the effects of the cladding layer on stress intensity factors, two stress intensity factor solutions were used: one was an edge crack in a 2D sheet that carries a uniform stress q over only the core material, as shown in figure 22(a); the other was an edge crack that carries uniform stress over the total crack length, as shown in figure 22(b). The cladding correction factor was then defined as the ratio of the stress intensity factors for the two crack configurations. The stress intensity factor for the partially loaded edge crack (ref. 47) is given by

$$K_{ce} = \sigma \sqrt{\pi a}\, \frac{\sqrt{2}}{\pi} \sum_{j=1}^{5} \frac{\beta_j \left(1 - \frac{\ell}{a} \right)^{j-1/2}}{2j - 1} \quad (12)$$

where $\beta_1 = 2$, $\beta_2 = 0.9788$, $\beta_3 = 1.1101$, $\beta_4 = -0.3194$, and $\beta_5 = -0.1017$. The corresponding
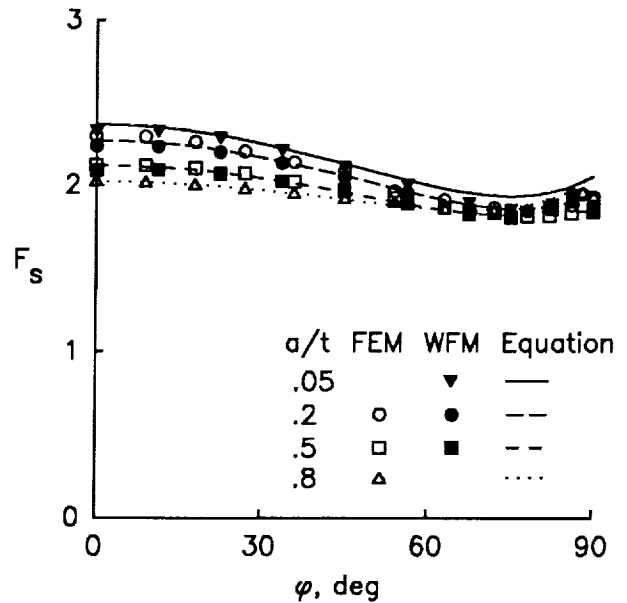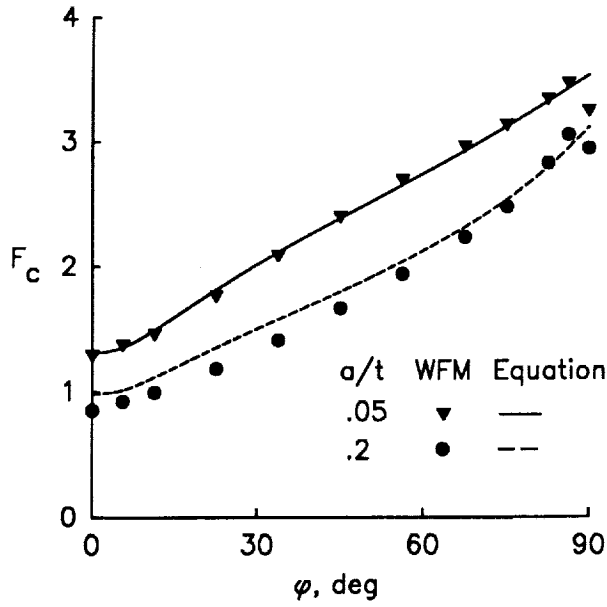
(a) $a/c = 0.2$.
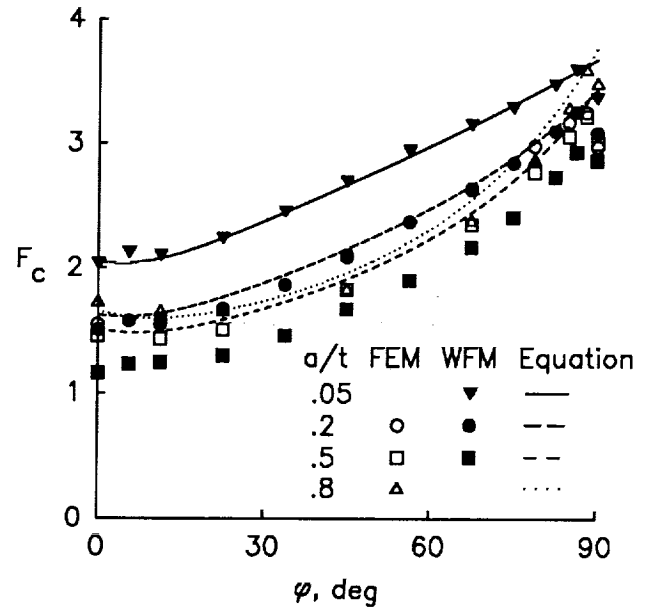
(b) $a/c = 0.4$.
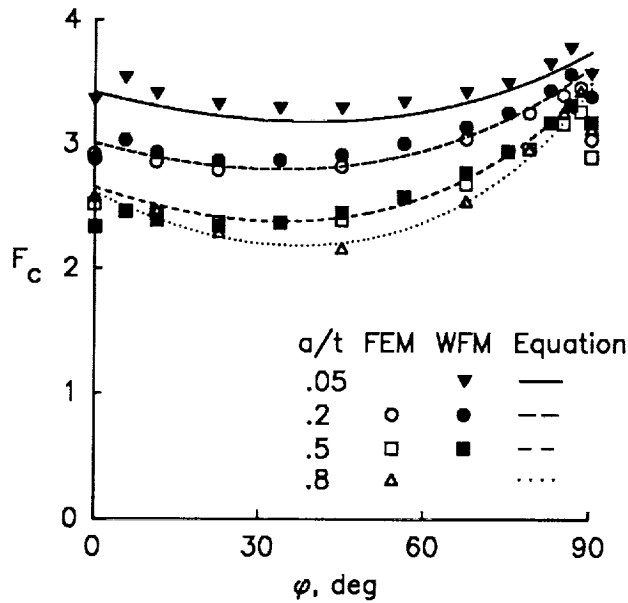
(c) $a/c = 1$.
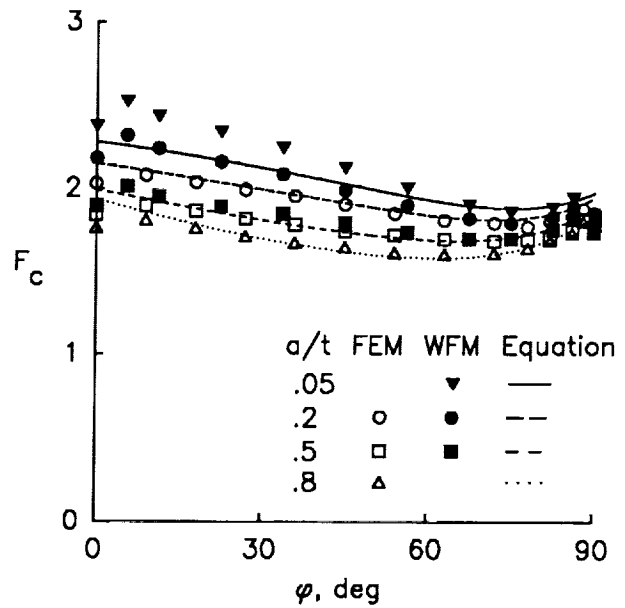
(d) $a/c = 2$.

Figure 20. Boundary-correction factors from FEM, WFM, and equations for corner crack at notch. $r/t = 1.5$.

stress intensity factor for the uniformly loaded edge crack (ref. 32) is

$$K_e = \sigma\sqrt{\pi a}\, 1.1215 \qquad (13)$$

The ratio of K_{ce}/K_e, the cladding correction factor, is

$$G_c = 0.4 \sum_{j=1}^{5} \frac{\beta_j \left(1 - \frac{\ell}{a}\right)^{j-1/2}}{2j - 1} \qquad (14)$$

If the crack length is equal to the cladding thickness, then $G_c = 0$, whereas if the crack length becomes large compared with cladding thickness, G_c approaches unity and the cladding has no effect on stress intensity factors.

The cladding correction must now be applied to a corner-crack configuration. (See fig. 22(c).) The angle φ is measured from the free surface. The edge-crack cladding correction can be directly applied to point A in that figure, point A being the intersection

22
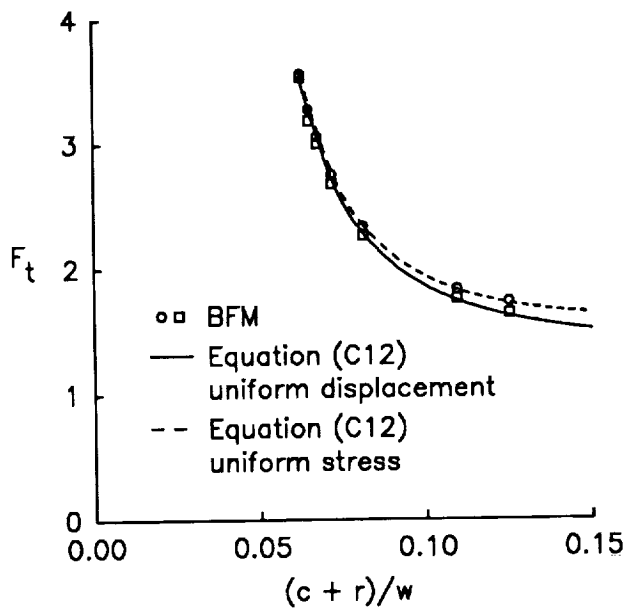
(a) Small through cracks.
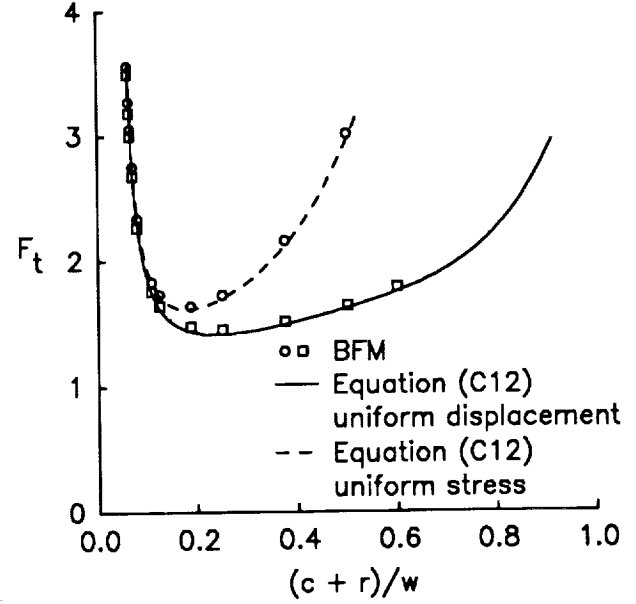
(b) Large through cracks.

Figure 21. Boundary-correction factors from BFM and equation for small through crack at notch. $r/w = 1/16$; $h/w = 1.5$.
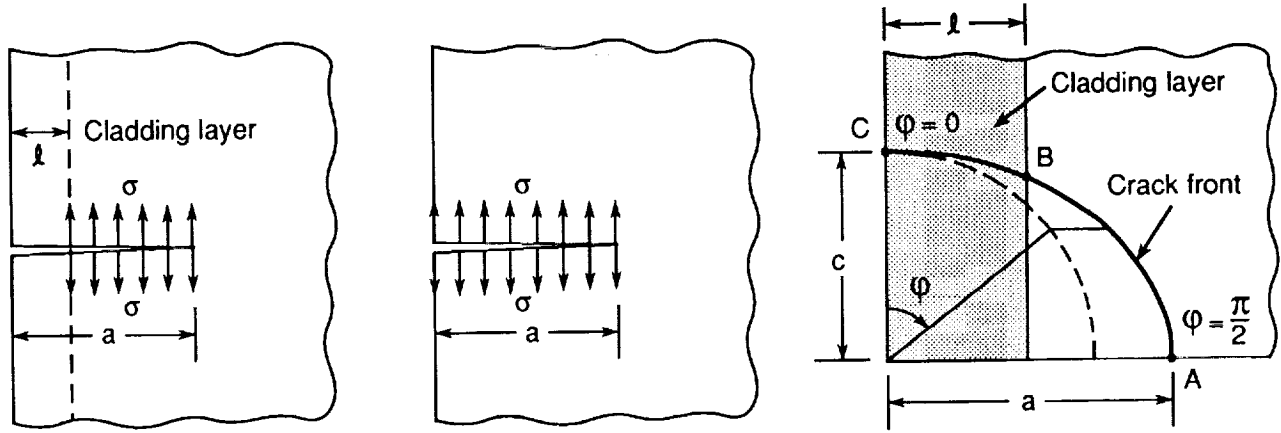
(a) Partially loaded edge crack.

(b) Uniformly loaded edge crack.

(c) Corner crack in clad material.

Figure 22. Crack configuration and loadings for estimating clad correction on stress intensity factors for corner crack at notch.

between the crack front and notch surface ($\varphi = \pi/2$) because it most closely resembles figure 22(a). However, the application of G_c at other locations is questionable. To grow a crack in the bare material, point B should be used to evaluate stress intensity factors. The parametric angle that defines point B will vary from $\pi/2$ when $a \approx \ell$ to $\varphi = 0$ when $a > \ell$. The stress intensity factors at point B will also be greatly reduced because the no-load-carrying clad has a similar effect as on stress intensity factors at point A. Thus, the 3D stress intensity factors for

a corner crack at the edge of a notch were modified by multiplying G_c times the stress intensity factor solution without the clad (eq. (10)). The corner-crack (boundary and clad) correction becomes $F_c' = F_c G_c$. Although the cladding correction factor was derived for the maximum depth location ($\varphi = \pi/2$), the same correction was applied at $\varphi = 0$ where the crack front intersects the sheet surface in the cladding layer. The selection of point C ($\varphi = 0$) was made for convenience because small corner cracks in the clad material grew in a nearly semicircular ($a/c = 1$)

23

manner for low a/t and the stress intensity factors for this configuration do not vary much with the parametric angle. (See fig. 20(c).)

5. Large-Crack Experimental Data

Experiments were conducted to determine the rates of fatigue crack growth on large cracks (>2 mm) at three constant-amplitude stress ratios and the Mini-TWIST loading sequence. The objective was to generate data for the two aluminum alloys for a wide range of rates, especially in the near-threshold crack-growth regime. Additional tests were also conducted on the LC9cs bare alloy to determine the effect of the cladding on large-crack-growth rates. All of these tests were conducted on 75-mm-wide CCT specimens. (See appendix E.) The method by which the data were recorded is presented in appendix G. These data will be used to define the regime in which large-crack data apply to small cracks and to establish the baseline data for use in life predictions. The results will be presented as ΔK against crack-growth rate.

5.1. Stress Ratio Effects on Large-Crack-Growth Rates

Fatigue crack-growth-rate tests for constant-amplitude loading on 7075-T6 and LC9cs aluminum alloy sheets were conducted at $R = -1$, 0, and 0.5. Tests on the LC9cs bare alloy were conducted at only $R = 0$ and 0.5. At each stress ratio, two types of tests were conducted: constant-amplitude loading and threshold (load-shedding) tests.

5.1.1. 7075-T6 Aluminum Alloy

The ΔK-rate data for large cracks are shown in figure 23 for the 7075-T6 alloy. At all stress ratios, the data from NASA and CAE agreed well, although some slight discrepancies were observed at the threshold level. The NASA data showed slightly higher ΔK thresholds than did the CAE data for $R = -1$ and 0. The data for $R = 0.5$ from each laboratory agreed very well. The data at each of these stress ratios parallel well with each other. The data also showed several "knees" or transitions (T_1, T_2, and T_3), which are sharp changes in the slope. These transitions occur at nearly the same crack-growth rate for all stress ratios. References 57 and 58 have shown for 7000 series and 2024 aluminum alloys, respectively, that these transitions correspond to loading conditions where the monotonic or cyclic plane-strain plastic-zone sizes become equal to characteristic microstructural features such as dispersoid
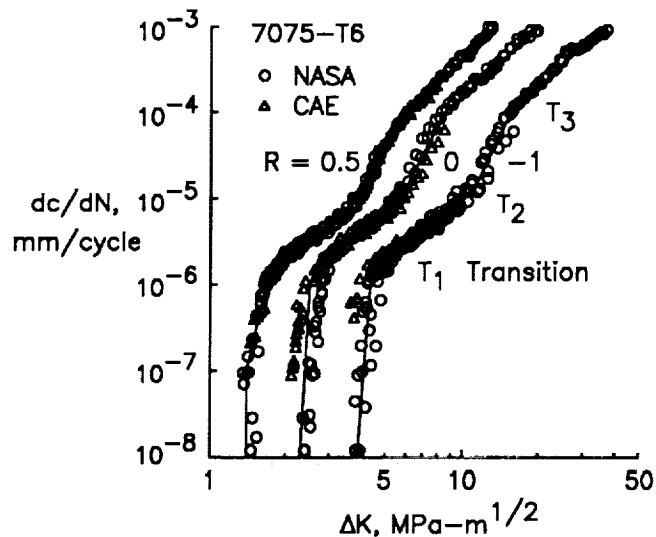
Figure 23. Crack-growth rate against ΔK for 7075-T6 aluminum alloy under various constant-amplitude loading.

spacing, dislocation cells, subgrain size, or grain size. Wanhill (ref. 58) pointed out that the cyclic plastic zone should be calculated with ΔK_{eff} to account for closure effects on reverse yielding. References 57 and 58 suggest the following correlations at the transition points:

T_1 cyclic plastic-zone size $\approx$ mean planar distance between dispersoids

T_2 cyclic plastic-zone size $\approx$ subgrain and dislocation cell sizes

T_3 monotonic plastic-zone size $\approx$ grain sizes

The transitions are also associated with changes in fracture surface topography. Between ΔK_{th} and T_2, the fracture surfaces are faceted. Above T_2 a gradual change to continuum (flat) fracture is characterized by fatigue striations. Above T_3 the flat fracture changes to slant crack growth (crack surface plane is at 45° to the loading axis through the thickness). The flat-to-slant crack growth is discussed further in section 8. Relationships between monotonic and cyclic plastic zones and the transitions observed in the current study are discussed in section 8.

The solid lines were drawn through the data points by a visual fit; the points used to define these lines are given in table V. These lines are compared with the small-crack data in section 6.

Figure 24 shows a comparison between the crack-growth rates generated in the cooperative program and the results of Hudson (ref. 59) on the same material. Wide-ranging stress ratios were tested in

Table V. Large-Crack Data Points for 7075-T6
Aluminum Alloy

R	Point	ΔK, MPa-m$^{1/2}$	dc/dN, mm/cycle
−1	1	3.9	1.00×10^{-8}
	2	4.4	1.40×10^{-6}
	3	11.0	1.20×10^{-5}
	4	15.5	1.00×10^{-4}
	5	40.0	1.30×10^{-3}
0	1	2.3	1.00×10^{-8}
	2	2.5	1.00×10^{-6}
	3	3.0	2.00×10^{-6}
	4	5.6	9.00×10^{-6}
	5	8.5	1.00×10^{-4}
	6	24.5	1.70×10^{-3}
0.5	1	1.4	1.00×10^{-8}
	2	1.4	1.00×10^{-7}
	3	1.7	1.20×10^{-6}
	4	3.8	8.00×10^{-6}
	5	5.7	8.50×10^{-5}
	6	15.5	1.50×10^{-3}
Mini-TWIST	1	5.3	6.00×10^{-8}
	2	8.6	1.20×10^{-6}
	3	35.0	7.40×10^{-5}
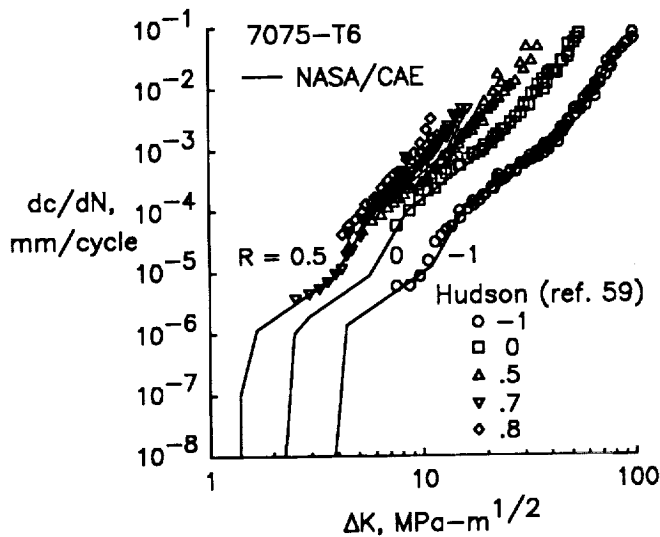
Figure 24. Crack-growth rate against ΔK from cooperative program and Hudson's data for 7075-T6 aluminum alloy.

Figure 25. Crack-growth rate against ΔK for LC9cs aluminum alloy for constant-amplitude loading.

reduce the data. The results of this cooperative program demonstrate why a calculation of point-to-point crack-growth rates is preferred more than a smoothing technique.

5.1.2. LC9cs Aluminum Alloy

The large-crack ΔK-rate data for the LC9cs clad alloy are shown in figure 25. In calculating ΔK, the full specimen thickness was used. The data from the CAE and NASA laboratories agreed fairly well for each stress ratio. Again, the NASA data showed slightly higher ΔK thresholds than did the CAE data. The three transitions observed in the data for the 7075-T6 alloy were also observed in the LC9cs alloy at about the same rates as measured for the 7075-T6 alloy. The solid lines were drawn through the data points by a visual fit; the points are given in table VI.

As mentioned, additional tests were conducted on the LC9cs bare alloy. These results are shown in figure 26 for $R = 0$ and 0.5. For comparison, the test data on the LC9cs alloy, shown in figure 25, were reanalyzed without the cladding layer in the calculation of ΔK (180 μm subtracted from the original thickness). The effective thickness t' was 93 percent of the original thickness. In the midrate region (10^{-6} to 10^{-4} mm per cycle), the results from the two sets of data agreed very well, indicating that the cladding layer could not carry a significant portion of the load. The LC9cs alloy showed somewhat higher ΔK thresholds than the LC9cs bare alloy. At the lower ΔK values, the cladding layer may carry enough load to affect the threshold.

reference 59; these results are shown as symbols and the results from the cooperative program are shown by the solid lines. Results for $R = -1$, 0, and 0.5 agreed quite well with the previous data. In some cases, the transition in Hudson's data is not as sharply defined as in the cooperative program because a smoothing technique was used to

Table VI. Large-Crack Data Points for LC9cs
Aluminum Alloy

R	Point	ΔK, MPa-m$^{1/2}$	dc/dN, mm/cycle
-1	1	4.0	1.00×10^{-8}
	2	4.0	2.00×10^{-7}
	3	4.6	2.00×10^{-6}
	4	8.7	1.00×10^{-5}
	5	11.5	4.70×10^{-5}
	6	36.5	1.00×10^{-3}
0	1	2.4	1.00×10^{-8}
	2	2.6	1.80×10^{-6}
	3	5.0	1.10×10^{-5}
	4	7.0	1.00×10^{-4}
	5	18.7	1.60×10^{-3}
0.5	1	1.6	1.00×10^{-8}
	2	1.7	1.00×10^{-6}
	3	2.0	2.70×10^{-6}
	4	3.2	7.00×10^{-6}
	5	4.5	4.60×10^{-5}
	6	10.0	7.60×10^{-4}
Mini-TWIST	1	6.0	1.00×10^{-7}
	2	10.0	2.50×10^{-6}
	3	27.0	4.20×10^{-5}

Figure 27. Crack-growth rate against ΔK for 7075-T6 and LC9cs aluminum alloys for constant-amplitude loading.

based on $t' = 0.93t$ in the calculation of ΔK. In the midrate region, the results for the 7075-T6 alloy and LC9cs bare alloy (with t') agreed fairly well, but some significant differences were evident in the ΔK thresholds. Even the LC9cs alloy showed slightly higher thresholds than the 7075-T6 alloy.

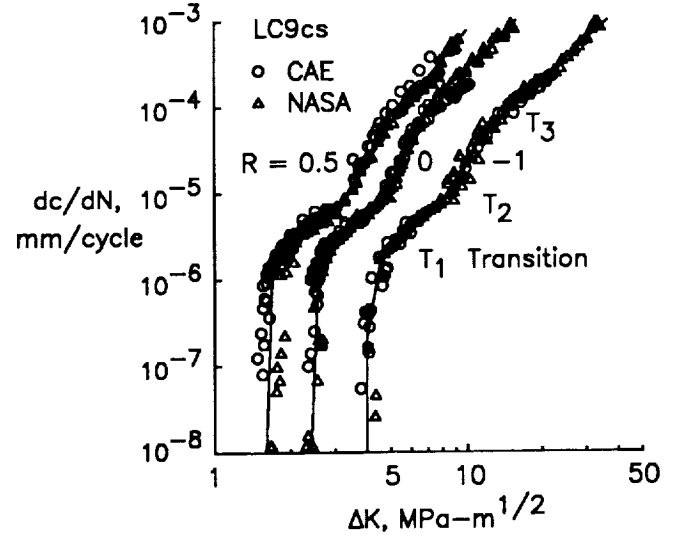### 5.2. Large-Crack-Growth Rates for Mini-TWIST Spectrum

Two types of spectrum crack-growth tests were conducted on CCT specimens made of 7075-T6 and LC9cs alloy sheets: constant load S_{mf} and load shedding. The objective of the load-shedding tests was to obtain ΔK-rate data to low stress intensity factor ranges to compare with the small-crack data. (See sec. 6.6.2.) The constant-mean flight-stress tests were conducted to obtain data at higher stress intensity factor ranges and to provide data on crack length against cycles to verify FASTRAN II. (See ref. 56.)

5.2.1. 7075-T6 Aluminum Alloy

Figure 28 shows the ΔK-rate data for the 7075-T6 alloy. The circular symbols are the results from load reduction tests and the triangular symbols are from the constant load tests. Recall that the ΔK values were computed by using the maximum and minimum stresses in the Mini-TWIST spectrum and the crack-growth rates generally were calculated by using the crack extension during one pass through the spectrum. At the higher rates, this procedure was not always possible. The results from the two types of tests agreed well. The solid lines were drawn

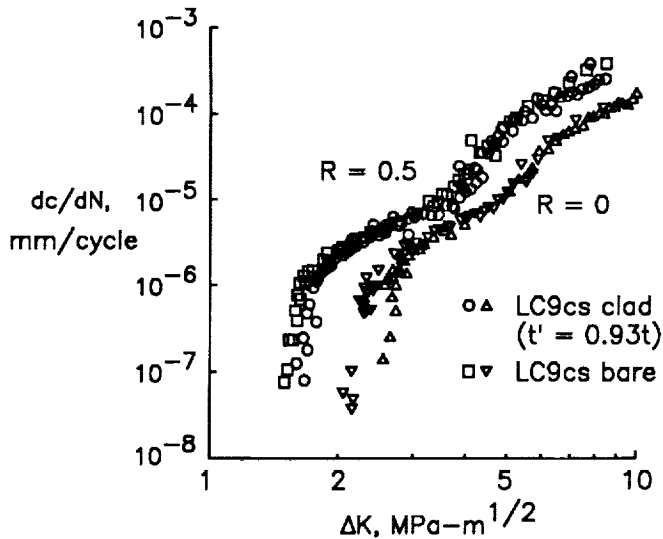Figure 26. Crack-growth rate against ΔK for LC9cs clad and bare aluminum alloys at two stress ratios.

5.1.3. Comparison of Alloys

A comparison of the ΔK-rate results for the two alloys is shown in figure 27. The solid lines show the fitted lines from the 7075-T6 alloy tests and the dashed lines show the results from the LC9cs alloy tests. The dotted lines show the LC9cs alloy results
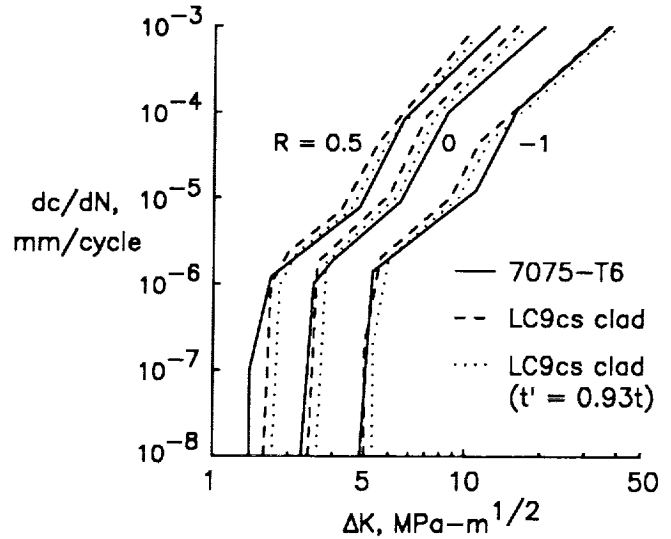
26

Figure 28. Crack-growth rate against ΔK for 7075-T6 aluminum alloy for Mini-TWIST load sequence.
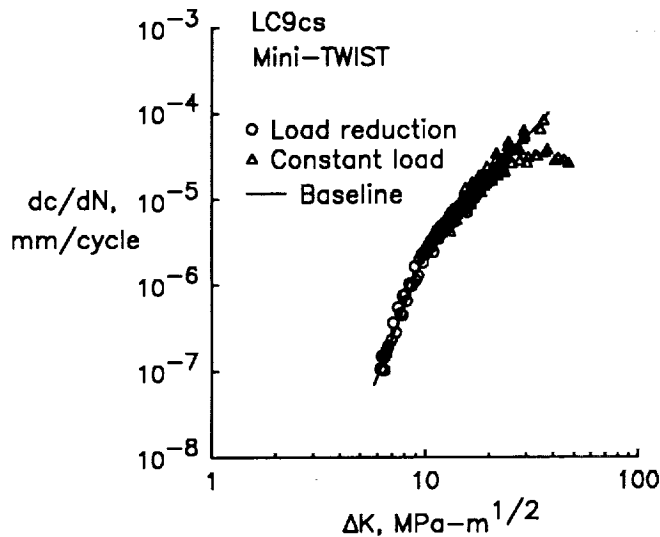
Figure 29. Crack-growth rate against ΔK for LC9cs aluminum alloy for Mini-TWIST load sequence.

through the data points by a visual fit; these points are given in table V.

5.2.2. LC9cs Aluminum Alloy

The large-crack ΔK-rate data for the LC9cs alloy from the Mini-TWIST spectrum are shown in figure 29. In calculating ΔK, the full specimen thickness was used. Results from both types of tests, load reduction and constant load, agreed well. Crack growth in one of the constant load tests, however, slowed near the end, as shown by the results near 25 MPa-m$^{1/2}$. This slowing occurred after the appli-
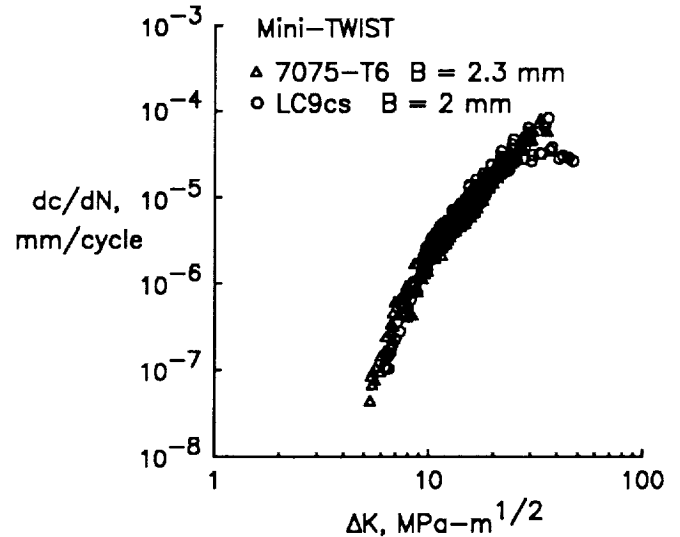
Figure 30. Crack-growth rate against ΔK for 7075-T6 and LC9cs aluminum alloys for Mini-TWIST load sequence.

cation of a severe flight. Again, the baseline large-crack relation is given in table VI.

5.2.3. Comparison of Alloys

Figure 30 shows a comparison between the ΔK-rate data for the 7075-T6 and LC9cs alloys for the Mini-TWIST spectrum. Here, the ΔK-rate data fall together quite well, even without the effective thickness for the clad alloy. The cracks in the LC9cs alloy should grow faster at the same ΔK value than they do in the 7075-T6 alloy, similar to what was observed for constant-amplitude loading, because the clad material carries very little load and the crack tip in the core material would have a higher ΔK. However, the cladding layer may affect loading interaction (retardation) more in the LC9cs alloy than in the bare 7075-T6 alloy.

6. Fatigue and Small-Crack Experimental Data

Researchers in the small-crack test program used two types of fatigue tests for both constant-amplitude and spectrum loading. Standard fatigue tests on SENT specimens were conducted to determine the S-N (stress-cycles) curves for the 7075-T6, bare, and LC9cs clad, especially near the endurance limit. Fatigue tests were also conducted on the LC9cs material with the cladding layer removed. Small-crack tests were conducted on SENT specimens based on stress levels selected from the fatigue test results.

This section presents information on initiation sites and the distribution of small cracks along the

bore of the notch for the two alloys. Small-crack data charts were used to record crack location and crack length against cycles from the replicas. Crack-shape data were obtained from examination of fracture surfaces of specimens that were broken early in life. These data, together with a crack noninteraction criterion, were used to determine ΔK-rate data for small surface and corner cracks at the notch. Comparisons are then made with large-crack ΔK-rate data discussed in section 5.

6.1. Fatigue Tests

Fatigue life tests were conducted on the SENT specimens of 7075-T6 and LC9cs alloys to aid in the selection of applied stress levels and replica intervals for the small-crack-growth-rate tests. These fatigue life data were also used to assess a total life-prediction method based solely on crack propagation from material microstructural defects or from the cladding layer. The effects of cladding and the replication process on fatigue lives were also studied.

6.1.1. Constant-Amplitude Loading

Fatigue life data for constant-amplitude loading at the three stress ratios are shown in figures 31 and 32 for 7075-T6 and LC9cs alloys, respectively. In those figures, N_f is the cycles to failure at S_{max}. Solid and open symbols show the results of standard fatigue tests conducted by each laboratory. NASA was the lead laboratory for the 7075-T6 alloy and CAE was the lead laboratory for the LC9cs alloy. The results from each laboratory agreed well for both alloys and all test conditions, although slight differences were observed for the LC9cs alloy, which exhibited more experimental scatter than the 7075-T6 bare alloy. As usual, an arrow indicates that a test was terminated before failure at the indicated cycles. The stress levels for the small-crack test were selected from these results and are listed in table IV. The lowest stress levels were near the endurance limit but high enough to give failures in about 100 000 cycles. The second stress level was selected to give about 50 000 cycles to failure. Table IV indicates that the notch root stresses are elastic for all constant-amplitude tests except those at $R = 0.5$.

6.1.2. Mini-TWIST Spectrum Loading

Fatigue test results for the Mini-TWIST loading sequence are shown in figures 33 and 34 for the 7075-T6 and LC9cs alloys, respectively. Fatigue life is plotted against S_{max}, which is equal to $2.6S_{mf}$ (the highest stress level in the sequence). The solid and open symbols distinguish the results from each
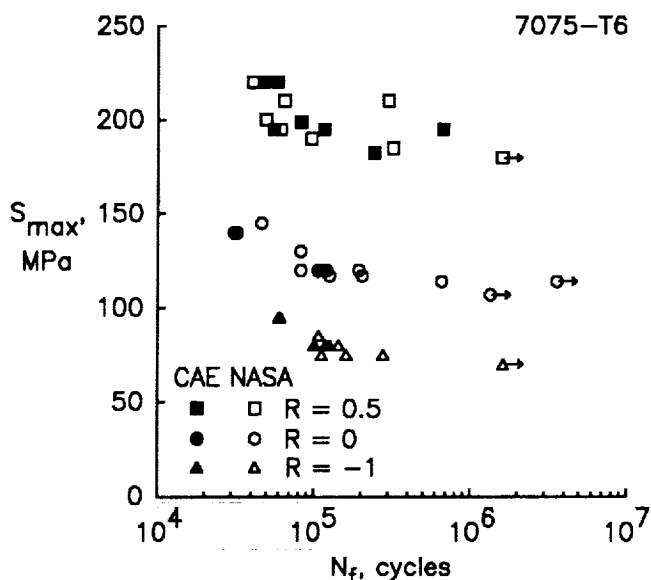
Figure 31. Fatigue lives of 7075-T6 aluminum alloy at various stress ratios.
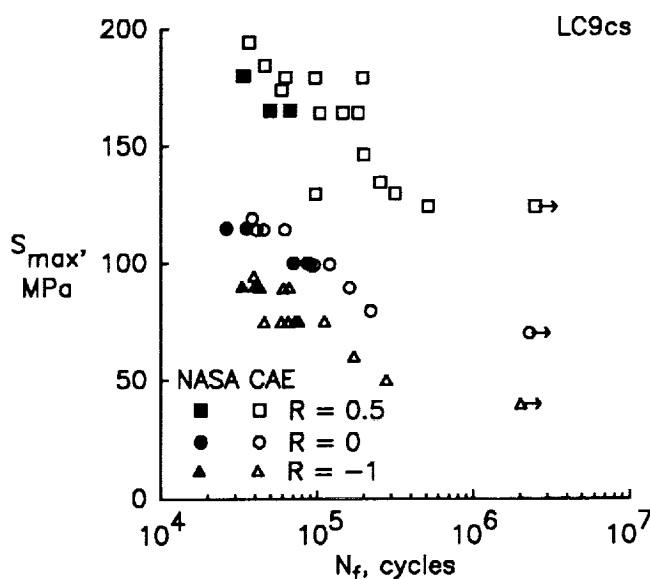
Figure 32. Fatigue lives of LC9cs aluminum alloy at various stress ratios.

laboratory; the close clustering reflects the good agreement between NASA and CAE tests. The stress levels selected for the small-crack tests are given in table IV; they were selected to give about 0.5 to 2 million cycles to failure. Three stress levels were selected for the LC9cs alloy because it has a lower endurance limit than the 7075-T6 alloy. Table IV shows that the notch root stresses are above the yield stress for the 7075-T6 alloy but are generally elastic for the LC9cs alloy. However, the cladding layer yields in all cases. (The estimated yield stress of the cladding was 50 MPa, as estimated from results shown in table II.)
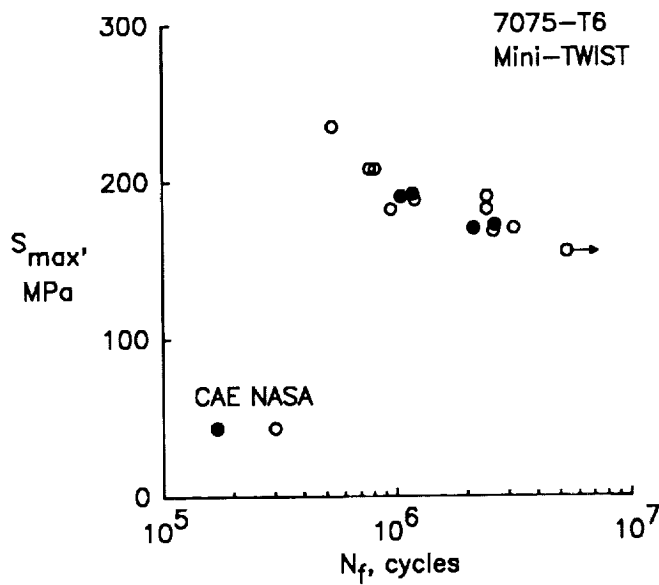
Figure 33. Fatigue lives of 7075-T6 aluminum alloy for Mini-TWIST load sequence.

Figure 35. Fatigue lives of 7075-T6 and LC9cs bare aluminum alloys at two stress ratios.

Figure 34. Fatigue lives of LC9cs aluminum alloy for Mini-TWIST load sequence.
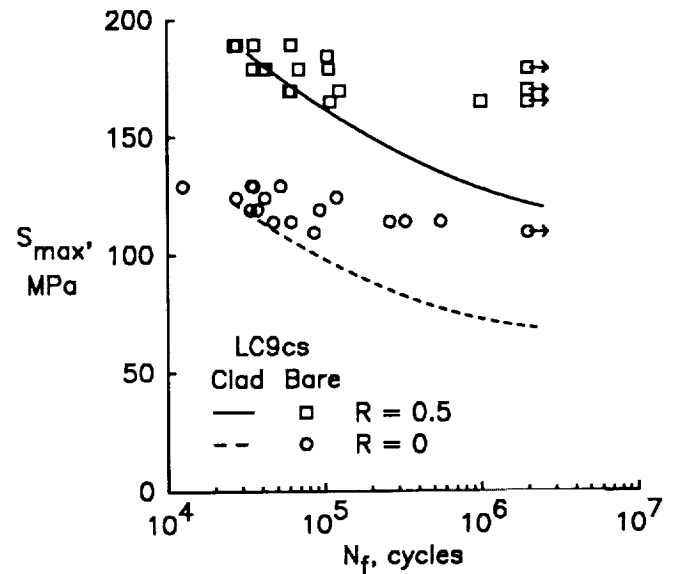
Figure 36. Fatigue lives of LC9cs clad and bare aluminum alloys at two stress ratios.

6.1.3. Effect of Cladding

Fatigue tests were also conducted on SENT specimens of LC9cs bare alloy. The objective of these tests was to assess the effect of cladding on fatigue lives at $R = 0$ and 0.5. Figure 35 shows a comparison of fatigue lives on bare LC9cs and bare 7075-T6 alloys. The endurance limits for both alloys were similar, but the fatigue lives of the LC9cs bare specimens generally were shorter than those for the 7075-T6 alloy. A comparison between LC9cs clad (curves) and bare (symbols) alloys is made in figure 36. These results show that removing the cladding greatly im-

proves the endurance limit. Fatigue lives at higher stress levels also show an improvement.

6.1.4. Effect of Replica Method

Fatigue life data for constant-amplitude and Mini-TWIST spectrum loading are shown in figures 37 and 38 for 7075-T6 alloy and in figures 39 and 40 for LC9cs alloy, respectively. The open symbols are the standard fatigue tests results previously shown. These tests were conducted for laboratory air conditions and were continuously cycled to failure without interruption. The solid symbols denote tests during which replicas were taken.
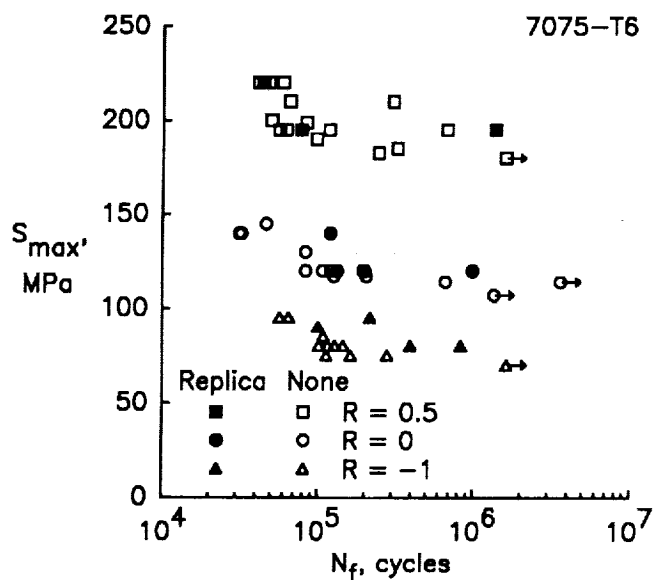
Figure 37. Effect of replica process on fatigue lives of 7075-T6 aluminum alloy for constant-amplitude loading.
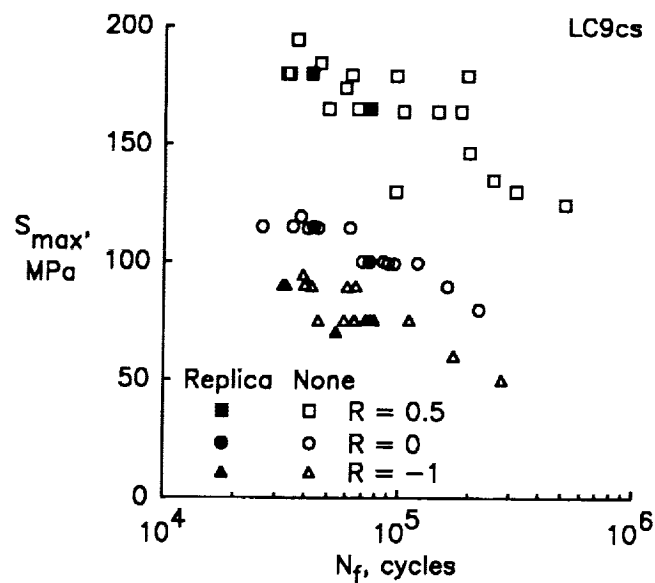
Figure 39. Effect of replica process on fatigue lives of LC9cs aluminum alloy for constant-amplitude loading.
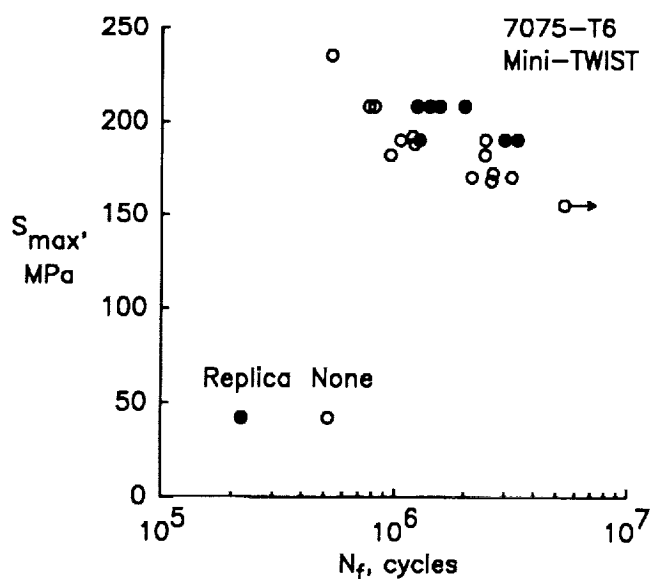
Figure 38. Effect of replica process on fatigue lives of 7075-T6 aluminum alloy for Mini-TWIST load sequence.
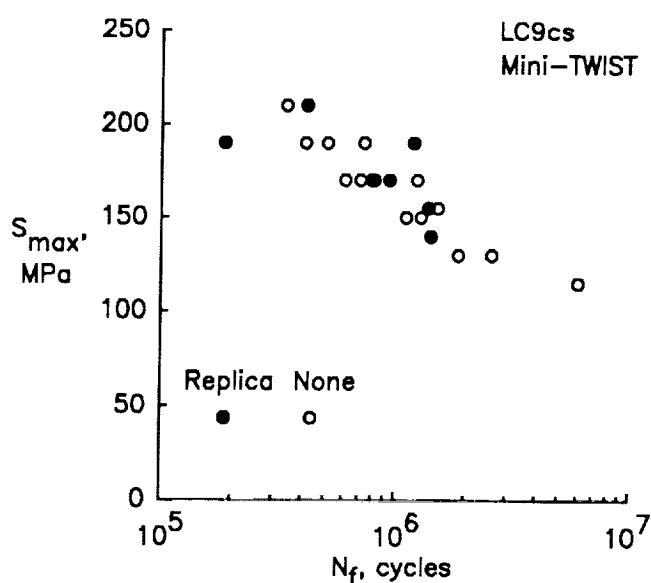
Figure 40. Effect of replica process on fatigue lives of LC9cs aluminum alloy for Mini-TWIST load sequence.

The limited results on the 7075-T6 alloy for constant-amplitude loading (fig. 37) indicated that the fatigue lives at $R = 0$ and -1 were affected by the replica process. The fatigue lives for $R = -1$ were nearly twice as long as the lives for tests without the replicas. Tests for the Mini-TWIST loading (fig. 38) also showed that the replica process strongly affects fatigue lives. Here, the fatigue lives were also doubled when replicas were taken. To identify the source of this effect, four additional tests were undertaken on this material with the Mini-TWIST spectrum ($S_{max} = 205$ MPa). In two tests, the fatigue cycle was

stopped periodically after the same cyclic interval in the replica tests, and the load was held for 10 minutes at the replica load (about 60 percent of S_{max}); however, no replica was taken. The resulting lives were slightly less than the lives from the standard fatigue tests at this stress level. For the other two specimens, the notch root was bathed with the acetone solution twice during the 10-minute hold at replica loading, but no replica was taken. The fatigue lives from these tests agreed with those from the tests with replicas. Thus, the longer fatigue lives of the replica test specimens are likely attributable to

a chemical effect connected with the acetone rather than a purely mechanical effect from holding the cracked specimens at constant tensile loading or from residual acetyl cellulose between the crack surfaces.

Whether the longer life is attributable to effects on initiation or on fatigue crack-growth rates was not determined in this study. However, Gao, Pao, and Wei (ref. 60) have shown that higher fatigue crack-growth rates are associated with higher water vapor pressures. They also found that crack-growth rates in moist air are greater than those in vacuum, argon, or oxygen, which they attributed to hydrogen embrittlement. Given the sensitivity of the 7075-T6 alloy to water vapor, the longer fatigue lives after replication may relate to the introduction of acetone, which reduced the environmental effects because it dries or protects the crack front region from the normal moisture levels in laboratory air. In the standard fatigue life tests, a baseline condition of water vapor exposure was established in laboratory air. Tests with the 10-minute holding time at loading are equally exposed to laboratory water vapor, which results in similar fatigue lives. In replica tests or when the holding time includes bathing the notch root with acetone, the water vapor concentration at the crack front may be reduced, thereby slowing crack-growth rates and producing longer fatigue lives.

The replica-effects tests on the LC9cs alloy are shown in figure 39 for constant-amplitude loading. The limited results here indicate that the replica process did not affect the fatigue lives for this alloy. Similarly, in extensive tests using the Mini-TWIST spectrum sequence (fig. 40) no effect of the replica process was evident on fatigue lives. As discussed, this alloy is nearly identical in composition and microstructure to the 7075-T6 alloy except for the 60-μm cladding layer on each sheet. Because the fatigue lives for the 7075-T6 alloy were longer because of the acetone solution, the LC9cs alloy should have shown longer lives. However, cracks in the LC9cs specimens initiated from slip bands in the low-strength ductile cladding and produced predominately corner cracks rather than initiating at inclusion particle sites as surface cracks as in the 7075-T6 alloy. (Crack initiation results for the two alloys are discussed in the next section.) When corner cracks are prevalent, no consistent difference is evident between the fatigue lives with or without replicas. The seeming indifference to the effects of acetone on fatigue life (and presumably crack-growth rates) may relate to the corner-crack configuration. Because replication is performed on only one surface (notch root), the corner-crack front is exposed to the water

vapor environment through the crack surface that intersects the side of the specimen.

Because the plastic replicas had an effect on the fatigue life of the 7075-T6 alloy and presumably on small-crack growth, the small-crack rates in the cooperative program may not reflect the true behavior of small cracks for laboratory air conditions. Therefore, analyses and comparisons based on these data should be viewed with caution. Fortunately, the replica method did not affect the fatigue life of LC9cs specimens because of corner-crack growth. Here, the complex interaction of the cladding on stress intensity factors may be evaluated without concern for replica effects.

6.2. Initiation Sites and Distributions for Small Cracks

A study of small cracks must invariably involve consideration of the surface and subsurface microstructure of the material. In the following sections, the initiation of cracks at microstructural defects, discontinuities, or cladding is discussed. Surface replicas taken early in life were used to locate where cracks initiated and to identify the microstructural feature that caused those cracks. Broken specimens were then used to identify the types of cracks (surface or corner) and their shapes.

Photomicrographs of sections along the notch-root surface and crack-surface plane for the 7075-T6 and LC9cs alloys are shown in figures 41(a) and 41(b), respectively. These photomicrographs show inclusion particles in the bare (or core) material and the grain structure. Cracks that initiate along the notch surface will grow as either surface or corner cracks. Crack growth along the bore of the notch will be in the $2a$-direction and crack growth away from the notch will be in the c-direction. The grain structure and inclusion-particle clusters of both alloys are elongated in the c-direction. The notch-surface planes in figures 41(c) and 41(d) show a similar pancake microstructure as do the crack-surface planes. Figure 41(d) also shows the cladding layer in the as-received condition. Chemical polishing of the SENT specimens reduced the cladding layer to 50–70 μm.

6.2.1. 7075-T6 Aluminum Alloy

A typical initiation site along the bore of the notch in the 7075-T6 alloy is shown in figure 42. This series of photomicrographs from surface replicas shows a surface crack initiating and growing from a pit, which may have been caused by the removal of
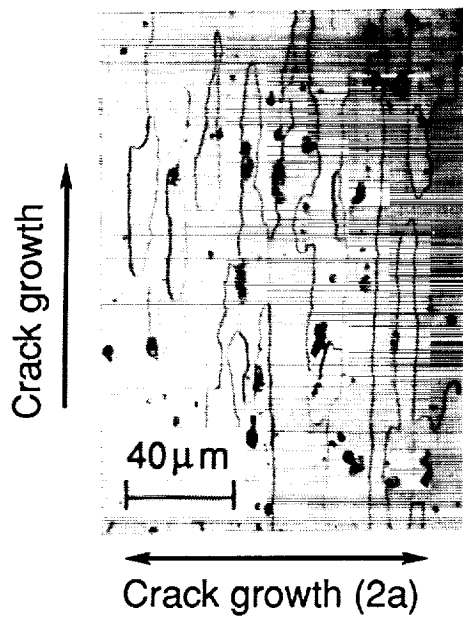
(a) 7075-T6 crack plane.

(b) LC9cs crack plane.
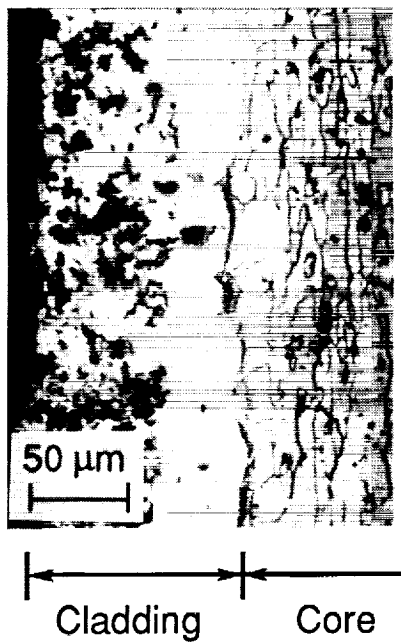
(c) 7075-T6 notch root.
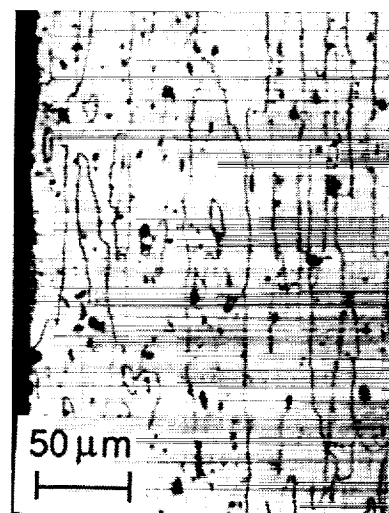
(d) LC9cs notch root.

L-93-50

Figure 41. Photomicrographs of sections along crack-surface plane and notch root surface for the two aluminum alloys.

(a) 13 000 cycles.

(b) 18 000 cycles.

(c) 28 000 cycles.
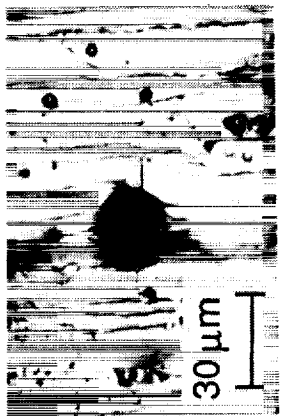
(d) 33 000 cycles.
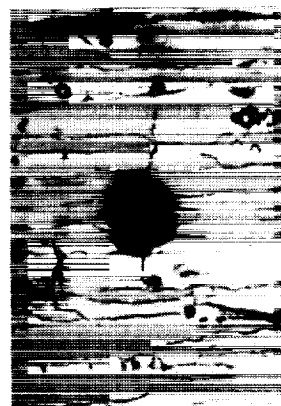
(e) 37 000 cycles.
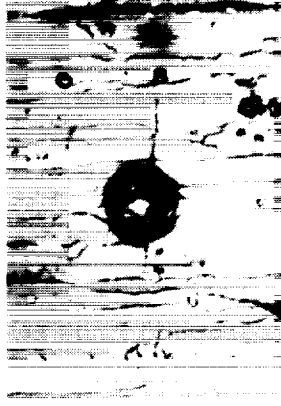
(f) 46 000 cycles.

(g) 54 000 cycles.

(h) 60 000 cycles.

30 μm

L-93-51

Figure 42. Photomicrographs of surface replicas showing initiation site and crack-growth history in 7075-T6 aluminum alloy. Specimen failed at 104 000 cycles.

33

an inclusion-particle cluster during the machining or polishing process. Here, the initial defect void size was surprisingly large, about 30 μm. A crack was observed to initiate at the void at about 17 percent of the total fatigue life. These photomicrographs show the progression of the crack for most of the life of the specimen. For the 7075-T6 alloy, crack initiation generally occurred early in life at inclusion-particle clusters or voids, similar to the crack initiations observed by Bowles and Schijve. (See ref. 61.)

Seven broken specimens were examined to identify the size of the inclusion-particle cluster or void that initiated the crack. In the SEM photomicrographs shown in figure 43, a specimen is shown that had two initiation sites along the bore of the notch. From this examination, the material defect size ranged from 4 to 8 μm in the $2a$-direction (along the notch root) and from 6 to 18 μm in the c-direction (away from the notch). (Note that these ranges do not include the unusually large void that is shown in fig. 42.) However, the defect sizes should be compared with the inclusion-particle sizes shown in figure 6. The defects that were sufficient to initiate surface cracks are at the upper portion of the particle size distributions. This outcome is expected because of the small volume of material used to generate the distribution chart. Thus, the initiation site should occur at one of the largest inclusion-particle sites or voids along or near the notch surface. From these results an initial defect (or crack size) $2a_i = 6$ μm was selected and the initial crack length was $c_i = 9$ μm to characterize the most probable initial defect.

6.2.2. LC9cs Aluminum Alloy

The initiation sites in the LC9cs alloy were nearly always in the cladding layer as shown in figure 44. This series of photomicrographs (again from surface replicas) shows slip bands and cracks in the cladding layer and cracks growing in the bare material. In figure 44, a crack was observed at about 17 percent of the life required to grow the crack across the full sheet thickness. Although this particular specimen broke in monotonic loading when the corner-crack length was equal to sheet thickness (breakthrough), the total fatigue life would have been only about 20 percent longer than the life to breakthrough. In the LC9cs alloy, cracks were also observed to initiate early in life, similar to the life in 7075-T6 alloy, even though they initiated in the cladding layer and grew predominately as corner cracks. The significance of the cladding layer on fatigue in aluminum alloys has been known for many years. (See ref. 62.) However, the analysis methods have only recently

been developed to analyze corner-crack growth and crack closure.

Some SEM photomicrographs of broken LC9cs specimens are shown in figure 45. These photographs show a corner crack that initiated in the cladding (fig. 45(a)) and a rare occurrence of a surface crack that initiated at a large void along the bore of the notch. (See fig. 45(b).) For these crack sizes, note that the crack fronts are nearly circular ($a/c = 1$ to 1.1). A detailed discussion on crack shapes is given in section 6.3.

6.2.3. Comparison of Alloys

A comparison of data on crack-initiation sites for the two alloys is shown in figure 46, which has an insert that shows a cross section of the notch root. The crack-initiation site, denoted t_i, is measured from the centerline of the specimen thickness. Half the sheet thickness is denoted t. When $t_i = 0$, the crack initiated at the specimen centerline; but when $t_i = t$, the crack initiated at the corner of the notch and specimen surface. The information on initiation site locations was obtained from the small-crack data charts made from plastic replicas taken early in life. Each specimen data chart documented one to five crack-initiation sites along the notch root. The cooperative program requirements were such that the five largest cracks were monitored from initiation to breakthrough ($L = B$). Because multiple cracks were more likely at the high stress levels than at the low stress levels, the low stress levels in the test program were selected as slightly higher than the endurance (fatigue) limit.

The initiation-site information from NASA and CAE was analyzed together. The distribution of initiation sites along the bore of the notch for nearly 65 cracks is plotted in figure 46. The number of cracks that initiated in each of 10 separate regions along the notch-root surface is plotted in relation to the ratio t_i/t. Each region is defined as 10 percent of the specimen thickness.

For the 7075-T6 alloy, most of the cracks initiated at $t_i/t < 0.5$ (middle half of specimen thickness) and grew as semielliptical surface cracks. Crack initiation in the middle of the notch root is promoted by an elevation of stress concentration in this region. The stress concentration factor at the notch is about 5 percent higher in the middle of the specimen than on the edge of the notch. (See ref. 38.) With the edges of the notch polished and deburred, the most likely location for crack initiation would be near the center of the specimen thickness. Therefore, for small cracks in the 7075-T6 alloy, modeling the crack as a
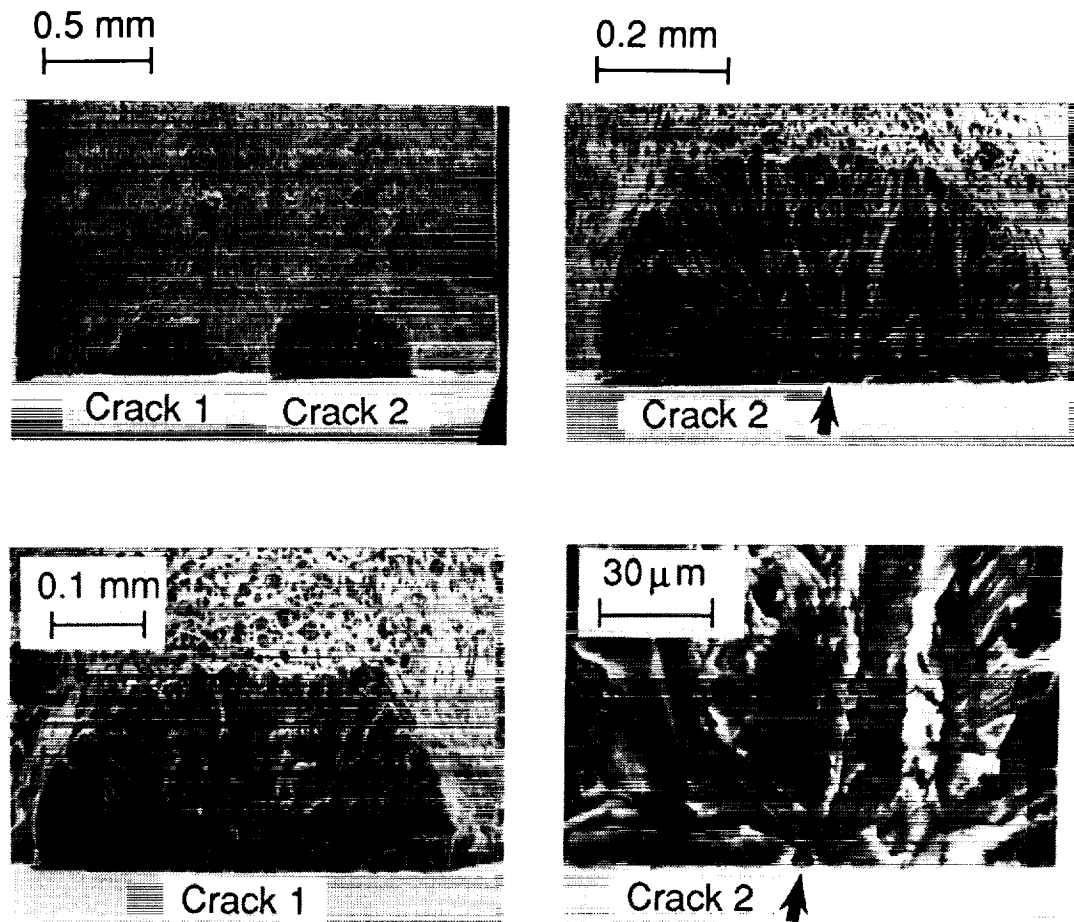
Figure 43. 7075-T6 aluminum alloy surface-crack initiation sites.

L-93-52

(a) 5000 cycles. (b) 8000 cycles. (c) 14 000 cycles.
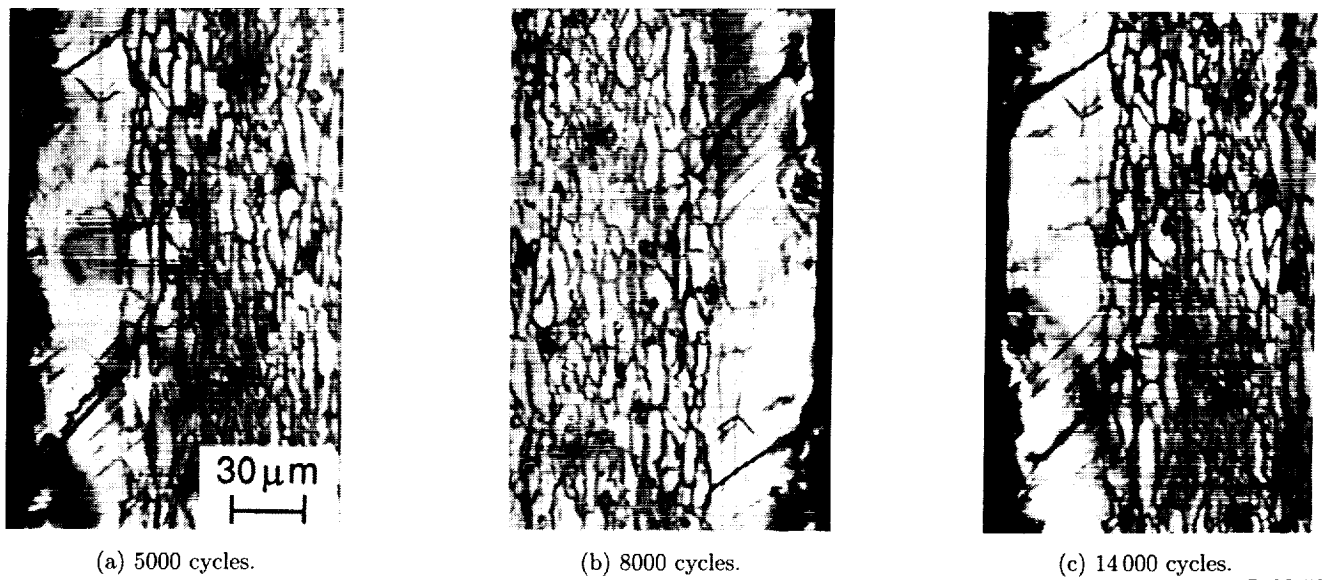
L-93-53

Figure 44. Photomicrographs of surface replicas showing initiation site in cladding and crack-growth history in LC9cs aluminum alloy. Cracks grew across thickness $(L = B)$ in 28 000 cycles.
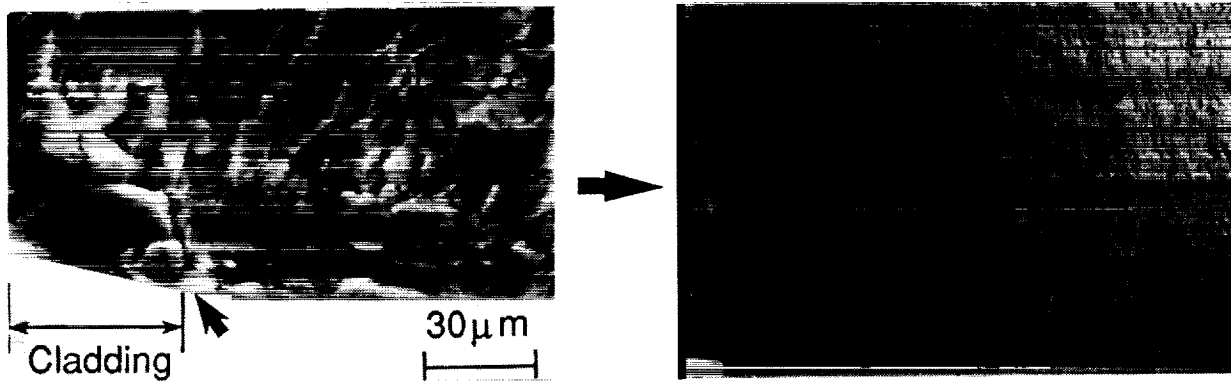
(a) Corner-crack initiation site in cladding.
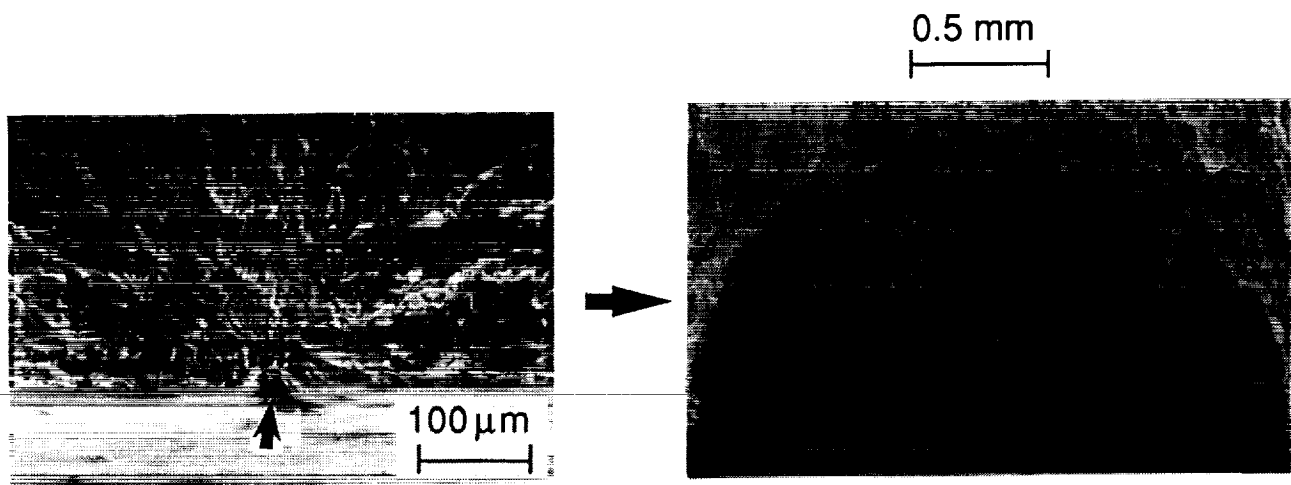
(b) Surface-crack initiation site at inclusion-particle void.

Figure 45. LC9cs aluminum alloy crack-initiation sites.

L-93-54

36
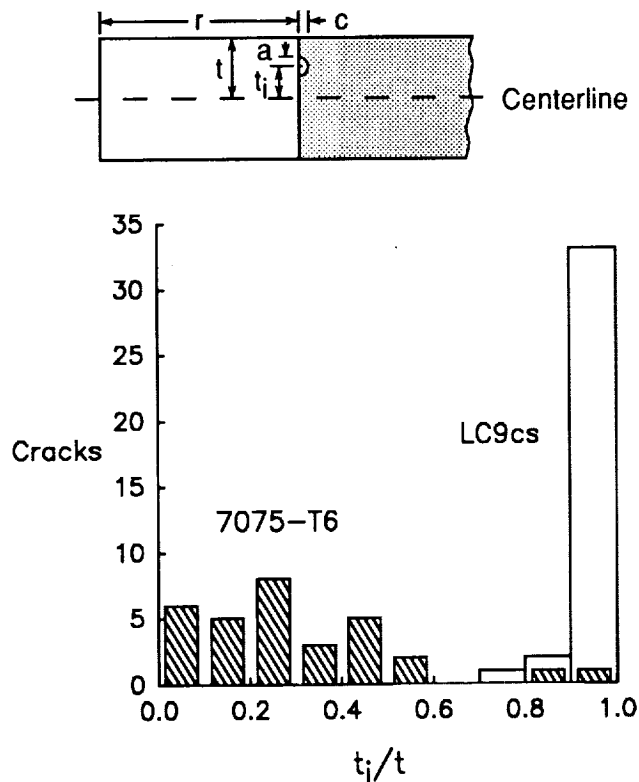
Figure 46. Distribution of crack-initiation sites along bore of notch for 7075-T6 and LC9cs aluminum alloys.
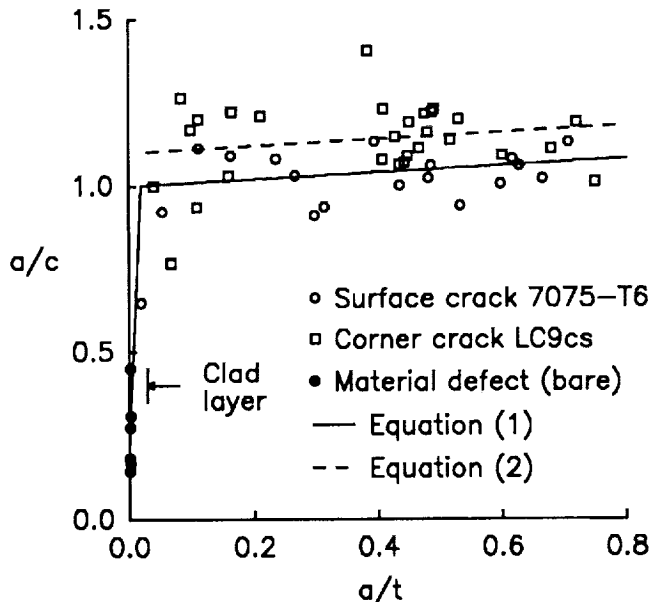
Figure 47. Surface- and corner-crack shapes and sizes for the two aluminum alloys.

defect that grows along the specimen centerline is a reasonable assumption. Multiple crack initiations and interactions were not considered in the cooperative program.

For the LC9cs alloy, more than 90 percent of the cracks initiated at the corner $(t_i/t = 1)$ and grew as quarter-elliptical corner cracks. Therefore, a corner crack was assumed in the analyses of small cracks in the clad alloy. Multiple crack initiations and interactions were not considered. In a few cases, a crack did initiate at the surface in the LC9cs alloy. These few surface crack results proved useful in assessments of cladding-layer effects on stress intensity factors. (See secs. 4.5.3 and 8.5.2.)

6.3. Small-Crack Shapes for Two Alloys

To calculate stress intensity factors for a surface or corner crack at the notch, crack dimensions a and c, must be known. The replica method was used to monitor crack length in the a-direction as a function of cycles. For information about crack growth in the c-direction, some specimens were pulled to failure (monotonic loading) at various stages during their lives. (See figs. 43 and 45.) Figure 47 shows the variation of a/c with a/t for naturally initiated cracks. The surface-crack data were obtained from the 7075-T6 alloy, whereas the corner-crack data were obtained from the LC9cs alloy.

In the 7075-T6 alloy, surface cracks initiated at inclusion-particle clusters or voids at or near the notch surface. The solid symbols show the material defects where cracks initiated in the bare alloy. These defects ranged from $a/t = 0.002$ to 0.004. The initial crack size selected to characterize the initial material defect $(a_i = 3~\mu m$ and $c_i = 9~\mu m)$ was an average of these defect sizes. For $a/t < 0.05$, very little information was obtained on experimental crack shapes. However, very early in life, the cracks in both alloys generally grew in a nearly semicircular $(a/c = 1)$ shape. However, the cracks grew more along the bore of the notch than away from the notch $(a/c > 1)$ as they deepened (larger a/t).

In the LC9cs alloy, corner cracks initiated from slip bands in the cladding layer very early in life. Figure 44 shows the cracks in these slip bands and the progression of crack growth into the core material. Again, very little information was obtained for $a/t < 0.03$. Corner cracks generally grew more along the bore of the notch than did surface cracks, as evidenced by the generally larger a/c ratio.

The solid and dashed lines in figure 47 show equations that were visually fitted to these data—equation (1) for surface cracks and equation (2) for corner cracks. These equations were used to calculate c from $(a$ or $2a)$ measurements made in the cooperative test program.
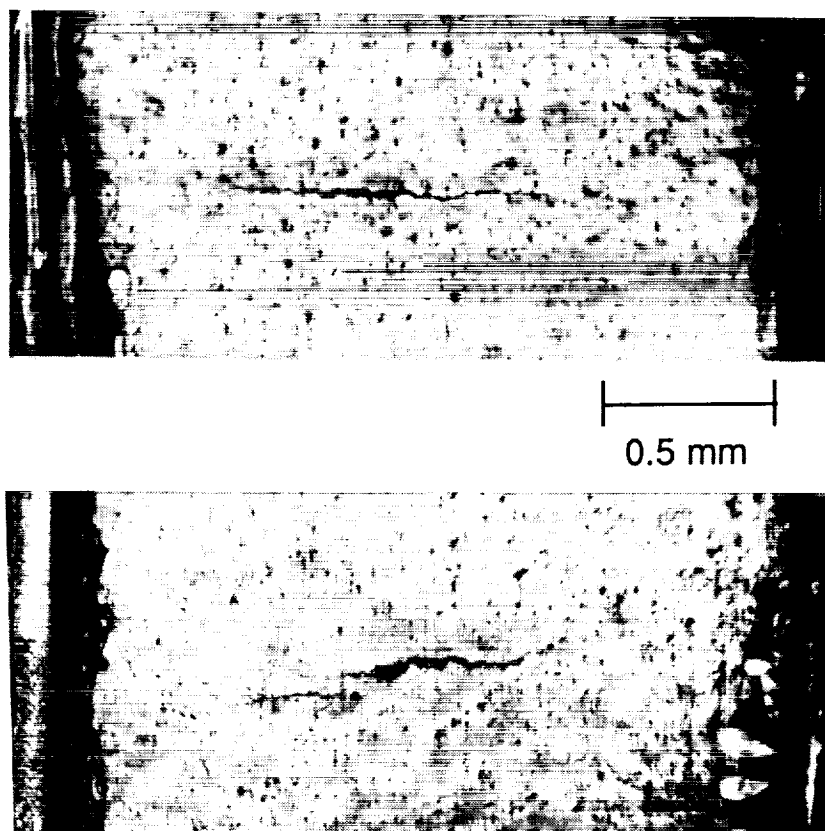
Figure 48. Surface replicas on notch root for 7075-T6 alloy with single and multiple surface cracks.

6.4. Crack Length Against Cycles for Small Cracks

Small-crack growth along the bore of the notch was measured by the plastic-replica method. Crack length against cycles was then recorded on data charts. (See appendix G.) Examples of replicas and typical crack-growth data are presented in the following sections.

6.4.1. 7075-T6 Aluminum Alloy

Figure 48 shows photomicrographs of surface replicas on the notch root for the 7075-T6 alloy. These examples show both single and multiple cracks along the notch surface. A plot of crack length against cycles for small cracks in constant-amplitude loading ($R = -1$; $S_{max} = 95$ MPa) is shown in figure 49. The tests at $R = -1$ were selected because small-crack effects are more pronounced for these conditions. The solid and dashed curves show test results from NASA and CAE, respectively, which agreed very well. Growth of naturally initiated cracks was detected early in life after about 5000 to 15 000 cycles. At these cycles, $L = 5$ to 15 μm. Although these particular tests were terminated af-
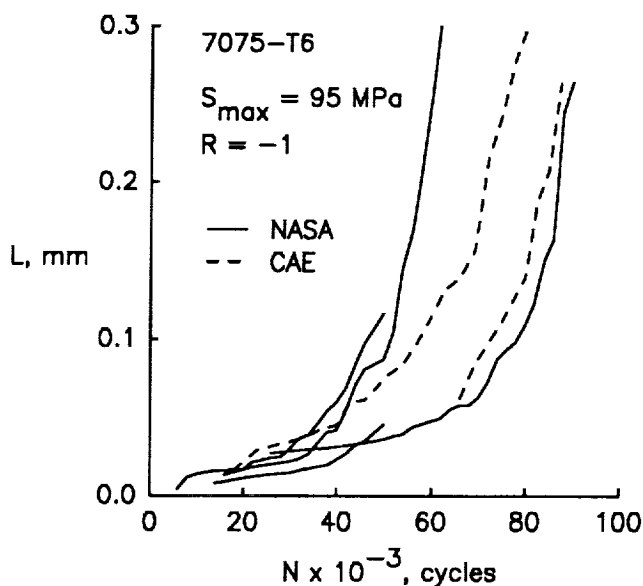
Figure 49. Experimental crack length against cycles for small cracks in 7075-T6 aluminum alloy.

ter the cracks grew across the sheet thickness, fatigue tests at these conditions (replica effects, fig. 37) would have lasted about 150 000 cycles. Thus, the

38

0.5 mm
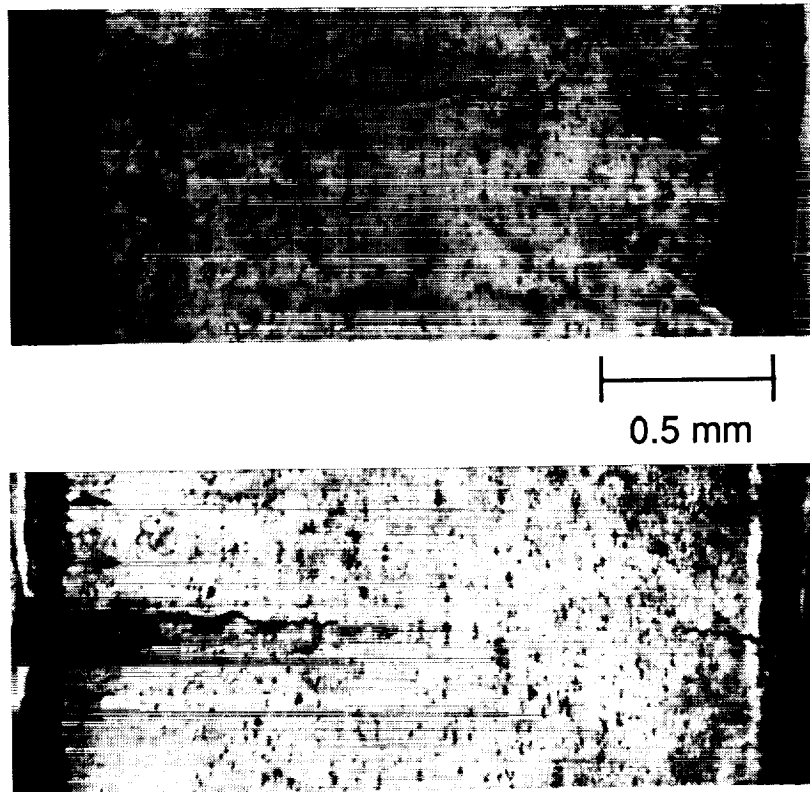
L-93-56

Figure 50. Surface replicas of notch root for LC9cs aluminum alloy with single and multiple corner cracks.

initiation phase, that is, the cycles before a crack was detected, was only about 3 to 10 percent of the total fatigue life.

6.4.2. LC9cs Aluminum Alloy

Corner-crack growth in the LC9cs alloy is shown in photomicrographs of surface replicas in figure 50. Single and multiple cracks also developed along the edges of the notch. A plot of crack length against cycles for small cracks at $R = -1$ and $S_{max} = 90$ MPa is shown in figure 51. The solid and dashed curves show test results from CAE and NASA, respectively. Here, also, the results from each laboratory agreed well. As mentioned, the clad alloy exhibited more scatter in fatigue life than did the 7075-T6 alloy; the scatter may account for the differences at about 20 000 cycles. Growth from naturally initiated cracks in the cladding also was detected early in life. Crack growth was recorded as early as 1000 cycles, but most initiated at about 4000 cycles. At these cycles, however, the cracks were from 60 to 100 μm long. Fatigue tests in these conditions (fig. 39) would have lasted about 40 000 cycles. Thus, the initiation phase for the clad alloy was also about 3 to 10 percent of the total fatigue life.

6.5. Small-Crack-Growth Noninteraction Criteria

As shown, multiple cracks did initiate in many tests. Because the development of multiple-crack stress intensity factor solutions was beyond the scope of this study, a small-crack noninteracting criterion was used. Application of this criterion permitted researchers to reject data when the stress fields of multiple cracks may have interacted. The approach was similar to the procedures developed in reference 19 but was modified for nonaligned multiple cracks. Figure 52 illustrates a simple system for rejecting crack-growth rates wherein such interactions could occur. Four cases were considered when data are rejected:

1. When cracks are on nearly the same path with each other (such as cracks 1 and 2, fig. 52(a)) and when the distance $d_{1,2}$ is less than the length of the largest crack L_1, then subsequent data from crack L_2 are rejected. When $d_{1,2}$ between the adjacent crack tips is less than the length of the smaller crack L_2, then subsequent data from L_1 are rejected. Here, the crack tips are expected to approach each other, so the rate of growth of each would accelerate.

39
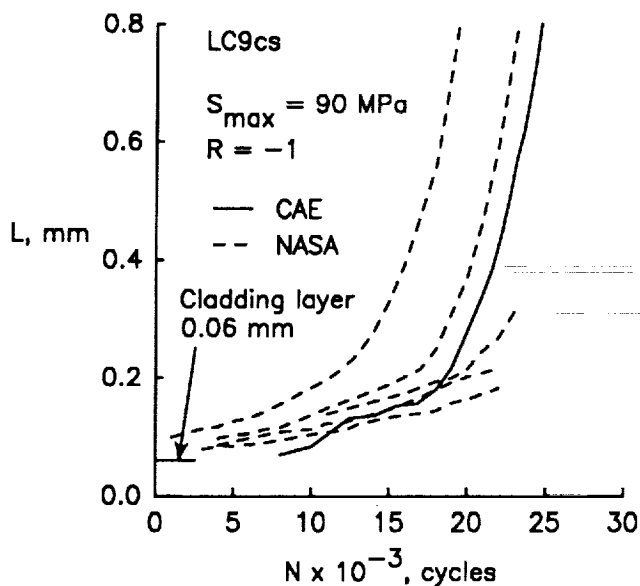
Figure 51. Experimental crack length versus cycles for small
cracks in LC9cs aluminum alloy.

2. After two cracks have joined (such as cracks 1
   and 2, fig. 52(b)), the crack-growth data are
   rejected from both cracks until L is twice the
   length of the combined cracks immediately after
   joining $L_1 + L_2$. Satisfying this criterion will allow
   the two cracks to merge and form a combined
   crack front before crack-growth rates are used.

3. When cracks intersect the same line parallel to
   the loading axis of the specimens (such as cracks 1
   and 3, fig. 52(a)) and when the distance between
   the two cracks $h_{1,3}$ is less than twice the length
   of the larger crack, then subsequent data from
   crack 3 are rejected. Data from crack 1 remain
   valid if $h_{1,3}$ is greater than twice the length
   of the smaller crack L_3. Here, L_1 would be
   expected to relieve stresses in the region of L_3
   and, consequently, the rate of growth of crack 3
   would slow.

4. For nonaligned cracks (fig. 52(a)), if rejection
   criteria 1 and 3 are both met, then data from
   L_1 are rejected. Similarly, if rejection criteria 1
   and 3 are both met for the secondary crack, then
   data from the secondary crack are also rejected.

These four conditions are referred to as the
noninteraction criteria. A simple way to visualize
criteria 1, 3, and 4 is to evoke the "box" criteria, as
illustrated in figure 52(a) by the dashed lines. The
coordinates of the dashed lines are set by criteria 1
and 3. The radial distance between the centers of
crack i and j is denoted $r_{i,j}$. Any crack outside

the box is considered valid and the crack-growth rate
may be used. However, if any crack (L_2 to L_5) is in-
side the box, then crack-growth rates from that crack
are rejected. All small-crack data presented in this
report satisfy the noninteraction criteria.

6.6. Small- and Large-Crack-Growth Rates

All small-crack-growth rates from the coopera-
tive program for constant-amplitude and spectrum
loading were analyzed by the procedures described
in section 3.5. The data for da/dN generated with
SENT specimens are presented herein as a function
of ΔK. For each loading condition, the small-crack-
growth rates are compared with the large-crack data
generated with CCT specimens for the same loading
conditions on the same material. (See sec. 5.)

6.6.1. Constant-Amplitude Loading

6.6.1.1. 7075-T6 aluminum alloy. The NASA
and CAE small-crack-growth rates at $R = -1$,
0, and 0.5 are shown in figures 53–55, respec-
tively. The range of stress levels for each series of
tests is as indicated. A comparison of results at
$R = -1$ is shown in figure 53. The data from each
laboratory agreed well in the midregion. The CAE
researchers generated more data for deeper cracks
(large a/t), whereas NASA researchers generated
more data for smaller cracks. These results show the
"classical" small-crack effect in that the small cracks
grew below the large-crack threshold (solid line at
ΔK of about 4 MPa-m$^{1/2}$). However, recall that the
replica method affected fatigue life and possibly fa-
tigue crack-growth rates. Without the replicas, the
crack-growth rates for small cracks should be higher
than those shown. Above 10^{-6} mm per cycle, the
small- and large-crack data generally merge.

The small-crack results at $R = 0$ (fig. 54) show
similar results as those for $R = -1$, except that
the deeper surface cracks grew more slowly than the
large through cracks at the same ΔK value. (Note
that the small-crack data are represented by the
ratio da/dN and the large-crack data by dc/dN.)
The growth rates in the a- and c-directions could
indeed be different at the same ΔK level. The
transitions in the ΔK-rate relation (see fig. 23) have
been attributed to grain or subgrain microstructure.
(See refs. 57 and 58.) Because the 7075-T6 alloy has a
pancake microstructure, the transitions in the ΔK-
rate relation in the a-direction would not coincide
with those in the c-direction. Also, deep surface
cracks should realistically be considered large cracks

(a) Multiple surface cracks at notch root.

(b) Interacting surface cracks for $d_{1,2} = 0$ (sec. A-A).
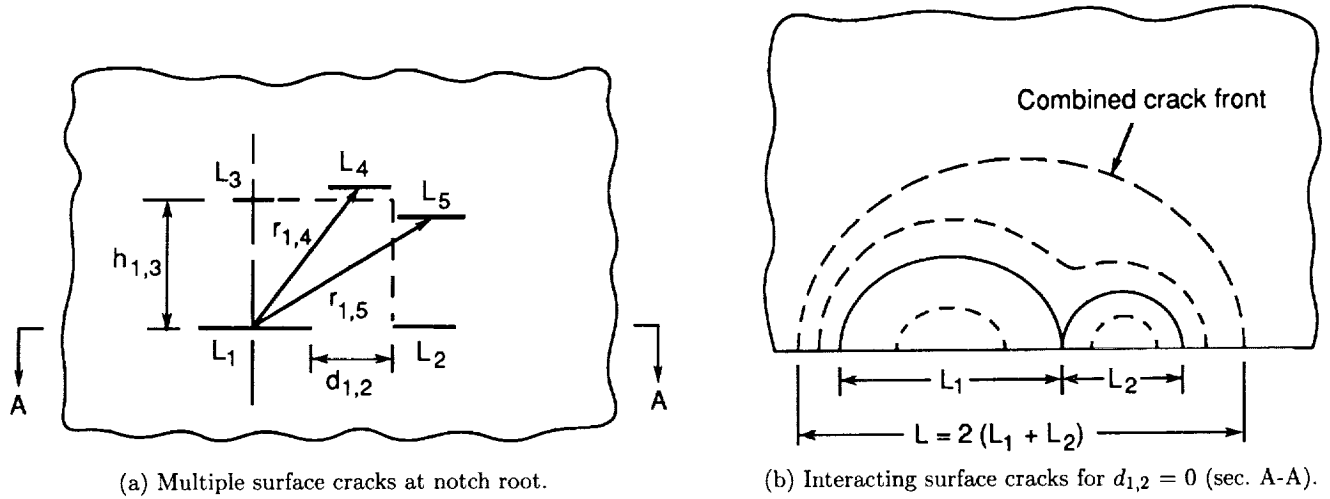
Figure 52. Definition of crack noninteraction criteria for crack coalescence and crack shadowing.
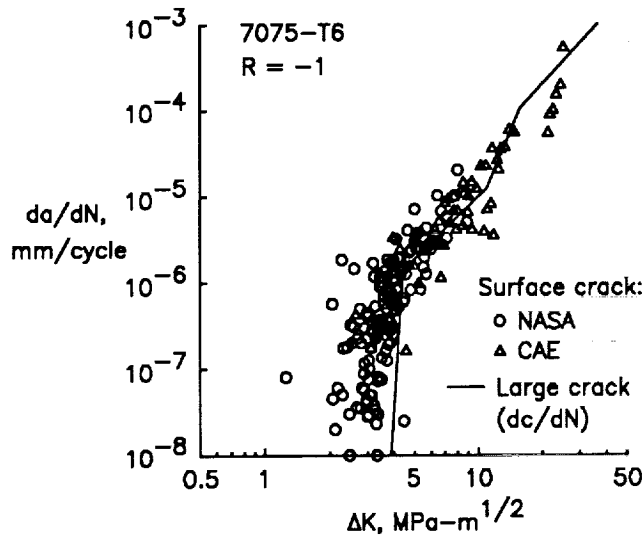
Figure 53. Small surface crack ($S_{max} = 80\text{--}95$ MPa) and large through crack growth rates against ΔK for 7075-T6 aluminum alloy for $R = -1$.
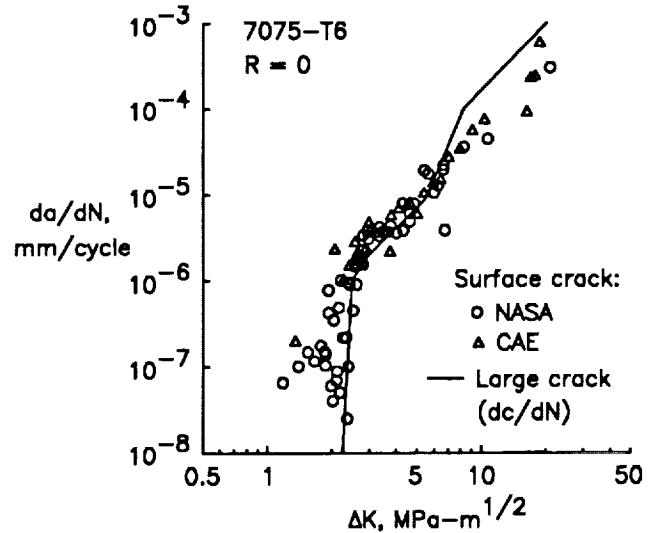
Figure 54. Small surface crack ($S_{max} = 120\text{--}140$ MPa) and large through crack growth rates against ΔK for 7075-T6 aluminum alloy for $R = 0$.

in the a-direction because they are more than 0.5 mm long and crack closure stresses have stabilized at the large-crack steady-state values. (See sec. 7.)

Small-crack results for $R = 0.5$ are shown in figure 55. Results from the two laboratories show good agreement for the measured range of rates. Here, the small cracks grew only slightly below the large-crack threshold (1.4 MPa-m$^{1/2}$). Also, da/dN at the higher rates was lower than dc/dN at the same ΔK value. These data also support the conclusion that the ΔK-rate relations in the a- and c-directions are different. At $R = 0.5$, crack closure becomes less

an issue (cracks are nearly fully open) and $\Delta K \approx \Delta K_{eff}$. These data were used to help establish the ΔK_{eff}-rate relation in the a-direction. A detailed discussion of effective stress intensity factors is in section 8.2.

6.6.1.2. LC9cs aluminum alloy. In the small-crack tests on the LC9cs alloy, primarily corner cracks were produced. These cracks were initiated by slip-band formation in the cladding layers very early in life. Because the yield stress of the cladding is only about 10 percent that of the bare alloy, the stress distribution at the corner of the notch is complex in that
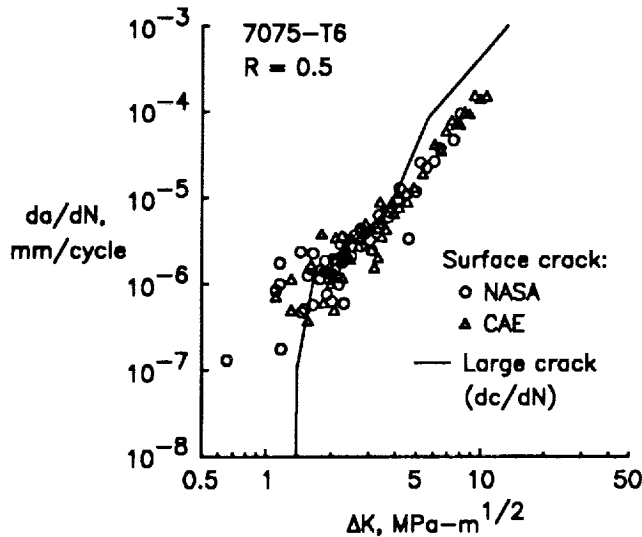
Figure 55. Small surface crack (S_{max} = 195 220 MPa) and large through crack growth rates against ΔK for 7075-T6 aluminum alloy for $R = 0.5$.
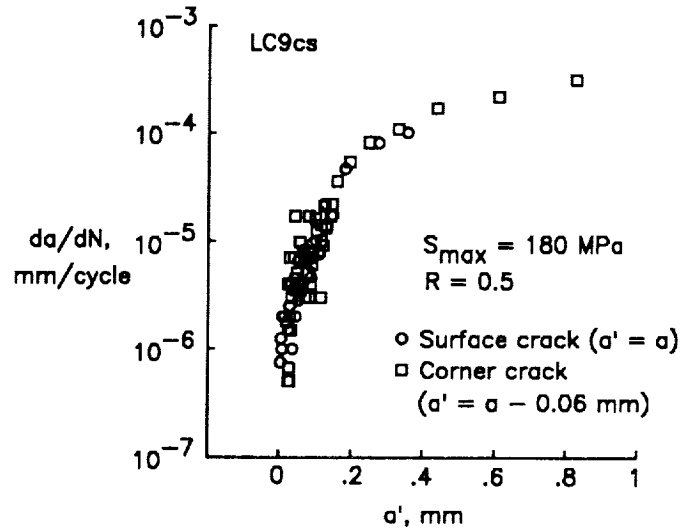
Figure 57. Crack-growth rate against crack length for surface crack in LC9cs bare and corner crack length minus clad thickness in LC9cs clad alloy.
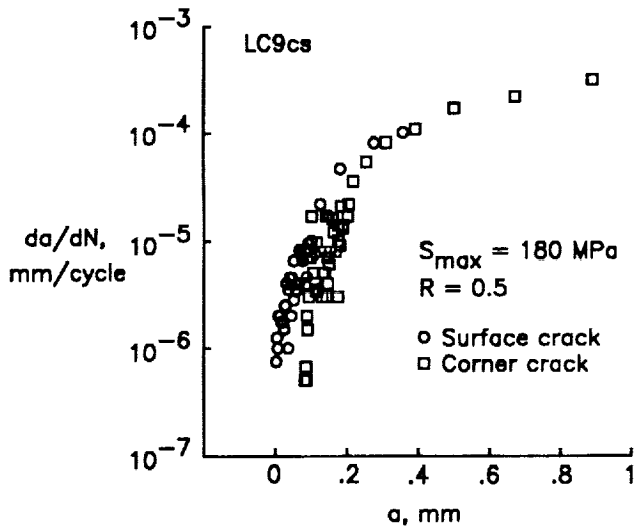
Figure 56. Crack-growth rate against crack length for surface crack in LC9cs bare and corner crack in LC9cs clad alloy.

the cladding yields and the core material carries most of the load. To calculate the effect of the cladding on stress intensity factors, a 3D finite-element analysis would be required. In lieu of such an analysis, an engineering estimate was used to develop a simple correction to the stress intensity factors for a corner crack. (See sec. 4.5.3.) The correction assumes that the cladding layer does not carry any load. The data generated in the small-crack test program will be used to evaluate this simple hypothesis.

As mentioned, several tests on the SENT specimens produced a surface crack along the bore of the

notch instead of a corner crack. These results were used to help assess the effect of the cladding layer on crack-growth rates and, consequently, on stress intensity factors. Figure 56 shows crack depth a plotted against da/dN for a surface crack and a corner crack growing in the core LC9cs alloy. At a given crack length, the corner crack grew at a much lower rate than the surface crack. Because these results were determined from a high stress ratio test ($R = 0.5$) and at the same maximum stress level (180 MPa), crack closure is not an issue. The results in figure 56 have been replotted in figure 57, but the average cladding-layer thickness (60 μm) has been subtracted from the crack length in the a-direction. Here, the results of crack length against growth rate for surface and corner cracks agree quite well and indicate that the cladding does not affect the rate of crack growth in the core material. Thus, the cladding layer may be assumed not to carry any load in the stress intensity factor calculations.

To show how well the clad correction (modification of the stress intensity factors) does in correlating small-crack data, the data at $R = 0.5$ are analyzed with no clad correction, then the data are analyzed with the simple clad correction. The small-crack data for $R = -1$ and 0 are analyzed with only the clad correction to the stress intensity factor solutions.

Figure 58 shows the results for small surface and corner cracks at $R = 0.5$. Stress intensity factors were calculated with the measured value of a, the calculated c from equations (1) or (2), and the equations in appendix D. The open symbols show the data for corner cracks and the solid symbols
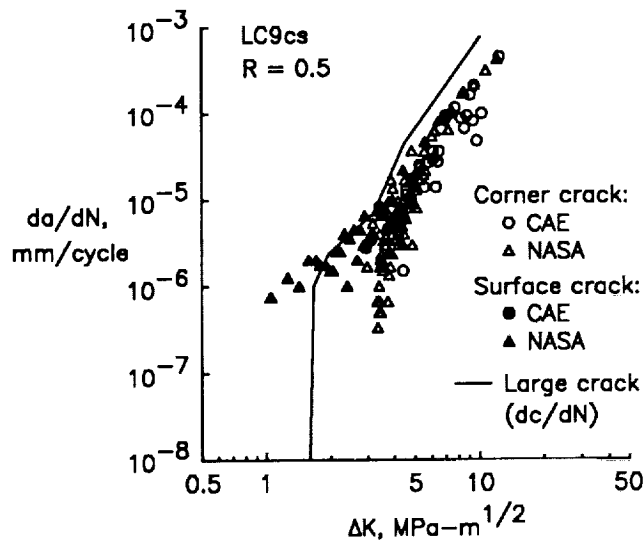
Figure 58. Small crack (S_{max} = 165 to 180 MPa) and large-crack-growth rates against ΔK with no clad correction for small cracks in LC9cs aluminum alloy for R = 0.5.
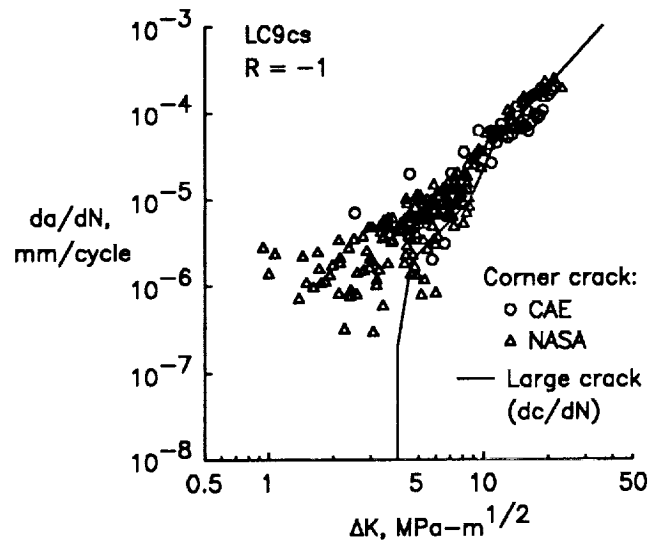
Figure 60. Small corner crack (S_{max} = 70 to 90 MPa) and large-crack-growth rates against ΔK with clad correction for small corner cracks in LC9cs aluminum alloy for R = −1.
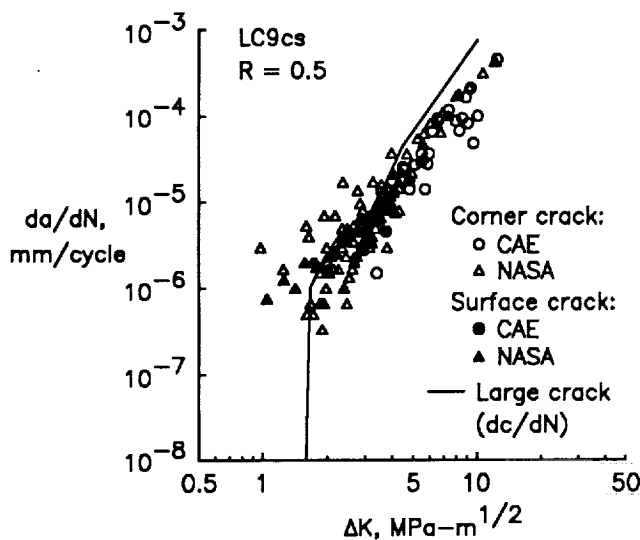
Figure 59. Small crack (S_{max} = 165 to 180 MPa) and large-crack-growth rates against ΔK with clad correction for small cracks in LC9cs aluminum alloy for R = 0.5.
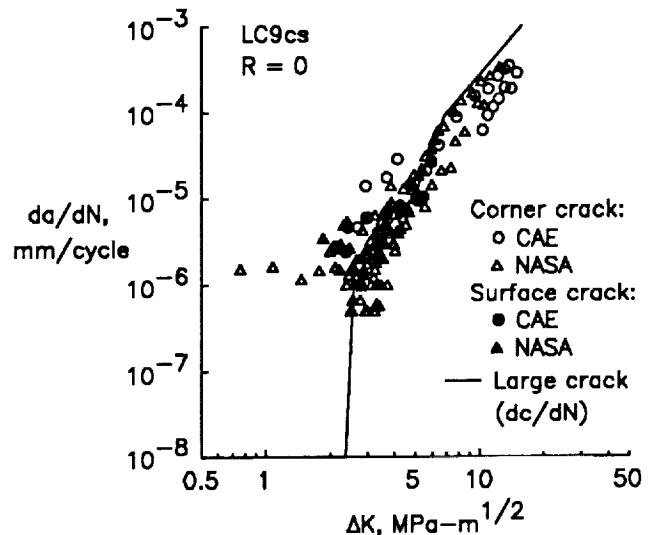
Figure 61. Small crack (S_{max} = 100 to 115 MPa) and large-crack-growth rates against ΔK with clad correction for small cracks in LC9cs aluminum alloy for R = 0.

show them for the surface cracks. Again, da/dN may not be the same as dc/dN at the higher rates, as discussed for the 7075-T6 alloy. However, the two sets of data separate sharply for rates below 10^{-5} mm per cycle. Below this point the surface-crack data agree well with those for large cracks in that same region. The corner-crack data do not agree with either the surface- or large-crack data at the lower rates. The high R data for corner cracks were reanalyzed with the clad correction; the results are

shown in figure 59. The corner-crack results now agree quite well with those for surface cracks over the range of measured rates. They also agree with the large-crack data at the lower rates. These results show the effectiveness of the simple clad correction for corner-crack stress intensity factors.

The results of CAE and NASA small-crack tests on the LC9cs alloy SENT specimens at R = −1 and 0 with the clad correction are shown in figures 60 and 61, respectively. Again, the data from each laboratory agreed well. The data in figure 60 show

43

more scatter in the lower region than the corresponding plot for the 7075-T6 alloy. (See fig. 53.) However, the most noticeable difference is the shape of the ΔK-rate results at ΔK values below the large-crack threshold (vertical solid line). In the LC9cs alloy, the crack-growth rates at ΔK values below the large-crack threshold were much higher than those measured for the 7075-T6 alloy. Of course, some of this difference may have been a result of the replica process on the 7075-T6 alloy small-crack data. Another source of difference may be the crack sizes. The data for the 7075-T6 alloy were generated at much smaller crack sizes than for the LC9cs alloy. The crack sizes in the 7075-T6 alloy ranged from 5 to 100 μm, whereas those in the clad material ranged from 80 to 300 μm. The shape of the ΔK_{eff}-rate curve in the region of lower rates and different crack-closure transients may also be responsible for some of these differences. A detailed analysis of these data with the crack-closure model is given in section 8.

Figure 61 shows the results of small surface and corner cracks for $R = 0$ constant-amplitude loading conditions. The solid and open symbols show the data for surface and corner cracks, respectively. In the midrate region, all surface-, corner-, and through-crack data agreed quite well. The SENT specimen data on large corner cracks also support the conclusion that da/dN is different from dc/dN at a given ΔK.

6.6.2. Mini-TWIST Spectrum Loading

6.6.2.1. 7075-T6 aluminum alloy. A plot of ΔK against rate for small surface cracks for the Mini-TWIST spectrum loading is shown in figure 62. For this assessment, ΔK is calculated with the highest and lowest stresses in the spectrum sequence. Also, the crack-growth rates are the average ones for about 30 000 cycles. The NASA and CAE data agreed very well. Here, the small-crack results also agreed with the large-crack data. However, this agreement may have been fortuitous because the replica method significantly affected the fatigue life for Mini-TWIST loading. (See fig. 38.) Thus, the measured rates for small cracks may be too low for a given value of ΔK.

6.6.2.2. LC9cs aluminum alloy. Small-crack rates for corner cracks in the LC9cs alloy for Mini-TWIST spectrum loading are shown in figure 63. Again, ΔK is calculated with the highest and lowest stresses in the spectrum, but the cladding correction is also used. The CAE and NASA data for this case did not agree except at the higher rates. As expected, the small cracks in the clad alloy grew faster than the
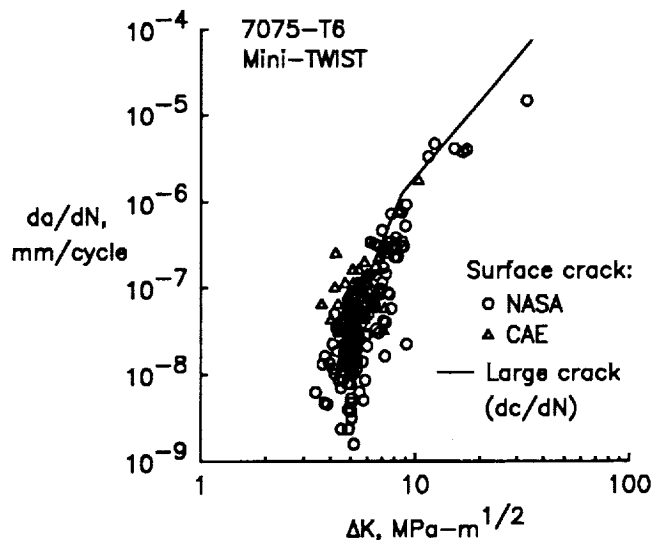
Figure 62. Small surface crack ($S_{\text{max}} = 190$ to 208 MPa) and large through crack-growth rates against ΔK for 7075-T6 aluminum alloy for Mini-TWIST load sequence.
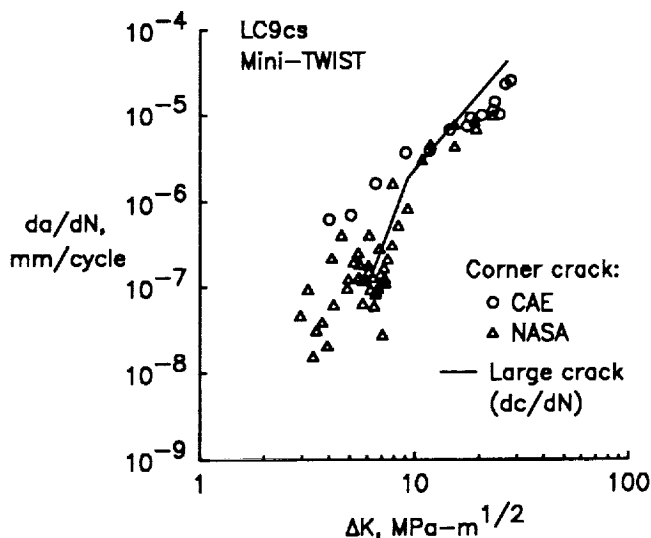
Figure 63. Small corner crack ($S_{\text{max}} = 125$ to 270 MPa) and large through crack-growth rates against ΔK with clad correction for small corner cracks in LC9cs aluminum alloy for Mini-TWIST load sequence.

large cracks at a given ΔK value in the region of low rates.

7. Crack-Closure Model for Small and Large Cracks

Numerous investigators have suggested (refs. 5–11) and verified (refs. 8, 19, and 63) that crack closure (ref. 22) (or lack of closure in the early stages of

(a) Maximum stress.

(b) Minimum stress.
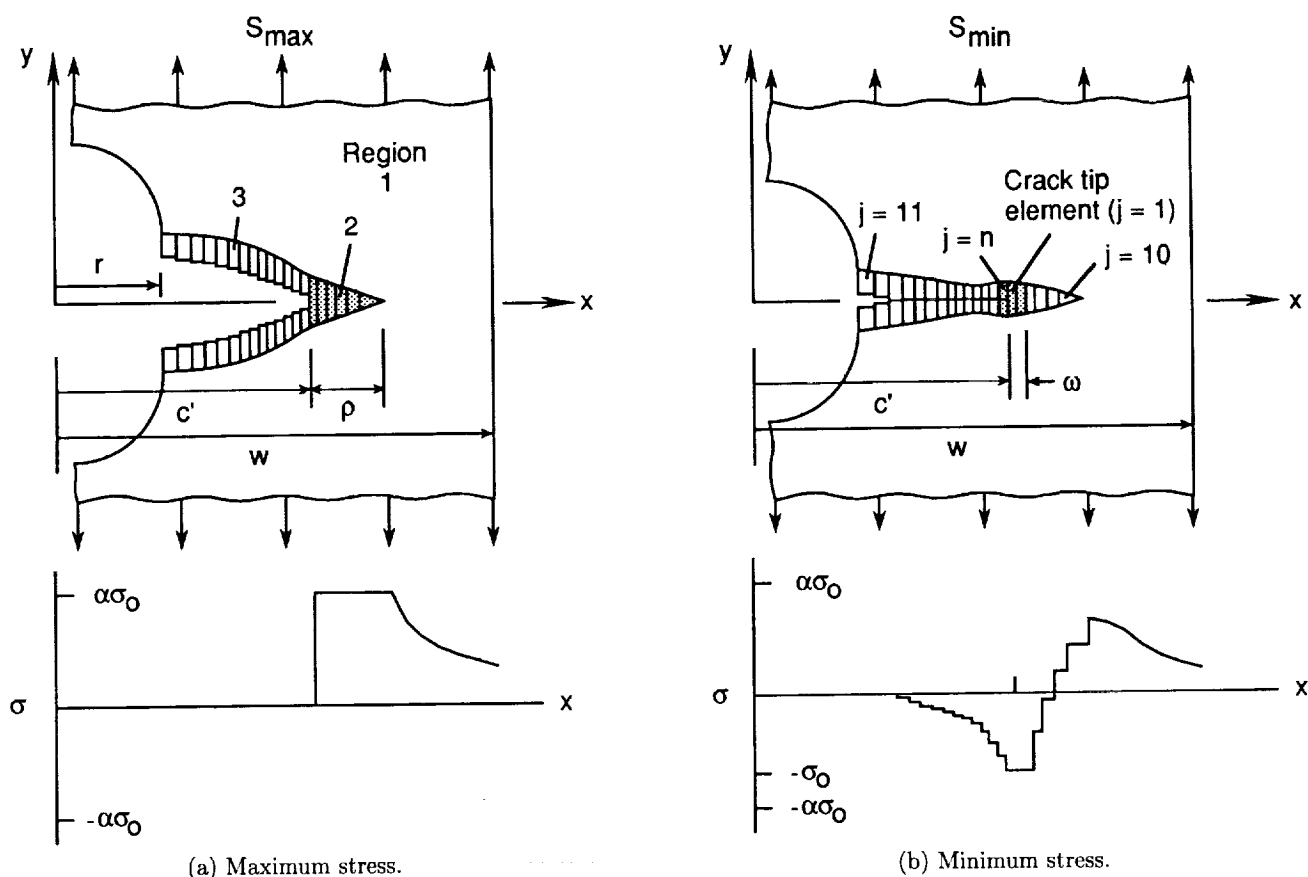
Figure 64. Analytical crack-closure model in cyclic loading.

crack growth) is a major factor in causing some differences between the growth of small and large cracks. Reference 64 has shown, on the basis of a crack-closure model, that a large part of the small-crack effect in an aluminum alloy was caused by a small crack emanating from a defect "void" of incoherent inclusion particles and from a breakdown of LEFM concepts. In the cooperative program, the same model, FASTRAN II (ref. 56), was used to calculate crack-opening stresses; to correlate large-crack-growth rates for constant-amplitude loading; and to predict large-crack growth, small-crack growth, and fatigue lives.

In the following sections, the model and recent modifications are briefly reviewed and some examples are presented on how crack-opening stresses vary as a function of load history for small and large cracks for constant-amplitude and spectrum loading. The crack-opening stress equations used to calculate effective stress intensity factor ranges and to correlate large-crack-growth rates are included for completeness. The method by which crack-opening stresses can be applied to surface- and corner-crack growth is also discussed.

7.1. Analytical Crack-Closure Model

The crack-closure model (ref. 65) was developed for a central crack in a finite-width specimen subjected to uniform applied stress. This model was later extended to through cracks emanating from a circular hole in a finite-width specimen. (See ref. 23.) In references 23 and 64, the model was applied to small cracks. The model is based on the Dugdale model (ref. 66), but it was modified to leave plastically deformed material in the wake of the crack. The primary advantage of this model is that the plastic-zone size and crack-surface displacements are obtained by superposition of two elastic problems: a crack in a plate subjected to remote uniform stress and uniform stress applied to a segment of the crack surface.

Figure 64 shows a schematic of the model at maximum and minimum applied stresses. The model is composed of three regions: a linear-elastic region containing a circular hole with a fictitious crack of half-length $c' + \rho$, a plastic region of length ρ, and a residual plastic deformation region along the crack surface. The physical crack is of length $c' - r$. (The

45

model was also assumed herein to apply for a crack emanating from a semicircular notch.) The compressive plastic zone is ω. Region 1 is treated as an elastic continuum. Regions 2 and 3 are composed of rigid, perfectly plastic (constant stress) bar elements with a flow stress σ_o, which is the average of the yield stress (σ_{ys}) and the ultimate strength (σ_u). The shaded regions in figures 64(a) and 64(b) indicate material that is in a plastic state. At any applied stress level, the bar elements are either intact (in the plastic zone) or broken (residual plastic deformation). To account for the effects of state of stress on plastic-zone size, a constraint factor α was used to elevate the tensile flow stress for the intact elements in the plastic zone. The effective flow stress $\alpha\sigma_o$ for simulated plane-stress conditions is σ_o (usual Dugdale model) and for simulated plane-strain conditions is $3\sigma_o$. The value of $3\sigma_o$ was established from elastic-plastic finite-element analyses for plane-strain conditions with an elastic, perfectly plastic material (normal stress elevation in the crack-tip region was about 2.7 from the analysis). The use of the modified Dugdale model for plane-strain conditions is a matter of convenience because the shape of the yield zone for plane-strain conditions is very different from that used in the strip-yield model. However, the calculated crack-opening stresses for these conditions agree well with finite-element calculations for plane-strain conditions (ref. 67); that is, stabilized $S_o/S_{max} \approx 0.2$. At the minimum applied stress, some elements in the plastic zone and elements along the crack surfaces that are in contact may yield in compression when the contact or compressive stress reaches $-\sigma_o$. This assumption was justified because when a crack closes, the large stress gradient at the crack tip is greatly reduced (loss of constraint) and a more uniform stress field is produced.

For thin-sheet alloy, full plane-strain conditions are not possible. Irwin (ref. 68) suggested accounting for through-the-thickness variation in stress state by introducing a constraint factor ($\alpha = 1.73$) to represent nominal plane-strain conditions. For thin-sheet 2024-T3 aluminum alloy (ref. 19), $\alpha = 1.73$ correlated crack-growth rate results for various stress ratios and gave crack-opening stresses that agreed with measurements. (See ref. 69.)

The closure model is used to calculate the applied stress level at which the crack surfaces fully open as a function of crack length and load history. This stress is denoted the crack-opening stress. The crack-opening stress calculated for a through crack was also assumed to apply along a surface- or corner-crack front. Special modifications are required when the crack front intersects a free surface. The crack-

opening stress is then used to calculate ΔK_{eff}. (See ref. 22.) In turn, the crack-growth rate is calculated from ΔK_{eff}-against-crack-growth-rate relation determined from large-crack data.

7.2. Crack-Opening Stresses From Model

The method used in the original closure model to calculate crack-opening stresses (S_o) assumed that the rate of crack growth was small compared with crack length. (See ref. 65.) In proof tests or severe spectrum loading, however, crack-growth increments may be large compared with crack length. Therefore, the closure model was modified. (See ref. 70.) The contact stress intensity factor equation for calculating crack-opening stress (eq. (27) in ref. 65) was changed to

$$S_o' = S_{min} - \sum_{j=11}^{n} \frac{2\sigma_j}{\pi} \left(\arcsin B_2 - \arcsin B_1\right)_j \quad (15)$$

where

$$B_k = \frac{\sin\left(\frac{\pi b_k}{2w}\right)}{\sin\left(\frac{\pi c'}{2w}\right)} \qquad \text{(for } k = 1 \text{ or } 2) \quad (16)$$

The modification changed the upper limit of the summation in equation (15) from $n-1$ to n to reflect the change in formulation from the crack length before growth to actual or current crack length. The prime denotes the modified crack-opening stress. The index j refers to elements along the crack surface that are used to model plastic and residual-plastic deformations, as shown in figure 64(b). The crack length c' is the sum of the hole radius plus all of the elements from $j = 11$ to n. Dimension b_k denotes the distance to an edge of an element and the width of an element is $b_2 - b_1$. Specimen width w is measured from the specimen centerline or edge. Element 1 is the first intact element at the crack tip. Elements 1 to 10 are always ahead of the current crack tip and model the plastic zone ρ. The intact elements in the plastic zone may carry tensile stresses to $\alpha\sigma_o$ and compressive stresses to $-\sigma_o$. Elements 11 to n are along the crack surface between the initial notch and the current crack tip.

In the physical model, the crack was extended by the width of the nth element at the maximum applied stress. (See ref. 65.) The physical crack extension and width of the nth element were denoted Δc^*. In the revised model, the total width of the nth element was not used in the computation of the crack-opening stress from equation (15). The element width w_n in the crack-opening stress calculations was

the largest crack-growth increment during the generation of Δc^*. For low fatigue crack-growth rates, w_n was generally very small compared with Δc^* and was neglected in the original model. But for proof testing or severe loading, w_n may be a large percentage of Δc^*. For proof tests, w_n is equal to Δc^*, the amount of crack extension during proof loading. Thus, the contribution of the crack-extension increment to subsequent crack-opening stresses is accounted for in the new calculations. At the minimum applied stress, elements along the crack surface that are in contact carry σ_j, the element contact stress; otherwise, the element stress is zero. Elements in the plastic zone carry either tensile or compressive stresses and may yield in compression if σ_j is less than $-\sigma_o$. For low fatigue crack-growth rates, S_o' calculated from equation (15) is nearly equal to S_o calculated from the equation developed in reference 71. However, for large-crack-growth increments (high crack-growth rates), S_o' from equation (15) is now a function of crack extension. See reference 70 for further details on this modification.

7.2.1. Constant-Amplitude Loading

In the following section, the crack-closure model is used to calculate crack-opening stresses for various constant-amplitude loading and constraint conditions. First, the model is used to demonstrate the effect of the initial defect void size on crack-closure behavior of small fatigue cracks emanating from these voids. Next, the effects of α and R on small-crack-closure behavior are shown.

Previous studies (refs. 23 and 64) have indicated that small-crack effects are more pronounced at negative stress ratios and for plane-stress conditions. Typical results of calculated S_o', normalized by the maximum applied stress as a function of a, are shown in figure 65. The crack-growth simulation was performed at $R = -1$ with the constraint factor of unity (plane stress). The value $S_{max}/\sigma_o = 0.15$ was used in the simulation. In bare aluminum alloys, cracks have been found to initiate at inclusion-particle clusters or voids left when these particles are removed during machining or polishing processes. An initial material defect (void or crack) with sizes $a_i = 3$ μm and $c_i = 9$ μm was selected for crack-growth simulations. The defect-void half-height b was selected as either 0 or 0.5 μm. The 0.5-μm value was selected so that the initial defect surfaces would not close even for $R = -1$ compressive loading. These calculations are shown as the lower solid curve in figure 65. As the crack grows, however, the newly created crack surfaces close and the crack-opening stresses rapidly rise and level off at the steady-state (large-crack) opening
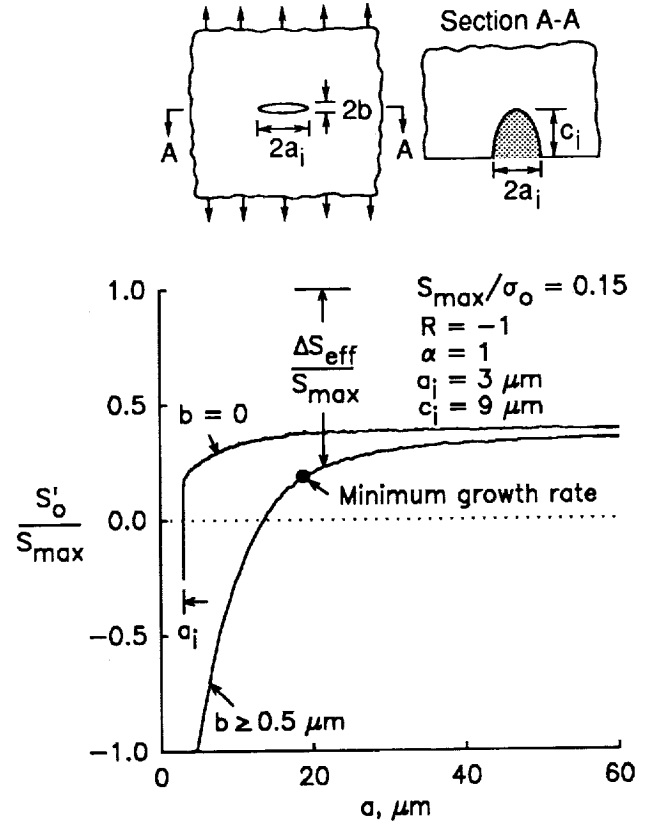
Figure 65. Calculated crack-opening stresses for various defect void heights as function of crack length for small crack.

stress value. A minimum crack-growth rate occurs at $c \approx 19$ μm. This behavior was caused by the rapid rise in crack-opening stresses. Initially, the small crack was fully open and $\Delta K_{eff} = \Delta K$. However, as the crack grew, the rapid rise in the crack-opening stresses reduced ΔK_{eff}, thereby also reducing crack-growth rates. However, as the crack-opening stresses began to stabilize, the rise in the stress intensity factor with longer crack lengths caused a reversal in the growth rate trend.

For a crack that initiates at a tight cluster of inclusion particles or voids, b may be nearly equal to zero. In figure 65, the defect surfaces do contact during compressive loading and the contacting surfaces greatly affect the amount of residual plastic deformation left behind as the crack grows. The calculated crack-opening stresses quickly stabilize at the steady-state large-crack value, as shown by the upper solid curve. These results suggest that the small-crack effect, at least in relation to crack closure, is a microcrack effect ($a < 20$ to 40 μm).

The effect of constraint on closure of small cracks is shown in figure 66, in which the constraint factor

47

α varies from plane-stress conditions ($\alpha = 1$) to simulated plane-strain conditions ($\alpha = 3$). In all cases, the initial crack-opening stress is at the minimum applied stress and rapidly rises as the crack grows. The initial response is nearly independent of α, but the stabilized values for large cracks are different; again, the crack-closure stresses stabilize for $a > 40$ μm.

For thin-sheet aluminum alloys, $\alpha = 1.7$ to 1.9 correlates crack-growth rates as a function of the effective stress intensity factor range below the transition from flat-to-slant crack growth. (See refs. 64 and 65.) The effect of R on calculated crack-opening stresses is shown in figure 67 for $\alpha = 1.8$. The particular values of $S_{\max}/\sigma_o$ used in the simulations are as indicated. As previously shown, the negative stress ratio simulation shows a significant crack-closure transient. However, at positive stress ratios, the crack-opening stresses stabilize after a smaller amount of crack growth. The results at $R = 0.5$ show that the crack surfaces were always fully open. These results are important because the ΔK values for high R conditions are the same as the ΔK_{eff} values, and tests with these conditions can help establish the ΔK_{eff}-rate relation for the material of interest. Tests at the lower stress ratios are then used to help determine the proper constraint factor to correlate the crack-growth rates as a function of ΔK_{eff}.

7.2.2. Mini-TWIST Spectrum Loading

In the cooperative test program, the Mini-TWIST loading sequence was used for both small- and large-crack tests. One of the most important features of the crack-closure model and life-prediction program (ref. 56) is the ability to calculate the effect of loading history on crack-opening stresses. Typical crack-opening stresses for the Mini-TWIST loading sequence for a small surface crack in the SENT specimens and for a large crack in the center-crack specimens are presented in the following sections.

7.2.2.1. Small crack.
In the small-crack simulation, the same initial defect-void size (a_i, c_i, b) was used as for the constant-amplitude loading cases. A variable-constraint option was selected for this simulation. (See refs. 56 and 64.) Thus, $\alpha = 1.8$ for crack-growth rates less than 7×10^{-4} mm per cycle and 1.2 for rates greater than 7×10^{-3} mm per cycle. (See sec. 8, "Fatigue Crack-Growth Rate and Life Prediction.") The mean flight stress in the Mini-TWIST spectrum was 73 MPa ($S_{\max} = 190$ MPa). Figure 68 shows crack-opening stress (normalized by the peak stress in the spectrum) as a function of the ratio of applied cycles N to N_f ($N_f \approx 800\,000$ cycles for these particular conditions). Only a part of the
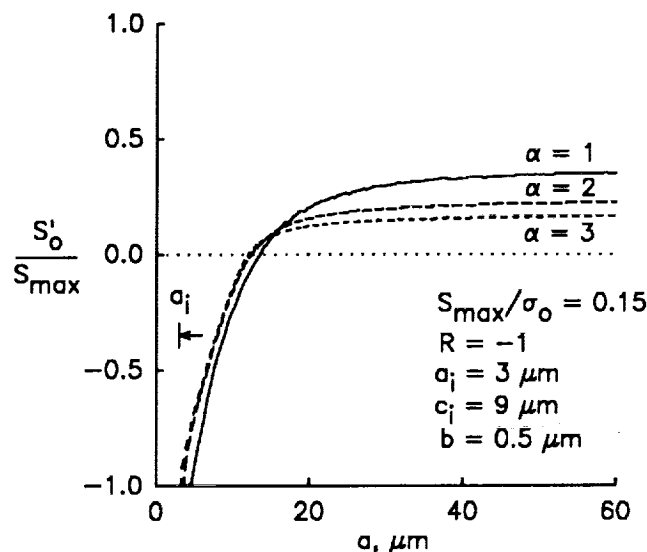
Figure 66. Calculated crack-opening stresses for various constraint factors as function of crack length for small crack.
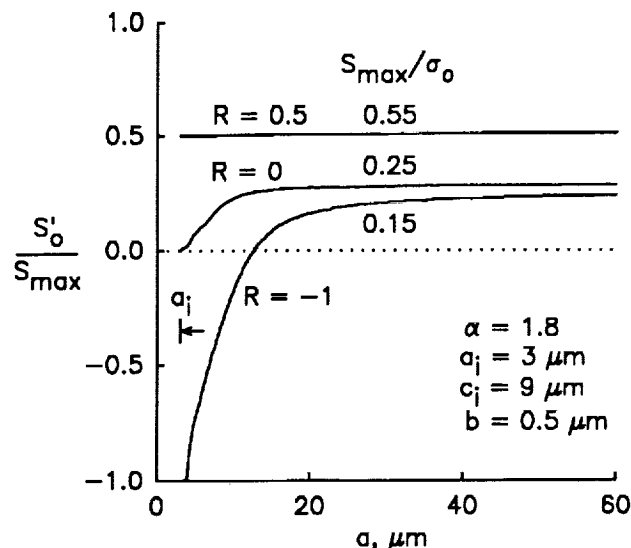
Figure 67. Calculated crack-opening stresses for various constant-amplitude loadings as function of crack length for small crack.

opening stresses calculated from the model is shown in the figure. These results show that the opening stresses start near the minimum stress in the spectrum and rise as the crack grows. Crack-opening stresses generally level off at $N/N_f = 0.6$ to 0.9. The rapid jump in $S_o'/S_{\max}$ for $N/N_f \approx 0.92$ is caused by the change in constraint from 1.8 to 1.2 during higher crack-growth rates. Incidentally, the surface crack became a through crack ($a/t = 1$) at $N/N_f \approx 0.9$.

7.2.2.2. Large crack.
Two objectives in the test program were to test CCT specimens with the

Mini-TWIST loading sequence to obtain large-crack data that could be compared with those of small cracks and to compare experimental and predicted crack length against cycles based on the crack-closure model. In the latter case, the CCT specimens were fatigue precracked at $R = 0$ from an initial sawcut notch c_n to a predetermined c_i; then the specimen underwent spectrum loading until failure. The maximum precracking stress was 50 percent of S_{max} in the spectrum.

Figure 69 shows some calculations from the model during both fatigue precracking and spectrum loading. Again, the crack-opening stresses have been normalized by S_{max}. From c_i to about 20 mm, the crack-opening stresses oscillate about a mean value. The constraint factor during most of these calculations was 1.8. Beyond about 20 mm, the constraint factor was 1.2 rather that 1.8 and higher crack-opening stresses were calculated. A drop in crack-opening stresses was calculated for c_i approaching w. The specimen failed when the crack length was about 90 percent of the specimen width.

7.3. Crack-Opening Stress Equations

Crack-opening stress equations for constant-amplitude loading were developed to facilitate the determination of ΔK_{eff}-against-crack-growth-rate relations for a given material, thickness, and environmental conditions. (See ref. 71.) These equations were developed from calculations made in the original model. However, because the method of calculating crack-opening stresses was modified to account for extreme crack-growth conditions, these equations have been modified. In the following sections, the original crack-opening stress equations and their modifications are presented. These equations are used in section 8 to correlate fatigue crack-growth rates for constant-amplitude loading conditions. Because the crack-closure model gives crack-opening stresses for only 2D crack configurations (plane-stress or simulated plane-strain conditions), further modifications have also been developed for surface- and corner-crack growth to account for variations in opening stresses along the crack front.

7.3.1. Constant-Amplitude Loading

The original crack-opening stress equations developed in reference 71 are presented here for completeness. These equations were developed by fitting to the calculated results from the closure model for a CCT specimen. Note that the crack-opening stress was calculated from equation (15) where n is replaced
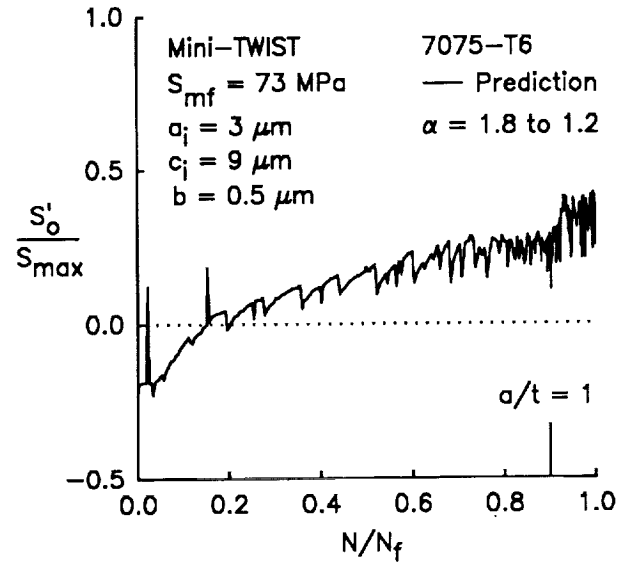
Figure 68. Calculated crack-opening stresses for small crack in 7075-T6 alloy for Mini-TWIST load sequence as ratio of applied to failure cycles.
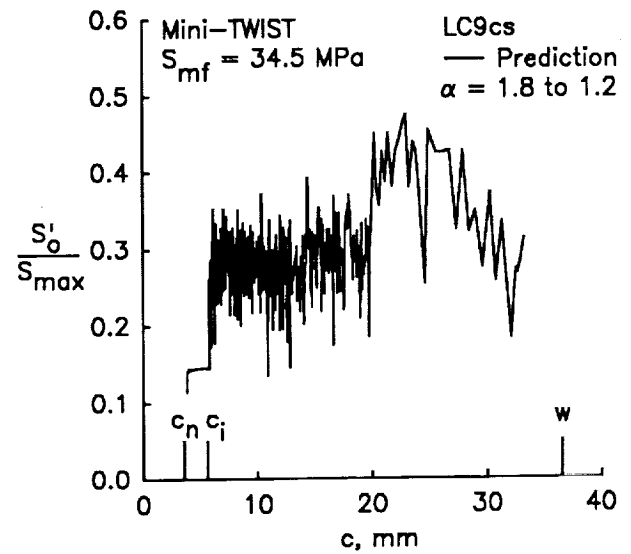
Figure 69. Calculated crack-opening stresses for large crack in LC9cs alloy for constant-amplitude precracking and Mini-TWIST load sequence.

by $n - 1$ (original formulation). The equations were given by

$$\frac{S_o}{S_{max}} = A_0 + A_1 R + A_2 R^2 + A_3 R^3 \quad \text{(for } R \geq 0\text{)} \quad (17)$$

and

$$\frac{S_o}{S_{max}} = A_0 + A_1 R \quad \text{(for } R < 0\text{)} \quad (18)$$

where $R = S_{min}/S_{max}$, $S_{max} < 0.8\sigma_o$, $S_{min} > -\sigma_o$, $S_o = S_{min}$ if S_o/S_{max} is less than R, and $S_o/S_{max} = 0$

if $S_o/S_{\max}$ is negative. The A_i coefficients are functions of α and $S_{\max}/\sigma_o$ and are given by

$$
\left.
\begin{aligned}
A_0 &= (0.825 - 0.34\alpha + 0.05\alpha^2)\left(\cos\frac{\pi S_{\max}F}{2\sigma_o}\right)^{\alpha^{-1}} \\[4pt]
A_1 &= (0.415 - 0.071\alpha)\frac{S_{\max}F}{\sigma_o} \\[4pt]
A_2 &= 1 - A_0 - A_1 - A_3 \\[4pt]
A_3 &= 2A_0 + A_1 - 1
\end{aligned}
\right\} \quad (19)
$$

for $\alpha = 1$ to 3. The boundary-correction factor F was added to these equations later to account for the effect of finite width on crack-opening stresses. (See ref. 70.)

7.3.2. Extreme Crack-Growth Rates

A modification to correct the original crack-opening stress equations for large-crack-growth extensions or rates was developed in reference 70. As discussed, a portion of the nth element was included in the calculation of crack-opening stress. (See eq. (15).) In the closure model analysis, the nth element always carried $-\sigma_o$ during unloading; the contribution of this element to the crack-opening stress was estimated as follows. An approximate equation for S_o' for constant-amplitude loading was derived from stress intensity factors for a crack in an infinite plate based on the assumption that the contact stress distribution was linear. The assumed contact stress distribution along the crack surfaces varied from $-\sigma_o$ at the crack tip to zero at the end of the contact region. The modification to correct the crack-opening stress equation is given by

$$
S_o' = S_o + 0.3\sigma_o\frac{\sqrt{\frac{\Delta c}{c}}}{F} \qquad \left(\text{for } \frac{S_{\max}}{\sigma_o} < 0.6\right) \quad (20)
$$

where Δc is the crack-growth increment (or rate per one cycle). The boundary-correction factor F was again added to account for the effect of finite width. The quantity S_o is calculated from equations (17)–(19). Comparisons with the model (ref. 70) showed that equation (20) was reasonably accurate for a range of constant-amplitude loading conditions in which $S_{\max}/\sigma_o < 0.6$. The difference between S_o' and S_o was significant (greater than a 2-percent effect on crack-opening stresses) only for growth rates greater than about 10^{-2} mm per cycle. For $S_{\max}/\sigma_o > 0.6$, the crack-opening stresses should be obtained from the FASTRAN II code (ref. 56) by conducting an analysis of the test specimen.

7.3.3. Surface- and Corner-Crack Growth

Early studies on crack growth predictions of semielliptical surface cracks demonstrated that surface-crack growth cannot be predicted solely by stress intensity factor ranges. (See refs. 72 and 73.) For $R = 0$ loading, small semicircular surface cracks grow in a self-similar fashion, although the stress intensity factor at the free surface is about 10 percent higher than the value at the maximum depth for low values of a/t. To account for this difference, Newman and Raju (ref. 72) multiplied the stress intensity factor range at the free surface by 0.9 and Jolles and Tortoriello (ref. 73) used 0.91. This factor was related to the crack-closure differences at the two locations. Assuming that crack closure at the free surface was plane stress and at the maximum depth location was plane strain, a crack-closure factor ratio β_R was derived and is given by

$$
\beta_R = 0.9 + 0.2R^2 - 0.1R^4 \quad (21)
$$

for $R \geq 0$ and $\beta_R = 0.9$ for $R < 0$. Therefore, for surface cracks, ΔK at the intersection of the crack front with the free surface is multiplied by β_R. However, for corner cracks, the stress intensity factors at the locations where the crack front intersects the free surface and the hole or notch surface are both multiplied by β_R.

8. Fatigue Crack-Growth Rate and Life Prediction

In the following sections, the experimental data on small and large cracks in the two aluminum alloys are summarized and compared with calculations or predictions from a ΔK-based analysis and the crack-closure model. First, the crack-growth rates for large cracks and for constant-amplitude loading are correlated by use of ΔK_{eff} calculated from the closure model. Similarly, the ΔK_{eff}-rate relation for cracks growing in the sheet thickness direction is established. The large-crack ΔK_{eff}-rate relation is then used to predict crack growth for Mini-TWIST spectrum loading. The small-crack data on initiation sites, shapes, length against cycles, and rates for both constant-amplitude and Mini-TWIST spectrum loading are reviewed and compared with predictions from the crack-closure model. Finally, a total fatigue life-prediction method is verified from the ΔK_{eff}-rate relations and the information obtained on small-crack initiation sites at material microstructural defects (inclusion particles or voids) and at slip-band locations in the cladding layer.

8.1. Correlation of Large-Crack-Growth Rates

To use the crack-closure model and life-prediction code, FASTRAN II (ref. 56), an effective stress intensity factor range against crack-growth rate relation must be obtained for the material, thickness, and environmental conditions of interest. The growth rates of large cracks for constant-amplitude loading and laboratory air were correlated against ΔK_{eff} with equations developed from the crack-closure model. (See sec. 7.3.) The following section describes how the ΔK_{eff}-rate relation was obtained from the large-crack data.

Center-crack tension specimens were used to obtain crack-growth rates for large cracks ($c > 2$ mm) in the 7075-T6 and LC9cs aluminum alloy sheets. Tests were conducted for $R = -1$ to 0.5. In the past, the spread in the ΔK_{eff}-rate results as a function of R, as shown in figures 23 and 25, has been used to estimate α for the closure model. The constraint factor is selected by trial and error to collapse the data onto a nearly single curve of ΔK_{eff} against rate. From past analyses on several aluminum alloys (refs. 64 and 65), $\alpha = 1.7$ to 1.9 has been shown to correlate constant-amplitude data for a wide range in rates. The effective stress intensity factor (ref. 22) is given by

$$\Delta K_{\text{eff}} = K_{\text{max}} - K_o' = \Delta K \frac{1 - \frac{S_o'}{S_{\text{max}}}}{1 - R} \qquad (22)$$

where K_o' is the stress intensity factor at the crack-opening stress and S_o' was calculated from equations (17)–(20).

8.1.1. 7075-T6 Aluminum Alloy

The ΔK_{eff}-rate relation for 7075-T6 alloy is shown in figure 70 for $R = -1$, 0, and 0.5. The data correlated quite well onto a nearly single curve with several transitions in slope at about the same rate for all stress ratios. Some differences were observed in the threshold regime, however. For these calculations, $\alpha = 1.2$ was used for rates greater than 7×10^{-3} mm per cycle (end of transition from flat-to-slant crack growth), and $\alpha = 1.8$ (nearly equivalent to Irwin's plane-strain condition) was used for rates lower than 7×10^{-4} mm per cycle (beginning of transition from flat-to-slant crack growth). For intermediate rates, α was varied linearly with the logarithm of crack-growth rate. The solid symbols denote measured rates at the transition from flat-to-slant crack growth from the cooperative program
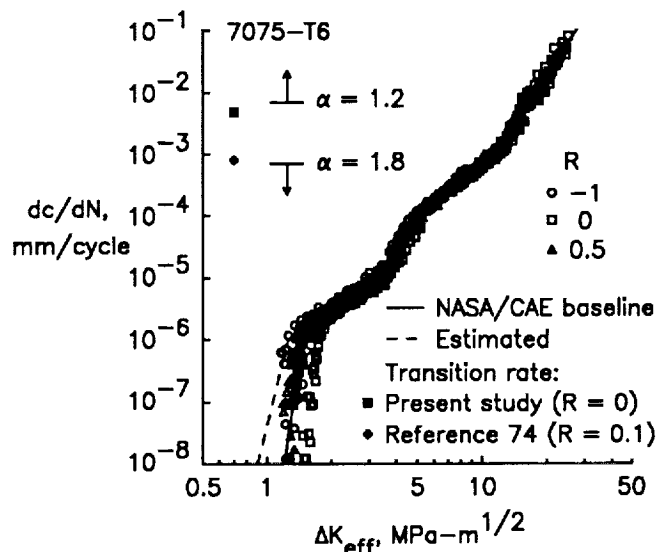
Figure 70. Effective stress intensity factor range against crack-growth rates for large cracks in 7075-T6 aluminum alloy for various stress ratios.
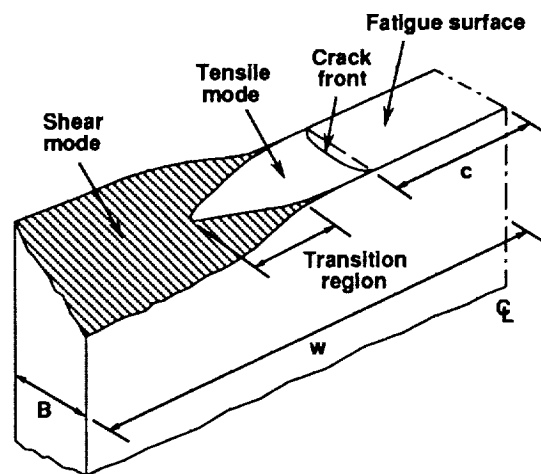
Figure 71. Transition from tensile to shear mode fatigue crack surfaces.

and from Vogelesang (ref. 74). (See illustration in fig. 71.) Schijve (ref. 75) has shown that the transition from flat-to-slant crack growth occurs at nearly the same rate for a range of stress ratios. Newman, Swain, and Phillips (ref. 64) have proposed that the flat-to-slant crack-growth transition region may be used to indicate a change from nearly plane-strain to plane-stress behavior and, consequently, to indicate a change in constraint. The importance of the variable-constraint option is shown later in crack-growth predictions made for the Mini-TWIST spectrum loading.

In the low crack-growth rate regime near and at the threshold, some tests (ref. 24) and analyses
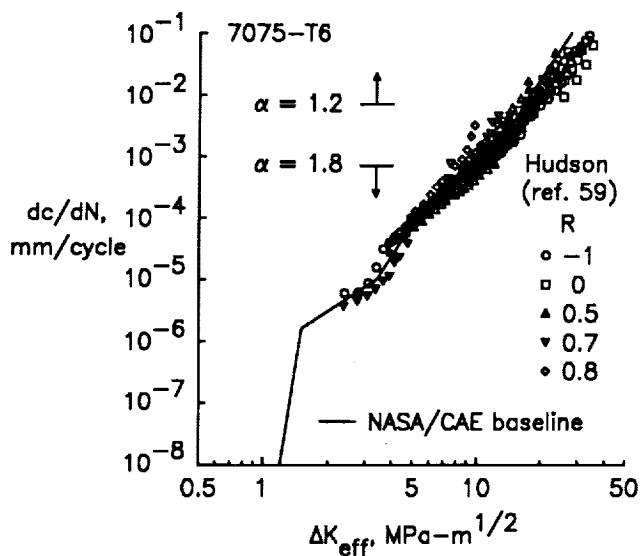
Figure 72. Effective stress intensity factor range against crack-growth rate from cooperative program and Hudson's data for 7075-T6 aluminum alloy.
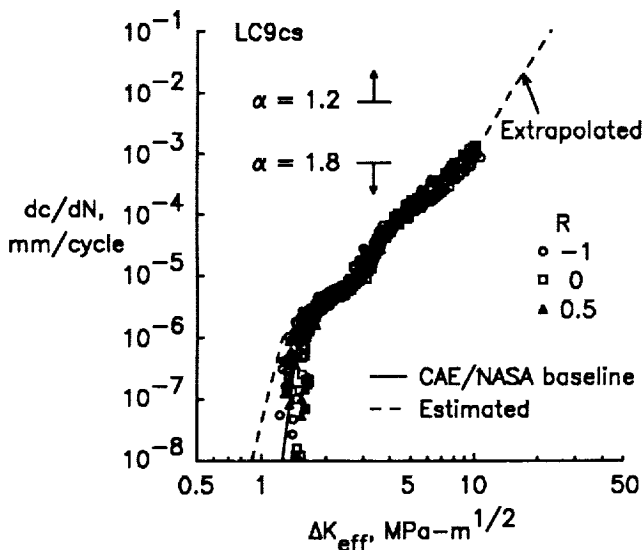
Figure 73. Effective stress intensity factor range against crack-growth rates for large cracks in LC9cs aluminum alloy for various stress ratios.

(ref. 23) have indicated that the threshold develops because of a rise in crack-opening stresses attributable to the load-shedding procedure. If a rise in crack-closure behavior does occur in the threshold regime, then the actual ΔK_{eff}-rate results would lie at lower values of ΔK_{eff} because the rise in crack-opening stresses has not been accounted for in the crack-closure model analysis. Further study is needed, however, to establish the actual ΔK_{eff}-rate behavior in this regime. The solid lines shown in figure 70 were drawn to fit dc/dN results; they are

used later to compare with da/dN results generated in the sheet thickness direction. The da/dN data from small cracks are then used to help establish the ΔK_{eff}-rate relation in the a-direction.

Figure 72 shows a comparison of large-crack (dc/dN) ΔK_{eff}-rate results from the cooperative program (baseline) with data obtained from Hudson (ref. 59) for a larger range of stress ratios than that used in the cooperative program. Although Hudson used a CCT specimen that was four times wider than the one used in the cooperative program, the data correlated reasonably well with the baseline relation except in the high crack-growth-rate regime. In this region, a plasticity-corrected ΔK_{eff} may be required to correlate these data. (See ref. 70.) Herein, only the elastic stress intensity factors are used.

8.1.2. LC9cs Aluminum Alloy

The ΔK_{eff}-rate results for the clad alloy are shown in figure 73. Again, the data for $R = -1$, 0, and 0.5 correlated quite well onto a single curve. As before, some differences were observed in the threshold region. For these calculations, the same variable-constraint regime that was selected for the 7075-T6 alloy was also used for the LC9cs alloy. A comparison of the baseline curves for 7075-T6 and LC9cs alloys showed similar trends, with the transitions in slope occurring at about the same rates. Therefore, the upper portion of the data for the 7075-T6 alloy was used to estimate the upper portion for the LC9cs alloy.

8.2. Effective Stress Intensity Factor Relations for Small Cracks

The surface-crack data from the small-crack test program produced data in the a-direction. Because the crack-opening behavior of small cracks stabilizes after a small amount of crack growth (about 40 μm for the tests in which $R = -1$, see fig. 67), these data may be used to help establish effective stress intensity factor relations in the a-direction. Based on a similar ΔK_{eff} analysis to the one discussed for cracks growing in the c-direction, baseline curves were developed for cracks growing in the a-direction. Comparisons among predictions made with these baseline curves and experimental data are made later.

8.2.1. 7075-T6 Aluminum Alloy

The large-crack baseline results for dc/dN (fig. 70) are shown in figure 74 as the solid lines. As mentioned, the data for rates less than about 1.0×10^{-6} mm per cycle (point A) may be affected by closure due to the load-shedding procedure (refs. 23
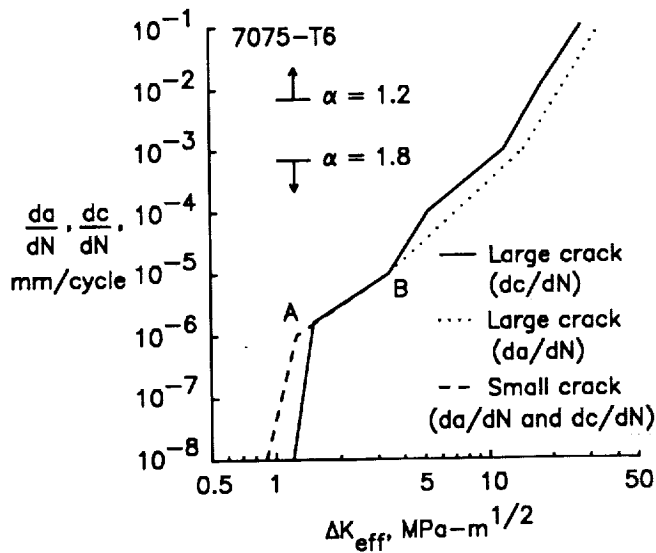
Figure 74. Effective stress intensity factor range against crack growth for small and large cracks in a- and c-directions for 7075-T6 aluminum alloy.
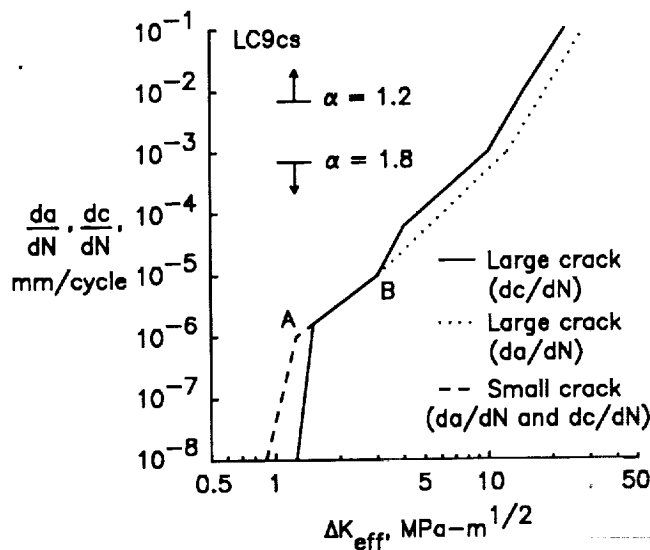
Figure 75. Effective stress intensity factor range against crack-growth for small and large cracks in a- and c-directions for LC9cs aluminum alloy.

and 24), which is not accounted for in the crack-opening stress equations. (See eqs. (17) and (18).) Thus, the ΔK_{eff} values for steady-state large-crack growth may be lower than those shown by the solid line. Further study is needed to resolve the issues associated with threshold behavior. The dashed line near point A is an estimate for steady-state da/dN and dc/dN behavior. This estimate was found by trial and error to fit the endurance-limit behavior from fatigue tests (shown later). An evaluation of these ΔK_{eff}-rate relations is made later for both small-crack growth and fatigue-life predictions.

Beyond 1.0×10^{-5} mm per cycle (point B) da/dN results (dotted line) deviated from dc/dN results (solid lines). This deviation is expected because a crack growing in the a-direction grows through a much different grain structure (see fig. 41) than one growing in the c-direction. (See refs. 56 and 57.) The upper portion of the da/dN relation (dotted line) was assumed parallel to dc/dN, and the final change in slope was assumed to occur at the same rate.

Instead of an equation to relate crack-growth rate to ΔK_{eff}, a table lookup procedure was chosen. The primary advantage of a table is that the baseline data can be described more accurately than with a multiparameter equation, especially in fitting the transitional regions. Multilinear segments were used to define the baseline ΔK_{eff}-rate relations in the a- and c-directions. These relations were then used in the analyses to predict small- and large-crack-growth rates and fatigue lives for constant-amplitude and spectrum loading. The end points of these segments are listed below:

ΔK_{eff}, MPa-m$^{1/2}$	dc/dN, m/cycle	da/dN, m/cycle
0.9	1.0×10^{-11}	1.0×10^{-11}
1.25	1.0×10^{-9}	1.0×10^{-9}
3.0	1.0×10^{-8}	1.0×10^{-8}
4.0	6.3×10^{-8}	
10.0	1.0×10^{-6}	
12.4		1.0×10^{-6}
14.8	1.0×10^{-5}	
23.0	1.0×10^{-4}	
28.4		1.0×10^{-4}

For values below or above the extremes listed in the above table, a power law that employed the first or last two points, respectively, was used to obtain rates. The upper limit for the power-law relation is, of course, defined by fracture toughness, which was 50 MPa-m$^{1/2}$. A lower limit or small-crack threshold $(\Delta K_{eff})_{th}$ was estimated to be 0.9 MPa-m$^{1/2}$ on the basis of the fatigue limits predicted in section 8.6.

8.2.2. LC9cs Aluminum Alloy

The dc/dN baseline data for the LC9cs alloy (fig. 73) is shown in figure 75 as the solid lines. Cracks in the core of the LC9cs alloy exhibit quite similar effects as those observed for the 7075-T6 alloy. The steady-state large-crack ΔK_{eff}-rate relation in both the a- and c-directions was assumed to be the dashed line near point A. Again, this behavior was found by trial and error but was closely modeled after

the data for the 7075-T6 alloy. Evaluations of these ΔK_{eff}-rate relations are made later in comparisons between experimental and calculated small-crack-growth rates and fatigue-life predictions.

Beyond 1.0×10^{-5} mm per cycle (point B), the da/dN results (dotted line) again differed from the dc/dN results (solid lines). The upper portions of the da/dN and dc/dN relations were assumed parallel to the dc/dN relation for the 7075-T6 alloy.

Linear segments in figure 75 that define the baseline ΔK_{eff}-rate relations in the a- and c-directions were used in all subsequent analyses. These relations were used to predict small- and large-crack-growth rates and fatigue lives. The end points of these segments are listed below:

ΔK_{eff}, MPa-m$^{1/2}$	dc/dN, m/cycle	da/dN, m/cycle
0.9	1.0×10^{-11}	1.0×10^{-11}
1.25	1.0×10^{-9}	1.0×10^{-9}
3.4	1.0×10^{-8}	1.0×10^{-8}
5.2	1.0×10^{-7}	
11.9	1.0×10^{-6}	
14.8		1.0×10^{-6}
17.6	1.0×10^{-5}	
27.5	1.0×10^{-4}	
34.0		1.0×10^{-4}

Again, for values below or above the extremes listed in the above table, a power law that employed the first or last two points, respectively, was used to obtain rates. The upper limit is defined by the fracture toughness, which was also 50 MPa-m$^{1/2}$. The $(\Delta K_{\text{eff}})_{\text{th}}$ was estimated to be 0.9 MPa-m$^{1/2}$ based on fatigue limits predicted in section 8.6.

8.3. Prediction of Large-Crack Growth

Several tests in the cooperative program were conducted on CCT specimens to monitor large-crack growth for the Mini-TWIST loading spectrum. For these tests, a constant-amplitude precracking stress ($R = 0$ and $S_{\text{max}} = 1.3 S_{\text{mf}}$) was used to grow a crack from the starter notch until a crack half-length had reached about 6 mm. At that point, the spectrum was applied until the specimen failed. These tests were used to evaluate the crack-closure model and life-prediction code (ref. 56) on large-crack growth.

8.3.1. 7075-T6 Aluminum Alloy

Five tests were conducted on the 7075-T6 alloy at three different S_{mf} levels. These test results are
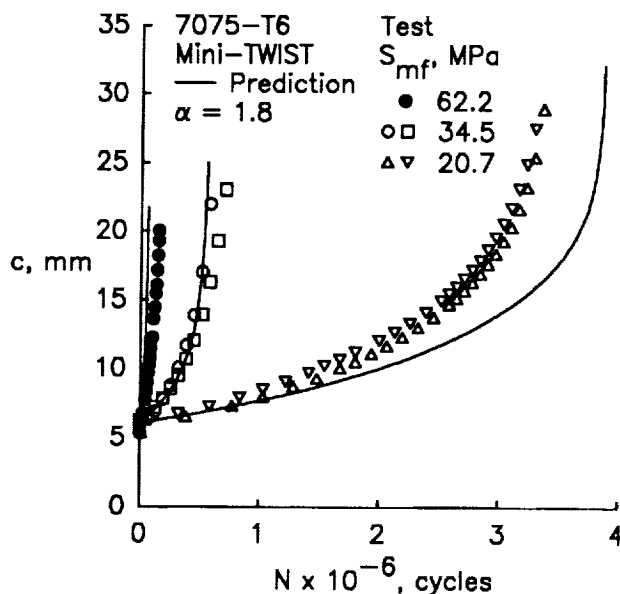
Figure 76. Experimental and predicted crack length against cycles for large cracks in 7075-T6 aluminum alloy for Mini-TWIST load sequence with constant constraint factor.

shown in figure 76. To illustrate the importance of the variable-constraint option for spectrum crack growth in aluminum alloys, the first set of predictions was made with a constant constraint factor ($\alpha = 1.8$). The solid curves show the predictions; the predicted results for the two lowest S_{mf} levels were within ± 20 percent of the test results. However, the predicted cycles to failure for the highest S_{mf} case were considerably less than the test results, but the predicted results using the variable-constraint option $\alpha = 1.8$ to 1.2, as shown in figure 77, agreed well with all of the test results (within ± 20 percent).

8.3.2. LC9cs Aluminum Alloy

Figure 78 shows the test results for five specimens made of LC9cs alloy. Here, only two S_{mf} levels were tested. Once again, variable α was used to predict crack length against cycles. Because the initial crack sizes for the low S_{mf} tests varied, the smallest and largest initial crack sizes were used in the predictions. Although the curves of the predicted crack length against cycles did not match those of the test results near failure, the test results generally fell within the upper and lower bounds. However, the two tests at $S_{\text{mf}} = 34.5$ MPa showed a large difference. The predicted results here fell within a factor of 2 of the average of these two tests. The radical change in the predicted crack length against cycles curve at about a 20-mm-long crack was caused by one of the severest flights in the spectrum that activated the low constraint value. The crack-opening stress history for

54
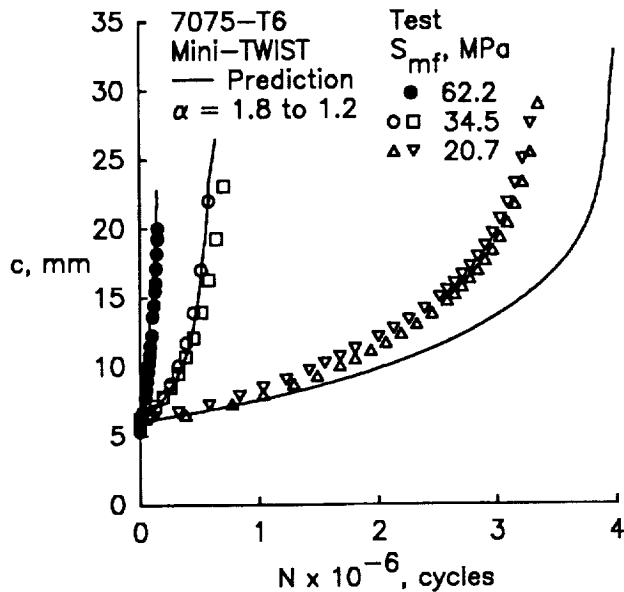
Figure 77. Experimental and predicted crack length against cycles for large cracks in 7075-T6 aluminum alloy for Mini-TWIST load sequence with variable constraint factor.
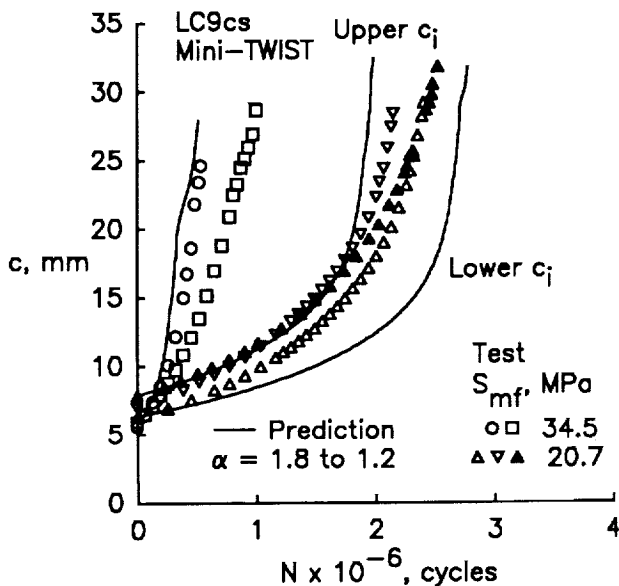
Figure 78. Experimental and predicted crack length against cycles for large cracks in LC9cs aluminum alloy for Mini-TWIST load sequence with variable constraint factor.

this particular test is shown in figure 69 in which the crack-opening stress levels rapidly rise at $c \approx 20$ mm. One of the tests showed a corresponding decrease in rate at $c \approx 22$ mm.

8.4. Initiation Sites and Crack Shapes for Small Cracks

One of the most difficult tasks in monitoring the growth of small surface or corner cracks is determin-

ing the crack shape. In many early reports of small-crack growth, researchers used the experimental calibration method in which specimens were broken at various stages and microscopic examinations of the fatigue surfaces revealed the crack shape. In many of these investigations, the researchers found that small cracks grow in nearly a semicircular shape ($a/c = 0.9$ to 1.1). For large surface cracks in some commercial alloys, the preferred propagation pattern is also nearly semicircular. (See ref. 55.) However, for highly anisotropic or textured materials, the propagation patterns are different. (See ref. 76.)

In the following sections, comparisons are made between experimental and predicted crack shape changes for surface and corner cracks at the edge notch for the two alloys. Because surface cracks generally initiate at inclusion particle clusters or voids in the 7075-T6 alloy, only surface cracks are considered. However, cracks in the LC9cs alloy nearly always initiate in the cladding layer and grow as corner cracks; therefore, only corner cracks are considered. Because the crack-growth rate properties are different in the a- and c-directions, analyses conducted here also address the influence of the two ΔK_{eff}-rate relations on surface- and corner-crack shape changes as the cracks grow along the notch root. Comparisons are made with the test data generated by NASA and CAE.

8.4.1. 7075-T6 Aluminum Alloy

Figures 79 and 80 show the crack shape changes for the 7075-T6 alloy. These figures show a/c against a/t. The solid symbols show the sizes and shapes of inclusion-particle clusters or voids that initiated the small cracks (average size was $a_i = 3$ μm and $c_i = 9$ μm). The data for a/c against a/t were determined from the experimental calibration method (specimens were broken at various stages in life and examined to determine the crack depths and lengths). In the analyses shown in figure 79, two different rate relations were used for da/dN. One analysis assumed that da/dN was the same as dc/dN as a function of ΔK_{eff}; the other analysis assumed that the two relationships were different as presented in the table on page 53. In the calculations, $R = 0$ and $S_{\text{max}} = 120$ MPa. The predicted shape with the same ΔK_{eff}-rate relations is shown as the dashed curve. The solid curve shows the predictions made with different rate relations for da/dN and dc/dN. In both analyses, the initial crack was an average of the inclusion particle sizes. Points A and B relate to the corresponding points shown in figure 74. At point B the ΔK_{eff}-rate relations begin to differ and a radical change in predicted crack shape is evident.
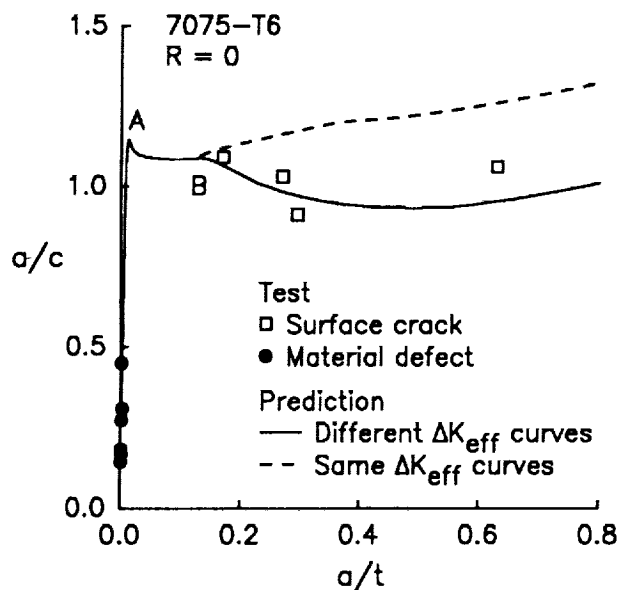
Figure 79. Experimental and predicted surface-crack shape changes in 7075-T6 aluminum alloy for same and different ΔK_{eff} curves in a- and c-direction for $R = 0$.

Figure 80. Experimental and predicted surface-crack shape changes in 7075-T6 aluminum alloy for various stress ratios.

For $a/t > 0.1$, the solid curve falls closer to the limited test data (symbols) than the dashed one. The tests and analyses show that small cracks approach a/c of about unity for a large part of their growth through the thickness.

Figure 80 shows the effect of stress ratio on crack shape. The results from the Mini-TWIST spectrum are also shown. The spectrum has an over-

Figure 81. Experimental and predicted corner crack shape changes in LC9cs aluminum alloy for same and different ΔK_{eff} curves in a- and c-directions with clad correction for $R = -1$.

all $R = -0.23$ (minimum to maximum stress in the spectrum). Maximum stress levels in the analyses were like those in the tests; however, the da/dN and dc/dN relationships were different. The sharp changes in crack shape as a function of a/t were caused by the multilinear ΔK_{eff}-rate curves. The predicted results for all stress ratios agreed reasonably well with the test data.

8.4.2. LC9cs Aluminum Alloy

Comparisons between tests and analyses on crack shape changes in the LC9cs alloy are shown in figures 81 and 82. Again, these figures show a/c against a/t. The average cladding-layer thickness was about 60 μm (indicated as the vertical line). As discussed, the experimental a/c and a/t values (symbols) were determined from the experimental calibration method. In the analyses shown in figure 81, two different rate relations were used for da/dN. In one analysis, da/dN was equal to dc/dN as a function of ΔK_{eff} (dashed curve); in the other analysis (solid curve), the two relationships were different as presented in the table on page 54. Here, the calculations were performed with $R = -1$ and $S_{\text{max}} = 80$ MPa. In both analyses, the initial crack was 77 μm in both the a- and c-directions. Again, points A and B relate to corresponding points on figure 75. Point B is where the ΔK_{eff}-rate relations begin to differ. The solid curve falls closer to the test data at $R = -1$ (symbols) than the dashed one and indicates that different ΔK_{eff} curves are appropriate.
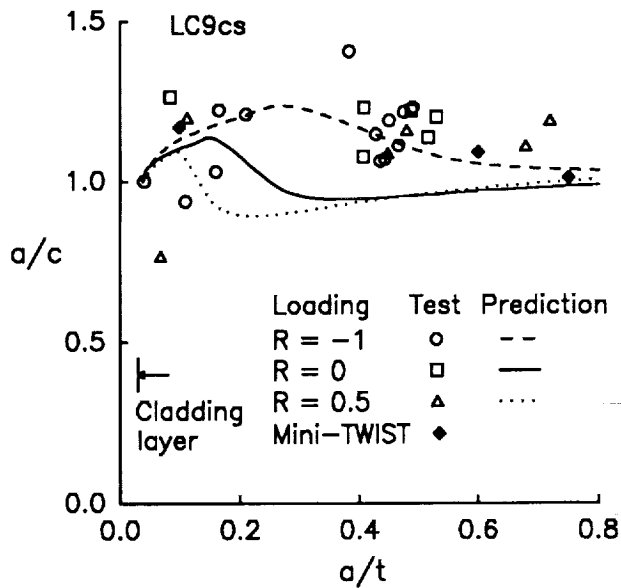
Figure 82. Experimental and predicted corner crack shape changes in LC9cs aluminum alloy for various stress ratios.
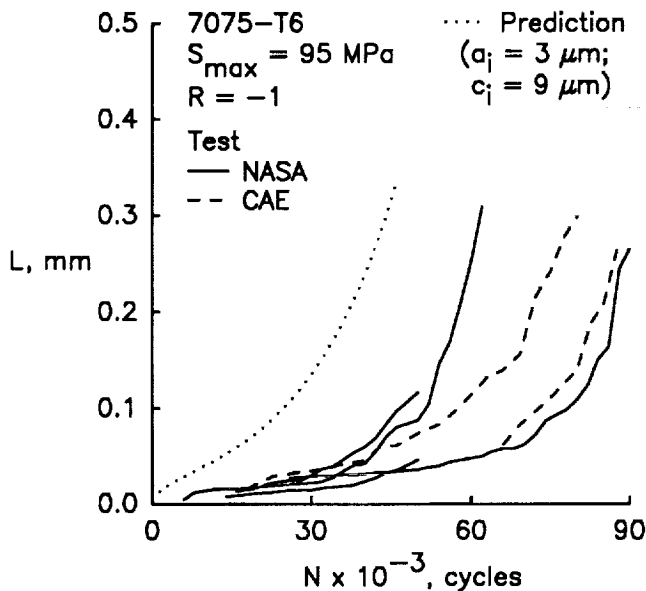
Figure 83. Experimental and predicted small surface crack growth in 7075-T6 aluminum alloy SENT specimens.

Figure 82 shows the influence of R on crack shape for the LC9cs alloy. Again, the initial crack size was 77 μm ($a_i/c_i = 1$) and the levels of S_{max} in the analyses were the average of those used in the tests. Although the predicted results for $R = -1$ agreed with the test results, those for $R = 0$ and 0.5 did not agree. The reason for the different trends between tests and analyses could not be determined.

8.5. Prediction of Small-Crack Growth

In the following, comparisons are made between measured and predicted crack length against cycles

for typical constant-amplitude loading conditions. Comparisons are also made on crack-growth rates against ΔK for small cracks for all cooperative program loading conditions. All experimental small-crack-growth results were analyzed with the non-interaction criteria. (See sec. 6.5.) Baseline results from the large-crack tests (see sec. 5) are also shown for comparison. Note that the small-crack growth rates are calculated for da/dN, whereas the large-crack rates are for dc/dN.

8.5.1. 7075-T6 Aluminum Alloy

Typical results of crack length against cycles for small cracks are shown in figure 83 for $R = -1$. These results were selected because previous studies have shown that the small-crack effect is more pronounced at negative stress ratios than at positive ones. The depth L from the plastic-replica method is plotted against cycles. The solid and dashed curves show NASA and CAE results, respectively. Based on an initial defect (or void) size ($a_i = 3$ μm, $c_i = 9$ μm, and $b = 0.5$ μm) in the analysis, the predicted results (dotted curve) fall considerably shorter than those in the tests. Because the plastic-replica method affected fatigue life (by about a factor of 2 at this stress level) and possibly small-crack-growth rates, the results shown in figure 83 may be expected.

Comparisons of experimental and predicted growth rates for small cracks are shown in figures 84–87 for $R = -1$, 0, 0.5, and Mini-TWIST loading, respectively. Even though the range in S_{max} in each test series is indicated, no stress-level effect was apparent in the test data; thus, all data have been grouped. In some cases, however, a range of stress levels was used in the analyses to show expected trends. The dotted lines show the large-crack (dc/dN) results and the dashed lines show the ΔK_{eff}-rate curve used in the analyses for da/dN.

Results for $R = -1$ are shown in figure 84. The solid curves show the predicted results based on an initial defect (or void) size of 3 by 9 by 0.5 μm for a range of maximum stress levels. All predictions start on the ΔK_{eff} curve because cracks at small voids are assumed to be fully open on the first cycle and $\Delta K = \Delta K_{eff}$. Clearly, the model predictions did not agree well with the test data for $S_{max} = 80$ to 95 MPa in the near-threshold regime. However, the predictions did agree with the test data in the mid- and high-rate range. At 70 MPa, the predictions show that the crack nearly arrested (minimum rate) at $\Delta K \approx 2$ MPa-m$^{1/2}$. At this point ΔK_{eff} was slightly greater than 0.9 MPa-m$^{1/2}$, the effective

57
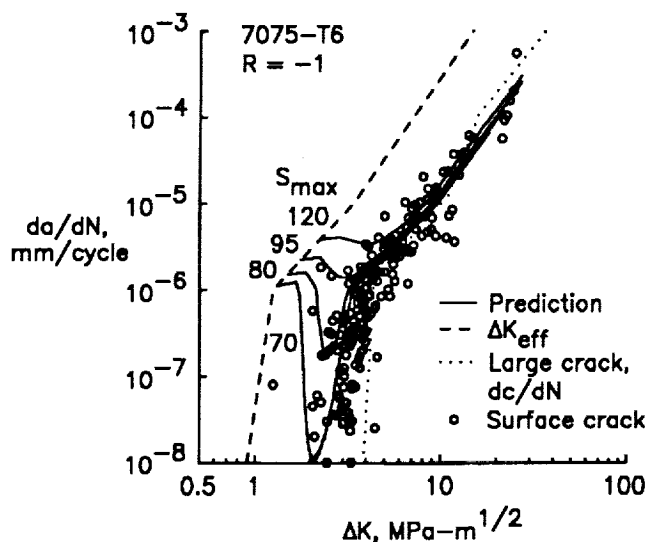
Figure 84. Experimental ($S_\text{max} = 80$ to 95 MPa) and predicted small surface crack-growth rates against ΔK in 7075-T6 aluminum alloy SENT specimens at $R = -1$.
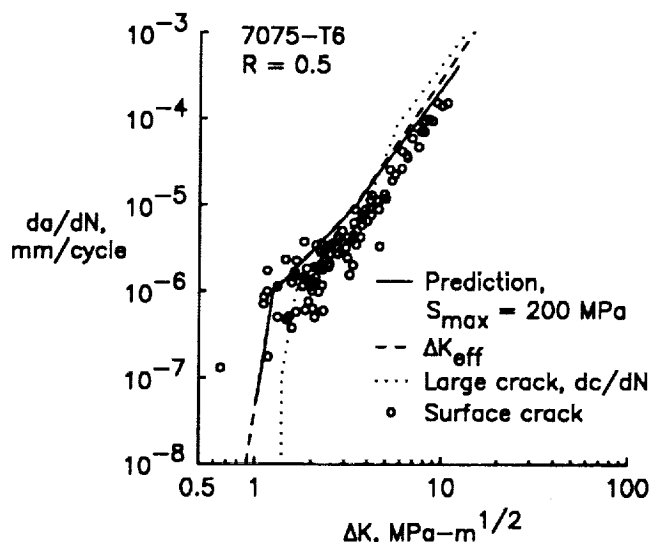
Figure 86. Experimental ($S_\text{max} = 195$ to 220 MPa) and predicted small surface crack-growth rates against ΔK in 7075-T6 aluminum alloy SENT specimens at $R = 0.5$.
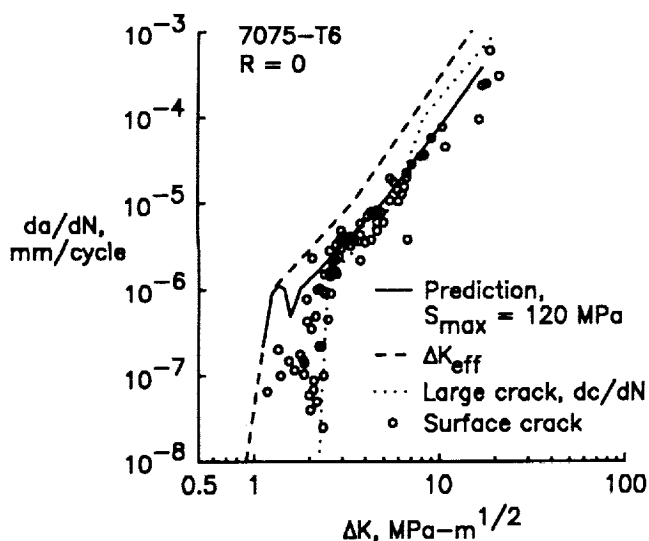
Figure 85. Experimental ($S_\text{max} = 120$ to 140 MPa) and predicted small surface crack-growth rates against ΔK in 7075-T6 aluminum alloy SENT specimens at $R = 0$.
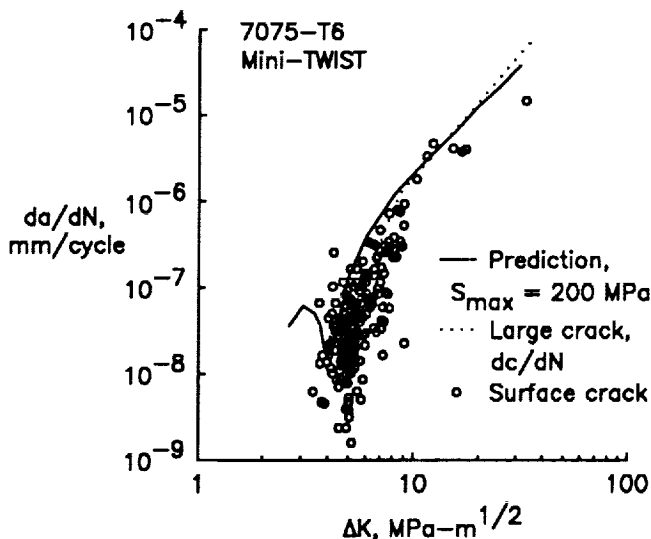
Figure 87. Experimental ($S_\text{max} = 190$ to 208 MPa) and predicted small surface-crack growth rates against ΔK in 7075-T6 aluminum alloy SENT specimens for Mini-TWIST load sequence.

threshold for small cracks. (Note that the fatigue limit for $R = -1$ was about 70 MPa, see sec. 8.6.1.)

The comparison of experimental and predicted results for $R = 0$ is shown in figure 85. The observed trends are nearly identical to those for $R = -1$, except that the cracks in the mid- to high-rate range grew more slowly than those predicted (solid curve). As R increases, the spread between the large-crack ΔK-rate and ΔK_eff-rate curves lessens, which helps explain why the small-crack effects are not as pronounced as those observed for $R = -1$.

Whereas the previous results for $R = -1$ and 0 had elastic notch-root stresses, the test conditions for $R = 0.5$ caused the notch root to yield. For these conditions, small cracks were observed to grow at considerably slower rates than those measured for large cracks at ΔK values greater than the large-crack threshold. (See fig. 86.) Of course, the plastic-replica method may be partly responsible, but this effect has been observed for 2024-T3 aluminum alloy (ref. 19) wherein the replica method did not appear

to have a significant effect. The slower rates for small cracks are still being investigated.

The measured and predicted small-crack-growth rates for the Mini-TWIST loading are shown in figure 87. Here the average crack-growth rate is plotted against the maximum range stress intensity factor. (See secs. 3.6.1 and 3.6.2.) To determine the predicted values, crack depth $(2a)$ and cycle results were taken from the analysis at nearly equal cyclic intervals between the initial crack depth and breakthrough $(a = t)$. From these values of crack depth and cycles, the average rate and maximum range stress intensity factor were calculated. The predicted results and experimental data showed similar trends, but the predicted rates were generally faster than those from the experiments. Again, the plastic-replica method may be responsible for some of the observed differences. At $S_{max} = 200$ MPa, fatigue tests in which the replica method was used gave fatigue lives that were nearly a factor of 2 longer than tests without the replicas.

8.5.2. LC9cs Aluminum Alloy

A comparison of experimental and predicted crack length against cycles for small cracks in the LC9cs alloy for $R = -1$ loading is shown in figure 88. The measured L from the plastic-replica method is plotted against cycles. The solid and dashed curves show data from CAE and NASA, respectively. In the analysis, a 77-μm quarter-circular corner crack was assumed for the initial crack size. From the experiments, this particular crack size seems reasonable. The predicted results (dotted curve) agreed well in the early growth period but showed slower rates for longer crack lengths. However, results from several tests, which were stopped at about 22 000 cycles, may have agreed better with the prediction if they had been allowed to continue.

Figures 89–92 show comparisons of the experimental and predicted ΔK against rates for small cracks for $R = -1$, 0, 0.5, and Mini-TWIST loading, respectively. Again, no stress-level effect was apparent in the test data; therefore, all data have been grouped. The dotted curves show the large crack (dc/dN) results and the dashed lines show the ΔK_{eff}-rate relation used in the analyses for da/dN. Predictions are shown as solid curves.

Figure 89 shows comparisons of experimental and predicted rates on the LC9cs alloy for $R = -1$ loading. The solid curves show the predicted results with a 77-μm initial corner crack for a range of S_{max}. All predictions start on the ΔK_{eff} curve because the initial crack is assumed to be fully open on the first
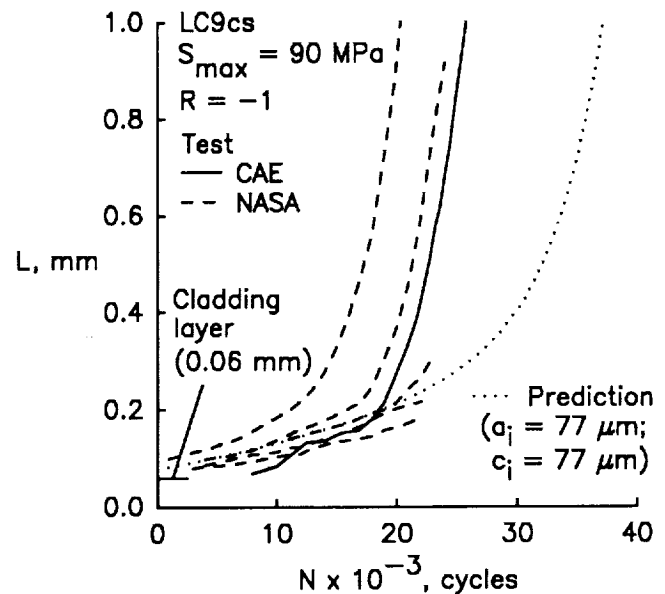
Figure 88. Experimental and predicted small corner-crack growth in LC9cs aluminum alloy SENT specimens.
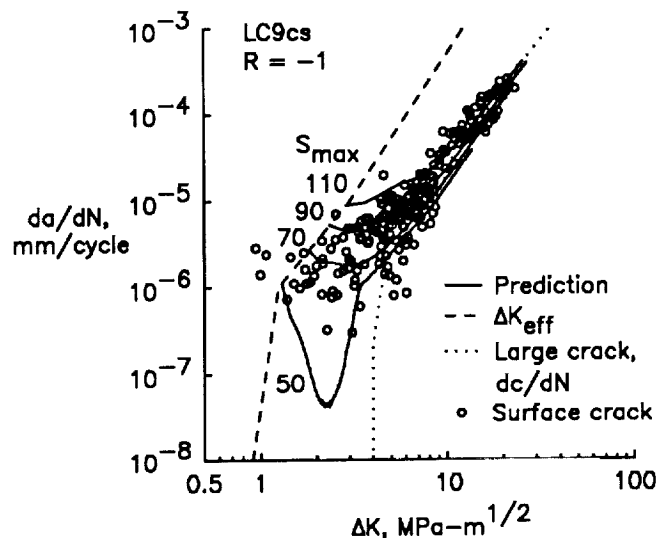
Figure 89. Experimental ($S_{max} = 70$ to 90 MPa) and predicted small-crack-growth rates against ΔK with small-crack clad correction in LC9cs aluminum alloy SENT specimens at $R = -1$.

cycle. As the corner crack grows, the residual plastic deformations build along the crack surfaces and cause the crack-opening stresses to stabilize at the large-crack conditions. Here, the predictions begin to agree with the large-crack results. The predictions from the model agree well with the test data for $S_{max} = 70$ to 90 MPa in the early stages of crack growth, but the predicted rates seem to be slightly low in the mid- to high-rate range. At $S_{max} = 50$ MPa, the predictions show a large drop in crack-growth
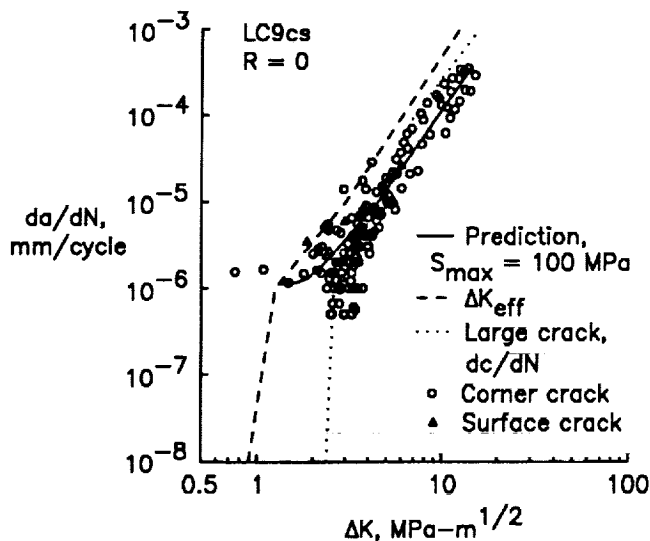
Figure 90. Experimental (S_{max} = 100 to 115 MPa) and predicted small-crack-growth rates against ΔK with small-crack clad correction in LC9cs aluminum alloy SENT specimens at $R = 0$.

Figure 91. Experimental (S_{max} = 165 to 180 MPa) and predicted small-crack-growth rates against ΔK with small-crack clad correction in LC9cs aluminum alloy SENT specimens at $R = 0.5$.

Figure 92. Experimental and predicted small-crack-growth rates (S_{max} = 125 to 170 MPa) against ΔK with small-crack clad correction in LC9cs aluminum alloy SENT specimens for Mini-TWIST load sequence.

rates, similar to those for the 7075-T6 alloy. This drop in rate is caused by a crack-closure transient, as illustrated in figure 65. The crack would have been predicted to arrest if S_{max} = 40 MPa had been used. Again, the effective threshold for small cracks was assumed to be 0.9 MPa-m$^{1/2}$. The fatigue limit for $R = -1$ was about 40 MPa.

A comparison of experimental and predicted results for $R = 0$ is shown in figure 90. Here, data on

both surface and corner cracks are shown. However, only corner-crack growth was predicted for the LC9cs alloy (solid curve). The predicted results agreed quite well with the test results.

The results for $R = 0.5$ are shown in figure 91. Again, small surface and corner cracks were observed to grow at slower rates than those measured for large cracks at ΔK values greater than the large-crack threshold. This slower growth may have resulted because the notch root yielded. Attempts to explain this observed effect from crack closure, constraint, or crack-shape changes have been unsuccessful. Further study is needed to determine the cause of this slower growth.

The rates for measured and predicted small-crack-growth rates for the Mini-TWIST loading are shown in figure 92. The predicted rates (solid curve) agreed well with the experiments for both small and large cracks.

8.6. Prediction of Fatigue Life

All of the elements are now in place to assess a total fatigue-life prediction methodology based solely on crack propagation from microstructural features, such as the inclusion-particle clusters (or voids) and the cladding layer. The fatigue tests that were conducted in the early part of the cooperative program are now used in this assessment. In this approach, a crack is assumed to initiate and grow at the notch root on the first cycle. The crack-closure model and the baseline ΔK_{eff}-rate relations are used to predict
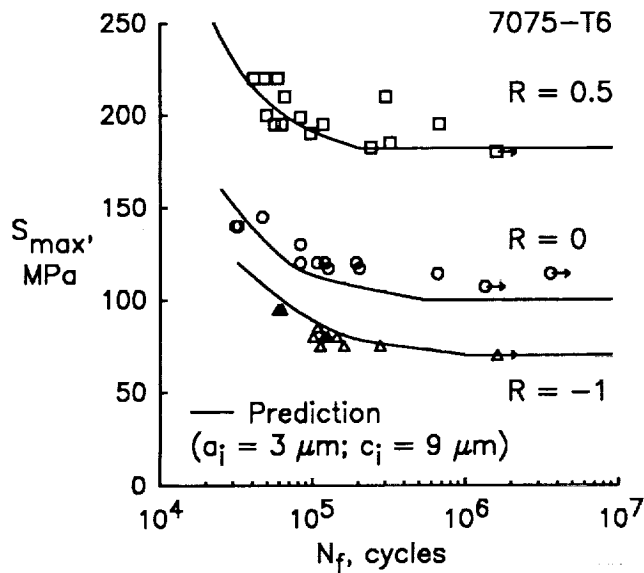
Figure 93. Experimental and predicted fatigue lives for 7075-T6 aluminum alloy at various stress ratios.
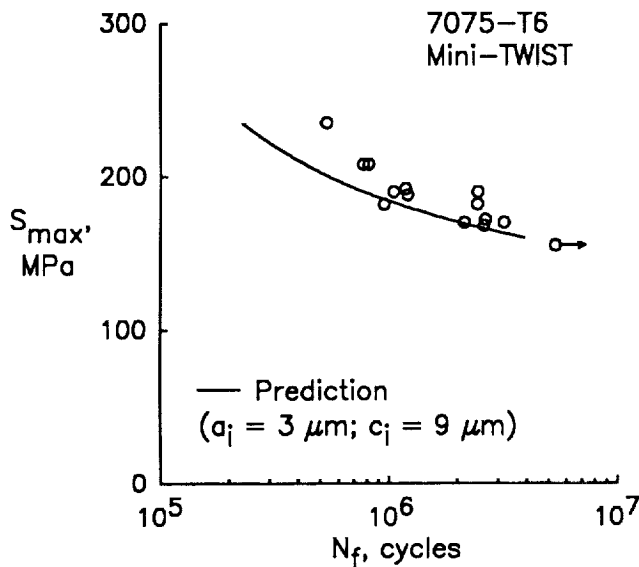
Figure 94. Experimental and predicted fatigue lives for 7075-T6 aluminum alloy for Mini-TWIST load sequence.

crack growth from the initial crack size to failure. Comparisons are made with the fatigue tests conducted on the SENT specimens. Because these tests were standard fatigue tests, the effects of the plastic-replica method on fatigue life for the 7075-T6 alloy are not an issue.

8.6.1. 7075-T6 Aluminum Alloy

The S-N data for the 7075-T6 alloy are shown in figures 93 and 94 for constant-amplitude and Mini-TWIST spectrum loading, respectively. A symbol
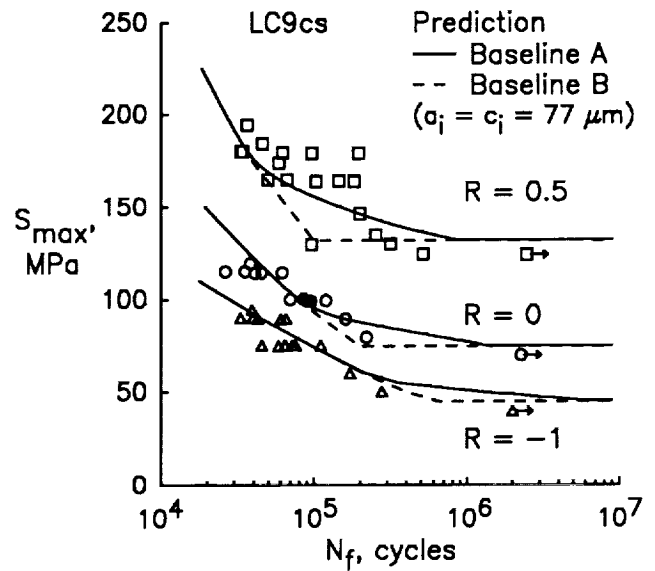
Figure 95. Experimental and predicted fatigue lives for LC9cs aluminum alloy at various stress ratios.

indicates a failure; when an arrow is attached, that test was terminated before failure. In the analysis, the initial crack size was $a_i = 3$ μm, $c_i = 9$ μm, and $b = 0.5$ μm. This crack size is the average defect size measured at actual crack-initiation sites. The effective stress intensity factor range against rate relations used in the analysis are given in the table on page 53 and the $(\Delta K_{eff})_{th}$ was assumed to be 0.9 MPa-m$^{1/2}$. The FASTRAN II code (ref. 56) was used to make life predictions for both constant-amplitude and spectrum loading. The solid curves show the predicted number of cycles to failure. The predicted lives were in reasonable agreement with the test lives for constant-amplitude loading. In addition to predicting fatigue life, the analysis methodology was also able to predict the fatigue limit as a function of R. For spectrum loading, the predicted results (fig. 94) fell near the lower bound of the data from the experiments.

8.6.2. LC9cs Aluminum Alloy

The results from experiments and predictions are shown in figure 95 for constant-amplitude fatigue tests on the LC9cs alloy. In these tests, the LC9cs alloy exhibited more scatter than the 7075-T6 alloy, especially at the $R = 0.5$ stress ratio condition. The solid curves show predictions using the baseline relations for da/dN and dc/dN given in the table on page 54 (baseline A). To show the sensitivity of the da/dN and dc/dN relations in the low-rate regime on fatigue life, the dashed curves show the predicted results from baseline B relations (as shown by the
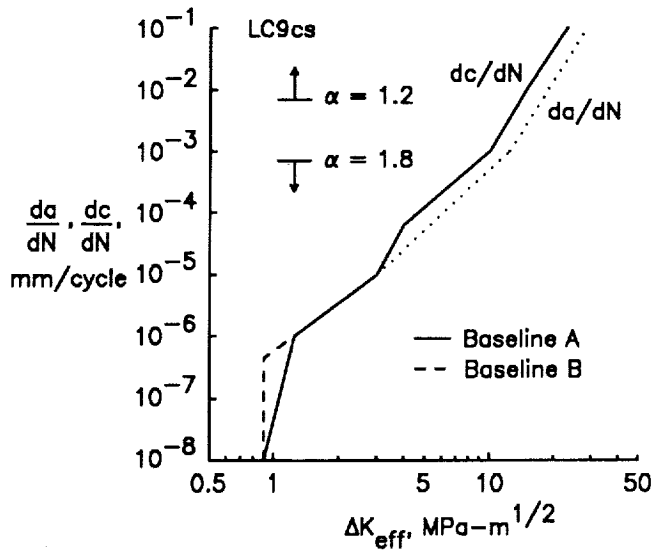
Figure 96. Effective stress intensity factor range against crack growth rates in a- and c-directions for baseline A and B relations.
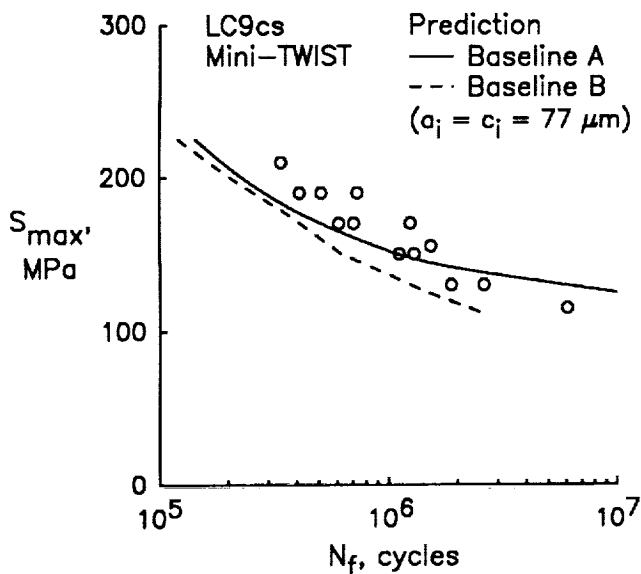
Figure 97. Experimental and predicted fatigue lives for LC9cs aluminum alloy for Mini-TWIST load sequence.

dashed lines in fig. 96). In both analyses, the initial corner-crack size was $a_i = 77$ μm, $c_i = 77$ μm, and $b = 0.5$ μm. This crack size is somewhat larger than the cladding-layer thickness, but it is consistent with observations from experiments made early in life. (See fig. 88.) Again, the effective stress intensity factor threshold for small cracks $(\Delta K_{eff})_{th}$ was assumed to be 0.9 MPa-m$^{1/2}$. The predicted lives were in reasonable agreement with the test results. In addition, the results indicated that the analysis method also could predict reasonable fatigue limits for the LC9cs alloy.

Fatigue lives for the LC9cs alloy for Mini-TWIST spectrum loading is shown in figure 97. The solid and dashed curves show the predictions with the two baseline relations (A and B). The predicted lives for baseline A cross the test data at low stress levels, but the results from baseline B fall near the lower bound of the test data.

9. Conclusions

The National Aeronautics and Space Administration and the Chinese Aeronautical Establishment have participated in a Fatigue and Fracture Mechanics Cooperative Program. The objectives were to study the behavior of small cracks in two high-strength aluminum alloys, to compare experimental and analysis results from each laboratory, and to evaluate an existing analytical model to predict the growth of such cracks. Both experimental and analytical studies were conducted on fatigue crack growth of small and large cracks in 7075-T6 bare and LC9cs clad aluminum alloy sheets. The analyses and experiments on single-edge-notch tension (SENT) and center-crack tension (CCT) specimens produced the following findings.

9.1. Analyses

1. Stress intensity factor solutions for surface and corner cracks at a notch determined by the three-dimensional finite-element method and by the weight-function method generally agree within ±3 percent for a range of crack-configuration parameters. However, the finite-element method requires a large mainframe computer, whereas the weight-function method used a personal computer.

2. Stress intensity factor solutions for a through crack at a notch in a plate subjected to remote uniform stress or displacement have been determined by a two-dimensional boundary-force method.

3. Stress intensity factor equations have been developed for a surface, corner, and through crack at a notch for a range of crack-configuration parameters.

4. A simple correction to estimate the influence of the low-yield cladding material on stress intensity factors for a corner crack at the notch has been developed from a two-dimensional weight-function analysis.

9.2. Experiments

1. Fatigue lives and small-crack-growth rates measured on SENT specimens for constant-amplitude

and Mini-TWIST spectrum loading from the two laboratories agree well for all loading conditions.

2. Large-crack-growth rates measured for three constant-amplitude stress ratios (-1, 0, and 0.5) from the two laboratories agree well, although slight discrepancies were observed in the near-threshold regime.

3. Small cracks grew below the large-crack threshold in both 7075-T6 and LC9cs alloys, especially for the lower stress ratio tests. Small-crack effects are more pronounced for the negative stress ratio tests.

4. Surface cracks in the 7075-T6 alloy initiate at inclusion-particle clusters or voids at or near the notch surface. More than 70 percent of the cracks initiate in the middle half of the sheet specimen thickness.

5. Corner cracks in the LC9cs alloy initiate from slip-band formation in the cladding layers. More than 90 percent of the cracks initiate at the intersections of the notch and sheet surfaces.

6. Both laboratories found that 80 to 97 percent of the fatigue lives for the two alloys is spent in propagating a crack from microstructural material defects (inclusion particles or void) or the cladding layer.

7. Fatigue lives, and presumably small-crack-growth rates, in the 7075-T6 aluminum alloy are affected by the plastic-replica method. However, the LC9cs clad alloy is apparently unaffected by this method.

8. Measured crack-growth rates of large surface and corner cracks at the notch indicate that the crack-growth properties in the length and depth directions probably differ.

9.3. Analytical Crack-Closure Model

1. For large cracks, the crack-closure concept correlates fatigue crack-growth rate against the effective stress intensity factor range data over 6 to 8 orders of magnitude in rate for three constant-amplitude stress ratio conditions.

2. The model predicts constant-amplitude and Mini-TWIST spectrum loading trends for small cracks like those observed in tests, especially for the LC9cs alloy. The discrepancies for the 7075-T6 alloy are attributed to the effect of the plastic-replica (acetone) method on small-crack-growth rates.

3. The crack-closure model predicts crack length against cycles for a large crack in a plate subjected to the Mini-TWIST spectrum loading within about ±25 percent for the two alloys.

4. Using a microstructural defect (inclusion-particle) size or the cladding-layer thickness as an initial crack, a total fatigue-life prediction method was demonstrated using the crack-closure model.

The cooperative program demonstrated that international cooperation between research organizations can be fruitful. The cooperative program has advanced the state of the art in fatigue and fracture mechanics and has provided the American and Chinese aerospace industries with useful data from experiments and with efficient analysis methods for improving life prediction. These results should ultimately improve the reliability and safety of aircraft structures.

NASA Langley Research Center
Hampton, VA 23681-0001
January 14, 1994

Appendix A

Finite-Element Analyses of Surface and Corner Cracks at a Semicircular Notch

In this section, the 3D finite-element analyses used to calculate the stress intensity factors for surface and corner cracks emanating from a semi-circular notch are presented. The finite-element program and method (singularity element and nodal-force method) developed by Raju and Newman (refs. 33 and 34) were used for semicircular and low-aspect-ratio (low a/c) cracks. For large-aspect-ratio cracks ($a/c = 2$), the finite-element program (non-singular elements) developed by Shivakumar and Newman (ref. 35) and the equivalent-domain integral (EDI) method (ref. 36) were used because the latter approach required less effort to generate large a/c models than the former one. The stress intensity factors were obtained for a range of semielliptical surface cracks at the center of the semicircular edge notch and quarter-elliptical corner cracks at the edge of the notch in a finite-thickness specimen. The ranges were $a/c = 0.4$ to 2 and $a/t = 0.2$ to 0.8. The hole-radius-to-plate-thickness (r/t) ratio was 3 for surface cracks and 1.5 for corner cracks. The SENT specimens were subjected to remote tensile loads.

Stress Intensity Factors

The mode I stress intensity factor for any location along the crack front was expressed as

$$K = S \left(\frac{\pi a}{Q}\right)^{1/2} F_j \left(\frac{a}{t}, \frac{a}{c}, \frac{r}{t}, \varphi\right) \qquad \text{(A1)}$$

where $j = s$ for a surface crack and $j = c$ for a corner crack. The r/w ratio was 1/16 and the half-height of the plate h was chosen large enough that height would have a negligible effect on stress intensity factors ($h/w \geq 2$). Values of F_j were calculated along the crack front for various combinations of configuration parameters (a/t, a/c, and φ). The crack dimensions and parametric angle φ are defined in figure A1. For an ellipse, Q is given by the square of the complete elliptic integral of the second kind. (See appendix D.)

Three-Dimensional Finite-Element Analyses

Singularity Elements and Nodal-Force Method

Stress intensity factor distributions in references 77 and 78 for surface and corner cracks at

a hole showed a precipitous drop near the region where the crack meets the hole surface. This drop was believed to have been caused by the boundary layer effect. (See ref. 79.) However, comparisons with other solutions in the literature (see refs. 48 and 80) showed that the stress intensity factors calculated by other investigators did not show this large drop in the boundary layer region. Therefore, Tan et al. (ref. 81) conducted a study to determine whether this drop was real and, if not, to determine the source of the anomaly. The models used in references 77 and 78 were reexamined; that examination revealed that the procedures used to generate the cracked solids produced models with some ill-shaped elements in the region where the crack intersects the hole boundary. The ill-shaped elements were defined as ones with aspect ratios greater than 100. These elements do not affect the results if they are in regions of small stress gradients. However, they may produce a stiffer model if they are in regions of large stress gradients. For $r/t = 1$, the elements in the region where the crack meets the hole boundary had aspect ratios of about 150. In the cooperative program, however, solutions were needed for $r/t \approx 3$. The aspect ratio for elements created with this mesh generator produced elements with aspect ratios of about 450! (Stress intensity factor solutions were never published for $r/t > 2$ (refs. 77 and 78).)

An investigation was undertaken (ref. 81) to study the effect of these ill-shaped elements on the stress intensity factor solutions and on the equations developed to fit these results. The investigation was conducted in two parts: in the first part, improved procedures were used to generate models for cracked solids and several different finite-element models were developed; in the second part, several different methods were used to extract the stress intensity factors from the finite-element solutions. Three different finite-element models were developed: model A used finite-element patterns (eight-noded elements) that were similar to those used in references 77 and 78 with the ill-shaped elements, model B was a newly developed finite-element model similar to model A but without ill-shaped elements, and model C with eight-noded elements used only nonsingular elements (without any ill-shaped elements). Models A and B had about 15 000 DOF. Model C had about 18 000 DOF. Two different LaRC computer programs (refs. 33 and 35) were used to analyze the various models. These programs verified the consistency of the results and determined whether undetected errors existed in the codes or analyses. (Stress intensity factors reported in NASA TM-101527 for $a/c = 2$ are in error because
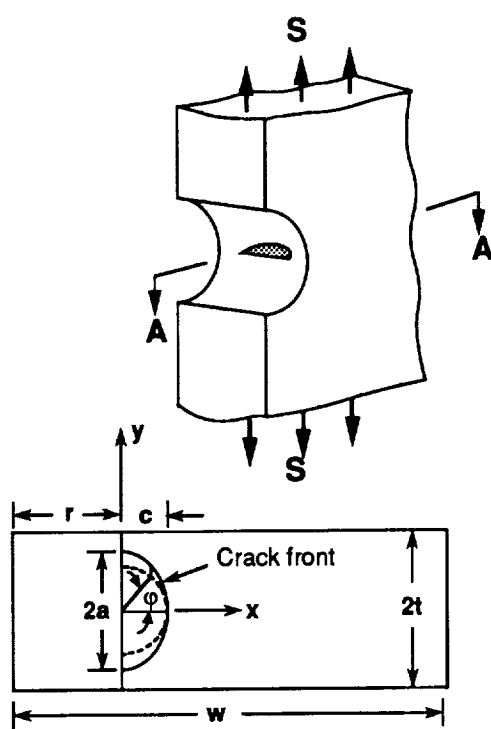
(a) Surface crack (A-A).
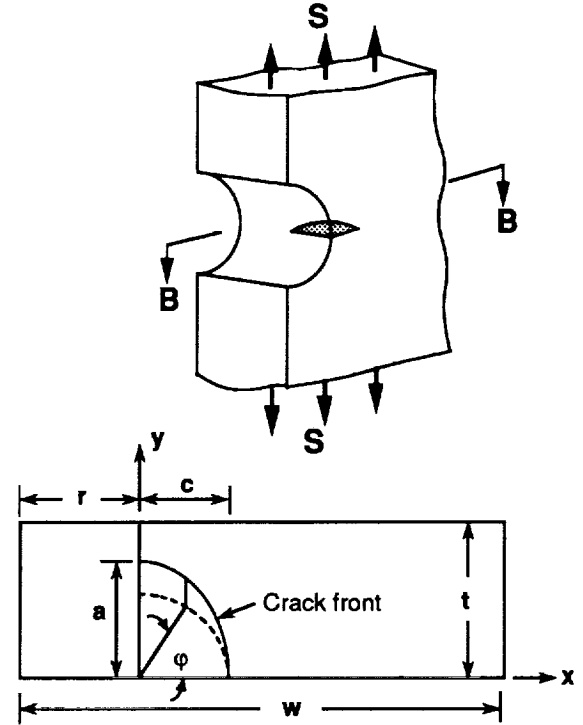
(b) Corner crack (B-B).

Figure A1. Specimen configurations and nomenclature for surface and corner crack at notch.

of a meshing problem. Results reported in ref. 81 for $a/c = 2$ were developed from a different mesh and method. These results are shown in fig. 19(d) and they compare very well with the weight-function results.)

Two specimen configurations with $r/t = 1$ and 3 were chosen for the study. Both specimens had a semicircular ($a/c = 1$) surface crack with $a/t = 0.2$. Figure A2 shows a typical finite-element model (model B) without the ill-shaped elements. These elements were avoided by use of an offset where the crack front intersected the hole or notch boundary. (See ref. 81.) Because the specimen was symmetrical, only one-quarter was modeled. The model shown in figure A2 has eight wedges on the crack plane and four layers on the hole. Pentahedral singularity elements were used along the crack front and eight-noded hexahedral elements were used elsewhere. The final models used in the analysis had 14 wedges on the crack plane and 10 layers on the hole. These models had about 15 000 DOF. The finite-element models were subjected to remote uniform stress. Stress intensity factors were calculated with the nodal-force method. Details of the formulation of these types of elements and the nodal-force method are given in reference 34 and are not repeated here. Details on the

development of the new finite-element models used here are given in reference 81.

Two methods for extracting stress intensity factors from the solutions were also studied: the nodal-force method (refs. 33 and 34) and the VCCT. (See ref. 37.) The nodal-force method was used in conjunction with models A and B and the VCCT was used in conjunction with model C. Note that the nodal-force method does not require an assumption of either plane stress or plane strain to extract the stress intensity factors. However, the VCCT method doeś need that assumption. The plane-strain assumption was used everywhere along the crack front except where the crack meets the notch surface ($\varphi = 90°$); at this location, a plane-stress condition was used. These types of plane-stress and plane-strain assumptions along the crack front are widely used in the literature.

Figure A3 presents the normalized stress intensity factor (or boundary-correction factor) distributions along the crack front ($a/c = 1$, $a/t = 0.2$, and $r/t = 1$) from all three models. Model A, with the ill-shaped elements (circular symbols), gave stress intensity factors that were significantly lower than the results from the other models, especially for $\varphi > 60°$. The results from models B and C agreed well for most

65
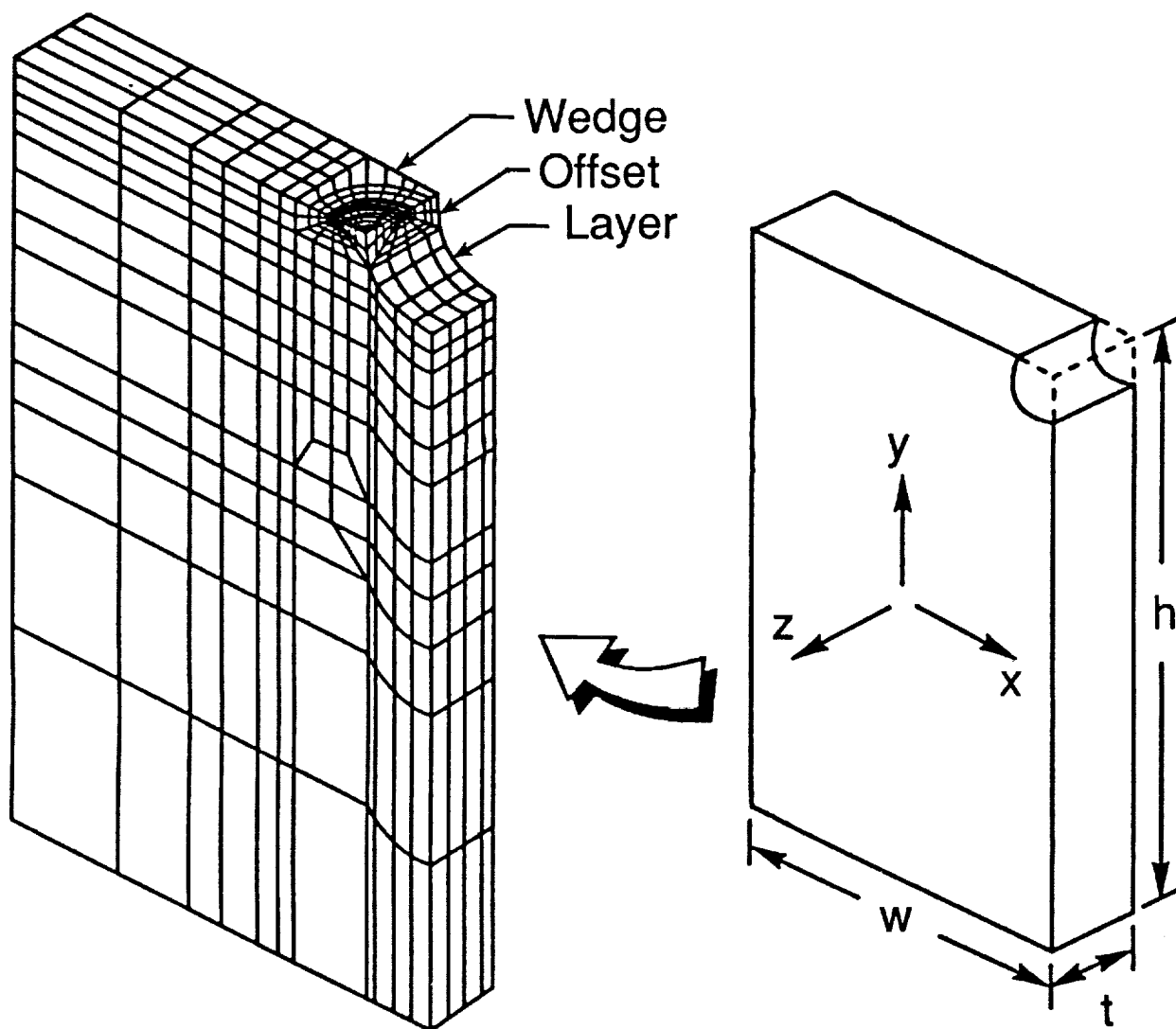
Figure A2. Typical finite-element idealization for surface and corner cracks at notch configuration.

of the crack front. Some slight discrepancy (about 2 percent) was observed for $\varphi > 80°$. The model with the ill-shaped elements was too stiff and gave lower stress intensity factors than models without these elements. The solid curve is an empirical equation for a surface crack at an edge notch that was based on previous finite-element results for surface cracks at holes and on engineering judgment. (See ref. 30.) Comparison with present finite-element results suggests that the equation is fairly accurate (within 5 percent) for this crack configuration.

Figure A4 presents the normalized stress intensity factors for the same crack shape and size as in figure A3 but for a larger notch-to-plate-thickness ratio $(r/t = 3)$. The nodal-force results from model B (without ill-shaped elements) agreed well with results from model C with the VCCT. The maximum difference between the two sets of results was ±1.5 percent.

Again, the solid curve is the stress intensity factors calculated from the empirical equation. (See ref. 30.) Here, the equation consistently underestimated the stress intensity factors (6 to 12 percent). Therefore, the equations for surface and corner cracks emanating from the semicircular edge notch were modified. (See appendix D.)

Recall that the nodal-force method was used to extract the stress intensity factors from the models with and without the ill-shaped elements (models A and B, respectively). The VCCT was used in conjunction with model C. All models without the ill-shaped elements showed nearly the same stress intensity factors along the crack front. This agreement demonstrates that the two methods of extracting stress intensity factors are reliable, provided that the models have appropriate elements.
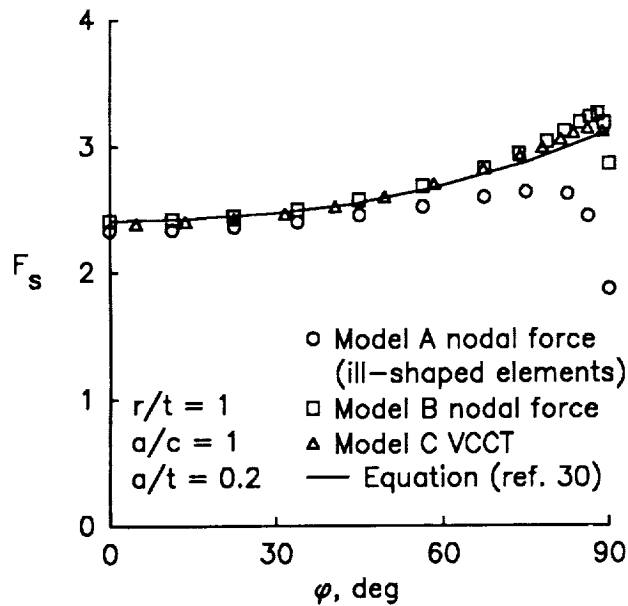
Figure A3. Boundary-correction factors for a surface crack at notch by various methods and models for $r/t = 1$.
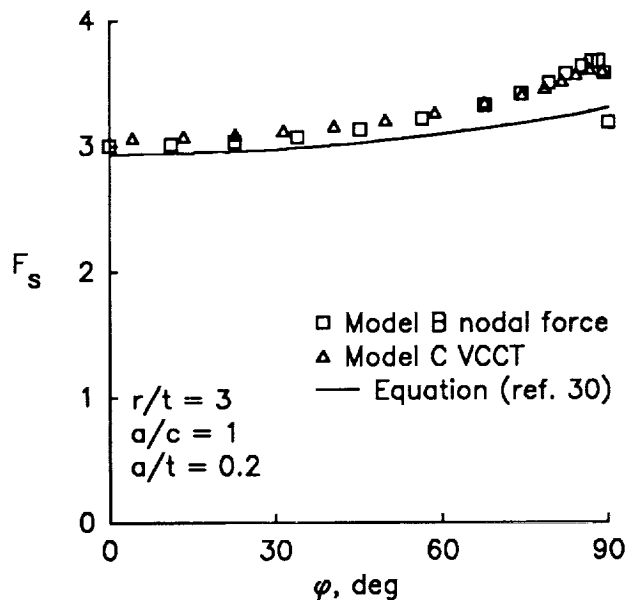
Figure A4. Boundary-correction factors for a surface crack at notch by various methods and models for $r/t = 3$.

Nonsingularity Elements and EDI Method

The method used by Raju and Newman (refs. 33 and 34) requires that singularity elements be used around the crack front and that the finite-element patterns be generated on orthogonal lines in the crack-front region. These requirements cause difficulty in developing models for large a/c cracks. To overcome these difficulties, the 3D finite-element pro-
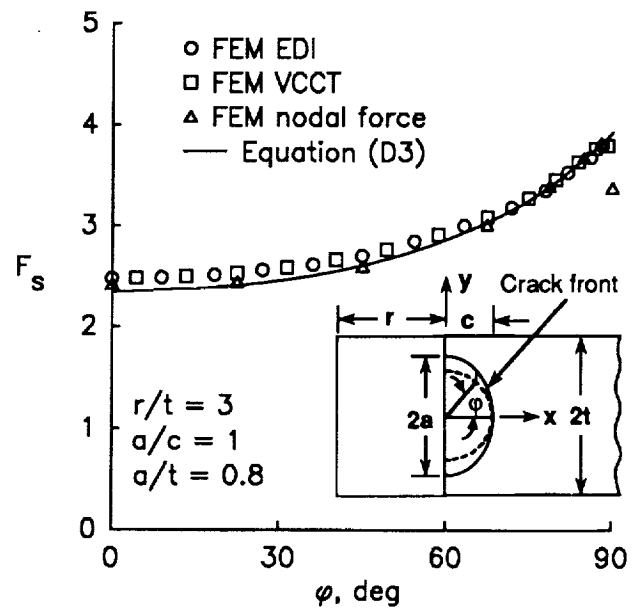
Figure A5. Boundary-correction factors for deep surface crack at notch by various methods.

gram ZIP3D (ref. 35) was developed and used in conjunction with the EDI method (ref. 36) to calculate stress intensity factors for large a/c surface and corner cracks at the semicircular edge notch. The EDI method is an extension of the well-known 2D J-integral method to 3D problems. The resulting surface integral is converted into a volume integral through an application of the divergence theorem and the use of an s-function suggested by DeLorenzi in reference 82. An advantage of the EDI method is that singularity elements are not needed and that the finite-element patterns need not be orthogonal at or near the crack front. (See ref. 83.)

To verify the models and EDI method, figure A5 shows the distribution of stress intensity boundary-correction factors along the crack front for a deep, semicircular, surface crack ($a/c = 1$, $a/t = 0.8$, and $r/t = 3$) by various models and methods. The circular symbols are from the EDI method. The square and triangular symbols show results from the nodal-force and VCCT methods, respectively. The finite-element models used in reference 81 and in the present analysis had orthogonal mesh patterns along the crack front. Thus, the VCCT and nodal-force methods should give accurate solutions. Results from all three methods agreed well (within 3 percent) all along the crack front except very near $\varphi = 90°$. The disagreement among the three methods here is mainly due to the free-surface boundary layer effect. (See ref. 79.) The peak values near the free surface are considered appropriate values for crack-growth studies. Equations were developed

67

to fit these and other results for surface cracks at the notch. The solid curve shows the equation for the boundary-correction factors developed in appendix D. The equation fits the finite-element results very well near the free surface and the equation is about 3 percent lower than the EDI results at maximum depth ($\varphi = 0°$) location.

Results and Discussion

The 3D FEM developed by Raju and Newman (refs. 33 and 34) and the newly developed mesh generator scheme (ref. 81) were used to calculate the mode I stress intensity factor variations along the crack front for a surface and corner crack ($a/c \leq 1$) emanating from a semicircular edge notch in a plate subjected to tensile loading. (See fig. A1.) For cracks with $a/c = 2$, the finite-element program (nonsingular elements) developed by Shivakumar and Newman (ref. 35) and the EDI method (ref. 36) were used. The details of these analyses are given in references 81 and 84 for $a/c \leq 1$ and in reference 85 for $a/c = 2$. In all of these analyses, Poisson's ratio was assumed to be 0.3.

A surface crack that emanates from the center and a corner crack that emanates from the edge of the semicircular edge notch in a plate subjected to tensile loading were considered herein. A range of crack sizes and shapes were analyzed for $r/t = 1$ to 3 for surface cracks and $r/t = 1.5$ for corner cracks. Note that the configuration for $r/t = 3$ corresponds to a small-crack specimen with a surface crack that was used in two AGARD studies (refs. 19 and 20) and in the cooperative program. The ranges of configuration parameters were $a/t = 0.2$, 0.5, and 0.8; and $a/c = 0.4$, 1, and 2. For each of these combinations, stress intensity factors were obtained all along the crack front. The normalized stress intensity factors obtained with the 3D finite-element analyses are presented in tables AI–AIV.

Table AI. Boundary-Correction Factors From FEM for Semielliptical Surface Crack
Emanating From Center of Semicircular Notch in Plate in Tension With $r/t = 1$

$$\left[F_{\mathrm{s}} = \frac{K}{S\left(\frac{\pi a}{Q}\right)^{1/2}} \right]$$

a/c	φ, deg	a/t		
		0.2	0.5	0.8
[a]0.4	0	1.113	0.869	0.833
	22.5	1.284	.997	.967
	45.0	1.678	1.296	1.274
	67.5	2.190	1.733	1.774
	78.8	2.567	2.129	2.232
	84.9	2.809	2.445	2.631
	88.0	2.938	2.655	2.951
	90.0	2.727	2.548	2.944
[a]1.0	0	2.402	1.865	1.697
	22.5	2.442	1.904	1.716
	45.0	2.574	2.046	1.841
	67.5	2.826	2.355	2.211
	78.8	3.043	2.646	2.599
	84.9	3.192	2.858	2.898
	88.0	3.263	2.975	3.089
	90.0	2.858	2.656	2.826
[b]2.0	3.0	2.007	1.647	1.474
	9.0	2.003	1.640	1.471
	18.0	1.997	1.627	1.466
	27.0	1.970	1.605	1.457
	36.0	1.920	1.582	1.449
	45.0	1.839	1.561	1.445
	54.0	1.830	1.558	1.452
	63.0	1.776	1.563	1.475
	72.0	1.744	1.576	1.503
	78.0	1.739	1.596	1.546
	82.0	1.751	1.625	1.602
	88.0	1.854	1.737	1.736
	89.3	1.900	1.827	1.808

[a]Nodal-force method (ref. 81).
[b]Equivalent-domain integral method (ref. 85).

Table AII. Boundary-Correction Factors From FEM for Semielliptical Surface Crack
Emanating From Center of Semicircular Notch in Plate in Tension With $r/t = 2$

$$\left[F_{\text{s}} = \frac{K}{S\left(\frac{\pi a}{Q}\right)^{1/2}} \right]$$

a/c	φ, deg	a/t		
		0.2	0.5	0.8
[a]0.4	0	1.405	1.081	0.989
	22.5	1.613	1.245	1.156
	45.0	2.070	1.634	1.553
	67.5	2.596	2.174	2.207
	78.8	2.943	2.595	2.764
	84.9	3.151	2.880	3.182
	88.0	3.252	3.044	3.469
	90.0	2.982	2.844	3.347
[a]1.0	0	2.789	2.316	2.128
	22.5	2.822	2.357	2.152
	45.0	2.929	2.497	2.303
	67.5	3.138	2.780	2.715
	78.8	3.323	3.028	3.105
	84.9	3.454	3.201	3.378
	88.0	3.509	3.285	3.533
	90.0	3.052	2.885	3.161
[b]2.0	3.0	2.189	1.943	1.817
	9.0	2.180	1.926	1.811
	18.0	2.152	1.914	1.799
	27.0	2.124	1.905	1.784
	36.0	2.074	1.871	1.761
	45.0	2.026	1.816	1.746
	54.0	1.986	1.791	1.726
	63.0	1.908	1.764	1.711
	72.0	1.835	1.746	1.721
	78.0	1.830	1.747	1.746
	82.0	1.865	1.770	1.792
	88.0	1.953	1.866	1.904
	89.3	2.000	1.946	1.979

[a]Nodal-force method (ref. 81).
[b]Equivalent-domain integral method (ref. 85).

Table AIII. Boundary-Correction Factors From FEM for Semielliptical Surface Crack Emanating From Center of Semicircular Notch in Plate in Tension With $r/t = 3$

$$\left[F_{\mathrm{s}} = \frac{K}{S\left(\frac{\pi a}{Q}\right)^{1/2}} \right]$$

a/c	φ, deg	a/t		
		0.2	0.5	0.8
[a]0.4	0	1.603	1.253	1.131
	22.5	1.831	1.442	1.325
	45.0	2.318	1.882	1.788
	67.5	2.839	2.460	2.534
	78.8	3.167	2.878	3.135
	84.9	3.361	3.145	3.559
	88.0	3.452	3.290	3.834
	90.0	3.151	3.044	3.655
[a]1.0	0	3.017	2.592	2.429
	22.5	3.045	2.630	2.454
	45.0	3.138	2.761	2.610
	67.5	3.328	3.022	3.032
	78.8	3.503	3.251	3.421
	84.9	3.629	3.411	3.685
	88.0	3.679	3.482	3.829
	90.0	3.192	3.040	3.398
[b]2.0	3.0	2.300	2.125	2.028
	9.0	2.295	2.121	2.021
	18.0	2.263	2.104	2.006
	27.0	2.207	2.072	1.983
	36.0	2.143	2.023	1.958
	45.0	2.086	1.973	1.928
	54.0	1.967	1.924	1.902
	63.0	1.913	1.864	1.865
	72.0	1.866	1.836	1.849
	78.0	1.847	1.815	1.852
	82.0	1.872	1.822	1.873
	88.0	1.949	1.881	1.962
	89.3	2.023	1.964	2.026

[a]Nodal-force method (ref. 81).
[b]Equivalent-domain integral method (ref. 85).

Table AIV. Boundary-Correction Factors From FEM for Quarter-Elliptical Corner Crack Emanating From Edge of Semicircular Notch in Plate in Tension With $r/t = 1.5$

$$\left[F_s = \frac{K}{S\left(\frac{\pi a}{Q}\right)^{1/2}} \right]$$

a/c	φ, deg	a/t		
		0.2	0.5	0.8
[a]0.4	0	1.553	1.459	1.736
	11.25	1.551	1.433	1.659
	22.5	1.668	1.508	1.666
	45.0	2.091	1.831	1.839
	67.5	2.634	2.352	2.392
	78.8	2.982	2.773	2.877
	84.9	3.172	3.059	3.292
	88.0	3.251	3.219	3.600
	90.0	2.977	3.009	3.491
[a]1.0	0	2.924	2.521	2.585
	11.25	2.861	2.449	2.465
	22.5	2.796	2.370	2.291
	45.0	2.825	2.395	2.166
	67.5	3.044	2.685	2.548
	78.8	3.251	2.965	2.961
	84.9	3.395	3.163	3.259
	88.0	3.456	3.263	3.429
	90.0	3.040	2.902	3.122
[b]2.0	3.0	2.128	1.932	1.852
	9.0	2.080	1.896	1.813
	18.0	2.037	1.866	1.764
	27.0	1.993	1.819	1.710
	36.0	1.956	1.783	1.672
	45.0	1.906	1.744	1.645
	54.0	1.851	1.719	1.613
	63.0	1.810	1.696	1.605
	72.0	1.795	1.686	1.611
	78.0	1.772	1.693	1.643
	82.0	1.804	1.708	1.689
	88.0	1.879	1.824	1.804
	89.3	1.945	1.910	1.876

[a]Nodal-force method (ref. 84).
[b]Equivalent-domain integral method (ref. 85).

Appendix B

Three-Dimensional Weight-Function Analyses of Surface and Corner Cracks at Semicircular Notch

In the following sections, the 3D WFM is briefly described for solving general 3D crack configurations. The method was used to determine the stress intensity factor distribution for a range of surface- and corner-crack configurations at a semicircular edge notch in a plate subjected to remote tensile loading.

Three-Dimensional Weight-Function Method

The 3D WFM that was developed in references 39 and 40 was based on a combination of the slice-synthesis procedure (refs. 41–43) and the general expressions for 2D weight functions. (See refs. 44–46.) In the 3D weight-function analysis, the actual cracked part is discretized into two sets of orthogonal slices of infinitesimal thickness parallel to the major and minor axes. The two sets of 2D slices with through-the-thickness cracks are analyzed with the 2D WFM. Reference 47 gives detailed information on the 2D weight-function approach, together with numerous stress intensity factor solutions. The coupling between the two sets of slices is accounted for by some unknown spring forces, which are determined through the condition of compatibility of the 2D crack-opening displacements at the slice intersections. To calculate 2D crack-opening displacements, 2D weight functions are again used. After the spring forces are determined, stress intensity factors are established for the two sets of slices. Finally, the stress intensity factors for the actual 3D crack configuration at any point along the crack front are obtained based on a general relation between the 2D and 3D stress intensity factors.

From the previous discussion, the key element in the analysis is clearly the 2D weight function for the slices. The 2D weight functions have been extensively studied and their application to the present 3D crack configurations need modification because the remaining area outside the sliced region will exert restraint on the discretized slices. The basic idea used to account for this effect is to transform the restraint based on the uncracked part of a 3D cracked body into a kind of elastic boundary condition on the 2D slices. Thus, some 3D nature is built into these slices. The modified 2D weight functions for the slices are constructed based on existing 2D weight functions. (See refs. 44–47.) The modification that reflects the
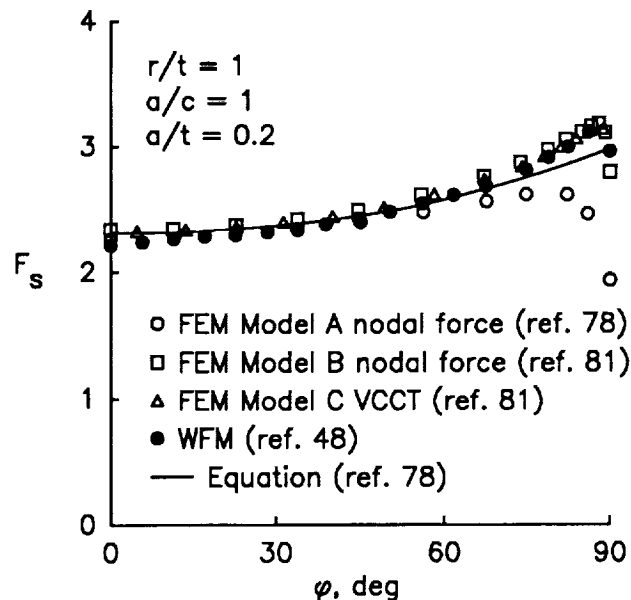
Figure B1. Stress intensity boundary-correction factors for surface crack at circular hole in plate subjected to remote tension.

restraint, which is characterized by a nondimensional restraint area R_i ($i = a$ or c), is made by an interpolation of two limiting cases of 2D weight functions—one for zero constraint ($R_i = 0$), the other for fixed constraint ($R_i = \infty$). For an infinite, semi-infinite, or quarter-infinite body where R_i tends to infinity, the 2D weight functions with fixed boundary conditions are directly applied and no modifications are needed. For a finite body, however, a reference 3D stress intensity factor solution is needed to determine an unknown interpolation parameter in the modified weight function for the slices. Details of the 3D WFM are presented herein and the related 2D weight functions are discussed in appendix C.

The 3D WFM has been applied to embedded elliptical cracks in plates (refs. 39 and 40); semi-elliptical surface cracks in plates (ref. 40) or at circular holes (ref. 48); and quarter-elliptical corner cracks in plates (ref. 40), at a notch (ref. 50), or at a circular hole (ref. 86) subjected to mode I loading. Of interest to the present investigation are the results for surface and corner cracks at holes. Typical comparisons among the WFM, FEM, and empirical equations are shown in figures B1 and B2. Figure B1 shows results for a shallow surface crack ($a/t = 0.2$) in a hole with $r/t = 1$. The solid symbols show the WFM results. (See ref. 48.) The open symbols show finite-element results obtained from three different models and two extraction methods (nodal force and VCCT). These models and methods are discussed in

73
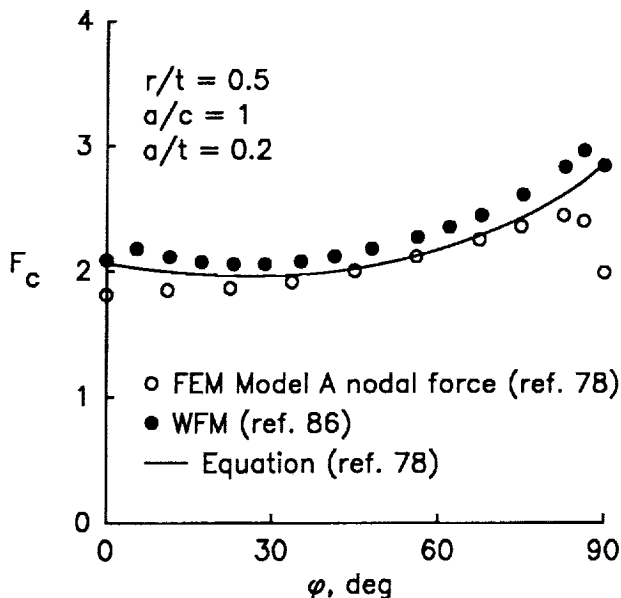
Figure B2. Stress intensity boundary-correction factors for corner crack at circular hole in plate subjected to remote tension.

appendix A. (See fig. A3.) The curve is an empirical equation developed to fit previous finite-element results. (See ref. 78.) All analyses and the equation agreed within 3 percent for parametric angles less than about 60°. Near the hole surface ($\varphi > 60°$), the WFM and FEM results also agreed well with those from models B and C. However, the FEM results from model A (using ill-shaped elements, see appendix A) did not agree with the other results. The equation that was fit to model A results in the interior is about 5 percent too low near the hole surface based on the new results.

Comparisons for a corner crack at a hole are shown in figure B2. Here, the WFM and FEM results did not agree, the results showing 5 to 20 percent differences. As discussed in appendix A, the FEM results (model A) were based on models that had some ill-shaped elements near the intersection of the crack front with the hole surface. Thus, the FEM results are expected to be lower than the true solution for $\varphi > 60°$. However, the WFM is expected to give higher stress intensity factors than the true solution because through-the-thickness variations in the normal stresses were not considered. In the current 3D WFM, a 2D stress distribution was assumed in the analysis; however, this assumption will cause an overestimation in stress intensity factors for small corner cracks. But the empirical equation (fit to model A FEM results in the interior) is expected to be accurate for this configuration.

The 3D WFM can be used to compute stress intensity factors for part-through cracks in arbitrary stress fields, which may vary in both plate thickness and width directions. This variance is actually the case for the normal stress distributions at stress concentrations even when the body is subjected to remote uniform tension, as shown by the 3D stress analysis results in figure 14. (See ref. 38.) The through-the-thickness variation depends upon r/t. This variation is the strongest at the hole or notch root and gradually disappears as x/r increases. The variation does not affect the 3D weight function itself for large R_i values (when no calibration is needed), but it will affect the resulting stress intensity factors through the crack-face loading. In the present analyses, the crack-face loading was taken from the 2D stress distribution, which assumed that the normal stress distribution around the notch root was uniform through the thickness. The 2D assumption was justified for the SENT specimens used in the cooperative study ($r/t = 3$) because through-the-thickness variations in normal stresses are small, as shown in figure 14. This small variance is especially true for a semielliptical surface crack in the middle of the plate thickness. For corner cracks, however, some overestimation is expected for small values of a/t because the actual stresses are several percent lower than the assumed 2D stress distribution.

Modeling and Weight Functions

The crack configurations analyzed for the cooperative program are shown in figures B3(a) and B3(b) for surface and corner cracks, respectively. Because the corner-crack configuration was analyzed in a similar manner as that for surface cracks, only the modeling of the surface-crack configuration is described herein. The detailed analyses of these crack configurations are given in reference 49 for surface cracks and in reference 50 for corner cracks.

The present method idealizes the cracked body as two series of orthogonal slices of infinitesimal thickness in the y-z, or x-z plane within the major or minor axis of the semielliptical crack, respectively, as shown in figures B4(a)–B4(d). Each slice is in a generalized plane-stress state. One family of slices, for example the a slices (slices parallel to the a axis of the semiellipse with a half-crack length of a_x), is set as the basic slices. The other slices, the c slices (slices parallel to the c axis of the semiellipse with a half-crack length of c_y), are set as the spring slices. The crack lengths for the slices are given by

$$a_x = a\sqrt{1 - \left(\frac{x}{c}\right)^2} \qquad \text{(B1a)}$$

74
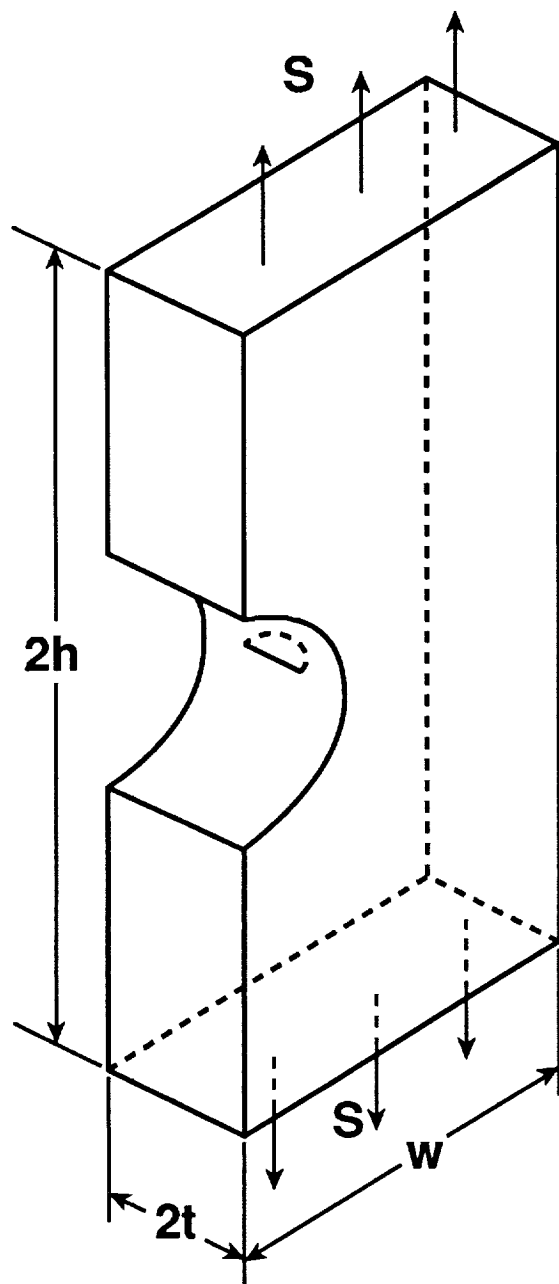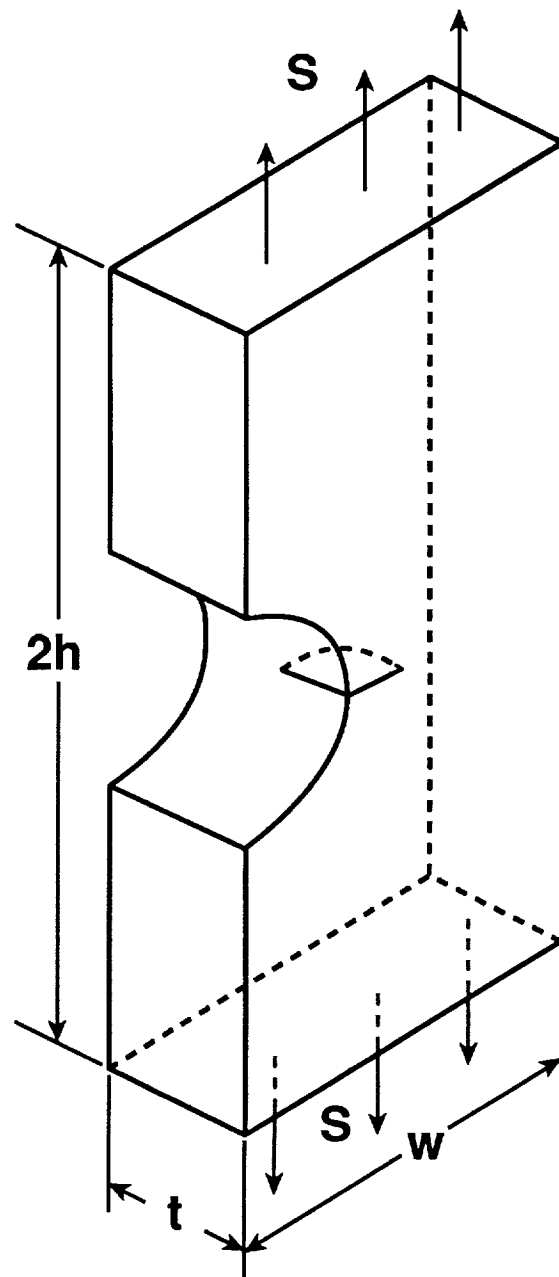
(a) Surface crack.   (b) Corner crack.

Figure B3. Surface and corner cracks at semicircular notch subjected to remote tension.

$$c_y = c\sqrt{1 - \left(\frac{y}{a}\right)^2} \qquad \text{(B1b)}$$

The basic slices shown in figure B4(c), which have the same elastic constants as the material of the plate, are subjected to S as well as $P(x,y)$ distributed along the crack face. The spring force represents the mechanical coupling between the adjacent basic slices because shear stress acts on the surfaces of the slices toward the z-axis. The springs with stiffness k_a

on both sides of each basic slice simulate the effect of the restraint from R_a, the uncracked area outside the region occupied by the basic slices and the notch. (See fig. B4(a).)

The spring slices, figure B4(d), which have the same Poisson's ratio as the material of the plate but a different elastic modulus, undergo only the spring force on the crack face with the same magnitude as but in opposite direction of those on the basic slices.

Figure B4. Slice model for surface crack at notch. Basic slices: (a), (c), (e), and (g); spring slices: (b), (d), (f), and (h).

The springs with stiffness k_c on the side of the spring slices toward which the crack extends all simulate the effect of the restraint from R_c, the uncracked area outside the region occupied by the spring slices and the notch. (See fig. B4(b).)

The corresponding slice model for the corner-crack configuration is shown in figure B5. The restraining areas shown in figures B4(a) and B4(b) were expressed in a nondimensional form as follows:

$$R_a = 2\frac{a}{c}\left(\frac{w}{c} - \frac{r}{c} - 1\right)\frac{t}{a} \qquad \text{(B2a)}$$

$$R_c = 2\frac{a}{c}\left(\frac{w}{c} - \frac{r}{c}\right)\left(\frac{t}{a} - 1\right) \qquad \text{(B2b)}$$

The nondimensional restraining areas in equations (B2a) and (B2b), R_i ($i = a$ or c), vary from zero to infinity as functions of a/c, a/t, c/w, and r/t. The stiffness k_i ($i = a$ or c) of the springs on the sides of the slices shown in figures B4(c) and B4(d) is a function of restraining area. When R_i tends to zero, k_i also tends to zero, which results in the cases shown in figures B4(e) and B4(f) for the example with a free center crack and a single-edge-notch-crack. When R_i tends to infinity, so does k_i. This case is shown in figures B4(g) and B4(h) for the example with the collinear center cracks and double-edge-notch cracks. These limiting conditions serve as the upper and lower bounds of the weight functions for the slices with a 3D nature. Thus, the weight functions W_i for the slices with elastic constraints shown in figures B4(c) and B4(d) are constructed as follows:

$$W_a = W_{\text{collinear}} + T_a(R_a)\left(W_{\text{free}} - W_{\text{collinear}}\right) \qquad \text{(B3a)}$$

$$W_c = W_{\text{double}} + T_c(R_c)\left(W_{\text{single}} - W_{\text{double}}\right) \qquad \text{(B3b)}$$

where $T_i(R_i)$ is the transition factor ($i = a$ or c) and represents the transition from fixed to free boundary conditions. The transition factor is an unknown function of restraining areas that satisfy the conditions $T_i(0) = 1$ and $T_i(\infty) = 0$.

Note that for the SENT specimens with $r/w = 1/16$, the nondimensional restraint factor R_i has large values when the surface or corner cracks are small. Thus, the 3D weight function in the present analysis has been limited to $a/t \leq 0.5$ and, thus, no reference 3D solution is needed.

Herein, only the semi-infinite width plate is considered—that is, $r/w = 0$. In this case, $R_i = \infty$ and equations (B3a) and (B3b) reduce to

$$W_a = W_{\text{collinear}} \qquad \text{(B4a)}$$

$$W_c = W_{\text{double}} \qquad \text{(B4b)}$$

with $W_{\text{double}} = W_{\text{single}}$. Now that the center-crack weight functions are replaced by those for edge cracks, the parallel relations for the corner-crack configuration are also obtained. These weight functions are available from previous work (refs. 44 and 45) with the function f_0 for the c slices replaced by the function $f(\alpha)$ for an edge crack emanating from a semicircular notch with $r/w = 1/16$. The function $f(\alpha)$ was obtained by substituting $\sigma(\xi)/S = 1$ into equation (C10). (See appendix C.) The numerical results were then fitted to the following polynomial for $f(\alpha)$ as

$$f(\alpha) = 1.121 - 0.711\alpha + 1.6\alpha^2 - 1.461\alpha^3 + 0.508\alpha^4 \qquad \text{(B5)}$$

where $\alpha = c/r$ for $\alpha \leq 1$.

Solution Procedures

After the weight functions were found, stress intensity factors for the slices were obtained according to weight-function theory (refs. 44, 87, and 88) as follows:

$$K_a(a_x) = \int_0^{a_x} [\sigma(x,y) - P(x,y)]\, W_a(R_a, a_x, y)\, dy \qquad \text{(B6a)}$$

$$K_c(c_y) = \int_0^{c_y} P(x,y)\, W_c(R_c, c_y, x)\, dx \qquad \text{(B6b)}$$

where $\sigma(x,y)$ is the stress distribution induced by the applied load along the location of the crack in the crack-free body. For this particular configuration, the stress distribution was obtained by fitting to Tan's 2D numerical solution (ref. 26) for a semicircular notch in a plate in remote tension. (See appendix C.) The resultant polynomial was

$$\sigma(\xi) = S\left(3.157 - 6.731\xi + 11.709\xi^2 - 10.687\xi^3 + 3.838\xi^4\right) \qquad \text{(B7)}$$

where $\xi = x/r$. (Note that the origin of the coordinate system is at the center of the crack for both the surface and corner crack.) In the WFM, the normal stress distribution was assumed uniform through the thickness—that is, $\sigma(x,y) = \sigma(\xi)$. This assumption is adequate for the r/t considered in the cooperative program because the 3D variation through the thickness is about ± 3 percent. (See ref. 38.) With the weight functions and stress intensity factors available, the crack-face displacements for the slices were determined using procedures in references 32 and 89. The crack-face displacements for these two series of slices should be equal to satisfy compatibility. This condition leads to an integral equation in terms of
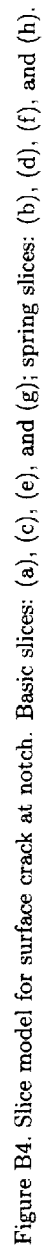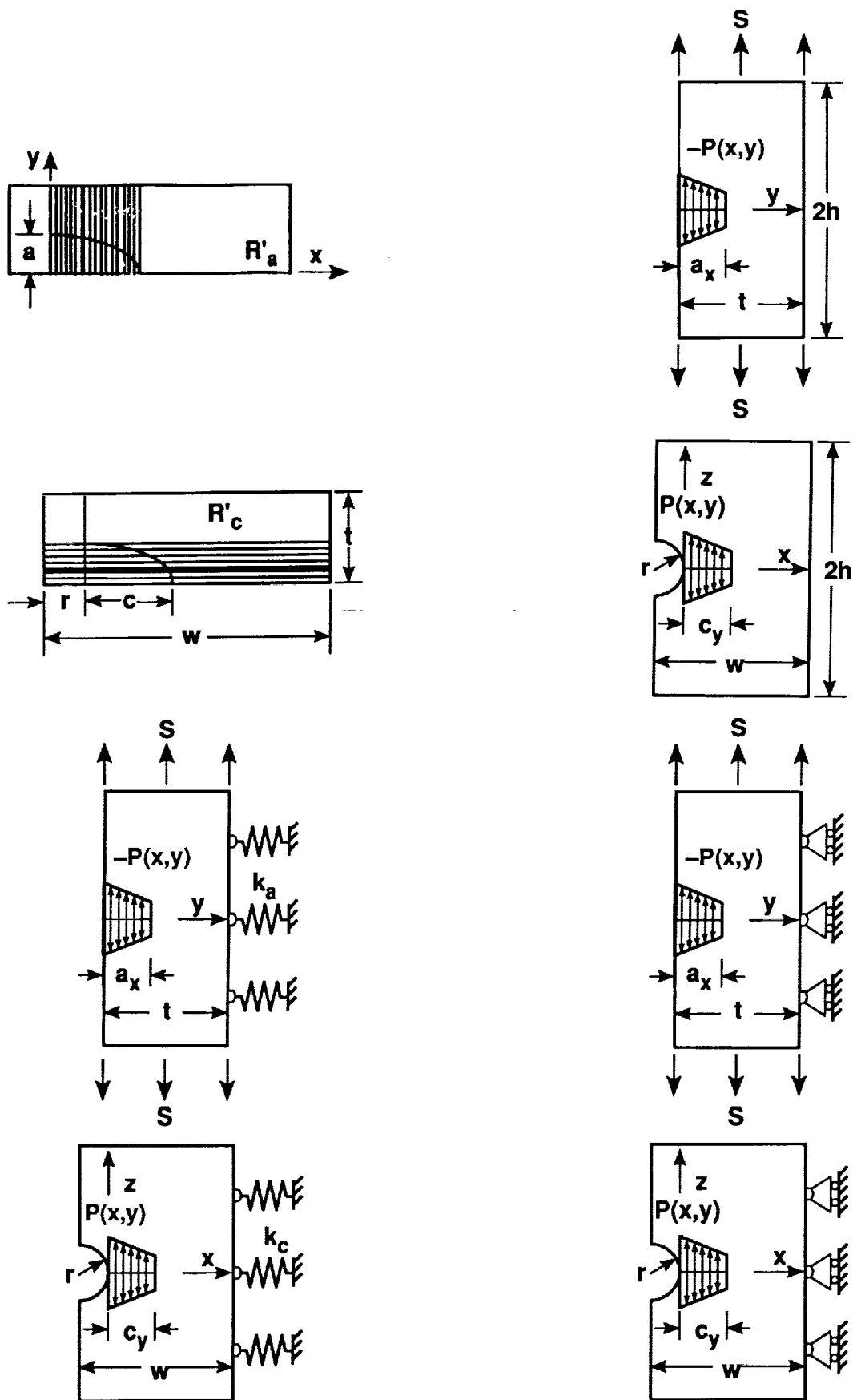
Figure B5. Slice model for corner crack at notch. Basic slices: (a), (c), (e), and (g); spring slices: (b), (d), (f), and (h).
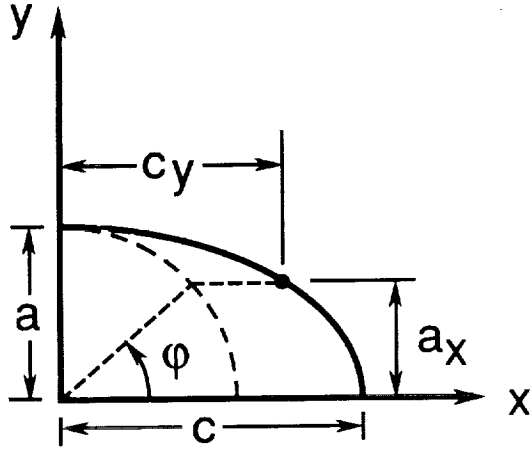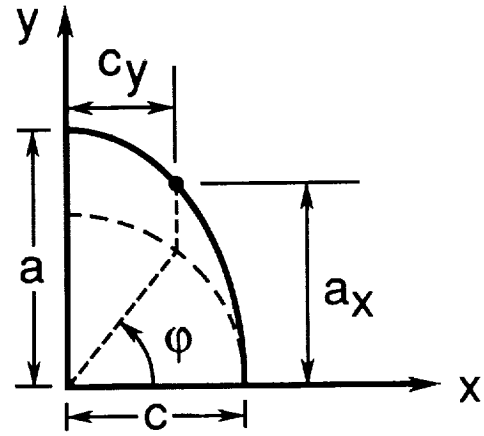
(a) $a/c \leq 1$. (b) $a/c > 1$.

Figure B6. Definition of φ and crack length for slices.

the unknown spring force on the crack faces. The integral equations were reduced to multiple linear equations by expression of the spring force as a special kind of polynomial with unknown coefficients as

$$P(x,y) = \sigma_j \left[\alpha_1 + \alpha_2 \left(\frac{x}{c}\right)^{1/3} + \alpha_3 \left(\frac{y}{a}\right)^{1/3} \right.$$
$$+ \alpha_4 \left(\frac{x}{c}\right)^{1/3} \left(\frac{y}{a}\right)^{1/3} + \alpha_5 \left(\frac{x}{c}\right) + \alpha_6 \left(\frac{y}{a}\right)$$
$$+ \alpha_7 \left(\frac{x}{c}\right) \left(\frac{y}{a}\right) + \alpha_8 \left(\frac{x}{c}\right)^2 + \alpha_9 \left(\frac{y}{a}\right)^2$$
$$+ \alpha_{10} \left(\frac{x}{c}\right)^2 \left(\frac{y}{a}\right)^2 + \alpha_{11} \left(\frac{x}{c}\right)^3 + \alpha_{12} \left(\frac{y}{a}\right)^3$$
$$\left. + \alpha_{13} \left(\frac{x}{c}\right)^4 + \alpha_{14} \left(\frac{y}{a}\right)^4 \right] \tag{B8}$$

where σ_j is a known reference stress and α_i are unknown coefficients. Substituting equation (B8) into equations (B6a) and (B6b) gives multiple linear equations. These equations were solved by a regression scheme to determine the values of α_i. (See refs. 39, 40, 49, and 50 for details.)

Now that the spring force has been determined, the stress intensity factors for the slices were obtained from equations (B6a) and (B6b). Then the stress intensity factor at φ (fig. B6) for a semi-elliptical surface crack or for a quarter-elliptical corner crack was obtained from the following equation derived in references 39 and 40:

$$K(\varphi) = \left\{ K_a^4(a_x) + \left[K_c(c_y)\frac{E}{E_s} \right]^4 \right\}^{1/4} \frac{(-1)^m}{1 - \eta^2} \tag{B9}$$

where $m = 1$ for $K_a \leq 0$ and $K_c \leq 0$, $m = 2$ for $K_a > 0$ and $K_c > 0$; $\eta = \nu$ for $\varphi < 90°$, $\eta = 0°$

for $\varphi = 90°$ for the surface crack; and $\eta = \nu$ for $0° < \varphi < 90°$, $\eta = 0°$ for $\varphi = 0°$ and $90°$ for the corner crack.

Finite-Width Effect

The weight functions previously obtained were for a plate of semi-infinite width $r/w = 0$. For a finite-width plate, a nonvanishing transition factor should generally be used in the weight-function expressions. (See eqs. (B3a) and (B3b).) The determination of the transition factor requires a 3D reference solution for the finite-width plate. For the surface- and corner-crack specimens considered in the cooperative program, $r/w = 1/16$. However, the effect of the transition factor on stress intensity factors for surface-crack configurations considered herein is small based on experience with embedded elliptical cracks for which the transition factor is known. (See refs. 39 and 40.) Thus, the effect of the transition factor was neglected. The effect of the transition factor on stress intensity factors for corner cracks was also neglected based on experience with other corner-crack configurations. However, for deep, low a/c corner cracks, some differences may be observed. For example, for the case of $a/c = 0.4$ with $a/t = 0.5$, stress intensity factors determined by the WFM for $r/w = 0$ are estimated to be about 6 percent lower than those for a plate with $r/w = 1/16$.

Results and Discussion

Application of the WFM (refs. 39, 40, and 48) has shown that for an embedded elliptical crack in an infinite solid, the WFM reproduced the exact solutions (ref. 90) for stress intensity factors and crack-face displacements for the uniform crack-face

79
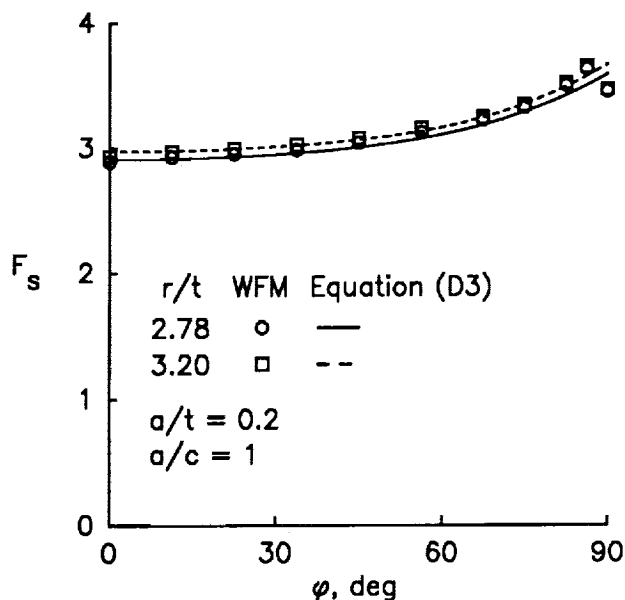
Figure B7. Stress intensity boundary-correction factors for surface crack at notch in plate subjected to remote tension for two values of r/t.

Figure B8. Stress intensity boundary-correction factors for corner crack at notch in plate subjected to remote tension for two values of r/t.

pressure case. The stress intensity factor solution also agreed within 2 percent of the exact solution for a nonuniform crack-face pressure. (See ref. 91.) For the same crack configurations in finite plates, the weight-function results obtained by the present method agreed well with Newman and Raju's finite-element solutions. (See ref. 78.) For two symmetrical surface cracks at a hole, the weight-function solutions were well within 5 percent of Newman and Raju's finite-element solutions (ref. 78), except in the region near the hole surface and in a few cases at the sharp curvature for low a/c cracks. For a single surface crack at a hole, the agreement between the weight-function results and Grandt's solutions by the finite-element alternating method (ref. 92) was also generally very good.

The WFM was used to calculate the stress intensity factors for semielliptical surface cracks and quarter-elliptical corner cracks at a semicircular notch in a plate subjected to remote tensile loading. These configurations are shown in figures B3(a) and B3(b). Poisson's ratio was assumed to be 0.3. (Note that stress intensity factors determined by the WFM are independent of Poisson's ratio for traction boundary conditions.) For the surface crack, $r/t = 2.78$ and 3.2; for the corner crack, $r/t = 1.39$

and 1.6. These values were selected to match the nominal ones used in the cooperative test program. For each configuration, the crack configurations considered were $a/c = 0.2, 0.4, 1$, and 2 with $a/t = 0.05$, 0.2, and 0.5. The results are given in tables BI–BIV. Typical comparisons for the surface- and corner-crack configurations are given in figures B7 and B8, respectively. These figures show the slight variation caused by the small difference in the r/t values. The curves show results from the stress intensity factor equations that were developed in appendix D. At the intersection of the crack with the notch surface ($\varphi = 90°$), the equation is 2 to 3 percent lower than the WFM solutions. The agreement between the equation and WFM solutions is better away from the free surface.

The WFM is very efficient in modeling and in calculating stress intensity factors. Computations are readily made on a personal computer (PC). The calculation for each set of configuration parameters required less than 3 minutes for each load case on a model 286 PC (with 80287 coprocessor). After the basic displacement information is obtained for a set of configuration parameters for one load case, the stress intensity factors for any other load case for the same configuration may be obtained in a few seconds.

Table BI. Boundary-Correction Factors From WFM for Semielliptical Surface Crack Emanating From Center of Semicircular Notch in Plate in Tension With $r/t = 2.78$

$$\left[F_s = \frac{K}{S \left(\frac{\pi a}{Q} \right)^{1/2}} \right]$$

a/c	φ, deg	a/t		
		0.05	0.2	0.5
0.2	0.1	1.192	0.847	0.629
	11.3	1.419	1.027	.799
	22.5	1.772	1.284	.981
	33.8	2.096	1.550	1.205
	45.0	2.395	1.833	1.469
	56.3	2.660	2.126	1.745
	67.5	2.881	2.422	2.042
	75.0	3.015	2.636	2.303
	82.5	3.170	2.902	2.697
	86.2	3.265	3.062	2.959
	89.9	3.054	2.914	2.919
0.4	0.1	1.844	1.507	1.190
	11.3	1.952	1.611	1.296
	22.5	2.163	1.793	1.440
	33.8	2.399	2.019	1.645
	45.0	2.644	2.276	1.905
	56.3	2.871	2.536	2.189
	67.5	3.056	2.779	2.495
	75.0	3.174	2.946	2.730
	82.5	3.334	3.157	3.026
	86.2	3.444	3.287	3.200
	89.9	3.230	3.106	3.069
1.0	0.1	3.150	2.891	2.534
	11.3	3.182	2.929	2.580
	22.5	3.199	2.954	2.616
	33.8	3.209	2.984	2.678
	45.0	3.240	3.041	2.779
	56.3	3.294	3.125	2.912
	67.5	3.357	3.223	3.075
	75.0	3.432	3.322	3.221
	82.5	3.593	3.499	3.437
	86.2	3.722	3.631	3.580
	89.9	3.531	3.452	3.424
2.0	0.1	2.330	2.229	2.071
	11.3	2.327	2.228	2.075
	22.5	2.287	2.194	2.052
	33.8	2.213	2.131	2.010
	45.0	2.114	2.046	1.951
	56.3	2.004	1.951	1.882
	67.5	1.895	1.857	1.816
	75.0	1.853	1.824	1.801
	82.5	1.887	1.862	1.852
	86.2	1.946	1.922	1.915
	89.9	1.859	1.838	1.837

Table BII. Boundary-Correction Factors From WFM for Semielliptical Surface Crack Emanating From Center of Semicircular Notch in Plate in Tension With $r/t = 3.2$

$$\left[F_s = \frac{K}{S \left(\frac{\pi a}{Q} \right)^{1/2}} \right]$$

a/c	φ, deg	a/t		
		0.05	0.2	0.5
0.2	0.1	1.216	0.887	0.663
	11.3	1.446	1.072	.835
	22.5	1.805	1.341	1.030
	33.8	2.132	1.618	1.263
	45.0	2.430	1.907	1.532
	56.3	2.693	2.202	1.818
	67.5	2.908	2.493	2.128
	75.0	3.036	2.698	2.393
	82.5	3.186	2.950	2.777
	86.2	3.277	3.099	3.025
	89.9	3.063	2.941	2.958
0.4	0.1	1.862	1.556	1.241
	11.3	1.971	1.660	1.347
	22.5	2.183	1.848	1.500
	33.8	2.420	2.077	1.714
	45.0	2.664	2.334	1.981
	56.3	2.889	2.592	2.271
	67.5	3.071	2.828	2.577
	75.0	3.186	2.988	2.806
	82.5	3.345	3.191	3.092
	86.2	3.453	3.318	3.260
	89.9	3.238	3.132	3.117
1.0	0.1	3.163	2.935	2.611
	11.3	3.195	2.971	2.657
	22.5	3.212	2.996	2.693
	33.8	3.220	3.023	2.751
	45.0	3.250	3.077	2.848
	56.3	3.303	3.156	2.977
	67.5	3.364	3.249	3.131
	75.0	3.438	3.344	3.271
	82.5	3.599	3.520	3.482
	86.2	3.728	3.651	3.624
	89.9	3.536	3.470	3.463
2.0	0.1	2.335	2.247	2.109
	11.3	2.332	2.246	2.112
	22.5	2.292	2.211	2.088
	33.8	2.217	2.146	2.042
	45.0	2.117	2.059	1.979
	56.3	2.007	1.961	1.906
	67.5	1.898	1.865	1.835
	75.0	1.855	1.830	1.816
	82.5	1.888	1.868	1.865
	86.2	1.947	1.928	1.928
	89.9	1.860	1.843	1.849

Table BIII. Boundary-Correction Factors From WFM for Quarter-Elliptical Corner Crack Emanating From Edge of Semicircular Notch in Plate in Tension With $r/t = 1.39$

$$\left[F_c = \frac{K}{S\left(\frac{\pi a}{Q}\right)^{1/2}} \right]$$

a/c	φ, deg	a/t		
		0.05	0.2	0.5
0.2	0.1	1.270	0.829	
	5.6	1.349	.901	
	11.3	1.433	.973	
	22.5	1.737	1.154	
	33.8	2.052	1.380	
	45.0	2.362	1.634	
	56.3	2.662	1.900	
	67.5	2.931	2.187	
	82.5	3.319	2.792	
	86.2	3.453	3.023	
	89.9	3.233	2.926	
0.4	0.1	2.019	1.476	1.133
	5.6	2.106	1.548	1.203
	11.3	2.083	1.544	1.221
	22.5	2.220	1.643	1.273
	33.8	2.439	1.831	1.430
	45.0	2.681	2.069	1.644
	56.3	2.927	2.332	1.868
	67.5	3.141	2.608	2.129
	82.5	3.464	3.073	2.697
	86.2	3.589	3.228	2.901
	89.9	3.358	3.067	2.845
1.0	0.1	3.343	2.845	2.296
	5.6	3.517	2.994	2.418
	11.3	3.392	2.896	2.349
	22.5	3.304	2.834	2.299
	33.8	3.276	2.840	2.329
	45.0	3.276	2.885	2.408
	56.3	3.327	2.980	2.539
	67.5	3.406	3.114	2.734
	82.5	3.641	3.417	3.140
	86.2	3.769	3.548	3.281
	89.9	3.560	3.369	3.150
2.0	0.1	2.368	2.165	1.868
	5.6	2.515	2.299	1.984
	11.3	2.427	2.223	1.923
	22.5	2.333	2.144	1.864
	33.8	2.240	2.072	1.822
	45.0	2.121	1.980	1.768
	56.3	2.004	1.890	1.717
	67.5	1.902	1.814	1.683
	82.5	1.888	1.827	1.744
	86.2	1.947	1.887	1.806
	89.9	1.852	1.799	1.730

Table BIV. Boundary-Correction Factors From WFM for Quarter-Elliptical Corner Crack Emanating From Edge of Semicircular Notch in Plate in Tension With $r/t = 1.6$

$$\left[F_{\mathrm{c}} = \frac{K}{S\left(\frac{\pi a}{Q}\right)^{1/2}} \right]$$

a/c	φ, deg	a/t		
		0.05	0.2	0.5
0.2	0.1	1.313	0.870	
	5.6	1.394	.941	
	11.3	1.479	1.013	
	22.5	1.793	1.207	
	33.8	2.113	1.442	
	45.0	2.425	1.703	
	56.3	2.722	1.979	
	67.5	2.982	2.276	
	82.5	3.352	2.866	
	86.2	3.480	3.082	
	89.9	3.253	2.966	
0.4	0.1	2.056	1.538	1.185
	5.6	2.145	1.611	1.255
	11.3	2.120	1.605	1.269
	22.5	2.260	1.711	1.330
	33.8	2.478	1.905	1.491
	45.0	2.720	2.147	1.708
	56.3	2.962	2.412	1.941
	67.5	3.171	2.684	2.214
	82.5	3.486	3.132	2.779
	86.2	3.609	3.283	2.976
	89.9	3.375	3.111	2.897
1.0	0.1	3.370	2.919	2.385
	5.6	3.545	3.072	2.511
	11.3	3.419	2.970	2.438
	22.5	3.329	2.905	2.389
	33.8	3.299	2.907	2.418
	45.0	3.296	2.946	2.496
	56.3	3.345	3.036	2.626
	67.5	3.421	3.162	2.816
	82.5	3.652	3.454	3.207
	86.2	3.780	3.585	3.347
	89.9	3.570	3.401	3.206
2.0	0.1	2.378	2.198	1.925
	5.6	2.525	2.334	2.044
	11.3	2.437	2.256	1.980
	22.5	2.342	2.175	1.919
	33.8	2.248	2.100	1.872
	45.0	2.127	2.004	1.813
	56.3	2.010	1.910	1.755
	67.5	1.906	1.829	1.714
	82.5	1.890	1.838	1.767
	86.2	1.950	1.898	1.829
	89.9	1.854	1.808	1.749

Appendix C

Two-Dimensional Weight-Function and Boundary-Force Analyses

The 2D WFM and the BFM are used to analyze through cracks in arbitrarily shaped bodies for various in-plane loading conditions. Brief descriptions of these methods are given herein. The BFM was used in the cooperative program to analyze a through crack emanating from the semicircular notch of a plate for remote tension. The BFM analysis was made on the SENT specimens for either remote uniform stress or displacement. The BFM was also used to analyze the uncracked SENT specimens to obtain the stress concentration factor and the normal stress distribution along the net section. The normal stress distribution, together with the corresponding stress intensity factors, was used in the 2D WFM to derive the weight function for a crack emanating from an edge notch. The weight function was then used in the 3D WFM to derive stress intensity factors for surface and corner cracks at the edge notch. A technique to extract experimental stress intensity factors for through cracks in the SENT specimen was also applied to verify the remote boundary conditions on the test specimen. Comparisons are made between experimental and calculated stress intensity factors.

Weight-Function Method

Analytical weight functions for 2D crack configurations (center and edge cracks) with finite boundaries have been developed in reference 44. For simplicity, a special loading of uniform crack-face pressure was employed as the reference solution for which stress intensity factors are known. This approach suffices for many crack configurations. For the present crack configuration, however, a reference stress intensity factor solution for uniform pressure loading on the crack faces is not available. The obstacle was overcome by applying a more general approach recently developed by Wu and Carlsson. (See ref. 47.) In this approach, the analytical weight functions are based on a reference solution to a polynomial crack-face load case. The derivation starts from a reference polynomial stress distribution on the crack faces as

$$\frac{\sigma_r(\xi)}{S} = \sum_{n=0}^{N} s_n \xi^n \qquad \text{(C1)}$$

A three-term representation for the crack-face displacements was assumed for this type of loading and
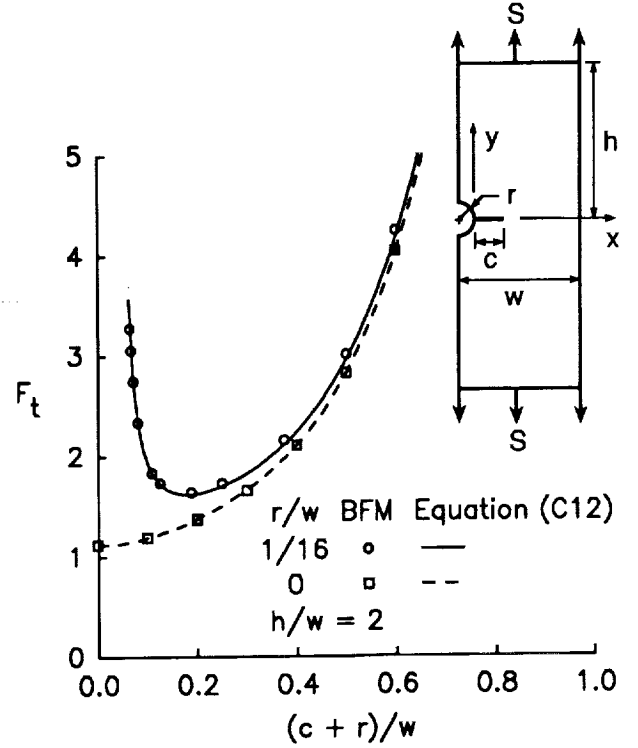
Figure C1. Stress intensity boundary-correction factors for through crack at notch in plate subjected to remote uniform stress for two values of r/w.

was given by

$$U_r(\alpha, \xi) = \frac{c\sigma_o}{E'(2)^{1/2}} \sum_{j=1}^{3} F_j(\alpha) \left(1 - \frac{\xi}{\alpha}\right)^{j-1/2} \qquad \text{(C2)}$$

where $\alpha = c/r$ and $\xi = x/r$. (See insert on fig. C1.) The three unknown functions of F_j were determined by using the following three conditions: crack-face displacement in the immediate wake of the crack tip, self-consistency of the weight function, and vanishing curvature along the edge crack surface at the crack mouth. The results are

$$F_1(\alpha) = 4f_r(\alpha) \qquad \text{(C3)}$$

$$F_2(\alpha) = \frac{15\left[2^{1/2}\pi\Phi(\alpha) - F_1(\alpha)E_1(\alpha)\right]F_1(\alpha)E_3(\alpha)}{15E_2(\alpha) - 3E_3(\alpha)} \qquad \text{(C4)}$$

$$F_3(\alpha) = \frac{F_1(\alpha)E_2(\alpha) - 3[2^{1/2}\pi\Phi(\alpha) - F_1(\alpha)E_1(\alpha)]}{15E_2(\alpha) - 3E_3(\alpha)} \qquad \text{(C5)}$$

where

$$\Phi(\alpha) = \alpha^{-2} \int_0^\alpha \ell f_r^2(\ell)\, d\ell$$

85

$$E_j(\alpha) = \sum_{n=0}^{N} \left[\frac{2^{n+1} n! s_n \alpha^n}{\prod_{k=0}^{n} (2k + 2j + 1)} \right] \quad (j = 1, 2, \text{ or } 3)$$

and $f_r(\alpha)$ is the dimensionless stress intensity factor for the reference load case, commonly expressed in a polynomial form,

$$f_r(\alpha) = \frac{K}{S(\pi c)^{1/2}} = \sum_{m=0}^{M} A_m \alpha^m \qquad \text{(C6)}$$

Based on these expressions, a general closed-form weight function for edge cracks was obtained and was given by

$$m(\alpha, \xi) = \frac{\sum_{i=1}^{4} \beta_i(\alpha) \left(1 - \frac{\xi}{\alpha}\right)^{i-3/2}}{(2 \pi \alpha)^{1/2}} \qquad \text{(C7)}$$

where the functions $\beta_i(\alpha)$ are given by the following expressions:

$$\left.\begin{aligned}
\beta_1(\alpha) &= 2 \\
\beta_2(\alpha) &= \frac{4\alpha f_r'(\alpha) + 2f_r(\alpha) + \frac{3}{2} F_2(\alpha)}{f_r(\alpha)} \\
\beta_3(\alpha) &= \frac{\alpha F_2'(\alpha) + \frac{1}{2}[5F_3(\alpha) - F_2(\alpha)]}{f_r(\alpha)} \\
\beta_4(\alpha) &= \frac{\alpha F_3'(\alpha) - \frac{3}{2} F_3(\alpha)}{f_r(\alpha)}
\end{aligned}\right\} \qquad \text{(C8)}$$

The only information needed for the determination of the edge crack weight function is the stress polynomial $\sigma_r(\xi)$ in the uncracked body from equation (C1) and the related nondimensional stress intensity factor $f_r(\alpha)$. For the edge notch crack in the present investigation, a solution for $f_r(\alpha)$ has been obtained by Tan, Raju, and Newman (ref. 51) using the BFM. The uncracked stress distribution along the prospective crack site was also determined by the BFM (discussed later). The following two sets of polynomial equations fit, respectively, the numerical results of $\sigma_r(\xi)$ and $f_r(\alpha)$ within ± 0.2 percent and are given by

$$\frac{\sigma_r(\xi)}{S} = 3.1635 - 6.9765\xi + 14.1306\xi^2 - 19.2171\xi^3$$
$$+ 16.8505\xi^4 - 8.9712\xi^5 + 2.6141\xi^6 - 0.3182\xi^7 \quad (\xi \leq 2)$$

$$f_r(\alpha) = 3.5479 - 7.2009\alpha + 15.7223\alpha^2 - 22.4661\alpha^3$$
$$+ 20.0387\alpha^4 - 10.5295\alpha^5 + 2.9601\alpha^6 - 0.3421\alpha^7 \quad (\alpha \leq 2)$$

(Note that these equations are valid only for $r/w = 1/16$.) With these two equations, the weight function

for an edge crack emanating from a semicircular edge notch ($r/w = 1/16$) in a rectangular plate (valid to $\alpha = 2$) is readily determined. Stress intensity factors for an arbitrary crack-face loading $\sigma(\xi)$ can be obtained by a simple quadrature as

$$K = S(\pi c)^{1/2} f \qquad \text{(C9)}$$

where

$$f = \int_0^{\alpha} \frac{\frac{\sigma(\xi)}{S} \left[\sum_{i=1}^{4} \beta_i(a) \left(1 - \frac{\xi}{\alpha}\right)^{i-3/2} \right] d\xi}{(2\pi\alpha)^{1/2}} \qquad \text{(C10)}$$

Boundary Force Method

The BFM was formulated for the two-dimensional stress analysis of complex configurations, with and without cracks, subjected to internal loadings and to traction or displacement boundary conditions. (See refs. 26 and 51.) The BFM uses the elasticity solution for concentrated forces and a moment in an infinite plate as the fundamental solution. For plates without a crack, Muskhelishvili's solution (ref. 52) for P, Q, and M in an infinite plate is used as the fundamental solution. For a plate with a crack, Erdogan's solution (ref. 53) for a pair of concentrated forces and a moment in an infinite plate with a crack is used as the fundamental solution. With Erdogan's solution the crack faces need not be modeled as part of the boundary because the stress-free conditions on the crack faces are exactly satisfied.

Because the fundamental solution satisfies all interior elasticity equations, the only remaining conditions to be satisfied are those on the boundary. The specified boundary conditions are satisfied by the application of concentrated forces and moments along an imaginary boundary traced on an infinite plate that corresponds to the actual configuration. The imaginary boundary is discretized into a number of straight segments. At the center of each segment, a pair of concentrated forces and a moment are applied at a small distance from the imaginary boundary and the region of interest. The magnitudes of these forces and moments are determined to approximately satisfy the prescribed boundary conditions.

To verify the accuracy of the method, the BFM has been used to analyze numerous 2D crack and notch configurations for which exact or accurate stress and displacement solutions are available in the literature. (See refs. 26 and 51.) The crack configurations considered included mode I and mixed-mode (modes I and II) problems. The method produced

stress and displacement fields and stress intensity factors that agreed well with those in the literature. In general, about 150 DOF was required for accurate solutions (better than 0.5 percent) to complex crack configurations.

The BFM was used to analyze the uncracked SENT specimen to obtain the stress concentration factor and the normal stress distribution along the net section. The BFM was also used to analyze a through crack emanating from the SENT specimen subjected to either remote uniform stress or displacement. The James and Anderson technique (ref. 54) to extract experimental stress intensity factors for through cracks in the SENT specimen was also used to verify the remote boundary conditions on the test specimen. Comparisons are made between experimental and calculated stress intensity factors.

Stress Distributions

The SENT specimen shown in figure 2 was held by flat-plate friction grips from the grip line to the ends. The dimension of w was fixed in all specimens to 50 mm. The height h is measured from the specimen centerline at the notch to a specified line drawn parallel to the grip line. Two values of h were assumed in the analysis. One height was arbitrarily selected as a line drawn below the optional hole ($h/w = 2$), and the other was along the grip line ($h/w = 1.5$). In the BFM analysis, uniform stress (S) or uniform displacement ($v = $ constant, $u = 0$) was applied parallel to the long dimension of the specimen at $y = \pm h$, and zero tractions were applied elsewhere.

Analyses of the uncracked SENT specimen with the BFM gave an elastic stress concentration factor $K_T = \sigma_{yy}/S = 3.17$ for uniform stress and 3.15 for uniform displacement for both values of h/w. The normal stress distribution along the specimen centerline at the notch root for remote uniform stress is shown in figure 3 as the solid curve. The stress concentration factor was about 5.5 percent higher than that for a circular hole in an infinite plate and the stress gradient is similar. This stress distribution was used in the 2D and 3D WFM to determine 2D weight functions for a crack emanating from the edge notch and 3D stress intensity factors for surface- and corner-crack configurations. (See appendix B.)

Stress Intensity Factors

The stress intensity factor for a through crack emanating from a semicircular notch subjected to remote uniform stress or displacement was expressed as

$$K = S(\pi c)^{1/2} F_t\left(\frac{c}{w}, \frac{c}{r}, \frac{r}{w}\right) \qquad \text{(C11)}$$

Table CI. Stress Intensity Boundary-Correction Factors for Single-Edge Crack Specimen Subjected to Remote Uniform Stress or Displacement

$$\left[F_t = \frac{K}{S(\pi c)^{1/2}} \right]$$

	Uniform stress	Uniform displacement	
c/w	$h/w = 2$	$h/w = 2$	$h/w = 1.5$
0	[a]1.123	[a]1.123	[a]1.123
.1	1.189	1.165	1.154
.2	1.367	1.255	1.231
.3	1.655	1.377	1.294
.4	2.108	1.527	1.418
.5	2.827	1.705	1.532
.6	4.043	1.913	1.702
.7	6.376	2.166	1.916
.8	11.99	2.507	2.239

[a]Limiting solution from Tada, Paris, and Irwin (ref. 32).

Table CII. Stress Intensity Boundary-Correction Factors for Crack Emanating From a Semicircular Edge Notch in Specimen Subjected to Remote Uniform Stress or Displacement

$$\left[\frac{r}{w} = \frac{1}{16}; \ F_t = \frac{K}{S(\pi c)^{1/2}} \right]$$

		Uniform stress	Uniform displacement	
$\frac{c+r}{r}$	$\frac{c+r}{w}$	$h/w = 2$	$h/w = 2$	$h/w = 1.5$
1.04	0.065	3.276	3.219	3.187
1.08	.0675	3.058	3.030	3.000
1.15	.0719	2.752	2.715	2.682
1.30	.0813	2.338	2.299	2.269
1.75	.1094	1.832	1.783	1.756
2.0	.125	1.732	1.674	1.641
3.0	.1875	1.638	1.515	1.477
4.0	.25	1.726	1.511	1.450
6.0	.375	2.160	1.627	1.513
8.0	.5	3.011	1.822	1.640
9.6	.6	4.248	2.022	1.789

where F_t is a boundary-correction factor that accounts for the effect of the notch and external boundaries. The BFM was used to calculate F_t for various crack configurations and boundary conditions. Boundary-correction factors are given in table CI for a single-edge-crack specimen and in table CII for a crack emanating from a semicircular edge notch in either remote uniform stress or displacement. Equations were then developed to fit the BFM results. The boundary-correction factor was expressed as

$$F_t = f_1 g_4 f_w \qquad \text{(C12)}$$

C-2

The functions f_1 and g_4 were selected to account for the effects of the notch and are given by

$$f_1 = 1 + 0.358\lambda + 1.425\lambda^2 - 1.578\lambda^3 + 2.156\lambda^4 \quad \text{(C13)}$$

where $\lambda = 1/[1 + (c/r)]$ and

$$g_4 = K_t \left[0.36 - \frac{0.032}{\left(1 + \frac{c}{r}\right)^{1/2}} \right] \quad \text{(C14)}$$

The effects of specimen width and remote boundary conditions were approximated by f_w, the finite-width correction, which was obtained by fitting to the calculations from the BFM.

For $h/w = 2$, the correction was

$$f_w = 1 - 0.2\gamma + 9.4\gamma^2 - 19.4\gamma^3 + 27.1\gamma^4 \quad \text{(C15a)}$$

for uniform stress and

$$f_w = 1 + 2.7\gamma^2 - 3.5\gamma^4 + 3.8\gamma^6 \quad \text{(C15b)}$$

for uniform displacement.

For $h/w = 1.5$,

$$f_w = 1 + 2.17\gamma^2 - 3.4\gamma^4 + 3.7\gamma^6 \quad \text{(C15c)}$$

for uniform displacement where $\gamma = \frac{c+r}{w}$. These equations are valid for $r/w = 1/16$ and $\frac{c+r}{w} < 0.6$.

The cracked SENT specimen was analyzed for $r/w = 1/16$ (cooperative program test specimen) and $r/w = 0$ (single-edge-crack specimen); these results (symbols) are shown in figures C1 and C2 for remote uniform stress and displacement ($h/w = 2$), respectively. The boundary-correction factor F_t is plotted against $\frac{c+r}{w}$. The curves show the equation (eq. (C12)) that was developed to fit these results. For $r/w = 0$, the boundary-correction factor is also given by equation (C12) where $f_1 = 1$, $g_4 = 1.123$, and f_w is given by equations (C15a)–(C15c). These results show that the remote boundary conditions have a significant effect on the correction factors.

The boundary-correction factor equations for the SENT specimen subjected to remote uniform stress or displacement for $h/w = 1.5$ are shown in figure C3 as dashed and solid curves, respectively. Because the stress and displacement boundary conditions gave such large differences in the boundary-correction factors, the James and Anderson technique (ref. 54) was also applied to help verify the correct external boundary condition on the cooperative program test specimens.
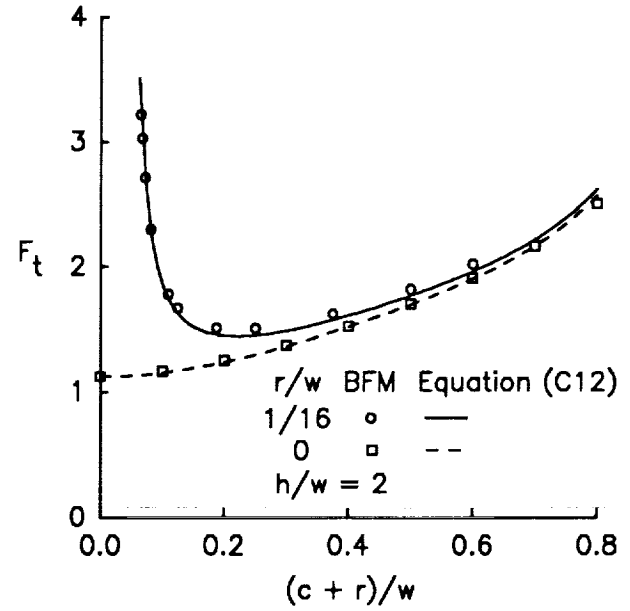
Figure C2. Stress intensity boundary-correction factors for through crack at notch in plate subjected to remote uniform displacement for two values of r/w.
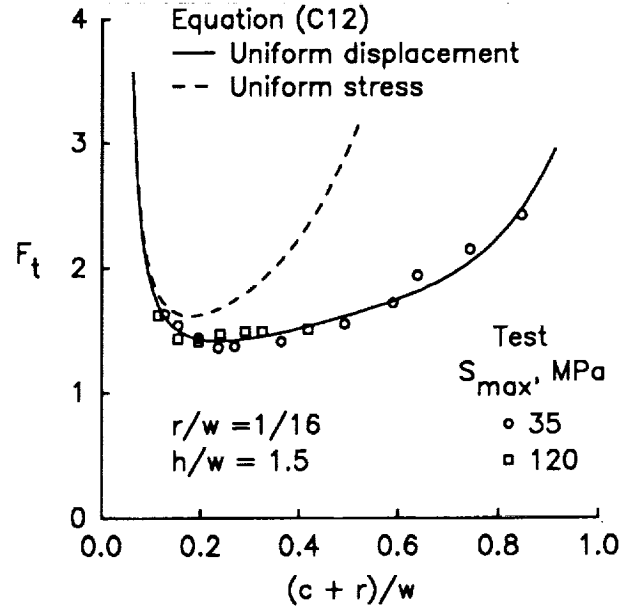
Figure C3. Experimental and calculated boundary-correction factors for through crack at notch in plate subjected to remote stress or displacement.

Comparison of Experiments and Analyses

In the James and Anderson technique, fatigue crack-growth rates from tests are used to determine an experimental value of the stress intensity factor as a function of crack length. The basis for this approach is in the uniqueness of the ΔK against rate

88

(dc/dN) relation for a material tested at a constant R. The point in question was whether the specimen and grip configuration produced uniform stress or uniform displacement conditions, and what was the effective specimen height. Two fatigue crack-growth rate tests were conducted on 7075-T6 aluminum alloy SENT specimens. One test was conducted at a low applied stress level to obtain data for a range of crack lengths; the other test was conducted at a high stress level that was typical of the stresses used in the cooperative test program. The latter test would sim-ulate any slippage or wear at the higher stress levels. Crack length was measured as a function of load cycles at $R = 0$. From the crack-length-against-cycles data, crack-growth rates and experimental values of stress intensity were determined by using the large-crack ΔK-rate relation. These experimental values are shown in figure C3 as symbols. The experimental data followed the calculated curve very well for uniform displacement for $h/w = 1.5$. Therefore, the f_w function defined by equation (C15c) was used in the test program.

Appendix D

Stress Intensity Factor Equations for a Surface, Corner, and Through Crack at a Semicircular Notch

Approximate stress intensity factor equations for a semielliptical surface crack at the center of a semicircular edge notch, a quarter-elliptical corner crack at the edge of the notch, and a through crack at the notch subjected to remote uniform stress or uniform displacement for $h/w = 1.5$ are given herein. These configurations are shown in figure 13. These equations have been developed from stress intensity factors calculated from the FEM and WFM for surface and corner cracks (appendixes A and B, respectively), from boundary force analyses of through cracks at a semicircular notch (ref. 51), and from previously developed equations for similar crack configurations at an open hole. (See refs. 78 and 93.) The stress intensity factors are expressed as

$$K = S \left(\frac{\pi a}{Q}\right)^{1/2} F_j \left(\frac{a}{c}, \frac{a}{t}, \frac{c}{r}, \frac{c}{w}, \frac{r}{t}, \frac{r}{w}, \varphi\right) \tag{D1}$$

where K is the stress intensity factor and t is defined here as one-half the full sheet thickness for surface cracks ($j = s$) and as the full sheet thickness for corner cracks ($j = c$). The equations have been developed for a range of configuration parameters with $r/w = 1/16$.

The shape factor Q is given by

$$Q = 1 + 1.464 \left(\frac{a}{c}\right)^{1.65} \qquad \left(\frac{a}{c} \leq 1\right) \tag{D2a}$$

$$Q + 1 + 1.464 \left(\frac{c}{a}\right)^{1.65} \qquad \left(\frac{a}{c} > 1\right) \tag{D2b}$$

Surface Crack at a Semicircular Notch

The boundary-correction factor equation for a semielliptical surface crack at the center of a semicircular edge notch (fig. 13(a)) subjected to remote uniform stress or displacement is

$$F_s = \left[M_1 + M_2 \left(\frac{a}{t}\right)^2 + M_3 \left(\frac{a}{t}\right)^4\right] g_1 g_2 g_3 g_4 g_5 f_\varphi f_w \tag{D3}$$

for $0.2 < a/c < 2$, $a/t < 1$, $1 < r/t < 3.5$, $(c+r)/w < 0.6$, $r/w = 1/16$, and $-\pi/2 < \varphi < \pi/2$. (Here t is defined as one-half the full sheet thickness.) For $a/c \leq 1$,

$$M_1 = 1 \tag{D4}$$

$$M_2 = \frac{0.05}{0.11 + \left(\frac{a}{c}\right)^{3/2}} \tag{D5}$$

$$M_3 = \frac{0.29}{0.23 + \left(\frac{a}{c}\right)^{3/2}} \tag{D6}$$

$$g_1 = 1 - \frac{\left(\frac{a}{t}\right)^4 \left(2.6 - \frac{2a}{t}\right)^{1/2}}{\left(1 + \frac{4a}{c}\right)} \cos \varphi \tag{D7}$$

$$g_2 = \frac{1 + 0.358\,\lambda + 1.425\,\lambda^2 - 1.578\,\lambda^3 + 2.156\,\lambda^4}{1 + 0.08\,\lambda^2} \tag{D8}$$

$$\lambda = \frac{1}{1 + \frac{c}{r}\cos(0.9\varphi)} \tag{D9}$$

$$g_3 = 1 + 0.1(1 - \cos \varphi)^2 \left(1 - \frac{a}{t}\right)^{10} \tag{D10}$$

$$g_4 = K_T \left(0.36 - \frac{0.032}{\left(1 + \frac{c}{r}\right)^{1/2}}\right) \tag{D11}$$

where K_T is the elastic stress concentration factor ($K_T = 3.17$ for uniform stress; $K_T = 3.15$ for uniform displacement) at the semicircular notch, and

$$g_5 = 1 + \left(\frac{a}{c}\right)^{1/2} \left[0.003 \left(\frac{r}{t}\right)^2 + 0.035 \left(\frac{r}{t}\right)(1 - \cos \varphi)^3\right] - 0.35 \left(\frac{a}{t}\right)^2 \left(1 - \frac{a}{2c}\right)^3 \cos \varphi \tag{D12}$$

For uniform stress, the correction f_w was

$$f_w = 1 - 0.2\gamma + 9.4\gamma^2 - 19.4\gamma^3 + 27.1\gamma^4 \tag{D13a}$$

and for uniform displacement,

$$f_w = 1 + 2.17\gamma^2 - 3.4\gamma^4 + 3.7\gamma^6 \tag{D13b}$$

with $h/w = 1.5$ where

$$\gamma = \left(\frac{a}{t}\right)^{1/2} \frac{c + r}{w}$$

The a/t term was included in γ to reflect the reduced influence of width on the finite-width correction for a surface and corner crack. The function f_φ is given by

$$f_\varphi = \left[\left(\frac{a}{c}\right)^2 \cos^2 \varphi + \sin^2 \varphi\right]^{1/4} \tag{D14}$$

For $a/c > 1$,

$$M_1 = \left(\frac{c}{a}\right)^{1/2} \left(1.04 - \frac{0.04c}{a}\right) \tag{D15}$$

The functions M_2, M_3, g_1, g_2, λ, g_3, g_4, g_5, and f_w are given by equations (D6)–(D13), respectively, and f_φ is given by

$$f_\varphi = \left[\left(\frac{c}{a}\right)^2 \sin^2 \varphi + \cos^2 \varphi\right]^{1/4} \tag{D16}$$

Corner Crack at a Semicircular Notch

The boundary-correction factor equation for a quarter-elliptical corner crack at the edge of a semicircular edge notch (fig. 13(b)) in remote uniform stress or displacement is

$$F_c = \left[M_1 + M_2 \left(\frac{a}{t}\right)^2 + M_3 \left(\frac{a}{t}\right)^4\right] g_1 g_2 g_3 g_4 g_5 f_\varphi f_w \tag{D17}$$

for $0.2 < a/c < 2$, $a/t < 1$, $1 < r/t < 2$, $(c + r)/w < 0.6$, $r/w = 1/16$, and $0 < \varphi < \pi/2$. (Here t is defined as the full sheet thickness.) For $a/c \leq 1$,

$$M_1 = 1.13 - \frac{0.09a}{c} \tag{D18}$$

$$M_2 = -0.54 + \frac{0.89}{0.2 + \frac{a}{c}} \tag{D19}$$

$$M_3 = 0.5 - \frac{1}{0.65 + \frac{a}{c}} \tag{D20}$$

91

$$g_1 = 1 + \left[0.1 + 0.2\left(\frac{a}{t}\right)^2\right](1 - \sin\varphi)^2 - 0.16\left(\frac{a}{t}\right)\sin\varphi\cos\varphi \qquad (D21)$$

$$g_2 = \frac{1 + 0.358\,\lambda + 1.425\,\lambda^2 - 1.578\,\lambda^3 + 2.156\,\lambda^4}{1 + 0.13\,\lambda^2} \qquad (D22)$$

$$\lambda = \frac{1}{1 + \frac{c}{r}\cos 0.8\varphi} \qquad (D23)$$

$$g_3 = \left(1 + 0.04\,\frac{a}{c}\right)\left[1 + 0.1(1 - \cos\varphi)^2\right]\left[0.97 + 0.03\left(\frac{a}{t}\right)^{1/4}\right] \qquad (D24)$$

The functions g_4, g_5, and f_w are given by equations (D11)–(D13), respectively, and f_φ is given by equation (D14). For $a/c > 1$,

$$M_1 = \left(\frac{c}{a}\right)^{1/2}\left(1 + \frac{0.04\,c}{a}\right) \qquad (D25)$$

$$M_2 = 0.2\left(\frac{c}{a}\right)^4 \qquad (D26)$$

$$M_3 = -0.11\left(\frac{c}{a}\right)^4 \qquad (D27)$$

$$g_1 = 1 + \frac{c}{a}\left[0.1 + 0.2\left(\frac{a}{t}\right)^2\right](1 - \sin\varphi)^2 - 0.16\left(\frac{a}{t}\right)\frac{c}{a}\sin\varphi\cos\varphi + 0.07\left(1 - \frac{a}{c}\right)\left(1 - \frac{a}{t}\right)\cos^2\varphi \qquad (D28)$$

$$g_3 = \left(1.13 - \frac{0.09\,c}{a}\right)\left[1 + 0.1(1 - \cos\varphi)^2\right]\left[0.97 + 0.03\left(\frac{a}{t}\right)^{1/4}\right] \qquad (D29)$$

The functions g_2 and λ are given by equations (D22) and (D23), g_4 by equation (D11), g_5 by equation (D12), f_w by equation (D13), and f_φ by equation (D16).

Through Crack at a Semicircular Notch

When the surface-crack length $2a$ reaches $2t$ or when the corner-crack length a reaches t, the crack is assumed to be a through crack of length c. The stress intensity factors for a through crack emanating from a semicircular notch subjected to remote uniform stress or displacement are presented in appendix C. (See eq. (C11).)

Appendix E

Specimen Machining and Polishing Procedures

Specimen Machining Procedures

The specimen blanks for the small-crack SENT and large-crack CCT specimens were sheared from aluminum alloy sheets (about 1200 mm by 2400 mm by supplied thickness) according to a shearing layout diagram. The long dimension of the specimens was parallel to the rolling direction (long dimension of the sheet). Each specimen blank was labeled by a number with an ink marker at the end so that reference could be made to the specimen location in the sheet in case of questions concerning uniformity of properties. Each sheet produced 105 SENT and 30 CCT specimens for each alloy.

The SENT specimens were milled to final overall dimensions (50 mm wide by 300 mm long by supplied thickness) as shown in figure E1(a). Six of the straightest or most flat specimens were selected and reserved for alignment specimens. (See appendix F.) In the remaining specimens, the semicircular notch was milled by final cuts of 0.25, 0.10, and 0.05 mm with a newly sharpened tool to achieve a final radius of 3.2 mm; this milling sequence was designed to minimize residual stresses in the notch. Then a hole of 10 mm radius was punched or drilled in the grip area at each end as shown in figure E1 to hold the SENT specimens in friction grips. Note that the hole was oversized for the bolts used and was positioned such that the bolt would not bear on the edge of the hole.

The CCT specimens were milled to final dimensions (75 mm wide by 300 mm long by supplied thickness) as shown in figure E1(b). The notches and holes in the grip area were necessary for the NASA-designed friction grips. A specimen number was inscribed into the specimen surface at each end. The details of the crack-starter notch machined in each specimen were left to each laboratory. NASA used the electrical discharge machining (EDM) process to form a central slot 5 mm long and 0.5 mm high.

Chemical Polishing Procedures

Chemical polishing of the SENT specimens was necessary to smooth machining marks on the semicircular notch surface and to debur the edges of the notch. This process also provides further assurance that no significant residual stresses remained at the notch root. Some of the specimens were weighed before and after polishing to monitor material removal.

A layer of material approximately 0.02 mm thick was removed by the polishing process.

To prepare them for polishing, the inked specimen number was removed with acetone and the specimen number was scribed at each end of the specimen. Next, the specimens were put into a DuPont Freon vapor degreaser for 10 minutes, were soaked in a detergent cleaner for 10 minutes, and finally were thoroughly rinsed in water.

To facilitate the polishing process, a specially designed polishing rack and tank were constructed to support a batch of 10 specimens. The rack and tank were fabricated from 347 stainless steel sheet and 304 stainless steel threaded rods. Ten specimens were positioned in the rack with the semicircular notches pointing toward the upper surface of the solution. All steps in the cleaning and polishing sequence were performed with the specimens in the rack. About 23.5 liters of solution was used in this tank with the rack described above.

The polishing process must be performed under a fume hood capable of handling the noxious fumes produced, especially when the specimen rack must be lifted from the polishing solution tank. The composition of the polishing solution is as follows:

80 percent	H_3PO_4	Phosphoric acid
5 percent	HNO_3	Nitric acid
5 percent	CH_3CO_2H	Acetic acid
10 percent	H_2O	Water

The solution was stirred and maintained between 100° and 105°C. Specimens were submerged in the solution for 5 minutes, then they were agitated to permit easy removal of gaseous reaction products from the specimen surface.

The solution was covered when not in use as the water, nitric acid, and acetic acid can evaporate. If the solution were to become chemically unbalanced, the specimens would be pitted and dull rather than bright and the material removal rates would be reduced. The balance may be returned to the solution by the addition of water, nitric acid, and acetic acid in a 2:1:1 ratio, as in the original formulation, until the original solution volume is achieved.

After polishing, the specimens were rinsed in water. A reddish cast was evident on the specimen surface from a copper-rich layer. This residue was removed when the specimens were dipped in a desmutting solution of 10 percent nitric acid by volume in water for 20 seconds. The specimens were again rinsed in water, then alcohol; thereafter, they were air dried. Specimens were wrapped in paper individually for storage or shipment.
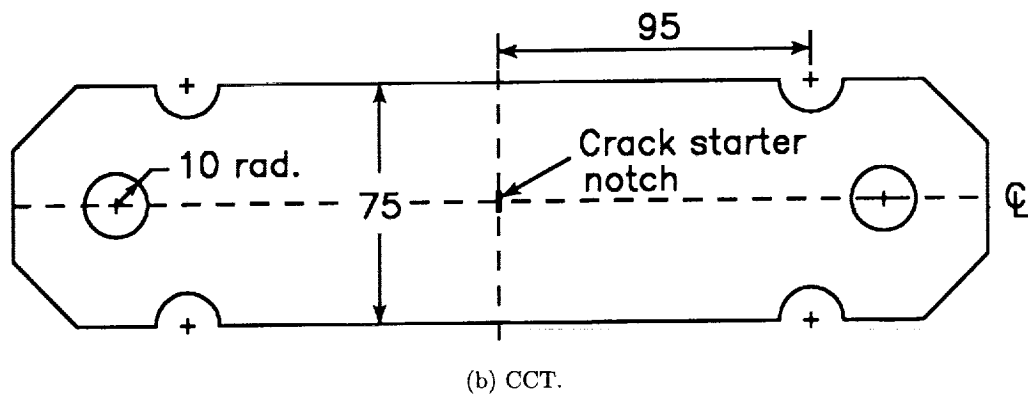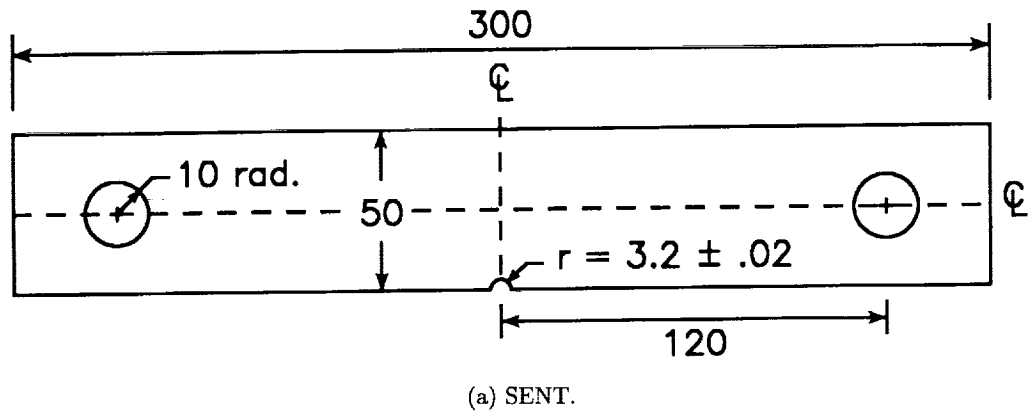
(a) SENT.

(b) CCT.

Figure E1. Specimen dimensions for small- and large-crack tests. Linear dimensions are in millimeters.

Appendix F

Specimen Gripping and Alignment Procedures

Specimen Grips

This appendix describes the specimen grips and alignment procedures that were used in the cooperative program. The particular set of grips was chosen simply because of past satisfactory experience with them during tests of 2- to 3-mm-thick specimens at loads to 30 kN. Many other methods of gripping the specimens would probably have been equally satisfactory. The following paragraphs give a brief description of the grips and of the procedures developed to help ensure uniform loading on the SENT and CCT specimens.

The grips were designed to transfer load to the specimens by friction only. They consisted of a single block of steel, machined into a yoke with two flat surfaces. Each leg of the yoke had a reduced section that gave the leg enough flexibility that the bolts through the yokes and specimen could maintain sufficient pressure to grip the specimen. The specimens were placed between these two flat surfaces with various shims on both sides to ensure placement along the center plane of the grips. Most of the shims were metal, although the shims that bore against the specimen were normally made from reinforced phenolic plastic (generally between 0.5 to 2 mm thick). However, other plastics and even brass metal have been used successfully. The sum of the thicknesses of all shims was such that a gap of only about 0.1 to 0.2 mm remained on each side before the bolts were tightened

to clamp the specimens in place. In addition to the single bolt through the specimens, four other bolts, two on each side, were also used in each grip. Care was taken so that neither of the central bolts bore on the holes in the specimens because this pressure could cause specimen failure in the grip area. The goal was to transfer all load from the grips to the specimen by friction.

Specimen Alignment Procedures

Each laboratory was required to align the test machines and gripping fixtures to produce a nearly uniform tensile stress field on a blank (unnotched) sheet specimen. The blank specimens (50 mm wide by 300 mm long by supplied thickness) were tested by strain gages as shown in figure F1. Strain gage readings were taken at all gages. The alignment verification procedures are as follows:

1. Zero all strain gage circuit outputs before installing the specimens in the test machine.

2. Install the specimens in the machine and read all strain gages at 0, 5, 10, 15, and 20 kN.

3. Remove the specimens from the machine, rotate the specimens 180° about the long axis, and install them in the new orientation. Read all strain gages at the same loads as in step 2.

4. Compute the measures of bending strain as indicated in table FI and compare these computed values with the acceptance criteria. If the specimen bending strains are too large, adjust the test machine alignment and repeat the alignment check procedure.

Table FI. Bending Measures and Acceptance Criteria for Alignment Check

Bending measure and computation formula for—		Acceptance criterion
First position	Rotated position	
$\epsilon_{TM} = [(\epsilon_1 + \epsilon_3 + \epsilon_5) - (\epsilon_2 + \epsilon_4 + \epsilon_6)]/6$	$+ [(\epsilon_2 + \epsilon_4 + \epsilon_6) - (\epsilon_1 + \epsilon_3 + \epsilon_5)]/6$	$|\epsilon_{TM}| < 75\mu\epsilon$
$\epsilon_{TU} = (\epsilon_7 - \epsilon_8)/2$	$+ (\epsilon_8 - \epsilon_7)/2$	$|\epsilon_{TU}| < 150\mu\epsilon$
$\epsilon_{TL} = (\epsilon_9 - \epsilon_{10})/2$	$+ (\epsilon_{10} - \epsilon_9)/2$	$|\epsilon_{TU}| < 150\mu\epsilon$
$\epsilon_{W1} = |[(\epsilon_1 + \epsilon_2) - (\epsilon_3 + \epsilon_4)]|$	$\epsilon_{W1} = |[(\epsilon_1 + \epsilon_2) - (\epsilon_3 + \epsilon_4)]|$	$|\epsilon_{W1}| < 200\mu\epsilon$
$\epsilon_{W2} = \Delta\epsilon_{12}/\Delta\epsilon_{34}$	$\epsilon_{W2} = \Delta\epsilon_{12}/\Delta\epsilon_{34}$	$0.95 < \epsilon_{W2} < 1.05$

where

$\epsilon_1-\epsilon_{10}$ individual strain gage readings

ϵ_{TM} average through-the-thickness strain difference at midlength gage

ϵ_{TU} average through-the-thickness strain difference at upper gage

ϵ_{TL} average through-the-thickness strain difference at lower gage

ϵ_{W1} across-width strain difference at midlength gage

ϵ_{W2} across-width strain difference at midlength gage

$$\Delta\epsilon_{12} = (\epsilon_1 + \epsilon_2)_{20\ kN} - (\epsilon_1 + \epsilon_2)_{0\ kN}$$

$$\Delta\epsilon_{34} = (\epsilon_3 + \epsilon_4)_{20\ kN} - (\epsilon_3 + \epsilon_4)_{0\ kN}$$
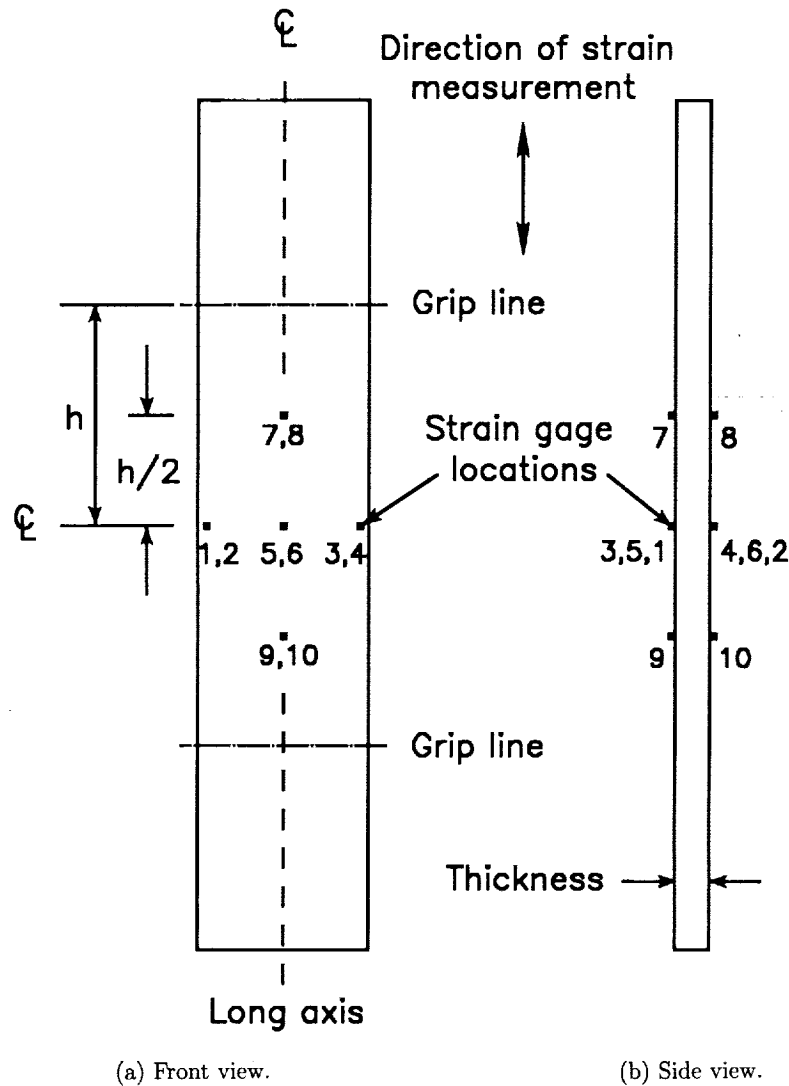

(a) Front view.   (b) Side view.

Figure F1. Location of strain gages on unnotched specimen used for alignment check.

Appendix G

Method of Recording Small- and Large-Crack Data

Small-Crack Data

Lengths of small cracks in the SENT specimens were measured by means of the plastic-replica method. (See appendix H.) The data from each small-crack test were recorded on a data table and on a diagram of the notch root, as shown by the sample case in figure G1. (Note that the sample data charts and tables in this appendix are not actual data but are for illustration purposes only.) This chart gave the location and length of each crack monitored and the initiation site. The data table (see the sample case in table GI) was constructed from the data charts and included specimen number, dimensions, type and magnitude of loading, crack initiation site coordinates, and L_i against number of cycles for up to five cracks (usually the largest and most dominant ones). The cyclic interval (in this example, 10 000 cycles) was determined by the frequency of the plastic replicas that were taken; that interval was selected to give about 25 replicas per test.

Table GI gives a sample data table for a small-crack test for constant-amplitude loading. Figure G1 shows the corresponding data chart. Only one data chart was required for each specimen; it was plotted on graph paper graduated in 10-μm units and covers the specimen thickness in the x-direction and 1 mm of the notch root in the y-direction. This example shows how the data chart appears when 50 000 cycles have been applied to a specimen. (A copy of the data chart was made before it was updated after the next cyclic interval. Thus, a history of crack initiation and growth was available for further analysis.) The dots indicate the approximate initiation site for each crack, the coordinates of which were also recorded. Cracks L_1 and L_2 have joined and their total depth is now L_1. (See fig. G1 at 50 000 cycles.) Crack 6

has initiated, but its location and length do not have to be recorded. The test was terminated when L_i reached B. As indicated in table GI, cracks L_1 and L_3 have joined at 80 000 cycles and the test was terminated ($L_1 = B$).

Large-Crack Data

Three types of large-crack tests were conducted in the test program: constant-amplitude loading, threshold or load shedding, and spectrum loading. The data from each of these tests were recorded on a data table that gives the specimen number; dimensions; type and magnitude of loading; and lists the maximum stress, crack length (L), number of cycles, and pertinent comments about the test. Table GII gives an example of constant-amplitude fatigue loading with a static fracture test (pull to failure) to terminate the test. (Only three of the nine constant-amplitude fatigue tests were pulled to failure with $L = 0.5w$.) The failure stress was recorded on the table. The comment column is used to indicate changes in the test procedure, such as stopping the fatigue test and pulling the specimen to failure.

Table GIII gives an example of a threshold test at $R = -1$. The level S_{max} was reduced by 6 percent after 1 mm of crack extension. The crack was grown about 2 mm from each end of the starter notch before the load-reduction procedure was initiated.

Table GIV gives an example of a Mini-TWIST spectrum test at a maximum spectrum stress of 210 MPa. The precracking from the starter notch was conducted for constant-amplitude fatigue loading with $S_{max} = 50$ percent of the maximum spectrum stress (210 MPa in this example) at $R = 0$. The crack was grown about 2 mm from each end of the starter notch before the spectrum loading was applied. The specimen was then cycled to failure in spectrum loading. Crack depth and total cycles were recorded after every 1 mm of crack extension.
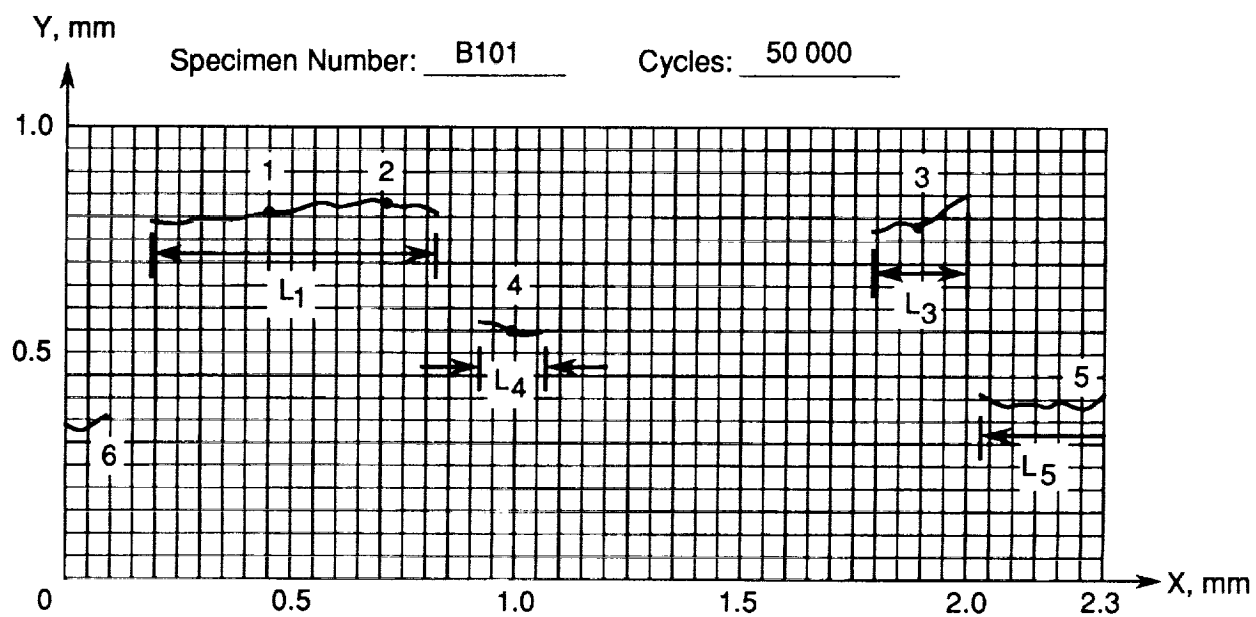
Figure G1. Sample data chart for small-crack test B101 at $N = 50\,000$ cycles. See table GI.

Table GI. Sample Data Table for Small-Crack Tests

Small-Crack Data Table

Specimen Number: __B101__   Page __1__ of __1__

Width: __50.0__ mm   Thickness: __2.3__ mm   Notch radius: __3.2__ mm

Loading: __Constant amplitude__ $S_{max} =$ __205__ MPa $R =$ __−1__

Crack-Initiation Coordinates, mm:

$i =$	1	2	3	4	5
$x =$	0.40	0.70	1.90	1.00	2.30
$y =$	0.80	0.82	0.85	0.55	0.40

Cycles	Crack Depth (L_i), mm				
	$i = 1$	2	3	4	5
10 000	0.010	0.008			
20 000	.015	.012	0.010		0.008
30 000	.050	.030	.020	0.010	.018
40 000	.200	.100	.060	.050	.070
50 000	.610	[a][1]	.210	.150	.280
60 000	.950		.510	.300	.420
70 000	1.61		.900	.580	.750
80 000	[b]2.30		[1]	.800	1.25

[a]Indicates crack 2 has joined crack 1 and combined length is given in column 1.
[b]Test terminated when $L_i = B$.

99

Table GII. Sample Data Table for Large-Crack (CCT) Constant-Amplitude Fatigue and Static Fracture Tests

Large-Crack Data Table

Specimen Number: __B614__   Page __1__ of __1__

Width: __75.0__ mm   Thickness: __2.3__ mm

Loading: __Constant amplitude__ $S_{max} = $ __175__ MPa $R = $ __0.5__

S_{max}, MPa	Cycles	L, mm	Comments
175	0	5.00	
	15 000	5.10	
	30 000	5.27	
	40 000	5.53	
	- - -	- - -	
	- - -	- - -	
	- - -	- - -	
	175 500	20.50	
	194 300	25.30	
	- - -	- - -	
	- - -	- - -	
	- - -	- - -	
175	215 300	37.50	Stopped test
248.3		37.50	Pulled to failure

Table GIII. Sample Data Table for Large-Crack (CCT) Threshold Test

Large-Crack Data Table

Specimen Number: __B601__   Page __1__ of __2__

Width: __75.0__ mm   Thickness: __2.3__ mm

Loading: __Threshold test__ S_{max} = __- - -__ MPa R = __-1__

S_{max}, MPa	Cycles	L, mm	Comments
100	0	5.03	Precracking
100	12 000	6.07	
100	25 000	7.18	
100	34 500	9.00	
94	57 000	10.00	Load reduction
88.4	67 000	11.00	
- - -	- - -	- - -	
- - -	- - -	- - -	
- - -	- - -	- - -	
47.6	1 207 000	21.00	
- - -	- - -	- - -	
- - -	- - -	- - -	
- - -	- - -	- - -	

(Test continued)

Table GIV. Sample Data Table for Large-Crack (CCT) Spectrum Test

Large-Crack Data Table

Specimen Number: __B315__   Page __1__ of __1__

Width: __75.0__ mm   Thickness: __2.3__ mm

Loading: __Mini-TWIST__ S_{max} = __210__ MPa R = __- - -__

S_{max}, MPa	Cycles	L, mm	Comments
[a]105	0	5.02	Fatigue precracking
105	5 000	5.05	
105	10 000	6.13	
105	12 000	9.00	
210	0	[b]9.00	Spectrum applied
210	20 000	10.00	
210	35 000	11.02	
- - -	- - -	- - -	
- - -	- - -	- - -	
- - -	- - -	- - -	
210	87 650	20.20	
	87 870		Specimen failed

[a]S_{max} = 50 percent of maximum spectrum stress and R = 0.
[b]Record measurements at about every 1-mm increment.

Appendix H

Plastic-Replica Method

The standard method of recording small-crack data at the notch root of the SENT specimens was the plastic-replica method. A replica of the notch surface was made after each cyclic interval. The cyclic interval was selected so that about 25 to 30 replicas are taken during a test. At each cyclic interval, a specimen was held at constant applied stress while the replica was taken. This stress level is defined later for constant-amplitude and spectrum loading. Replicas were examined for crack-length measurements by either a scanning electron or optical microscope.

Before each replica was made, the notch surface was cleaned with acetone (applied with a cotton swab). The acetyl cellulose replica film (about 0.08 mm thick and cut into pieces about 7 mm by 25 mm) was held in place loosely against the notch surface by a rod that was slightly less than the diameter of the notch. The replica film was centered over the notch with the long dimension of the film lying along the circumference of the notch. A few drops of acetone were allowed to flow between the film and the notch surface. The film was then touched lightly to the specimen surface where it adhered and was left to dry for at least 5 minutes. (Best results were achieved by applying the minimum pressure necessary to cause adherence.) While the replica was in place on the specimen, the replica was inspected with a low-power microscope for bubbles and other artifacts. Any defective replica, such as one containing bubbles, was discarded and a new replica was made. When dry, the replica was removed from the specimen; this was accomplished by grasping the film at one end with tweezers and peeling slowly (peel from top of notch to bottom of notch or vice versa). One of the top corners of the finished replica film was clipped away with scissors to aid in orienting the replica for analysis. Each replica was stored in a container that was labeled with the specimen number and the number of cycles accumulated.

Constant Amplitude Loading

Replicas were made at each cyclic interval while the specimen was held at $S = 0.8S_{max}$. This stress was selected to ensure that any cracks present would be open and, therefore, would leave a clear trace on the replica. Because the stress level was below the maximum stress level, crack growth should not have been affected by the replica process. Previous tests on 2024-T3 aluminum alloy (ref. 30) have shown no significant effect on fatigue life among specimens where replicas were or were not taken. (During small-crack tests on the 7075-T6 aluminum alloy, the replica process did affect the fatigue life and, probably, the growth behavior of the small cracks. These results are discussed in sec. 6.1.)

Spectrum Loading (Mini-TWIST)

For spectrum loading, replicas were made while the loading was being held at one of the peak levels in the spectrum. The spectrum-loading software was written so that after a prescribed period, the loading stopped and held at the next occurrence of the selected peak level. The spectrum loading continued from the point of interruption after the replica was made. For the Mini-TWIST spectrum, load level number VIII (see fig. 2 in ref. 26) was selected for taking replicas. This level corresponds to 59 percent of the maximum load in the spectrum and it occurs in flights 1 and 2001 of the 4000-flight-sequence loading.

Replica Analysis

For observation in the SEM, replicas were gripped at each end in a sample holder and coated with a thin layer of sputtered metal such as Cr or Au-Pd. The electron beam energy of the SEM was lowered to 10 keV to minimize damage to the replica from heating. Even so, at magnifications above 1000 times, the beam should not be focused on one area for extended periods or thermal damage will result. Analysis of the replicas from the last replica to those made early in life permitted easy location of the crack(s). Patterns in the grain structure and inclusion particles were used to locate the crack on the earlier replicas.

Occasionally a replica was twisted or had an unusually large curvature, which made crack length measurements less accurate. For this reason, the position of the crack tip from each replica should be marked on a montage of photographs taken (at high magnification) of the crack when it was large. This method required photographs only of the crack tip area rather than of the entire crack on many of the replicas. Careful calibration of the magnification of the SEM was required for accurate crack length measurements.

For observation in an optical microscope, the replicas may be coated with metal. If the replicas are not coated, then both faces of the replica will be observed under the microscope. A slight bubble pattern may be observed on the face opposite that containing the crack impression. It was still possible to obtain crack length information from an uncoated replica because the image of the bubble pattern was slightly out of focus when the crack image was sharply focused.

References

1. Pearson, S.: Initiation of Fatigue Cracks in Commercial Aluminum Alloys and the Subsequent Propagation of Very Short Cracks. *Eng. Fract. Mech.*, vol. 7, no. 2, June 1975, pp. 235–247.

2. Kitagawa, H.; and Takahashi, S.: Applicability of Fracture Mechanics to Very Small Cracks or the Cracks in the Early Stage. *Proceedings of the Second International Conference on Mechanical Behavior of Materials*, American Soc. for Metals, 1976, pp. 627–631.

3. El Haddad, M. H.: A Study of the Growth of Short Fatigue Cracks Based on Fracture Mechanics. Ph.D. Thesis, Univ. of Waterloo, Aug. 1978.

4. El Haddad, M. H.; Dowling, N. E.; Topper, T. H.; and Smith, K. N.: *J* Integral Application for Short Fatigue Cracks at Notches. *Int. J. Fract.*, vol. 16, no. 1, Feb. 1980, pp. 15–30.

5. Broek, D.: *The Propagation of Fatigue Cracks Emanating From Holes.* NLR-TR-72134-U, National Aerospace Lab. Amsterdam (Netherlands), Nov. 1972.

6. Morris, W. L.; James, M. R.; and Buck, O.: Growth Rate Models for Short Surface Cracks in A12219-T851, *ASME Trans.: Phys. Metall. & Mater. Sci.*, vol. 12A, Jan. 1981, pp. 57–64.

7. Hudak, S. J., Jr.: Small Crack Behavior and the Prediction of Fatigue Life. *J. Eng. Mater. & Technol.*, vol. 103, Jan. 1981, pp. 26–35.

8. Nisitani, H.; and Takao, K.-I.: Significance of Initiation, Propagation, and Closure of Microcracks in High Cycle Fatigue of Ductile Metals. *Eng. Fract. Mech.*, vol. 15, no. 3–4, 1981, pp. 445–456.

9. Schijve, J.: Difference Between the Growth of Small and Large Fatigue Cracks—The Relation to Threshold K-Values. *Fatigue Thresholds—Fundamentals and Engineering Applications*, Volume II, J. Bäcklund, A. F. Blom, and C. J. Beevers, eds., Engineering Materials Advisory Services Ltd., 1982, pp. 881–908.

10. Taylor, D.; and Knott, J. F.: Fatigue Crack Propagation Behavior of Short Cracks—The Effect of Microstructure. *Fatigue Eng. Mater. & Struct.*, vol. 4, no. 2, 1981, pp. 147–155.

11. Leis, B. N.; and Forte, T. P.: Fatigue Growth of Initially Physically Short Cracks in Notched Aluminum and Steel Plates. *Fracture Mechanics: Thirteenth National Symposium*, R. Roberts, ed., Spec. Tech. Publ. 743, American Soc. for Testing & Materials, 1981, pp. 100–124.

12. Lankford, J.: The Growth of Small Fatigue Cracks in 7075-T6 Aluminum. *Fatigue Eng. Mater. & Struct.*, vol. 5, no. 3, 1982, pp. 233–248.

13. Wood, H. A.; Rudd, J. L.; and Potter, J. M.: Evaluation of Small Cracks in Airframe Structures. *Some Considerations on Short Crack Growth Behaviour in Aircraft Structures*, AGARD-R-696, Mar. 1983, pp. 1-1–1-12. (Available from DTIC as AD A130 952.)

14. Anstee, R. F. W.; and Edwards, P. R.: A Review of Crack Growth Threshold and Crack Propagation Rates at Short Crack Lengths. *Some Considerations on Short Crack Growth Behaviour in Aircraft Structures*, AGARD-R-696, Mar. 1983, pp. 2-1–2-12.

15. *Behaviour of Short Cracks in Airframe Components.* AGARD-CP-328, Apr. 1983. (Available from DTIC as AD A131 159.)

16. Leis, B. N.; Kanninen, M. F.; Hopper, A. T.; Ahmad, J.; and Broek, D.: *A Critical Review of the Short Crack Problem in Fatigue.* AFWAL-TR-83-4019, U.S. Air Force, Jan. 1983. (Available from DTIC as AD A131 349.)

17. Miller, K. J.; and De Los Rios, E. R., eds.: The Behaviour of Short Fatigue Cracks. *Mechanical Engineering Publications* (London), 1986.

18. Ritchie, R. O.; and Lankford, J., eds.: *Small Fatigue Cracks.* Metallurgical Soc., Inc., 1986.

19. Newman, J. C., Jr.; and Edwards, P. R.: *Short-Crack Growth Behaviour in an Aluminum Alloy—An AGARD Cooperative Test Programme*, AGARD-R-732, Dec. 1988.

20. Edwards, P. R.; and Newman, J. C., Jr., compilers: *Short-Crack Growth Behaviour in Various Aircraft Materials.* AGARD-R-767, Aug. 1990.

21. Newman, J. C., Jr.: Fracture Mechanics Parameters for Small Fatigue Cracks. *Small-Crack Test Methods*, James M. Larsen and John E. Allison, eds., STP 1149, American Soc. for Testing & Materials, 1992, pp. 6–33.

22. Elber, Wolf: The Significance of Fatigue Crack Closure. *Damage Tolerance in Aircraft Structures*, Spec. Tech. Publ. 486, American Soc. for Testing & Materials, 1971, pp. 230–242.

23. Newman, J. C., Jr.: A Nonlinear Fracture Mechanics Approach to the Growth of Small Cracks. *Behaviour of Short Cracks in Airframe Components*, AGARD-CP-328, Apr. 1983, pp. 6-1–6-26.

24. Minakawa, K.; and McEvily, A. J.: On Near-Threshold Fatigue Crack Growth in Steels and Aluminum Alloys. *Fatigue Thresholds—Fundamentals and Engineering Applications*, Volume I, J. Bäcklund, A. F. Blom, and C. J. Beevers, eds., Engineering Materials Advisory Services Ltd. (United Kingdom), 1982, pp. 373–390.

25. Phillips, E. P.; and Newman, J. C., Jr.: Impact of Small-Crack Effects on Design-Life Calculations. *Exp. Mech.*, vol. 29, June 1989, pp. 221–225.

26. Tan, Paul William N. Y.: The Boundary Force Method for Stress Analysis of Arbitrarily Shaped Plates With Notches and Cracks. D. of Sci. Diss., George Washington Univ., 1986.

27. Lowak, H.; DeJonge, J. B.; Franz, J.; and Schuetz, D.: *MINITWIST: A Shortened Version of TWIST.* LBF-TB-146, Laboratorium fur Betriebsfestigkeit, 1979.

28. Gangloff, R. P.: Electrical Potential Monitoring of Crack Formation and Subcritical Growth From Small Defects. *Fatigue Eng. Mater. & Struct.*, vol. 4, no. 1, 1981, pp. 15–33.

29. Walker, A. C.: *Continuous Fatigue Crack Inspection of Aluminum Alloy Plate Specimens Undergoing Spectrum Loading Using Ultrasonic Surface Waves.* LTR-ST-1465, National Aeronautical Establ., National Research Council of Canada, July 1983.

30. Swain, M. H.; and Newman, J. C., Jr.: On the Use of Marker Loads and Replicas for Measuring Growth Rates for Small Cracks. *Fatigue Crack Topography*, AGARD-CP-376, Nov. 1984, pp. 12-1–12-17.

31. Brown, C. W.; and Smith, G. C.: A Two Stage Plastic Replication Technique for Monitoring Fatigue Crack Initiation and Early Fatigue Crack Growth. *Advances in Crack Length Measurement*, C. J. Beevers, Engineering Materials Advisory Services Ltd. (United Kingdom), 1982, pp. 41–51.

32. Tada, Hiroshi (with the cooperation of Paul C. Paris and George R. Irwin): *The Stress Analysis of Cracks Handbook, Second ed.* Paris Productions Inc., (and Del Research Corp.), 1985.

33. Raju, I. S.; and Newman, J. C., Jr.: *Three-Dimensional Finite-Element Analysis of Finite-Thickness Fracture Specimens.* NASA TN D-8414, 1977.

34. Raju, I. S.; and Newman, J. C., Jr.: Stress-Intensity Factors for a Wide Range of Semi-Elliptical Surface Cracks in Finite-Thickness Plates. *Eng. Fract. Mech.*, vol. 11, no. 4, 1979, pp. 817–829.

35. Shivakumar, K. N.; and Newman, J. C., Jr.: ZIP3D: *An Elastic and Elasti-Plastic Finite-Element Analysis Program for Cracked Bodies.* NASA TM-102753, 1990.

36. Nikishkov, G. P.; and Atluri, S. N.: An Equivalent Domain Integral Method for Computing Crack-Tip Integral Parameters in Non-Elastic, Thermo-Mechanical Fracture. *Eng. Fract. Mech.*, vol. 26, no. 6, 1987, pp. 851–867.

37. Shivakumar, K. N.; Tan, P. W.; and Newman, J. C., Jr.: A Virtual Crack-Closure Technique for Calculating Stress Intensity Factors for Cracked Three-Dimensional Bodies. *Int. J. Fract.*, vol. 36, Mar. 1988, pp. R43–R50.

38. Folias, Efthymios S.: Some Remarks on Three-Dimensional Fracture. *Fracture Mechanics—Proceedings of the Nineteenth National Symposium*, Thomas A. Cruse, ed., Spec. Tech. Publ. 969, American Soc. for Testing & Materials, 1988, pp. 56–72.

39. Zhao, W.; Wu, X. R.; and Yan, M. G.: Weight Function Method for Three-Dimensional Crack Problems. I. Basic Formulation and Application to an Embedded Elliptical Crack in Finite Plates. *Eng. Fract. Mech.*, vol. 34, no. 3, 1989, pp. 593–607.

40. Zhao, W.: Weight Function Theory and Application for Analysis of Three-Dimensional Crack Problems. D. of Sci. Diss., Inst. of Aeronautical Materials, 1988.

41. Fujimoto, W. T.: Determination of Crack Growth and Fracture Toughness Parameters for Surface Flaws Emanating From Fastener Holes. *Proceedings—AIAA/ASME/SAE 17th Structures, Structural Dynamics, and Material Conference*, May 1976, pp. 522–531.

42. Dill, H. D.; and Saff, C. R.: *Environment Load Interaction Effects on Crack Growth.* AFFDL-TR-78-137, U.S. Air Force, Nov. 1978. (Available from DTIC as AD A071 660.)

43. Saff, C. R.; and Sanger, K. B.: Part-Through Flaw Stress Intensity Factors Developed by a Slice Synthesis Technique. *Fracture Mechanics: Fifteenth Symposium*, R. J. Sanford, ed., ASTM Spec. Tech. Publ. 833, American Soc. for Testing & Materials, 1984, pp. 24–43.

44. Wu, X. R.; and Carlsson, J.: The Generalized Weight Function Method for Crack Problems With Mixed Boundary Conditions. *J. Mech. Phys. Solids*, vol. 31, no. 6, 1983, pp. 485–497.

45. Wu, X. R.: Approximate Weight Functions for Center and Edge Cracks in Finite Bodies. *Eng. Fract. Mech.*, vol. 20, no. 1, 1984, pp. 35–49.

46. Wu, X. R.: *Weight Functions and Stress Intensity Factors for Radial Crack(s) Emanating From a Circular Hole in an Infinite Sheet.* Rep. 63, Royal Inst. of Technology (Stockholm, Sweden), Oct. 1985.

47. Wu, Xue-Ren; and Carlsson, A. Janne: *Weight Functions and Stress Intensity Factor Solutions.* Pergamon Press, Inc., 1991.

48. Zhao, W.; Wu, X. R.; and Yan, M. G.: Weight Function Method for Three Dimensional Crack Problems. II. Application to Surface Cracks at a Hole in Finite Thickness Plates under Stress Gradients. *Eng. Fract. Mech.*, vol. 34, no. 3, 1989, pp. 609–624.

49. Zhao, W.; and Wu, X. R.: Stress Intensity Factor Evaluation by Weight Function for Surface Crack in Edge Notch. *Theor. & Appl. Fract. Mech.*, vol. 13, July 1990, pp. 225–238.

50. Zhao, W.; and Wu, X. R.: Stress Intensity Factor for Corner Cracks at a Semi-Circular Notch Under Stress

Gradients. *Fatigue & Fract. Eng. Mater. & Struct.*, vol. 13, no. 4, 1990, pp. 347–360.

51. Tan, Paul W.; Raju, Ivatury S.; and Newman, James C., Jr.: Boundary Force Method for Analyzing Two-Dimensional Cracked Plates. *Fracture Mechanics: Eighteenth Symposium*, D. T. Read and R. P. Reed, eds., ASTM Spec. Tech. Publ. 945, 1988, pp. 259–277.

52. Muskhelishvili, N. I. (J. R. M. Radok, transl.): *Some Basic Problems of the Mathematical Theory of Elasticity — Fundamental Equations, Plane Theory of Elasticity, Torsion, and Bending.* P. Noordhoff Ltd. (Groningen, Netherlands), 1963.

53. Erdogan, Fazil: On the Stress Distribution in Plates With Collinear Cuts Under Arbitrary Loads. *Proceedings of the Fourth U.S. National Congress of Applied Mechanics*, Volume I, American Soc. of Mechanical Engineers, 1962, pp. 547–553.

54. James, L. A.; and Anderson, W. E.: A Simple Experimental Procedure for Stress Intensity Factor Calibration. *Eng. Fract. Mech.*, vol. 1, 1969, pp. 565–568.

55. Newman, J. C., Jr.; and Raju, I. S.: Prediction of Fatigue Crack-Growth Patterns and Lives in Three-Dimensional Cracked Bodies. *Advances in Fracture Research*, Volume 3, S. R. Valluri, D. M. R. Taplin, P. Rama Rao, J. F. Knott, and R. Dubey, eds., Pergamon Press, Inc., 1986, pp. 1597–1608.

56. Newman, J. C., Jr.: *FASTRAN II: A Fatigue Crack Growth Structural Analysis Program.* NASA TM-104159, 1992.

57. Yoder, G. R.; Cooley, L. A.; and Crooker, T. W.: *On Microstructural Control of Near Threshold Fatigue Crack Growth in 7000 Series Aluminum Alloys.* NRL-MR-4787, U.S. Navy, Apr. 1982. (Available from DTIC as AD A113 486.)

58. Wanhill, R. J. H.: Low Stress Intensity Fatigue Crack Growth in 2024-T3 and T351. *Eng. Fract. Mech.*, vol. 30, no. 2, 1988, pp. 233–260.

59. Hudson, C. Michael: *Effect of Stress Ratio on Fatigue-Crack Growth in 7075-T6 and 2024-T3 Aluminum Alloy Specimens.* NASA TN D-5390, 1969.

60. Gao, Ming; Pao, P. S.; and Wei, R. P.: Chemical and Metallurgical Aspects of Environmentally Assisted Fatigue Crack Growth in 7075-T651 Aluminum Alloy. *Metall. Trans. A.*, vol. 19A, July 1988, pp. 1739–1750.

61. Bowles, C. Q.; and Schijve, J.: The Role of Inclusions in Fatigue Crack Initiation in an Aluminum Alloy. *Int. J. Fract.*, vol. 9, no. 2, June 1973, pp. 171–179.

62. Schijve, J.; Jacobs, F. A.; and Tromp, P. J.: *The Significance of Cladding for Fatigue of Aluminum Alloys in Aircraft Structures.* NLR-TR-76065-U, National Aerospace Lab. (Amsterdam, Netherlands), Sept. 1976.

63. Lee, J. J.; and Sharpe, W. N., Jr.: Short Fatigue Cracks in Notched Aluminum Specimens. *Small Fatigue Cracks*, Robert O. Ritchie and James Lankford, eds., Metallurgical Soc., Inc., 1986, pp. 323–339.

64. Newman, J. C., Jr.; Swain, M. H.; and Phillips, E. P.: An Assessment of the Small-Crack Effect for 2024-T3 Aluminum Alloy. *Small Fatigue Cracks*, Robert O. Ritchie and James Lankford, eds., Metallurgical Soc., Inc., 1986, pp. 427–452.

65. Newman, J. C., Jr.: A Crack-Closure Model for Predicting Fatigue Crack Growth Under Aircraft Spectrum Loading. *Methods and Models for Predicting Fatigue Crack Growth Under Random Loading*, J. B. Chang and C. M. Hudson, eds., Spec. Tech. Publ. 748, American Soc. for Testing & Materials, 1981, pp. 53–84.

66. Dugdale, D. S.: Yielding of Steel Sheets Containing Slits. *J. Mech. Phys. Solids*, vol. 8, 1960, pp. 100–104.

67. Fleck, Norman A.; and Newman, James C., Jr.: Analysis of Crack Closure Under Plane Strain Conditions. *Mechanics of Fatigue Crack Closure*, J. C. Newman, Jr., and Wolf Elber, eds., Spec. Tech. Publ. 982, American Soc. for Testing & Materials, 1988, pp. 319–341.

68. Irwin, G. R.: Structural Aspects of Brittle Fracture. *Appl. Mater. Res.*, vol. 3, no. 2, Apr. 1964, pp. 65–81.

69. Phillips, Edward P.: The Influence of Crack Closure on Fatigue Crack Growth Thresholds in 2024-T3 Aluminum Alloy. *Mechanics of Fatigue Crack Closure*, J. C. Newman, Jr., and Wolf Elber, eds., Spec. Tech. Publ. 982, American Soc. for Testing & Materials, 1988, pp. 505–515.

70. Newman, J. C., Jr.; Poe, C. C., Jr.; and Dawicke, D. S.: Proof Test and Fatigue Crack Growth Modeling on 2024-T3 Aluminum Alloy. *Fatigue 90 – Proceedings of the 4th International Conference on Fatigue and Fatigue Thresholds*, Volume 4, Hideo Kitagawa and Tsuneschichi Tanaka, eds., Materials and Component Engineering Publ., Ltd. (Birmingham, England), 1990, pp. 2407–2416.

71. Newman, J. C., Jr.: A Crack Opening Stress Equation for Fatigue Crack Growth. *Int. J. Fract.*, vol. 24, no. 4, Apr. 1984, pp. R131–R135.

72. Newman, J. C., Jr.; and Raju, I. S.: *Analyses of Surface Cracks in Finite Plates Under Tension or Bending Loads.* NASA TP-1578, 1979.

73. Jolles, M.; and Tortoriello, V.: Geometry Variations During Fatigue Growth of Surface Flaws. *Fracture Mechanics: Fourteenth Symposium—Volume I: Theory and Analysis*, J. C. Lewis and George Sines, eds., ASTM Spec. Tech. Publ. 791, American Soc. for Testing & Materials, 1983, pp. I-297–I-307.

74. Vogelesang, L. B.: *The Effect of Environment on the Transition From Tensile Mode to Shear Mode During Fatigue Crack Growth in Aluminum Alloys: A Model for Environmentally Assisted Crack Growth.* Rep. VTH-LR-286, Delft Univ. of Technology, Oct. 1979.

75. Schijve, J.: Significance of Fatigue Cracks in Micro-Range and Macro-Range. *Fatigue Crack Propagation,* ASTM Spec. Tech. Publ. 415, American Soc. for Testing & Materials, 1967, pp. 415–457.

76. Ravichandran, Kakkaveri S.; and Larsen, James M.: Behavior of Small and Large Fatigue Cracks in Ti-24Al-11 Nb: Effects of Crack Shape, Microstructure, and Closure. *Fracture Mechanics: Twenty-Second Symposium* (Volume I), H. A. Ernst, A. Saxena, and D. L. McDowell, eds., STP 1131 (Volume I), American Soc. for Testing & Materials, 1992, pp. 727–748.

77. Raju, I. S.; and Newman, J. C., Jr.: Stress Intensity Factors for Two Symmetric Corner Cracks. *Fracture Mechanics: Proceedings of the Eleventh National Symposium.* Part 1, C. W. Smith, ed., Spec. Tech. Publ. 677, American Soc. for Testing & Materials, 1979, pp. 411–430.

78. Newman, J. C., Jr.; and Raju, I. S.: Stress Intensity Factor Equations for Cracks in Three-Dimensional Finite Bodies. *Fracture Mechanics: Fourteenth Symposium— Volume I: Theory and Analysis,* J. C. Lewis and George Sines, eds., ASTM Spec. Tech. Publ. 791, American Soc. for Testing & Materials, 1983, pp. I-238–I-265.

79. Hartranft, R. J.; and Sih, G. C.: An Approximate Three-Dimensional Theory of Plates With Application to Crack Problems. *Int. J. Eng. Sci.,* vol. 8, no. 8, Aug. 1970, pp. 711–729.

80. Nishioka, T.; and Atluri, S. N.: An Alternating Method for Analysis of Surface-Flawed Aircraft Structural Components. *AIAA J.,* vol. 21, May 1983, pp. 749–757.

81. Tan, P. W.; Raju, I. S.; Shivakumar, K. N.; and Newman, J. C., Jr.: Evaluation of Finite-Element Models and Stress-Intensity Factors for Surface Cracks Emanating From Stress Concentrations. *Surface-Crack Growth: Models, Experiments and Structures,* Walter G. Reuter, John H. Underwood, and James C. Newman, Jr., eds., Spec. Tech. Publ. 1060, American Soc. for Testing & Materials, 1990, pp. 34–48.

82. DeLorenzi, Horst G.: Energy Release Rate Calculations by the Finite Element Method. *Eng. Fract. Mech.,* vol. 21, no. 1, 1985, pp. 129–143.

83. Shivakumar, K. N.; and Raju, I. S.: Treatment of Singularites in Cracked Bodies, *Int. J. Fract.,* vol. 45, no. 3, Oct. 1, 1990, pp. 159–178.

84. Tan, P. W.; Bigelow, C. A.; and Newman, J. C., Jr.: Three-Dimensional Finite-Element Analyses of Corner Cracks at Stress Concentrations. *Durability of Metal Aircraft Structures,* S. N. Atluri, C. E. Harris, A. Hoggard, N. Miller, and S. G. Sampath, eds., Atlanta Technology Publ., 1992, pp. 187–199.

85. Shivakumar, K. N.; and Newman, J. C., Jr.: Stress Intensity Factors for Large Aspect Ratio Surface and Corner Cracks at a Semi-Circular Notch in a Tension Specimen. *Eng. Fract. Mech.,* vol. 38, no. 6, 1991, pp. 467–473.

86. Zhao, W.; Wu, X. R.; and Yan, M. G.: Stress Intensity Factors for Corner Cracks at a Circular Hole under Remote Tension, *Acta Mechanica Sinica,* vol. 7, 1991, pp. 76-81.

87. Bueckner, H. F.: Novel Principle for the Computation of Stress Intensity Factors. *Z. Angew. Math. & Mech.,* vol. 50, Sept. 1970, pp. 529–546.

88. Rice, J. R.: Some Remarks on Elastic Crack-Tip Stress Fields. *Int. J. Solids & Struct.,* vol. 8, June 1972, pp. 751–758.

89. Wu, X. R.; and Zhao, W.: Dugdale Model Solution for Compact Specimen. *Mechanical Behaviour of Materials— Proceedings of the 5th International Conference,* Volume 1, Pergamon Press, Inc., 1988, pp. 243–248.

90. Irwin, G. R.: Crack-Extension Force for a Part-Through Crack in a Plate. *Trans. ASME, Ser. E: J. Appl. Mech.,* vol. 29, no. 4, Dec. 1962, pp. 651–654.

91. Shah, R. C.; and Kobayashi, A. S.: Stress-Intensity Factor for an Elliptical Crack Under Arbitrary Normal Loading. *Eng. Fract. Mech.,* vol. 3, July 1971, pp. 71–96.

92. Grandt, A. F., Jr.: Crack Face Pressure Loading of Semielliptical Cracks Located Along the Bore of a Hole. *Eng. Fract. Mech.,* vol. 14, no. 4, 1981, pp. 843–852.

93. Newman, J. C., Jr.; and Raju, I. S.: Stress-Intensity Factor Equations for Cracks in Three-Dimensional Finite Bodies Subjected to Tension and Bending Loads. *Computational Methods in the Mechanics of Fracture,* Satya N. Atluri, ed., Volume 2 in Computational Methods in Mechanics, Elsevier Science Publ. Co., Inc., 1986, pp. 311–334.

REPORT DOCUMENTATION PAGE

Public reporting burden for this collection of information is estimated to average 1 hour per response, including the time for reviewing instructions, searching existing data sources, gathering and maintaining the data needed, and completing and reviewing the collection of information. Send comments regarding this burden estimate or any other aspect of this collection of information, including suggestions for reducing this burden, to Washington Headquarters Services, Directorate for Information Operations and Reports, 1215 Jefferson Davis Highway, Suite 1204, Arlington, VA 22202-4302, and to the Office of Management and Budget, Paperwork Reduction Project (0704-0188), Washington, DC 20503.

1. AGENCY USE ONLY *(Leave blank)*	2. REPORT DATE May 1994	3. REPORT TYPE AND DATES COVERED Reference Publication

4. TITLE AND SUBTITLE
Small-Crack Effects in High-Strength Aluminum Alloys
A NASA/CAE Cooperative Program

5. FUNDING NUMBERS
WU 505-63-50-04

6. AUTHOR(S)
J. C. Newman, Jr., X. R. Wu, S. L. Venneri, and C. G. Li

7. PERFORMING ORGANIZATION NAME(S) AND ADDRESS(ES)
NASA Langley Research Center
Hampton, VA 23681-0001

8. PERFORMING ORGANIZATION REPORT NUMBER
L-17244

9. SPONSORING/MONITORING AGENCY NAME(S) AND ADDRESS(ES)
National Aeronautics and Space Administration
Washington, DC 20546-0001

10. SPONSORING/MONITORING AGENCY REPORT NUMBER
NASA RP-1309

11. SUPPLEMENTARY NOTES
Newman: Langley Research Center, Hampton, VA; Wu and Li: Institute of Aeronautical Materials, Beijing, People's Republic of China; Venneri: National Aeronautics and Space Administration, Washington, D.C.

12a. DISTRIBUTION/AVAILABILITY STATEMENT

Unclassified–Unlimited

Subject Category 39

12b. DISTRIBUTION CODE

13. ABSTRACT *(Maximum 200 words)*
The National Aeronautics and Space Administration and the Chinese Aeronautical Establishment participated in a Fatigue and Fracture Mechanics Cooperative Program. The program objectives were to identify and characterize crack initiation and growth of small cracks (10 μm to 2 mm long) in commonly used US and PRC aluminum alloys, to improve fracture mechanics analyses of surface- and corner-crack configurations, and to develop improved life-prediction methods. Fatigue and small-crack tests were performed on single-edge-notch tension (SENT) specimens and large-crack tests were conducted on center-crack tension specimens for constant-amplitude (stress ratios of -1, 0, and 0.5) and Mini-TWIST spectrum loading. The plastic replica method was used to monitor the initiation and growth of small fatigue cracks at the semicircular notch. Crack-growth results from each laboratory on 7075-T6 bare and LC9cs clad aluminum alloys agreed well and showed that fatigue life was mostly crack propagation from a material defect (inclusion particles or void) or from the cladding layer. Finite-element and weight-function methods were used to determine stress intensity factors for surface and corner cracks in the SENT specimens. Equations were then developed and used in a crack-growth and crack-closure model to correlate small- and large-crack data and to make life predictions for various load histories. The cooperative program produced useful experimental data and efficient analysis methods for improving life predictions. The results should ultimately improve aircraft structural reliability and safety.

14. SUBJECT TERMS
Fatigue; Fracture mechanics; Small cracks; Weight function; Finite elements; Crack closure

15. NUMBER OF PAGES
118

16. PRICE CODE
A06

17. SECURITY CLASSIFICATION OF REPORT Unclassified	18. SECURITY CLASSIFICATION OF THIS PAGE Unclassified	19. SECURITY CLASSIFICATION OF ABSTRACT	20. LIMITATION OF ABSTRACT